Material and Structural Performance of Fiber-Reinforced Polymer Composites at Elevated and High Temperatures

THÈSE N^{O} 4340 (2009)

PRÉSENTÉE LE 11 MARS 2009

À LA FACULTÉ ENVIRONNEMENT NATUREL, ARCHITECTURAL ET CONSTRUIT
LABORATOIRE DE CONSTRUCTION EN COMPOSITES
PROGRAMME DOCTORAL EN STRUCTURES

ÉCOLE POLYTECHNIQUE FÉDÉRALE DE LAUSANNE

POUR L'OBTENTION DU GRADE DE DOCTEUR ÈS SCIENCES

PAR

Yu BAI

acceptée sur proposition du jury:

Prof. E. Brühwiler, président du jury
Prof. T. Keller, directeur de thèse
Dr E. Hugi, rapporteur
Dr Y. Wang, rapporteur
Prof. X.-L. Zhao, rapporteur

ÉCOLE POLYTECHNIQUE
FÉDÉRALE DE LAUSANNE

Suisse
2009

Contents

Appendices on CD-ROM

Abstract

As the range of applications for fiber-reinforced polymer (FRP) composite materials in civil engineering constantly increases, there is more and more concern with regard to their performance in critical environments. The fire behavior of composite materials is especially important since complex physical and chemical processes such as the glass transition and decomposition occur when these materials are subjected to elevated and high temperatures, possibly leading to considerable loss of stiffness and strength.

This stiffness and strength degradation in composite materials under elevated and high temperatures is the result of changes in polymer molecular structures. When polyester thermosets are subjected to elevated and high temperatures, they undergo three transitions (glass transition, leathery-to-rubbery transition, and rubbery-to-decomposed transition), corresponding to four different states (glassy, leathery, rubbery and decomposed). At a certain temperature, a composite material can therefore be considered as a mixture of materials that are in different states. As the content of each state varies with temperature, the composite material exhibits temperature-dependent properties. Since these changes in state can be described using kinetic theory, the quantity of material in each state can be estimated and the thermophysical and thermomechanical properties of the mixture can thus be determined.

These concepts formed a basis for the development of thermophysical and thermomechanical property sub-models for composites at elevated and high temperatures and even for the description of post-fire status. Incorporating these thermophysical property sub-models into a heat transfer governing equation, thermal responses were calculated using a finite difference method. Integrating the thermomechanical property sub-models within structural theory, the mechanical responses were described using a finite element method and the time-to-failure was also predicted by defin-

ing a failure criterion.

The modeling results for temperature responses, mechanical responses and post-fire behavior were compared with those obtained from structural endurance experiments on full-scale cellular GFRP (glass fiber-reinforced polymer, in this case polyester resin) panels subjected to a four-point bending configuration and fire from one side. The modeling results for time-to-failure were compared with those from the experiments carried out on GFRP tubes under combined compressive and thermal loadings. In each experimental setup, two different thermal boundary conditions were investigated – with and without water cooling through specimen cells – and good agreement was found.

The understanding gained and modeling of the behavior of GFRP composites under elevated and high temperatures carried out in this thesis could be applicable for different composite materials, and also benefit investigations regarding both active and passive fire protection techniques in order to improve the fire resistance of structures made of such materials.

Keywords:
Polymer-matrix composites; thermophysical properties; thermomechanical properties; thermal responses; mechanical responses; post-fire behavior; time-to-failure; modeling; finite difference method; finite element method

Résumé

Le nombre d'applications pour les matériaux composites, tels que les polymères renforcés de fibres (FRP), dans le génie civil augmente constamment ; il y a de plus en plus de questions à l'égard de leurs performances dans des environnements critiques. Le comportement au feu des matériaux composites est particulièrement important, puisque des processus physiques et chimiques complexes, tels la transition vitreuse et de la décomposition, se produisent lorsque ces matériaux sont soumis à des températures modérées à élevées ; par conséquent la perte de rigidité et de résistance sont des questions auxquelles in convient de trouver une réponse.

La dégradation de la rigidité et de la résistance de matériaux composites sous l'effet des températures modérées à élevées est le résultat de changements dans la structure moléculaire des polymères. Quand les résines de polyester thermodurcissables sont soumises à des températures modérées à élevées, ils subissent différentes transitions. À une température donnée, un matériau composite peut donc être considéré comme un mélange de matériaux qui se trouve dans des états différents. Comme la proportion de chaque état varie avec la température, le matériau composite présente des propriétés dépendantes de cette dernière. Ces changements dans l'état peuvent être décrits en utilisant la théorie cinétique, la quantité de matière dans chaque état peut être estimée et aussi les propriétés thermophysiques et thermomécaniques du mélange peuvent donc être déterminées.

Ces concepts forment une base pour le développement de sous-modèles décrivant les propriétés thermophysiques et thermomécaniques de matériaux composites soumis à des températures élevées, de même pour la description du comportement postèrerieure à l'exposition au feu. Par l'intégration des sous-modèles décrivant les propriétés thermophysiques dans l'équation du transfert de chaleur, les réponses thermiques ont été calcu-

lées selon une méthode des différences finies. Quant à l'intégration des sous-modèles décrivant les propriétés thermomécaniques dans une théorie structurelle, les réponses mécaniques ont été décrites en utilisant une méthode des éléments finis et le temps-à-rupture a aussi été prédit par la définition d'un critère de rupture.

Les résultats de modélisation des réponses thermiques, des réponses mécaniques et comportement postèrerieure à l'exposition au feu ont été comparés avec ceux obtenus à partir des essais d'endurance structurelle, effectuées à grande échelle cellulaire sur panneaux PRFV (polymère renforcé de fibre de verre, dans ce cas, résine de polyester) soumis à une flexion en quatre points et au feu d'un côté. Les résultats de la modélisation de temps-à-rupture ont été comparés à ceux des essais effectués sur des tubes de PRFV sous l'effet combiné de compression et de charges thermiques. Pour chaque essai, deux conditions aux limites thermiques ont été étudiées – avec et sans refroidissement à l'eau par le biais des cellules des échantillons - une bonne entente entre les résultats des essais et la modélisation a été trouvée.

La compréhension acquise et la modélisation du comportement des composites de PRFV sous l'effet des températures modérées à élevées, réalisée dans cette thèse pourrait être applicable pour des différents matériaux composites, et également sera bénéfique aux enquêtes concernant à la fois les techniques active et passive de protection contre l'incendie afin d'améliorer la résistance au feu des structures construites de ces matières.

Mots-clés:

Polymère composites à matrice; propriétés thermophysiques; propriétés thermomécanique; réponses thermiques; réponses mécaniques; comportement post-incendie; temps à rupture; modélisation; méthode des différences finies; méthode des éléments finis

Zusammenfassung

Ein stetig wachsender Einsatz von glas- und kohlefaserverstärkten Kunststoffen (GFK/CFK) im Hoch- und Tiefbau erfordert eine genaue Betrachtung dieser Verbundwerkstoffe in kritischen Umgebungen. Das Brandverhalten ist dabei besonders wichtig, da unter erhöhten und hohen Temperaturen komplexe physikalische und chemische Prozesse wie Glasübergang und Zersetzungen der Kunststoffe auftreten, die zu einem erheblichen Steifigkeits- und Festigkeitsverlust führen können.

Die Veränderungen der molekularen Strukturen der Kunststoffe unter erhöhten und hohen Temperaturen sind Grund für diesen Steifigkeits- und Festigkeitsverlusts. Werden Polyester-Duroplaste erhöhten und hohen Temperaturen ausgesetzt durchlaufen sie drei Veränderungen (glas-zu-ledrig, ledrigen-zu-gummiartig, und gummiartig-zu-zersetzt) mit vier verschiedenen Zuständen (glasig, ledrigen, gummiartige und zersetzt). Bei einer bestimmten Temperatur kann daher ein Verbundwerkstoff als eine Mischung aus Materialien in verschiedenen Zuständen bezeichnet werden. Da die Anteile der verschiedenen Zustände in den Kunststoffen von der Temperatur abhängig sind, haben Verbundwerkstoffe temperaturabhängige Eigenschaften. Da diese Zustandsveränderungen nach der kinetischen Theorie beschrieben werden können, kann der Anteil jedes Zustandes abgeschätzt werden und somit die thermophysikalischen und thermomechanische Eigenschaften des Verbundwerkstoffes ermittelt werden.

Dieses Konzept bildet sowohl die Grundlage für die Entwicklung von Submodellen von thermophysikalischen und thermomechanische Eigenschaften von GFK bei erhöhten und hohen Temperaturen, als auch für die Beschreibung der Eigenschaften nach dem Brand. Die Einbeziehung der Submodelle von thermophysikalischen Eigenschaften in die Wärmegleichung mit Hilfe der Finite-Differenzen-Methode ermöglichte die Bestim-

mung des thermischen Verhaltens. Zur Beschreibung des mechanischen Verhaltens wurden die Submodelle der thermomechanischen Eigenschaften in der Finiten Elemente Methode integriert und die Dauer bis zum Bruch unter einem definierten Versagenskriterium vorhergesagt.

Die Ergebnisse der Modellierung des temperaturabhängigen Verhaltens, des mechanischen Verhaltens und des Verhaltens nach dem Brand wurden mit Tragfähigkeitsversuchen an grossmassstäblichen GFK Hohlkörperplatten (mit Polyester-Harz) verglichen. Bei den Versuchen handelte es sich um Vier-Punkt-Biegeversuche unter einseitiger Brandlast. Des Weiteren wurden die Ergebnisse der Modellierung für die Standzeit unter Brandlast mit experimentellen Ergebnissen von GFK-Rohren unter kombinierter Druck- und Temperaturlast verglichen. In beiden Versuchen wurden zwei unterschiedliche thermische Randbedingungen untersucht: mit und ohne Wasserkühlung. Die Modellierung zeigte in beiden Fällen eine gute Übereinstimmung mit den Versuchsergebnissen.

Das in dieser Arbeit gewonnene Verständnis und die erarbeiteten numerischen Modelle zur Beschreibung des Verhaltens von GFK-Profilen unter erhöhten und hohen Temperaturen können auf verschiedene faserverstärkte Kunststoffmaterialien übertragen werden. Des Weiteren können weitere Untersuchungen von aktiven und passiven Brandschutzmassnahmen darauf aufbauen, um den Feuerwiderstand von Strukturen aus faserverstärkten Kunststoffen zu verbessern.

Schlagwörter:
Polymer-Matrix-Verbundwerkstoffe; thermophysikalische Eigenschaften; thermomechanische Eigenschaften; thermische Reaktionen, mechanische Eigenschaften; Nachbrand-Verhalten; Standzeit unter Brandlast; Modellierung, Finite-Differenzen-Methode; Finite-Elemente-Methode

Acknowledgements

In the course of my doctoral research, I have been fortunate enough to be supported and inspired by a large group of colleagues and friends. I would like to express my most sincere gratitude to:

Professor Dr. Thomas Keller for offering me the opportunity to do this research, for his support, guidance and counsel, and for his trust in me right from the beginning;

The Swiss National Science Foundation for providing the funding for the research (Grant Nos. 200020-109679/1 and 117592/1);

Fiberline Composites, Denmark for their generous donation of the experimental materials;

My thesis defense committee for the time and effort they devoted to reading and evaluating the thesis: Dr. Erich Hugi, Laboratory for Fire Testing, EMPA, Switzerland; Prof. XiaoLing Zhao, Department of Civil Engineering, Monash University, Australia; Dr. YongChang Wang, School of Mechanical, Aerospace and Civil Engineering, University of Manchester, UK; and Prof. Eugen Brühwiler, Laboratory of Maintenance and Safety of Structures (MCS), EPFL, Switzerland.

Dr. Till Vallée for our fruitful discussions concerning many different fields, and for his constant encouragement;

Dr. Aixi Zhou for introducing me to the new topic of composites, and for his suggestions with regard to scientific research;

Dr. Craig Tracy for providing me with much valuable and detailed experimental information, and for selflessly sharing his unique knowledge and experience relating to this topic with me;

Professor Dr. Jack Lesko and his group, especially Dr. Nathan L. Post, for their support with the experiments performed at Virginia Tech., USA, to investigate the thermophysical and thermomechanical properties of an E-glass fiber-reinforced polyester composite;

Mr. François Bonjour for conducting the dynamic mechanical analysis tests at the laboratory of composite and polymer technology (LTC), EPFL;

The technicians at IS-EPFL for their steadfast support with the experimental work: Sylvain Demierre, Gilles Guignet, Gérald Rouge, Patrice Gallay, François Perrin, Roland Gysler, and Hansjakob Reist;

Margaret Howett for her scrupulous English corrections;

Magdalena Schauenberg and Marlène Sommer for their administrative support;

My colleagues at CClab-EPFL – Dr. Anastasios Vasilopoulos, Dr. Julia DeCastro, Dr. Florian Riebel, Dr. Erika Schaumann, Ye Zhang, Behzad Dehghan, Ping Zhu, Omar Moussa, and Roohollah Sarfaraz Khabbaz – for their help and friendship and for creating an international environment that broadened my views of other cultures.

Lastly my gratitude goes to my family – my mother ShouFeng He, my father FuYuan Bai, my sister Lin Bai – for the unconditional love and commitment they have always shown towards me; and my wife Li Jiang, to whom I am forever indebted for her tireless support and understanding, which I will never forget.

CHAPTER 1

Introduction

1 Introduction

1.1 Motivation

The increasing use of fiber-reinforced polymer (FRP) composites in major load-bearing structures presents material scientists and structural engineers with many challenges. One of these challenges involves the understanding and prediction of the changes in the thermophysical and thermomechanical properties and resulting thermomechanical responses of FRP composites under elevated (30- 200°C) and high (> 200°C) temperatures.

The progressive changes that occur in the thermophysical and thermomechanical properties of FRP composites with increasing temperature result from the alteration in the molecular structure of their polymer component. The bonds existing in thermoset polymers (which have frequently been used as the resin in composite materials) can be divided into two major groups: primary and secondary. The first group includes the strong covalent intra-molecular bonds in the polymer chains and cross-links. The dissociation energy of such bonds varies between 50 and 200 kcal/mol. Secondary bonds include much weaker bonds, e.g. hydrogen bonds (dissociation energy: 3-7 kcal/mol), dipole interaction (1.5-3 kcal/mol), and Van der Waals interaction (0.5-2 kcal/mol). Consequently, secondary bonds can be much more easily dissociated.

When temperature increases, secondary bonds are broken during glass transition and the material state changes from glassy to leathery. As temperature is raised further, the polymer chains form entanglement points where molecules, because of their length and flexibility, become knotted together. This state, designated the rubbery state, is also characterized by intact primary and broken secondary bonds, but in an entangled molecular structure. When even higher temperatures are reached, the primary bonds

are also broken and the material decomposes, which is known as the decomposition process.

Consequently, four different states (glassy, leathery, rubbery and decomposed) and three transitions or processes (glass transition, leathery-to-rubbery transition and decomposition) can be defined when temperature is raised in accordance with statistical mechanics, since an aggregation of a large population of molecules (or other functional units) changes continuously from one state to another.

These physical and chemical processes lead to an obvious degradation of the stiffnesses and strengths of FRP composite materials. Figure 1 shows a cross section of the lower face sheet of a DuraSpan® bridge deck (E-glass fiber-reinforced polyester resin) subjected to an ISO-834 fire curve (in a high temperature range up to 1000°C) on the underside. It can be seen that almost all the resin was decomposed, leaving only the fibers in the pultrusion direction, but since these fibers no longer provide composite action, the load-bearing capacity of such a deck is considerably reduced.

Fig. 1. Cross section of FRP profile after fire exposure

Even if temperature is increased to only approximately 200°C in an elevated range, most of the E-modulus of a polyester matrix FRP material has already been lost, as demonstrated in Fig. 2 by the dynamic mechanical analysis (DMA) of such material using a three-point bending setup.

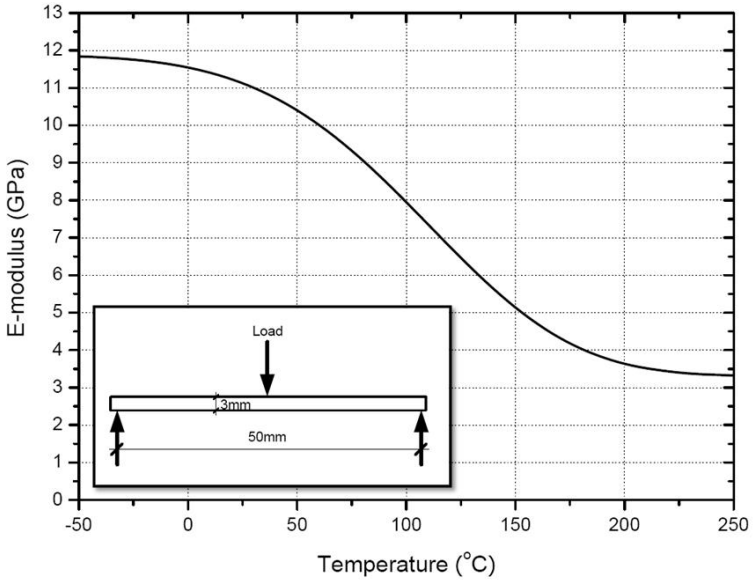

Fig. 2. E-modulus degradation of FRP composites in elevated temperature range measured by DMA (see Section 2.2 for details)

If FRP composites are to be used in load-bearing structural applications, it must be possible to build structures that resist extended excessive heating and/or fire exposure and to understand, model and predict their endurance when subjected to structural loads for long durations. The increasing application of FRP materials in structures requiring extended excessive heating resistance and/or fire resistance, such as building structures, necessitates a study of the changes that occur in the thermophysical and thermomechanical properties and resulting thermomechanical responses of large-scale and complex composite structures over longer time periods.

Most of the previous studies concerning FRP composites under elevated and high temperatures involve military applications and marine and offshore structures. The required endurance times for marine and offshore composite structures are longer than for the initial military applications, though they are still low in comparison to civil infrastructure, especially in building construction. For example, most multistory buildings in Switzerland (and many other countries) are required to resist 90 minutes of fire exposure. It has been recognized that structural system behavior under excessive heating and fire conditions should be considered as an integral

part of structural design, whereas only very limited research has been conducted concerning the progressive thermomechanical and thermostructural behavior of FRP composites for building construction.

Although several thermochemical and thermomechanical models have been developed for the thermal response modeling of polymer composites, most are based on thermophysical and thermomechanical property submodels without a clear physical and chemical background (empirical curves from experimental observations). Very few have considered the thermomechanical response of composites subjected to excessive heating and/or fire exposure lasting longer than one hour. Existing thermochemical or thermomechanical models cannot adequately consider the progressive material state and property changes and structural responses that occur during the extended excessive heating and/or fire exposure of large-scale FRP structures. In addition, after excessive heating or fire exposure, the condition of these load-bearing composite structures has to be assessed. Very often, the major parts of a structure will not be decomposed or combusted but only experience thermal loading at elevated and high temperatures. Information and models relating to the assessment of post-fire properties for load-bearing FRP structures are still lacking.

1.2 Objectives

This research focuses on the changes that occur in the thermophysical and thermomechanical properties and the resulting thermomechanical responses of FRP composites under elevated and high temperatures. Based on the above analysis, the objectives of this research can therefore be defined as the following:

1. To understand and model the progressive changes in states of composite materials in the temperature range from 20°C to 600°C based on statistical mechanics and kinetic theory, covering the glass transition, leathery-to-rubbery transition and decomposition processes for most thermoset resins;

2. To model the progressive changes in the thermophysical properties

(including density, thermal conductivity, and specific heat capacity) and thermomechanical properties (including elastic modulus, viscosity, and strength) of composite materials under elevated and high temperatures by adopting appropriate distribution functions, based on an understanding of the progressive changes of material states. If these changes in material states are considered as being kinetic processes, such material property models should be able to consider the effects of differences in thermal loading history, and are therefore not only temperature-dependent, but also time-dependent;

3. To predict the thermal responses of composite materials in fire by incorporating the thermophysical property sub-models in a heat transfer governing equation;

4. To predict the mechanical responses of composite materials in fire by integrating the thermomechanical property sub-models (elastic modulus and viscosity) in a structural theory;

5. To predict the time-to-failure of composite materials in fire;

6. To develop models for the assessment of the post-fire behavior of composite materials based on an understanding of the progressive changes occurring in these materials.

1.3 Methodology

To achieve these objectives, theoretical methods originating not only from civil engineering but also other interdisciplinary fields were explored, specifically:

1. Kinetic theory was used for the understanding and modeling of the progressive changes of states occurring in composite materials under elevated and high temperatures (Objective 1). Thus, four different states (glassy, leathery, rubbery and decomposed) and three transitions (glass transition, leathery-to-rubbery transition and decomposition) can be defined for composite materials subjected to temperature increase. At a certain temperature, a composite material can be considered as a mixture of materials that are in different states, and the quantity of material in each

state can therefore be estimated;

2. By choosing appropriate distribution functions, the thermophysical and thermomechanical properties of the mixture can be determined, once the content and the properties of each state are established as above (Objective 2);

3. The thermal response model in Objective 3 was developed based on heat transfer theory and a finite difference method;

4. The mechanical response model referred to in Objective 4 was developed based on structural theory (the Timoshenko beam theory) and a finite element method;

5. Objective 5 was achieved by comparing the strength degradation sub-models resulting from Objective 2 with a predefined failure criterion;

6. Objective 6 was achieved based on the results of Objectives 1 and 2.

Meanwhile, experimental work was performed to validate the modeling results obtained for each objective.

1.4 Composition of the work

Corresponding to Objectives 1 to 6 listed above, technical and research papers have been published or are currently under review and the structure of this thesis is based on these papers.

Chapter 2 presents the publications to date:

1. Section 2.1 presents the modeling of thermophysical properties, including density, thermal conductivity and specific heat capacity, for composite materials under elevated and high temperatures.

2. Section 2.2 presents the modeling of thermomechanical properties, including E-modulus, viscosity and effective coefficient of thermal expansion, for composite materials under elevated and high temperatures.

3. Section 2.3 presents the modeling of strength degradation for FRP composites under elevated and high temperatures, including compressive, tensile and shear strengths.

4. Section 2.4 presents an experimental investigation of the thermophysical and thermomechanical properties of a particular composite ma-

terial (E-glass fiber-reinforced polyester resin) in order to provide the basic material information for subsequent work, and further validate the proposed theoretical models in Sections 2.1 and 2.2.

5. Section 2.5 introduces and explains the time dependence of the properties and responses of composite materials in fire, something that has not yet been considered in previous models, but can be taken into account by the proposed models.

6. Section 2.6 presents the modeling of the thermal responses of composite materials under elevated and high temperatures, incorporating the sub-models for thermophysical properties developed in Section 2.1.

7. Integrating the sub-models for thermomechanical properties from Section 2.2, Section 2.7 presents the modeling of mechanical responses of composite materials under elevated and high temperatures, including both elastic and viscoelastic behaviors.

8. Incorporating the sub-models for strength degradation from Section 2.3, Section 2.8 introduces the modeling of time-to-failure for pultruded GFRP materials under combined thermal and compressive loadings, where different thermal boundary conditions were achieved by using a water-cooling system;

9. Section 2.9 presents the modeling approach for the post-fire stiffness of composite materials.

Chapter 3 summarizes the advantages and limitations of the proposed modeling system, and also suggests possibilities for future work.

The correlations between the objectives, methodology and corresponding publications are shown in the following table:

Objective (Section 1.2)	Methodology (Section 1.3)	Publication (Section 1.4)
1. Material states	Kinetic theory	Sections 2.1 and 2.2
2. Modeling of thermophysical properties	Kinetic theory and distribution function	Section 2.1
2. Modeling of stiffness degradation	Kinetic theory and distribution function	Section 2.2
2. Modeling of strength degradation	Kinetic theory and distribution function	Section 2.3
2. Experimental validation	Experimental investigation	Section 2.4
2. Time dependence of thermophysical and thermomechanical properties	Kinetic theory and distribution function	Section 2.5
3. Thermal responses	Heat transfer theory and finite difference method	Section 2.6
4. Mechanical responses	Structural theory and finite element method	Section 2.7
5. Time-to-failure	Failure criteria	Section 2.8
6. Post-fire behavior	Based on objectives 1 and 2	Section 2.9

Table 1. Correlations between objectives, methodology and corresponding publications in Chapter 2

CHAPTER 2

Publications

2. Publications

This chapter presents a compilation of the publications resulting from this thesis. Each paper is preceded by an introductory summary and reference details.

2.1 Modeling of thermophysical properties

Summary

The mechanical responses (stress, strain, displacement and strength) of FRP composites in fire are significantly affected by their thermal exposure. These mechanical responses, on the other hand, have almost no influence on the thermal responses of these materials. As a result, the mechanical and thermal responses can be decoupled by firstly estimating the thermal responses based on the modeling of the thermophysical properties, and then predicting the mechanical responses of the FRP composites based on the modeling of the thermomechanical properties.

Rather than using direct fitting approaches, this paper attempts to model the changes in the thermophysical properties of composite materials in fire, including mass transfer, thermal conductivity and specific heat capacity, based on an understanding of the thermophysical and thermochemical processes involved.

A model for resin decomposition was derived from chemical kinetics. The temperature-dependent mass transfer was obtained using the decomposition model for the resin. Taking into account the fact that FRP composites are comprised of undecomposed and decomposed states, the temperature-dependent thermal conductivity was obtained based on a series model and the specific heat capacity was obtained based on the Einstein model and mixture approach. The content of each phase was directly obtained from the decomposition model and mass transfer model. The effects of the

endothermic decomposition of the resin on the specific heat capacity and the shielding effect of the voids developing in the resin on thermal conductivity are dependent on the rate of decomposition. These were also described by the decomposition model and the effective specific heat capacity and thermal conductivity models were subsequently obtained. Each model was compared with experimental data or previous models and good agreement was found.

Reference detail

This paper was published in Composites Science and Technology 2007, volume 67, pages 3098-3109, entitled

"Modeling of thermophysical properties for FRP composites under elevated and high temperatures" by Yu Bai, Till Vallée and Thomas Keller.

Part of the content of this paper was presented at the first Asia-Pacific Conference on FRP in Structures (APFIS) 12-14 December 2007, Hong Kong, entitled

"Modeling of thermophysical properties and thermal responses for FRP composites in fire" by Yu Bai, Till Vallée and Thomas Keller, presented by Yu Bai.

MODELING OF THERMOPHYSICAL PROPERTIES FOR FRP COMPOSITES UNDER ELEVATED AND HIGH TEMPERATURE

Yu Bai, Vallée Till and Thomas Keller

Composite Construction Laboratory CCLab, Ecole Polytechnique Fédérale de Lausanne (EPFL), BP 2225, Station 16, CH-1015 Lausanne, Switzerland.

ABSTRACT:

A decomposition model for resin in glass fiber-reinforced polymer composites (GFRP) under elevated and high temperature was derived from chemical kinetics. Kinetic parameters were determined by four different methods using thermal gravimetric data at different heating rates or only one heating rate. Temperature-dependent mass transfer was obtained based on the decomposition model of resin. Considering that FRP composites are constituted by two phases – undecomposed and decomposed material – temperature-dependent thermal conductivity was obtained based on a series model and the specific heat capacity was obtained based on the Einstein model and mixture approach. The content of each phase was directly obtained from the decomposition model and mass transfer model. The effects of endothermic decomposition of the resin on the specific heat capacity and the shielding effect of evolving voids in the resin on thermal conductivity are dependent on the rate of decomposition. They were also described by the decomposition model; the effective specific heat capacity and thermal conductivity models were subsequently obtained. Each model was compared with experimental data or previous models, and good agreements were found.

KEYWORDS:

Polymer-matrix composites; thermal properties; modeling; pultrusion

1 INTRODUCTION

The estimation of the thermal responses of fiber-reinforced polymer (FRP) composites under elevated and high temperatures is largely dependent on the description of thermophysical properties such as mass or density, specific heat capacity, and thermal conductivity. During the heating process, these properties experience significant changes that influence the temperature distribution inside the material [1-3]. Much experimental and modeling work has been conducted to characterize the temperature-dependent thermophysical material properties at different stages [1] (e.g. below and above the glass transition (T_g) and the decomposition (T_d) temperature). The change of mass when temperature increases can be obtained by Thermogravimetric Analysis (TGA), in which the mass of the sample is monitored against the time and temperature at a constant heating rate. The mass of FRP composites decreases only very little from the ambient temperature up to the onset of decomposition, while during decomposition the mass drops remarkably. As a chemical reaction, this process can be described by the Arrhenius law. Appropriate models of mass transfer based on Arrhenius law were proposed, while it appears that the determination of kinetic parameters used in these models still remain a great extent of uncertainty [4-8]. Only the Friedman method was discussed by Henderson et al. [9] as a multiple heating rate method. Some other methods to determine these kinetic parameters, however, still need to be introduced.

Experimental results have shown that the specific heat capacity for FRP composites does not change significantly or increases only slightly with the temperature before decomposition [10-13]. The specific heat capacity was consequently described as linearly dependent on temperature [5-8, 13, 14] or assumed to be a constant before decomposition [1]. Additional energy is required during the process of evaporation of the absorbed moisture and decomposition of resin. The terms “effective” or “apparent” are used to describe the total energy needed for all these physical and chemical changes, while the term “true” is used to specify the energy

needed only for increasing the temperature of the material [13-15]. Although the energy related to chemical and physical changes can be considered as an additional term in the final governing equation of the thermal response model, the “effective” specific heat capacity can be directly obtained by a Differential Scanning Calorimeter (DSC). Thus before being assembled into the finial governing equation, the model for the specific heat capacity can be verified on the material property level first. The mathematical models of “effective” specific heat capacity proposed in [1, 14-15] increased the true specific heat capacity by adding peak points to represent the energy for evaporation and endothermic decomposition. The curve between the peak points and the initial points was determined by linear interpolation, and without the comparison with experimental data.

Experimental investigations have shown that the thermal conductivity remains almost constant [16] or increases from the ambient temperature to resin decomposition [10, 12, 17]. Consequently, similar to the specific heat capacity, the thermal conductivity before decomposition has been modeled as a constant value [14] or a linear function dependent on temperature [5-8]. Samanta et al. [7] showed that the thermal conductivity rises during the moisture evaporation due to water in the pores, which is a better conductor of heat than air and the heat is also transferred by the migration of the moisture. Furthermore, the glass transition of the polymer also occurs at this temperature range (before its decomposition). The phase change of the polymer contributes to an increase in effective thermal conductivity, since the probability of the particles being in contact with one another becomes greater and the effect of particles interacting with each other cannot be neglected. When fibers (of a higher conductivity than resin) are in contact with each another, paths of low resistance for heat flow are formed, which contribute to an increase in the effective thermal conductivity [18]. During the decomposition process, the formation of voids and cracks within the matrix as well as delamination of fabrics and the associated shielding effect will influence greatly the thermal conductivity [1-2]. The concept of “effective” is also used to consider all

these effects (moisture migration, phase change, crack formation). In the previous effective models, the thermal conductivity decreases and linearly approaches the thermal conductivity of the fully decomposed FRP composite [1, 14, 19]. However, similar to the models for effective specific heat capacity, it is possible that the physical meaning is largely compromised by this linear interpolation process.

In this paper, material models are proposed to describe the progressive changes of thermophysical properties (mass transfer, specific heat capacity, thermal conductivity) of FRP composites under elevated temperatures (room temperature-200 °C) and high temperature (above 200 °C) as continuous functions related to temperature instead of discontinuous curves used in the previous research works. The output from each model forms the basic input to thermal response models, which give the temperatures in the time and space domains. The material models are validated through comparisons to experimental results.

2 MODELING OF TEMPERATURE-DEPENDENT MASS TRANSFER

2.1 Decomposition model

The mass of FRP composites shows little change until decomposition starts. The decomposition process can be described by the theory of chemical reaction rate and the Arrhenius law [20-27]. Considering the decomposition process as a one-stage chemical reaction, the rate of decomposition is determined by the temperature, T, and the quantity of reactants as follows:

$$\frac{d\alpha}{dt} = k(T) \cdot f(\alpha) \tag{1}$$

where α is the degree of decomposition ($\alpha=(M_i-M)/(M_i-M_e)$, M is the mass, M_i is the initial mass and M_e is the final mass after decomposition), $d\alpha/dt$ is the rate of mass loss (i.e. rate of decomposition), $k(T)$ describes the effect of temperature and $f(\alpha)$ the effect of the reactant quantity to the reaction rate.

The function $f(\alpha)$ can be expressed as follows:

$$f(\alpha) = (1-\alpha)^n \tag{2}$$

where n is the reaction order, while the function $k(T)$ can be obtained from the Arrhenius equation:

$$k(T) = A \cdot \exp\left(\frac{-E_A}{R \cdot T}\right) \tag{3}$$

where A is the pre-exponential factor, E_A is the activation energy, R is the universal gas constant (8.314 J/mol·K).

During TGA tests, a constant heating rate is used:

$$\frac{dT}{dt} = \beta \tag{4}$$

Combining Eqs. (1), (2), (3) and (4) gives:

$$\frac{d\alpha}{dT} = \frac{A}{\beta} \cdot \exp\left(\frac{-E_A}{R \cdot T}\right) \cdot (1-\alpha)^n \tag{5}$$

From Eq. (5), the decomposition degree can be determined as a function of the temperature, T, if the kinetic parameters A, E_A and n are known.

Properties	Resin	Fiber
Volume fraction	48%	52%
Mass fraction	39%	61%
T_g	117°C	-
T_d	300°C	-
T_s	-	830°C

Table 1. Properties of DuraSpan material (T_g, T_d, T_s denote glass transition temperature, decomposition temperature of resin and softening temperature of fibers) [15]

To validate Eq. (5), TGA tests were conducted on FRP composite samples originating from the face panels of an FRP bridge deck system (DuraSpan 766® from Martin Marietta Composites). This deck system is currently produced commercially by the pultrusion process. The material consists of E-glass fibers and a polyester resin; detailed information of the material is summarized in Table 1. The samples used for the TGA tests were created by grinding the material into powder, which was analyzed on a TA2950 TGA instrument. The experiment was run from room temperature to 550°C in an air atmosphere. Four heating rates (2.5°C/min, 5°C/min,

10°C/min, and 20°C/min) were used for the study. Two samples were tested for each of the heating rates (series 1 and 2). The material sample size was kept consistent for all runs: 5.3 mg ± 0.4 mg. The kinetic parameters were estimated based on the experimental results from series 1. The theoretical values calculated from Eq. (5) were then compared to the experimental series 2 values (since the kinetic parameters were not expected to change between nominally identical sample series).

2.2 Estimation of kinetic parameters

Four different methods will be presented in this paper that were used to estimate the kinetic parameters (A, E_A, n). Three of the methods use different TGA curves at different heating rates (the so called "multi-curves method"), while the fourth method employs only one TGA curve from only one heating rate.

	α	E_A [J/mol]	A (min^{-1})	n
	0.2	184732	2.46×10^{16}	8.84
	0.3	163447	3.18×10^{14}	7.82
Friedman	0.4	146055	9.10×10^{12}	6.99
Method	0.5	155574	6.36×10^{13}	7.44
	0.6	153662	4.31×10^{13}	7.35
	0.7	163217	3.03×10^{14}	7.81
Kissinger Method		163417	1.60×10^{13}	1
	0.2	190743	1.20×10^{17}	11.93
	0.3	178038	2.80×10^{15}	5.85
Ozawa	0.4	166435	1.12×10^{14}	3.19
Method	0.5	159235	1.34×10^{13}	1.79
	0.6	156476	4.38×10^{12}	0.99
	0.7	159393	4.31×10^{12}	0.52

Table 2. Kinetic parameters by "multi-curves" methods

2.2.1 Friedman Method [20]

By taking the logarithm of each side of Eq. (5), the following relationship can be found:

$$\ln\left(\beta\frac{d\alpha}{dT}\right)=\ln(A)+n\cdot\ln(1-\alpha)-\left(\frac{E_A}{RT}\right)=k_1+k_2T^{-1} \tag{6}$$

For a specified α, the first two terms on the right hand side are constant, and if A, E_A and n are thought to be independent of the heating rate β, the plot of the left side versus T^{-1} produces a straight line, as shown in Fig. 1. E_A can be obtained from the slope of this straight line. In addition, n and A can be calculated by plotting E_A/RT_0 against $\ln(1-\alpha)$, where T_0 is the temperature at which $\ln\left(\beta\frac{d\alpha}{dT}\right)=0$ [21]. This process was applied to the experimental results (series 1) and the results are summarized in Table 2.

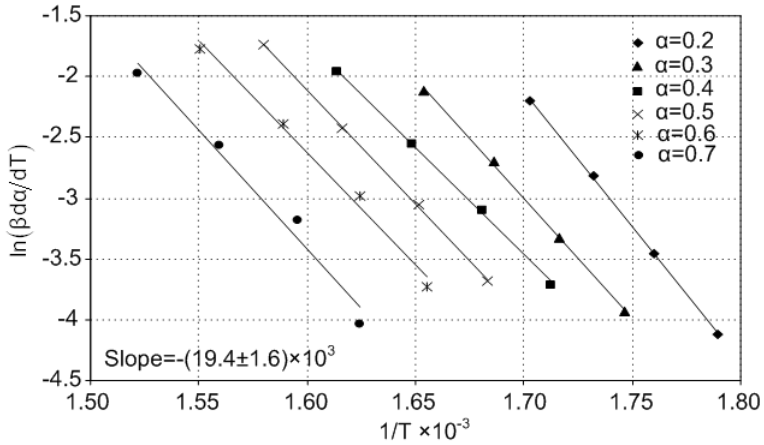

Fig. 1. Determination of E_A from Friedman method (experimental data and fitted straight lines for different decomposition degrees)

2.2.2 Kissinger Method [22]

When the maximum reaction rate occurs at temperature T_m, i.e. $d^2\alpha/dT^2$ (see Fig. 2), the derivative of Eq. (5) gives:

$$\frac{E_A\beta}{RT_m^{\,2}}=An(1-\alpha)_m^{\,n-1}\cdot\exp\left(\frac{-E_A}{RT_m}\right) \tag{7}$$

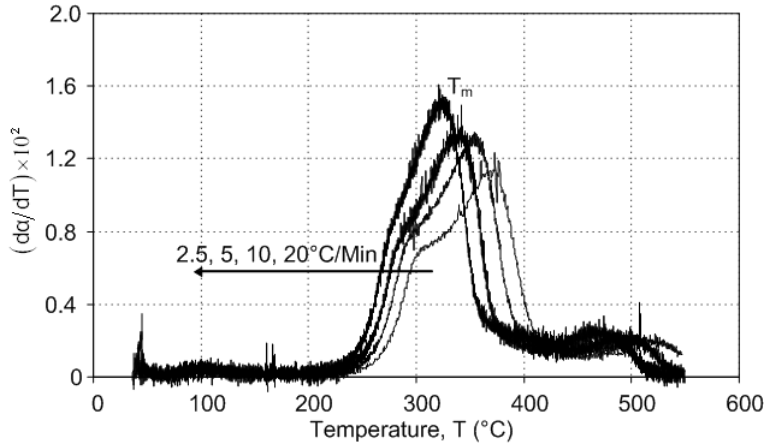

Fig. 2. Change in $d\alpha/dT$ with respect to temperature

Equation (8) can then be obtained by taking the logarithm of Eq. (7) and then deriving with respect to $1/T_m$:

$$\frac{d\left(\ln\left(\beta/T_m^2\right)\right)}{d\left(1/T_m\right)} = -\frac{E_A}{R} \tag{8}$$

As a result, a plot of $-\ln(\beta/T_m^2)$ versus $1/T_m$ results in a slope of E_A/R (see Fig. 3).

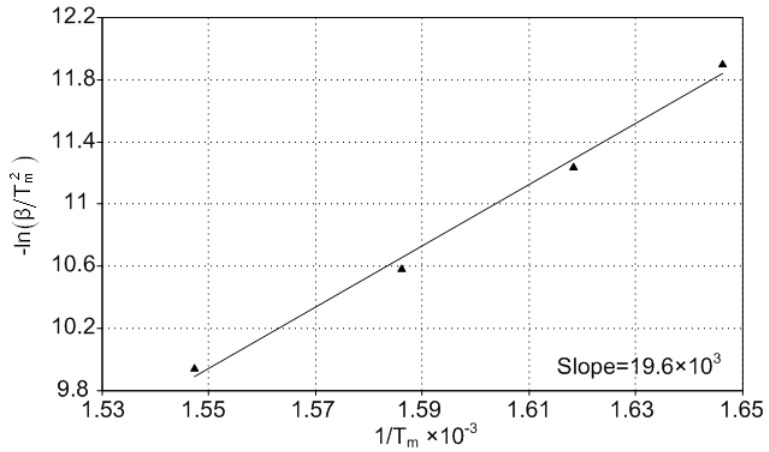

Fig. 3. Determination of E_A from Kissinger method (experimental data and fitted straight lines)

The reaction order, n, can be determined by Eq. (9) for $n \neq 1$ [23]:

$$-n\left(1-\alpha_m\right)^{n-1} = 1 + \left(n-1\right)\frac{2RT_m}{E_A} \tag{9}$$

where α_m is the decomposition degree at temperature T_m (see Fig. 2). The pre-exponential factor A can be determined by substituting n and E_A into Eq. (7). The results from these calculations for the FRP composite that was used in this study are summarized in Table 2.

2.2.3 Ozawa Method [24]

Integrating Eq. (5) gives:

$$g(\alpha)=\int_0^{\alpha}\frac{d\alpha}{(1-\alpha)^n}=\frac{AE}{R\beta}\cdot p(x) \tag{10}$$

where $p(x)=-\int_{\infty}^{x}\frac{e^{-x}}{x^2}dx$ and $x = E_A/RT$.

By taking the logarithm of Eq. (10), the following is obtained:

$$\log g(\alpha)=\log(AE_A/R)-\log\beta+\log p(x=E_A/RT) \tag{11}$$

While log *p(x)* can be approximated by Eq. (12) [25]:

$$\log p(x)\approx -2.315-0.4567x \text{ , if } 20<x<60 \tag{12}$$

Equation (13) can then be expressed as:

$$\log g(\alpha)=\log(AE_A/R)-\log\beta-2.315-0.4567\,E_A/RT \tag{13}$$

Deriving Eq. (13) with respect to $1/T$ at fixed decomposition degrees, Eq. (14) is obtained:

$$E_A=-\frac{R}{0.4567}\cdot\frac{d(\log\beta)}{d(1/T)} \tag{14}$$

E_A can be calculated from the slopes of the straight lines by plotting logβ versus $1/T$, as shown in Fig. 4.

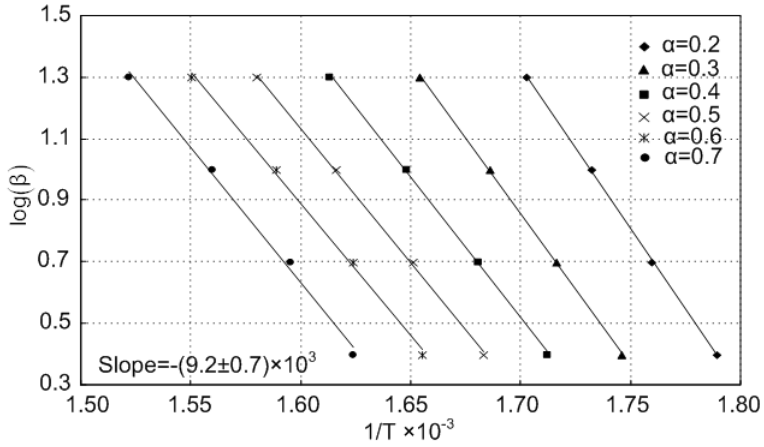

Fig. 4. Determination of E_A from Ozawa method (experimental data and fitted straight lines for different decomposition degrees)

The mean value of the pre-exponential factor A at each heating rate can be calculated from Eq. (15) [21]:

$$\log A = \log \beta + \log E_A + 0.434\, E_A/RT - \log R - 2\log T \tag{15}$$

After obtaining the values of A and E_A, n can be determined by substituting Eq. (16) into (Eq. 17) [21]:

$$g(\alpha) \approx \frac{1-(1-\alpha)^{1-n}}{1-n}, \text{ when } n \neq 1 \tag{16}$$

$$\log g(\alpha) = \log(AE_A/R) - \log \beta^* - 2.315 \tag{17}$$

where $\log \beta^*$ is the y-intercept of the lines in Fig. 4 (i.e. the value of $\log\beta$ when E_A/RT is taken as zero in Eq. (13)). The calculated values of A, E_A and n at different decomposition degrees, based on the experimental results of series 1, are summarized in Table 2.

2.2.4 Modified Coats-Redfern method [26, 27]

For the so-called "multi-curves" methods introduced above, TGA curves of different heating rates are required. Coats and Redfern [26, 27] proposed a method to determine E_A in order to obtain kinetic parameters from only one curve. As introduced in the Coats-Redfern method, the right side of Eq. (10) can be expressed as:

$$(ART^2/\beta E_A)\cdot(1-2RT/E_A)\cdot\exp(-E_A/RT) \tag{18}$$

whereas the left hand side can be expanded to:

$$\alpha + (n\alpha^2/2) + n(n+1)(\alpha^3/6) + \ldots \tag{19}$$

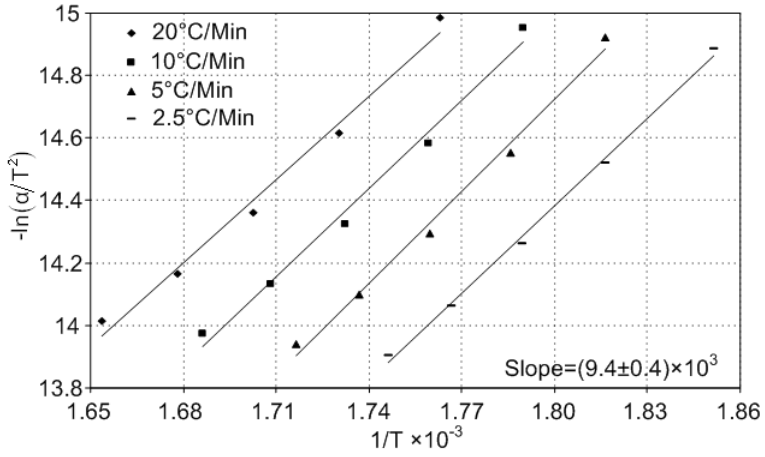

Fig. 5. Determination of E_A from Coats-Redfern method (experimental data and fitted straight lines at different heating rates)

In the case of low values of α, terms in α^2 and higher can be neglected giving:

$$\alpha \approx \left(ART^2/\beta E_A\right)\cdot\left(1-2RT/E_A\right)\cdot\exp\left(-E_A/RT\right) \tag{20}$$

By logarithm transform, Eq. (20) results in:

$$\ln\left(\alpha/T^2\right)=\ln\left(AR/\beta E_A\right)\cdot\left(1-2RT/E_A\right)-\left(E_A/RT\right) \tag{21}$$

Thus a plot of $-\ln(\alpha/T^2)$ versus $1/T$ should give a straight line with a slope of E_A/R since $\ln(AR/\beta E_A)\cdot(1-2RT/E_A)$ is nearly constant. As a result, E_A is obtained from one curve at one constant heating rate, as shown in Fig. 5. Substituting E_A into Eq. (17), the values of A at different decomposition degrees, α, are obtained. Since the terms of α^2 (and higher, which are related to n in Eq. 19) are neglected in the Coats-Redfern method, the value of n can not be directly calculated based on this approach. Considering that only one curve is available, reference to Eq. (7) of the Kissinger method can be made. Substituting the values of E_A and A into the Eq. (7), the value of n at different heating rates is obtained. The results from this method are summarized in Table 3.

	β=20	β=10	β=5	β=2.5
E_A [J/mol]	74099	78136	81686	77878
A (min^{-1})	444856	727157	1073086	316990
n	1.49	1.37	1.34	1.08

Table 3. Kinetic parameters by modified Coats-Redfern method

2.2.5 Comparison of methods

Kinetic parameters were estimated based on the TGA results of series 1 and summarized in Table 2 for "multi-curves" methods and in Table 3 for the modified Coats-Redfern method. Since kinetic parameters can be obtained at different decomposition degrees in Friedman and Ozawa methods, the range of α is taken from α=0.2 to α=0.7, considering the measurement noise in lower and higher decomposition degrees (see Fig. 2 for $d\alpha/dT$). For the Kissinger method and the modified Coats-Redfern method, only one set of kinetic parameters was obtained for a specified heating rate.

As shown in Table 2, the activation energy, E_A, from "multi-curves" methods is in the range of 145 to 200 kJ/mol, while the pre-exponential factor, A, varies more between 10^{12} and 10^{18}. The reaction order, n, is estimated to be approximately 7, with little variance using the Friedman method, while it varies from 11.93 to 0.52 when using the Ozawa method. Similar variance was found in the estimation of thermal decomposition kinetic parameters of epoxy resin by Lee in 2001 [21], in which the activation energy, E_A, varied from 180 to 300 kJ/mol, and the pre-exponential factor, A, from 10^{16} to 10^{24}. A decrease in the reaction order, n, with the decomposition degree as was seen in the Ozawa method, was also found by Zsakó [28], where n varied from 82 at α=0.2 to 7.45 at α=0.7.

As shown in Table 3, the kinetic parameters were obtained at different heating rates for the modified Coats-Redfern method. The activation energy, E_A , and reaction order, n, are stable, while A shows great variance. The values of kinetic parameters differ greatly between the "multi-curve" methods (Table 2) and the modified Coats-Redfern method (Table 3). These differences are likely resulted from the different assumptions made in these methods. For the "multi-curve" methods, it is assumed that the kinetic parameters do not depend on the heating rate (thus, the points from different heating rates give a straight line and E_A is determined by the slope of the straight line, see Figs. 1, 3 and 4). For the modified Coats-Redfern method, however, it is assumed that the kinetic parameters do not depend on the decomposition degree (thus the points from different decomposition degrees give a straight line and E_A is determined by the slope of the straight line, see Fig. 5).

More or less variance could be found in the estimation of kinetic parameters based on the above simple TGA tests and other research efforts [21, 28]. However, it should be noted that the thermal decomposition of composites involves complicated processes, including the destruction of the initial architecture of the composite, the adsorption and desorption of gaseous products, the diffusion of the gases, heat and mass transfer, and many other elementary processes. The real processes and mechanism in

the decomposition process can therefore not be represented by means of a general equation with one set of kinetic parameters. Nevertheless, the intent in this paper is to describe the mass transfer of composites during decomposition and not to obtain the real meanings and genuine values of the kinetic parameters. In this respect, the kinetic parameters from Table 2 and 3 are empirical parameters characterizing the experimental TGA curves [29]. This approach based on TGA allows the kinetic parameters to be obtained by performing simple tests, and makes it possible to build macro models that describe changes in thermophysical properties during the decomposition process of composites.

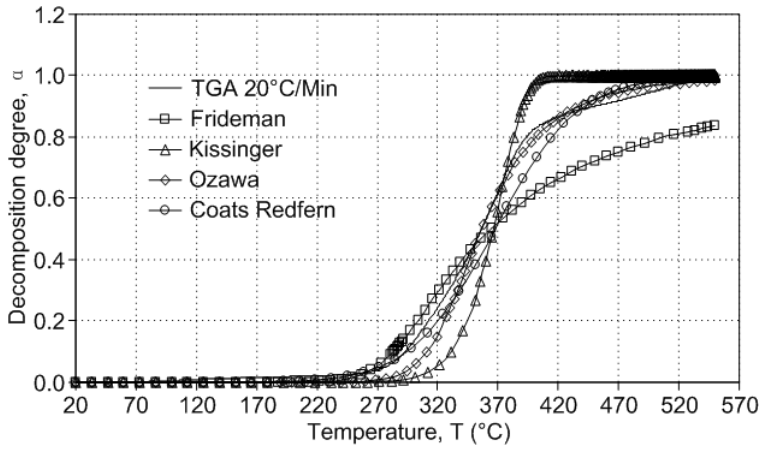

Fig. 6. Decomposition degree from own TGA tests compared with results from four different modeling methods

Figure 6 shows the comparison between four theoretical curves (based on Eq. (5)) at a heating rate of 20°C/min and the experimental curve at the same heating rate from series 2 (kinetic parameters were selected from Table 2 and 3, the values at α=0.4 for the Friedman and Ozawa methods). Although the kinetic parameters differ significantly in these methods, all calculated curves show tendencies similar to the experimental curve. In particular, the results from the Ozawa and modified Coats-Redfern methods are in good agreement with the experimental data. Using these two methods, the theoretic curves at different heating rates were obtained and compared well with the experimental series 2, as shown in Fig. 7 and 8 for all heating rates.

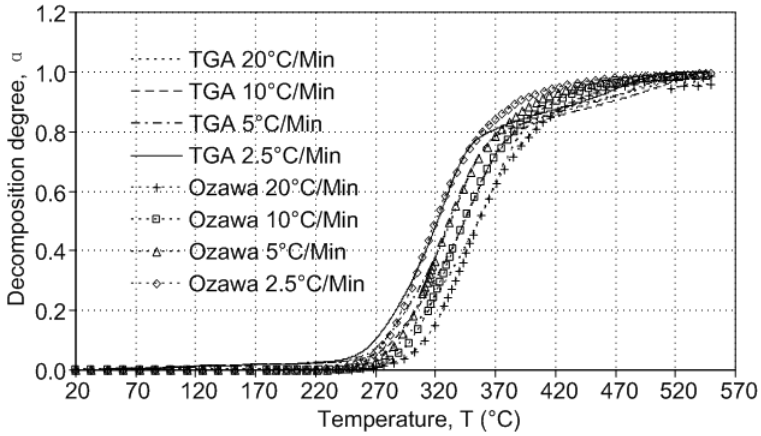

Fig. 7. TGA data from present study at different heating rates compared with modeling results from Ozawa method

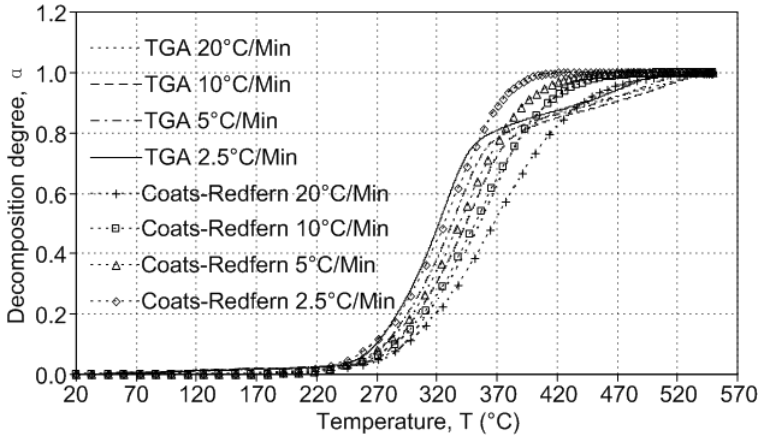

Fig. 8. TGA data from present study at different heating rates compared with results from modified Coats-Redfern method

As a result, when TGA curves at different heating rates are available, both the Ozawa and modified Coats-Redfern methods can be applied. However, if only one heating rate is available, so called "multi-curves" methods are not applicable, while the modified Coats-Redfern method can still give a good approximation. It should be noted, however, that a differential process needs to be performed on initial TGA data in order to obtain T_m in Eq. (7). The peak points (where $d^2\alpha/dT^2=0$, corresponding to the maximum reaction rate) and T_m are not easy to locate due to measurement noise (see Fig. 2).

2.3 Mass transfer model

After the determination of the decomposition model, the mass transfer

during decomposition can be obtained according to Eq. (22):

$$M = (1-\alpha)\cdot M_i + \alpha \cdot M_e \tag{22}$$

where M is the temperature-dependent mass, M_i (M_e) is the initial (final) mass. Since only resin decomposes to gases when the temperature exceeds the decomposition temperature, most of M_e is composed of fibers. The TGA experiments showed that about 86% of the remaining materials are fibers [15]. Accordingly, Eq. (22) can be expressed as:

$$\begin{aligned} M &= (1-\alpha)\cdot M_i \cdot (f_{f0} + f_{m0}) + \alpha \cdot M_i \cdot f_{f0} \\ &= M_i \cdot f_{f0} + M_i \cdot f_{m0} \cdot (1-\alpha) = M_i - \alpha \cdot M_i \cdot f_{m0} \end{aligned} \tag{23}$$

where f_{f0} (f_{m0}) is the initial fiber (resin) mass fraction. Furthermore, the temperature-dependent mass fraction, f_b (f_a), and volume fraction, V_b (V_a), of the undecomposed (subscript b) and decomposed (subscript a) material can be obtained from Eqs. (24) to (27):

$$f_b = \frac{M_i \cdot (1-\alpha)}{M_i \cdot (1-\alpha) + M_e \cdot \alpha} \tag{24}$$

$$f_a = \frac{M_e \cdot \alpha}{M_i \cdot (1-\alpha) + M_e \cdot \alpha} \tag{25}$$

$$V_b = \frac{f_b / M_i}{f_b / M_i + f_a / M_e} = 1-\alpha \tag{26}$$

$$V_a = \frac{f_a / M_e}{f_b / M_i + f_a / M_e} = \alpha \tag{27}$$

The temperature-dependent fiber mass fraction, f_f, and resin mass fraction, f_m, are given by Eqs. (28) and (29):

$$f_f = \frac{M_i \cdot f_{f0}}{M} \tag{28}$$

$$f_m = \frac{M_i \cdot f_{m0} \cdot (1-\alpha)}{M} \tag{29}$$

3 MODELING OF TEMPERATURE-DEPENDENT THERMAL CONDUCTIVITY

3.1 Formulation of basic equations

At a specified temperature, the thermal conductivity of FRP composite

materials depends on the properties of the constituents at this temperature, as well as the content of each constituent. As a result, if the temperature-dependent thermal conductivity is known for both fibers and resin, the property of the composite material can be estimated. During decomposition, however, decomposed gases and delaminating fiber layers will influence significantly the thermal conductivity (true against effective thermal conductivity). An alternative method to determine the effective thermal conductivity is to suppose that the materials are only composed of two phases: "the undecomposed material" and "the decomposed material". The content of each phase can thereby be determined from the mass transfer model introduced above. As a result, the effects due to decomposition can be described.

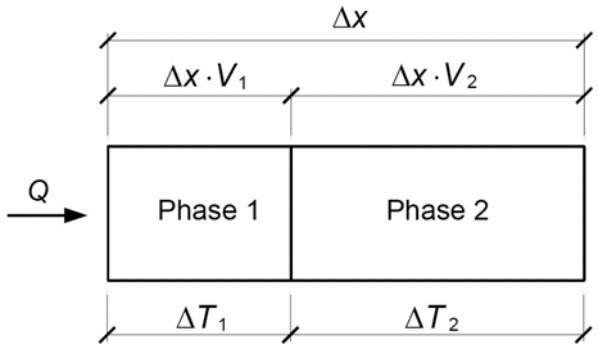

Fig. 9. Series model for composites with two phases

Many methods were developed to estimate the properties of systems composed of several phases of different properties [30-36]. For example, the series model can be used to obtain the thermal conductivity of composites with two phases. Considering that the heat flow, Q, is through the length, Δx, and unit area, A, of a composite with a volume fraction, V_1, for phase 1 and a volume fraction, V_2, for phase 2, the following Eqs. (30) and (31) can be obtained based on the definition of thermal conductivity (see also Fig. 9):

$$k_1 = \frac{Q \cdot \Delta x \cdot V_1}{A \cdot \Delta T_1} \tag{30}$$

and

$$k_2 = \frac{Q \cdot \Delta x \cdot V_2}{A \cdot \Delta T_2} \tag{31}$$

where k_1 and k_2 are the thermal conductivities for phases 1 and 2, respectively, ΔT_1 and ΔT_2 are the temperature gradients in phases 1 and 2, respectively. The thermal conductivity of a composite, k, can then be expressed as:

$$k = \frac{Q \cdot \Delta x}{A \cdot (\Delta T_1 + \Delta T_2)} = \frac{1}{\frac{V_1}{k_1} + \frac{V_2}{k_2}} \quad \text{or} \quad \frac{1}{k} = \frac{V_1}{k_1} + \frac{V_2}{k_2} \tag{32}$$

Considering that phase 1 is the undecomposed material and phase 2 is the decomposed material, Eq. (33) can be obtained:

$$\frac{1}{k_c} = \frac{V_b}{k_b} + \frac{V_a}{k_a} \tag{33}$$

where k_c denotes the thermal conductivity for the composite material over the entire temperature range, k_b (k_a) is the thermal conductivity for the undecomposed (decomposed) material. It should be noted that the volume fraction V_b (V_a) of the undecomposed (decomposed) material will change at different temperatures, according to Eqs. (26) and (27), based on the decomposition and mass transfer model. Thus, the temperature-dependent thermal conductivity, k_c, can be obtained by combing Eqs. (5), (26), (27) and (33). Glass softening and melting of fibers were not considered here since generally these processes occur above 800°C (see Table 1). The radiation of the gasses in the voids is also not considered since the contribution of gas radiation to the effective thermal conductivity is still low when the temperature is below 800°C [2, 14, 19].

3.2 Estimation of k_b and k_a

As introduced above, k_b is the thermal conductivity of the undecomposed material composed of fibers (constituent 1) and resin (constituent 2). Accordingly, the following can be obtained:

$$\frac{1}{k_b} = \frac{V_f}{k_f} + \frac{V_m}{k_m} \tag{34}$$

where k_f (k_m) is the thermal conductivity of the fibers (resin), V_f (V_m) is the volume fraction of the fibers (resin). A thermal conductivity of 0.35 W/m·K for the FRP material used in the present study was measured at room

temperature by Tracy in 2005 [15]. Substituting k_f=1.1, k_m=0.2 [7-8], and V_f and V_m according to Table 1 into Eq. (34), k_b can be calculated as 0.348 W/m·K, which is in good agreement with the experimental result.

The thermal conductivity of the decomposed material, k_a, can be estimated using the same method, although at this time the resin has already been decomposed. Gaps and voids are left back from the decomposed resin and are filled with gases, which induce significant thermal resistance. The decomposed material can therefore be considered as consisting of another two constituents: fibers and remaining gases. The following equation is then obtained:

$$\frac{1}{k_a} = \frac{V_f}{k_f} + \frac{V_g}{k_g} \tag{35}$$

where k_g is the thermal conductivity of decomposed gases and V_g is its volume fraction. Since all the resin decomposes to gases at the end, the volume fraction of the remaining gases should be equal to the initial volume fraction of the resin. Considering that k_f=1.1 and k_g=0.05 W/m·K (the thermal conductivity of dry air is about 0.03 W/m·K) and V_g = V_m, k_a can be estimated at 0.1 W/m·K. This latter value was also used in [1] and [14].

3.3 Comparison to other models

Substituting k_b and k_a obtained above into Eq. (33) and combing Eq. (5), (26) and (27), the temperature-dependent effective thermal conductivity is obtained and shown in Fig. 10. In this figure, the initial thermal conductivity in the temperature range below approximately 200 °C is verified by the experimental result at room temperature. When the temperature increases and approaches $T_{d,onset}$ (approximately 255°C), the resin starts to decompose. During this process, gases are generated and fill the spaces of the decomposed resin and between delaminating fiber layers, exhibiting a rapid decrease of thermal conductivity in the temperature range from 200°C to 400 °C. Thermal conductivity of the decomposed material (above 400 °C) is obtained by considering that the resin is fully replaced by the gases generated during decomposition.

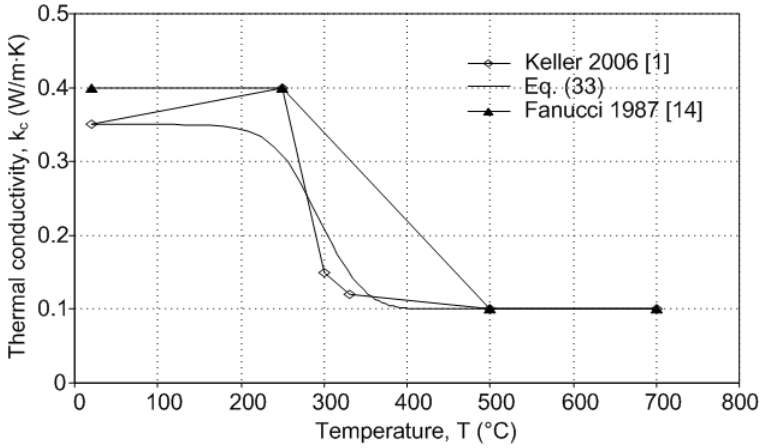

Fig. 10. Comparison of temperature-dependent thermal conductivity models

Similar curves to those shown in Fig. 10 were also found in previous studies [1, 14]. For the curve proposed by Fanucci 1987 [14], however, the conductivity was artificially adjusted to reflect the decrease during the decomposition process. In Keller et al. 2006 [1], the curve from ambient temperature to T_d was adopted from Samanta et. al [7] and proportionally adjusted to match the experimentally measured ambient temperature value. In [7], the conductivity of a similar material was reported as a linear function of temperature, while no experimental proof was given. The curve above T_d in Keller et al. 2006 is similar as in [14]. This portion of the curve shows an artificially decreasing thermal conductivity up to k_a, which serves to capture the conductivity-reducing effects during the decomposition process. Compared with the previous models, since the volume fraction of each phase was directly obtained from the decomposition model, a continuous model for thermal conductivity is achieved in this paper, instead of the stepped function and linear interpolation process used in [1, 14].

4 MODELING OF TEMPERATURE-DEPENDENT SPECIFIC HEAT CAPACITY

4.1 Formulation of basic equations

The true specific heat capacity is related to the quantity of heat required

to raise the temperature of a specified mass of material by a specified temperature. For composites, it can be estimated based on the mixture approach. Considering again that the material is composed of two phases - undecomposed and decomposed material - the total heat, E, required to raise the temperature by ΔT of the material with the mass M should be equal to the sum of the heat required to raise the temperature of all its phases to the same level, as shown in Eq. (36):

$$C_{p,c} = \frac{E}{\Delta T \cdot M} = \frac{C_{p,b} \cdot \Delta T \cdot M \cdot f_b + C_{p,a} \cdot \Delta T \cdot M \cdot f_a}{\Delta T \cdot M} = C_{p,b} \cdot f_b + C_{p,a} \cdot f_a \tag{36}$$

where $C_{p,c}$ is the specific heat capacity of the composite material, $C_{p,b}$ ($C_{p,a}$) is the specific heat capacity of the undecomposed (decomposed) material, and f_b (f_a) is the temperature-dependent mass fraction of the undecomposed (decomposed) material according to Eqs. (24) and (25).

For the effective specific heat capacity, the energy change during decomposition (i.e. decomposition heat) must be considered. The rate of energy absorbed for decomposition (endothermic reaction) is determined by the reaction rate, i.e., the decomposition rate, which is obtained by the decomposition model (Eq. 5). Combining Eqs. (5) and (36) gives:

$$C_{p,c} = C_{p,b} \cdot f_b + C_{p,a} \cdot f_a + \frac{d\alpha}{dT} \cdot C_d \tag{37}$$

where C_d is the total decomposition heat, α is the decomposition degree defined in Eq. (5). As a result, by combining Eq. (5), (24), (25) and (37), the temperature-dependent effective specific heat capacity is obtained.

4.2 Estimation of $C_{p,b}$ and $C_{p,a}$

As mentioned, many experimental results have shown that the specific heat for composites increases slightly with temperature before decomposition. In some previous models, the specific heat was described as a linear function. Theoretically, however, the specific heat capacity for materials will change as a function of temperature since, on the micro level, heat is the vibration of the atoms in the lattice. Einstein (1906) and Debye (1912) individually developed models for estimating the contribution of atom vi-

bration to the specific heat capacity of a solid. The dimensionless heat capacity is defined according to Eqs. (38) and (39) and illustrated in Fig. 11 [37]:

$$\frac{C_v}{3Nk} = 3\left(\frac{T}{T_D}\right)^3 \int_0^{T_D/T} \frac{x^4 e^x}{\left(e^x - 1\right)^2} dx \tag{38}$$

$$\frac{C_v}{3Nk} = \left(\frac{T_E}{T}\right)^2 \frac{e^{T_E/T}}{(e^{T_E/T} - 1)^2} \tag{39}$$

where C_v/Nk is the dimensionless heat capacity, T_D (T_E) is the Debye (Einstein) temperature, which are calculated from Eq. (40) to Eq. (43).

$$T_D = \frac{h \cdot \nu_D}{k}, \text{ or } T_E = T_D \cdot \sqrt[3]{\pi/6} \tag{40}$$

$$\nu_D = \sqrt[3]{\frac{9N}{4\pi V} \cdot \left(\frac{2}{{c_T}^3} + \frac{1}{{c_L}^3}\right)^{-1}} \tag{41}$$

$$c_T = \sqrt{\frac{3(1-2\gamma)}{2\rho\kappa(1+\gamma)}} \tag{42}$$

$$c_L = \sqrt{\frac{3(1-\gamma)}{\rho\kappa(1+\gamma)}} \tag{43}$$

where h is Planck's constant (6.63×10^{34}), k is Boltzmann constant (1.38×10^{23}), ν_D is the Debye frequency in Eq. (40), V is the volume, N is the number of atoms in the volume, V (estimated from its mole volume and Avogadro's number (6.02×10^{23}), c_T and c_L are the velocities of an elastic wave propagating in two different directions, ρ is the density, κ is the compressibility factor ($\kappa = 3(1-2\gamma)/E$), γ is the Poisson ratio, E is the elastic modulus. If $T<<T_D$, the heat capacity of crystal material is proportional to T^3, and if $T>>T_D$, the heat capacity will approach a constant as shown in Fig. 11 (also known as Dulong-Petit Law) [37].

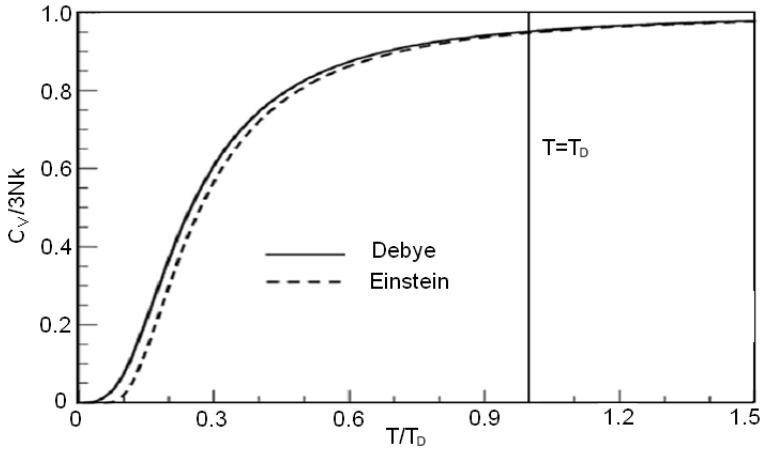

Fig. 11. Debye model and Einstein model

Considering that the E-glass fibers are composed of SiO_2 with E=73 GPa, γ=0.2, ρ=2600 kg/m^3 [38], T_E is calculated as 387.8 K (114.8 °C). Substituting T_E into Eq. (38) and considering that its specific heat capacity is 840 J/kg·K at 20°C [39], the temperature-dependent specific heat capacity of E-glass fibers ($C_{p,f}$) is obtained.

For the polymer matrix, it should be noted that the Debye temperature, T_D, for polyester is lower than 27°C [12]. Consequently, in the range of elevated and high temperature, the specific heat capacity of polyester ($C_{p,m}$) can be assumed as almost a constant (see Fig. 11, the portion of curve above T_D). As a result, $C_{p,b}$ can be expressed as:

$$C_{p,b} = C_{p,f} \cdot f_{f0} + C_{p,m} \cdot f_{m0} \tag{44}$$

where $C_{p,f}$ ($C_{p,m}$) is the specific heat capacity of fibers (matrix), f_{f0} (f_{m0}) is the mass fraction of the fibers (matrix) of the initial material. $C_{p,m}$=1600 J/kg·K was used for polyester at room temperature in [7, 8]. The specific heat capacity of the FRP material used for this study and measured at room temperature was 1170 J/kg·K [15]. Substituting $C_{p,f}$ (840 J/kg·K), $C_{p,m}$ (1600 J/kg·K) and the initial mass fraction of fiber and resin according to Table 1 into Eq. (43), a value of 1135 J/kg·K results or 97% of the experimental value (1170 J/kg·K).

$C_{p,a}$ is the specific heat capacity of the decomposed material. Since the polymer matrix almost decomposed into gases, most mass of the material after decomposition is composed of fibers. As a result, $C_{p,a}$ is approximately equal to the specific heat capacity of the fibers (since the mass fraction

of the remaining gases in the composition is negligible compared to that of the fibers):

$$C_{p,a} = C_{p,f} \tag{45}$$

Substituting Eqs. (44) and (45) into Eq. (37), and using Eqs. (24), (25), (28), (29) gives:

$$\begin{aligned} C_{p,c} &= \left(C_{p,f} \cdot f_{f0} + C_{p,m} \cdot f_{m0}\right) \cdot f_b + C_{p,f} \cdot f_a + \frac{d\alpha}{dT} \cdot C_d \\ &= C_{p,f} \cdot f_f + C_{p,m} \cdot f_m + \frac{d\alpha}{dT} \cdot C_d \end{aligned} \tag{46}$$

Eq. (46) shows that combining the properties of undecomposed and decomposed materials leads to the same results as by combination of the fibers and matrix properties.

4.3 Decomposition heat, C_d

The value of the decomposition heat can be obtained from DSC tests by integrating the measured heat from $T_{d,\,onset}$ to $T_{d,\,end}$, and subtracting the heat required for increasing the temperature of the material (true value). This method was proposed by Henderson in 1982 and 1985 [5, 13] and the decomposition heat of phenol-formaldehyde (phenolic) resin was calculated as C_d=234 kJ/kg. A similar value of 235 kJ/kg was also used in [7-8] as the decomposition heat of polyester resin.

4.4 Moisture evaporation

Heat is also required to transform moisture from a liquid to gas (latent heat C_w=2260 kJ/kg). The total heat depends on the moisture content of the material and the rate of change is determined by the evaporating rate. Evaporation also can be described by the equations of chemical kinetics [40]. If the mass change of water during the heating process in known, the kinetic parameters can be estimated by the methods introduced previously. In Samanta 2004 [8], a 1% mass of moisture content was assumed, while in Keller 2006 [1-2] a 0.5% mass of moisture content was taken. In both cases, the effects of moisture evaporation on heat capacity was assumed

roughly as a triangular function dependent on temperature without kinetic considerations.

The effects of moisture on the specific heat capacity is not included in Eq. (46), since the content of moisture is negligible compared to the energy change due to the decomposition of resin, and measurement noise will also influence the measured moisture content to a great extent due to the small quantity.

4.5 Comparison of modeling results

Experimental results for the effective specific heat capacity were obtained by DSC tests in [13]. MXB-360 (Phenol-formaldehyde resin) with a 73.5% mass fraction of glass fibers was used in those tests. $C_{p,b}$, $C_{p,a}$ and C_d were given in [13] as follows:

$$C_{p,b} = 1097 + 1.583T \ \text{(J/kg·K)} \tag{47}$$

$$C_{p,a} = 896 + 0.879T \ \text{(J/kg·K)} \tag{48}$$

$$C_d = 385259 \ \text{(J/kg)} \tag{49}$$

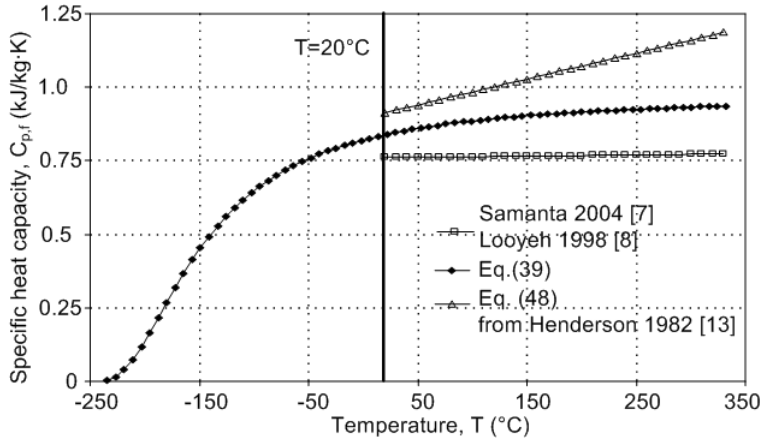

Fig. 12. Comparison of temperature-dependent specific heat capacity models of E-glass fibers

Most of the char material was composed of glass fiber and $C_{p,a}$ was therefore considered as the specific heat capacity of the glass fibers. The results from Eq. (48) are compared with the results from the Einstein model (Eq. 39) in Fig. 12, as well as with the model used in previous studies [7, 8]. A linear function dependent on temperature for the specific

heat capacity of fiber was used by Samanta 2004 [7] and Looyeh in 1997 [8], however, without direct experimental validation. As shown in Fig. 12, the theoretical curve based on the Einstein model (Eq. 39) gives a reasonable estimation for the specific heat capacity of glass fibers.

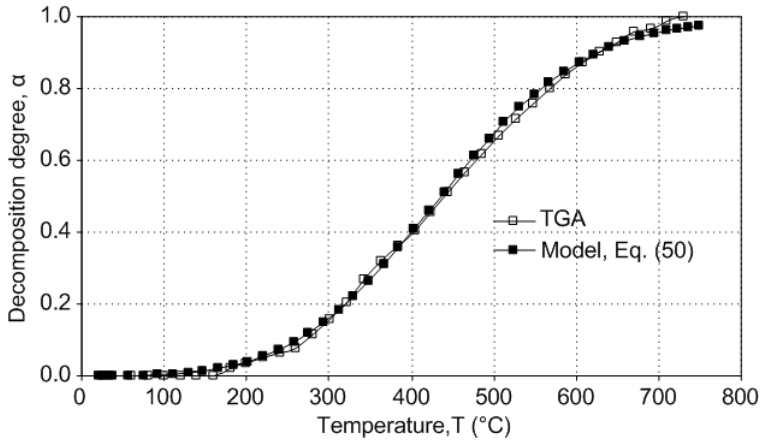

Fig. 13. Comparison of results from decomposition model and TGA data of MXB-360 (from Henderson [13])

Based on the TGA data in [13], a decomposition model was constructed with the parameters determined by the modified Coats-Redfern method (since only one heating rate curve was available from [13]). The comparison between the resulting model (Eq. 50):

$$\frac{d\alpha}{dT} = \frac{11.85}{20}\exp\left(\frac{-26527.86}{RT}\right)(1-\alpha) \tag{50}$$

and experimental TGA data is shown in Fig. 13. A good match was found. Equation (51) for the specific heat capacity can be obtained by substituting Eqs. (47) to (50) into Eq. (37):

$$C_{p,c} = (1097 + 1.583T)\cdot f_b + (896 + 0.879T)\cdot(1-f_b) + \frac{11.85}{20}\exp\left(\frac{-26527.86}{RT}\right)(1-\alpha)\cdot 385259 \tag{51}$$

In Eq. (51), the temperature-dependent parameters α, f_b and f_a are given by Eq. (5), (24) and (25). The effective specific heat capacity, $C_{p,c}$, can then be determined by one variable, i.e., temperature.

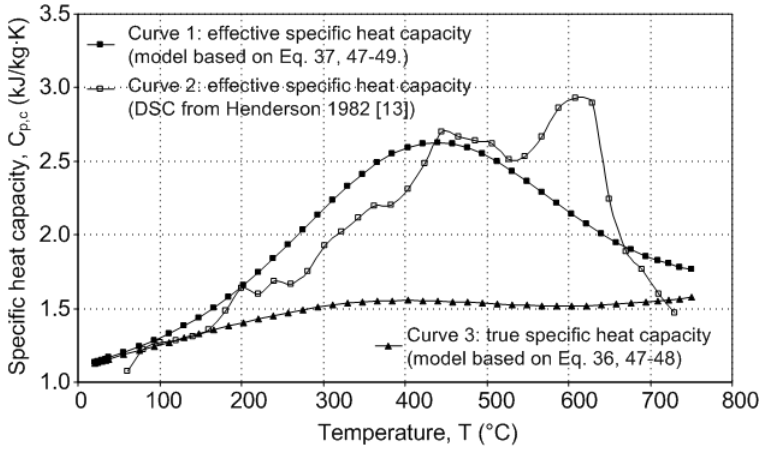

Fig. 14. Comparison of effective heat capacity model and DSC data of MXB-360 (from Henderson [13])

A comparison between the resulting model (curve 1 based on Eq. (51)) and DSC results (curve 2 from experimental results in [13]) is shown in Fig. 14. The change of effective specific heat capacity can be reasonably predicted from room temperature up to about 530°C, including the increase in specific heat capacity due to decomposition represented by the peak point in curve 1. An additional peak was found in curve 2 at around 600°C. The nature of this second peak is not addressed in [13] and, therefore, cannot be further discussed. The true specific heat capacity can also be obtained by combing Eq. (36), (47), (48) and (50) as shown by curve 3 in Fig. 14. No peaks result from the decomposition heat for the true specific heat capacity. Comparing the effective specific heat capacity from model and DSC (curve 1 and 2) with the true specific heat capacity (curve 3) in Fig. 14, the area between curves 1 and 3 compares well to that between curves 2 and 3. This area denotes the total decomposition heat given in Eq. (49).

The same method can be applied to the Duraspan material also used in Keller et al. 2006 [1]. The resulting curve is obtained in Fig. 15 (continuous curve 1) and compared with the previous model (stepped curve 2 [1]). The two curves are both effective specific heat capacity models, thus showing the peaks during decomposition (the first peak in the curve 2 resulted from the latent heat, C_w, of water evaporation at 100°C, which was not considered in curve 1). The two curves are in good agreement at low

temperatures, since both used the same initial value based on experimental results (1170 J/kg·K at room temperature). Points at higher temperatures for curve 2 were subjectively determined based on a triangle and trapezoid area, corresponding to the latent heat of evaporation and decomposition heat, respectively. In contrast, the effective specific heat capacity during decomposition in curve 1 was obtained from the decomposition model (Eq. 5 and 37). This is why the two models show a big variance during decomposition. The smaller gap between the two curves at the highest temperatures is because the true specific heat capacity was assumed as a constant in curve 2, while it was obtained based on the mixture approach (Eq. 36) for curve 1. However, the areas below the curves that denote the decomposition heat compare well.

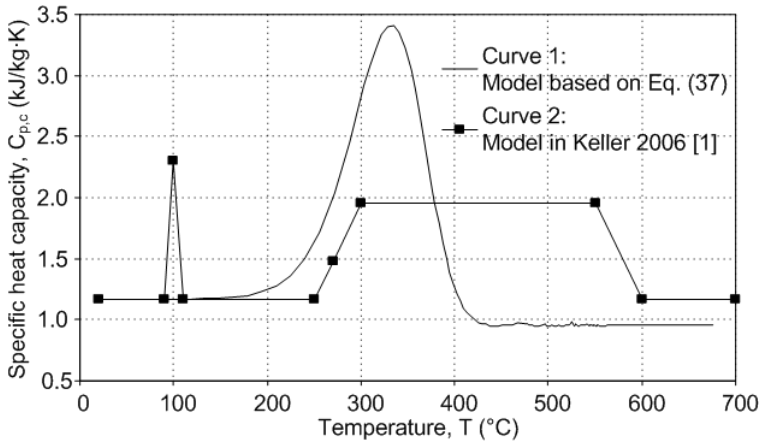

Fig. 15. Comparison of effective heat capacity model (Eq. 37) and previous model from Keller [1]

5 CONCLUSION

The decomposition process of resin in composite materials was modeled and the kinetic parameters were determined using TGA data based on "multi-curves" (e.g. Ozawa) methods and a "single-curve" (e.g. Coats-Redfern) method. Although a certain variance between parameters obtained from different methods was seen, each method gave a reasonable match with experimental results. Based on the decomposition degree calculated from the decomposition model, a temperature-dependent mass transfer model was obtained.

Considering that composites are combined of two different phases (un-

decomposed and decomposed material), the volume fraction of each phase was directly obtained from the decomposition model and mass transfer model. The temperature-dependent thermal conductivity was then estimated by the series model. The rapid decrease of thermal conductivity during the decomposition process was also modeled by considering the concept of effective thermal conductivity.

The true specific heat capacity was obtained by a general mixture approach and the mass fraction of each phase was determined by the decomposition and mass transfer model. The true specific heat capacity of each phase was derived based on the Einstein or Debye model, instead of using a linear function dependent on temperature from curve fitting. The effective specific heat capacity was obtained by assembling the true specific heat capacity with the decomposition heat, which was also described by the decomposition model. The effective specific heat capacity is useful in capturing the endothermic decomposition of resin and can be further verified by DSC tests.

Each model was compared with experimental data collected in the course of the present study, or previous models and experimental results, and good agreements were found. Based on these results, the temperature responses can be predicted by assembling these models of thermophysical properties into the final governing equation of thermal response models.

ACKNOWLEDGEMENT

The authors would like to thank the Swiss National Science Foundation (Grant No. 200020-109679/1) for financial support of this project.

REFERENCES

1. Keller T, Tracy C, Zhou A. Structural response of liquid-cooled GFRP slabs subjected to fire. Part I: material and post-fire modeling. *Composites Part A* 2006, 37(9): 1286-1295.

2. Keller T, Tracy C, and Zhou A. Structural response of liquid-cooled GFRP slabs subjected to fire. Part II: thermochemical and thermomechan-

ical modeling. *Composites Part A* 2006, 37(9): 1296-1308.

3. Ashby MF, Jones DRH. Engineering materials 2: An introduction to microstructures, processing and design. 3rd edition, Elsevier, 2006.

4. Dimitrienko YI. Thermomechanical behavior of composite materials and structures under high temperatures: 1. Materials. *Composites Part A* 1997, 28(5): 453-461.

5. Henderson JB, Wiebelt JA, Tant MR. A Model for the Thermal Response of Polymer Composite Materials with Experimental Verification. *Journal of Composite Materials* 1985, 19: 579-595.

6. Henderson JB, Wiecek TE. A Mathematical Model to Predict the Thermal Response of Decomposing, Expanding Polymer Composites. *Journal of Composite Materials* 1987, 21: 373-93.

7. Samanta A, Looyeh MRE, Jihan S, McConnachie J. Thermo-mechanical assessment of polymer composites subjected to fire. Engineering and Physical Science Research Council & the Robert Gordon University, 2004, Aberdeen, UK.

8. Looyeh MRE., Bettess P, Gibson AG. A one-dimensional finite element simulation for the fire-performance of GRP panels for offshore structures. *International Journal of Numerical Methods for Heat & Fluid Flow* 1997, 7(6): 609-625.

9. Henderson JB, Tant MR, Moore GR, Wiebelt JA. Determination of kinetic parameters for the thermal decomposition of phenolic ablative materials by a multiple heating rate method. *Thermochimica Acta* 1981, 44: 253-264.

10. Halverson H, Bausano J, Case SW, Lesko JJ. Simulation of response of composite structures under fire exposure. *Science and Engineering of Composite Materials* 2005, 12(1-2): 93-101.

11. Tant MR. High Temperature Properties and Applications of Polymeric Materials. Proceedings of the ACS Symposium Series 603, 1994, San Diego, CA, USA.

12. Hilal AS, Abousehly AM, Dessouky, MT, ABD El-hakim AA. Measurement of thermophysical properties of polyester cured with styrene in

the range 300-450 K. *Journal of Applied Polymer Science* 1993, 49: 559-563.

13. Henderson JB, Wiebelt JA, Tant MR, Moore GR. A method for the determination of the specific heat and heat of decomposition of composite materials. *Thermochimica Acta* 1982, 57: 161-171.

14. Fanucci JP. Thermal response of radiantly heated kevlar and graphite/epoxy composites. *Journal of Composite Materials* 1987, 21(2): 129-139.

15. Tracy C. Fire endurance of multicellular panels in an FRP building system. Ph.D. Thesis (No. 3235), Swiss Federal Institute of Technology-Lausanne, Switzerland, April 2005.

16. Henderson JB, Verma YP, Tant MR, Moore GR. Measurement of the thermal conductivity of polymer composites to high temperature using the line source techniques. *Polymer composites* 1983, 4(4): 219-224.

17. Garrett KW, Rosenberg HM. The thermal conductivity of epoxy-resin/powder composites materials. *Journal of Physics D: Applied Physics* 1974, 7: 1247-1258.

18. Ganapathy D, Singh K, Pjelan PE, Prasher R. An effective unit cell approach to compute the thermal conductivity of composites with cylindrical particles. *Journal of heat transfer* 2005, 127: 553-559.

19. Griffis CA, Masumra RA, Chang CI. Thermal response of graphite epoxy composite subjected to rapid heating. *Journal of Composite Materials 1981*, 15: 427-442.

20. Friedman HL. Kinetics of thermal degradation of char-forming plastics from thermo-gravimetry: Application to a phenolic plastic. *Journal of Polymer Science: Part C* 1965, 6: 183-195.

21. Lee JY, Shim MJ, Kim SW. Thermal decomposition kinetics of an epoxy resin with rubber-modified curing agent. *Journal of Applied Polymer Science* 2001, 81(2): 479-485.

22. Kissinger HE. Reaction Kinetics in Differential Thermal Analysis. *Analytical Chemistry* 1957, 29: 1702-1706.

23. Regnier N, Guibe C. Methodology for multistage degradation of polyi-

mide polymer. *Polymer Degradation and Stability* 1997, 55: 165-172.

24. Ozawa T. A new method of analysing thermogravimetric data. *Bulletin of the Chemical Society of Japan* 1965, 38(11): 1881-1886.

25. Doyle CD. Kinetic analysis of thermogravimetric data. *Journal of Applied Polymer Science* 1961, 5(15): 285-292.

26. Coats AW, Redfern JP. Kinetic parameters from thermogravimetric data. *Nature* 1964; 201: 68-69.

27. Coats AW, Redfern JP. Kinetic parameters from thermogravimetric data II. *Polymer letters* 1965, 3: 917-920.

28. Zsakó J. Kinetic analysis of thermogravimetric data XXIX: Remarks on the 'many curves' methods. *Journal of Thermal Analysis and Calorimetry* 1995, 46(6): 1845-1864.

29. Zsakó J. Kinetic analysis of thermogravimetric data VI: Some problems of deriving kinetic parameters from TG curves. *Journal of thermal analysis* 1973, 5: 239-251.

30. Tavman IH, Akinci H. Transverse thermal conductivity of fiber reinforced polymer composites. *International Communications in Heat and Mass Transfer* 2000, 27 (2): 253-261.

31. Hàkansson B, Ross RG. Effective thermal conductivity of binary dispersed composites over wide ranges of volume fraction, temperature, and pressure. *Journal of Applied Physics* 1990, 68(7): 3285-3292.

32. Bernasconi J, Wiesmann HJ, Effective-medium theories for site-disordered resistance networks. *Physical Review B* 1976, 13(3): 1131-1139.

33. Vladimir K, Alexei C. Effective thermal conductivity of a low-density polyethylene and ionic salts composite. *Journal of Applied Physics* 1992, 73(5): 2259-2263.

34. Hatta H, Taya M. Effective thermal conductivity of a misoriented short fiber composite. *Journal of Applied Physics* 1985, 58(7): 2478-2486.

35. Al-Sulaiman FA, Al-Nassar YN, Mokheimer EMA. Prediction of the thermal conductivity of the constituents of fiber-reiforced composite laminates: voids effect. *Journal of Composite Materials* 2006, 40(9): 797-814.

36. Zou M, Yu B, Zhang D, Ma Y. Study on optimization of transverse

thermal conductivities of unidirectional composites. *Journal of Heat Transfer* 2003, 125: 980-987.

37. Rief F. Fundamentals of Statistical and Thermal Physics. McGraw-Hill Book Company, 1965.

38. Keller T. Use of fiber reinforced polymers in bridge construction. Structural Engineering Documents 2003, Zurich: International Association for Bridge and Structural Engineering (IABSE).

39. Drysdale D. An introduction to fire dynamics. John Wiley & Sons, Inc., New York, NY, 1998.

40. Rusdi M, Moroi Y. Study on water evaporation through 1-alkanol monolayers by the thermogravimetry method. *Journal of Colloid and Interface Science* 2004, 272: 472-479.

2.2 Modeling of stiffness degradation

Summary

When FRP composites are subjected to elevated and high temperatures, their mechanical properties, such as the E-modulus and viscosity, undergo significant changes. Such changes are mainly caused by the glass transition of the resin, which occurs within a lower temperature range than decomposition. Rather than modeling these behaviors by directly fitting the experimental curves using an assumed form of function, an attempt is made to first model the related thermally induced changes in material states.

At a certain temperature, a composite material can be considered as being a mixture of materials that are in a glassy, leathery, rubbery or decomposed state, and the transitions between these different states are designated the glass transition, leathery-to-rubbery transition, and rubbery-to-decomposed transition (decomposition, modeled in Section 2.1). The mechanical properties of the mixture are determined by the content and properties of each state and the content of each state can be estimated using kinetic theory. In this way, a model was developed to predict the temperature-dependent E-modulus, G-modulus, viscosity and effective coefficient of thermal expansion of FRP composites in the different temperature ranges, including the glass transition and decomposition of the polymer resin. The prediction of the temperature-dependent mechanical properties was compared with experimental results obtained by Dynamic Mechanical Analysis (DMA), and good agreement was found.

Reference detail

This paper was published in Composites Science and Technology 2008, volume 68, pages 3099-3106, entitled

"Modeling of stiffness of FRP composites under elevated and high temperatures" by Yu Bai, Thomas Keller and Till Vallée.

Part of the content of this paper was presented at the Fourth International Conference on FRP Composites in Civil Engineering (CICE) 22-24

July 2008, Zurich, Switzerland, entitled

"Modeling of thermomechanical properties and responses for FRP composites in fire" by Yu Bai, Thomas Keller and Till Vallée, presented by Yu Bai.

MODELING OF STIFFNESS OF FRP COMPOSITES UNDER ELEVATED AND HIGH TEMPERATURES

Yu Bai, Thomas Keller and Vallée Till

Composite Construction Laboratory CCLab, Ecole Polytechnique Fédérale de Lausanne (EPFL), BP 2225, Station 16, CH-1015 Lausanne, Switzerland.

ABSTRACT:

When subjected to elevated and high temperatures, the mechanical properties of FRP composites, such as the E-modulus and viscosity, experience significant changes. At a certain temperature, a composite material can be considered a mixture of materials that are in a glassy, leathery, rubbery or decomposed state. The mechanical properties of the mixture are determined by the content and the property of each state. The content of each state can be estimated by kinetic theory. A model based on the Arrhenius equation was developed to predict the temperature-dependent E-modulus, G-modulus, viscosity and effective coefficient of thermal expansion of FRP composites during the different temperature ranges, including the glass transition and the decomposition of the polymer resin. The kinetic parameters, such as activation energy and pre-exponential factor, were estimated by a modified Coats-Redfern method. The prediction of the temperature-dependent mechanical properties was compared with experimental results obtained by Dynamic Mechanical Analysis (DMA), and a good agreement was found.

KEYWORDS:

Polymer-matrix composites; thermomechanical properties; modeling; pultrusion

1 INTRODUCTION

The continually expanding use of FRP composites in large structural applications requires a better understanding of the interdependent thermal and mechanical responses of the FRP when it is subjected to elevated and high temperatures. The thermomechanical behavior of FRP composites depends mainly on that of the polymer resin. Generally, the elastic modulus and strength of a polymer drops significantly and the viscosity increases when the temperature reaches and exceeds the glass transition temperature. In order to design structures with FRP components, it is necessary to describe in detail the different material states and to accurately model the variation of the mechanical properties over a broad temperature range, including glass transition and decomposition of the polymer resin.

Thermomechanical models using temperature-dependent mechanical properties for FRP materials were developed in the 1980s. A comprehensive review of these models was reported by Keller et al. in 2005 [1, 2]. In many of the suggested thermomechanical models, temperature-dependent E-moduli were developed as stepped functions achieved by connecting experimentally gathered key points, such as the glass transition temperature (T_g) and the decomposition temperature (T_d). E-modulus values at different temperatures were obtained by Dynamic Mechanical Analysis (DMA), as presented by Chen et al in 1985 [3], by Griffis et al in 1985 [4], by Dao and Asaro in 1999 [5], by Bausano et al in 2004 [6], and by Halverson et al in 2004 [7].

A temperature-dependent E-modulus function was empirically proposed by Springer in 1984 [8] and is described by Eq. (1):

$$\frac{E}{E_0} = 1 - \left(\frac{\Delta m(t)}{\Delta m_{end}} \right)^g \tag{1}$$

where E_0 is the E-modulus at initial temperature (usually room temperature), E is the E-modulus at time t, $\Delta m(t)$ is the mass loss at time t, Δm_{end} is the maximum mass loss at t_{end}, and g is an experimentally determined, material dependent constant. Another empirical relation was proposed by Dutta and Hui in 2000 [9] to calculate the temperature-dependent E-

modulus:

$$E(t_0,T_0)=\left(\frac{\rho\cdot T}{\rho_0\cdot T_0}\right)E(t,T) \tag{2}$$

where $E(t_0,T_0)$ is the initial E-modulus at a time t_0 and temperature T_0, ρ and ρ_0 are the densities of the polymer at temperatures T in time t and T_0 in time t_0, respectively.

Gibson et al. presented a temperature-dependent E-modulus model in 2004 [10]. Mechanical properties were assumed to degrade during the glass transition as described by Eq. (3):

$$E(T)=\frac{E_u+E_r}{2}-\frac{E_u-E_r}{2}\tanh\left(k\left(T-T'\right)\right) \tag{3}$$

where E_u and E_r are the moduli before and after transition respectively, T' is the temperature at which the value of the E-modulus falls most rapidly (and is assumed to be the glass transition temperature), and k is a constant related to the sharpness of the transition.

A theoretical model for a temperature-dependent E-modulus was developed by Mahieux et al. [11-13]. In this model, Weibull-type functions were used to describe the modulus change over the full range of transition temperatures.

$$\begin{aligned}E=&\left(E_1-E_2\right)\cdot\exp\left(-\left(\frac{T}{T_1}\right)^{m_1}\right)+\\&\left(E_2-E_3\right)\cdot\exp\left(-\left(\frac{T}{T_2}\right)^{m_2}\right)+E_3\cdot\exp\left(-\left(\frac{T}{T_3}\right)^{m_3}\right)\end{aligned} \tag{4}$$

where E_i (i=1, 2, 3) represents the instantaneous stiffness of the material at the beginning of each plateau or state, T_i corresponds to the temperature at each transition (as given by the maximum of the peaks on the tangent delta versus temperature of a DMA curve), and m_i are Weibull moduli corresponding to the statistics of the bond breakage. Experimental validation of Eq. (4) was conducted on six different polymers. In each case the degradation of the modulus during glass transition was accurately described by the model if appropriate m_i values were determined. A further application of this model to predict the mechanical responses of composites was carried out by Burdette et al in 2001 [14].

An empirical model a temperature-dependent E-modulus was proposed by Gu and Asaro in 2005 [15]:

$$E(T) = E_0\left(1 - \frac{T - T_r}{T_{ref} - T_r}\right)^g \tag{5}$$

where E_0 is the modulus at room temperature, T_{ref} is the temperature at which the E-modulus tends to zero, T_r is room temperature, and g is a power law index that varies between 0 and 1.

In the above-cited work, the investigations focused on the temperature-dependent E-modulus and the related mechanical responses. Less information, however, exists on temperature-dependent viscosity (particularly, of the polymer resin), which is necessary to describe the long-term behavior of FRP structures. At room temperature and under quasi-static (short-term) loading, the viscosity of FRP composites is not noticeable, while, when the temperature increases, the viscosity changes significantly and influences considerably the mechanical responses of the FRP [16-18]. It appears, however, that numerical modeling work on temperature-dependent viscosity is seldom performed.

In this paper a new model is proposed to describe the progressive changes in the E-modulus and viscosity of FRP composites under elevated and high temperatures. Theoretical results are compared with corresponding experimental results from DMA experiments. By assembling these temperature dependent visco-elastic properties, the mechanical responses of FRP structures can be further predicted over the whole temperature range, covering glass transition and decomposition.

2 DYNAMIC MECHANICAL ANALYSIS

2.1 Basic equations

DMA experiments allow for a description of the changes in the E-modulus and viscosity of a certain material as a function of the change in temperature [16]. Though many variations of the DMA exist, the basic procedure is the same: specimens are loaded cyclically (usually a sinusoidal load path) within the elastic region of their stress-strain curve (low stress level), and

the temperature is slowly varied at a constant heating rate. Sensors measure the temperature, load, and strain. For example in a DMA experiment, strain, ε, is imposed as:

$$\varepsilon = \varepsilon_0 \sin(\omega \cdot t) \tag{6}$$

Where ε_0 is the strain amplitude, t denotes the time and ω the circle frequency. The corresponding stress, σ, is expressed as:

$$\sigma = \sigma_0 \sin(\omega \cdot t + \delta) \tag{7}$$

where σ_0 is the stress amplitude and δ is the phase angle between stress and strain. Then the storage modulus E', loss modulus E'' and damping factor $\tan\delta$ are expressed as [16]:

$$E' = (\sigma_0/\varepsilon_0)\cos\delta \tag{8}$$

$$E'' = (\sigma_0/\varepsilon_0)\sin\delta \tag{9}$$

$$\tan\delta = E''/E' \tag{10}$$

An appropriate physical model should be used to relate the specimen parameters (storage modulus, loss modulus and damping factor) obtained in the DMA to the effective properties (E-modulus, viscosity) of the material. Considering the Voight model [16], consisting of the association of a spring and dashpot in parallel, the equation of motion can be expressed as:

$$\sigma(t) = \varepsilon(t) E_m + \eta_m \frac{d\varepsilon(t)}{dt} \tag{11}$$

where the spring represents the E-modulus, E_m, and the dashpot the viscosity, η_m. The relaxation time of the model is defined as:

$$\tau_m = \eta_m / E_m \tag{12}$$

Based on the Voight model, the following equations can be derived from DMA results [16]:

$$E_m = E'(\omega) \tag{13}$$

$$\eta_m = E_m \cdot \tau_m = E''(\omega)/\omega \tag{14}$$

2.2 DMA experiments on pultruded glass FRP laminate

DMA experiments on a pultruded glass fiber-reinforced polyester laminate

were performed. The glass transition temperature and decomposition temperature of the resin were T_g = 117°C and T_d = 300°C, respectively; the void content was less than 2% [17]. Cyclic dynamic loading was imposed to a 54×12×3 mm^3 specimen in a three-point-bending configuration within a Rheometrics Solids Analyzer. The specimen was scanned in the "dynamic temperature ramp mode" using a dynamic oscillation frequency of 1 Hz (corresponding to $\omega = 2\pi$) from temperatures ranging between -40°C to 250°C, at a heating rate of 5°C/min. The oven was purged with nitrogen during the scans.

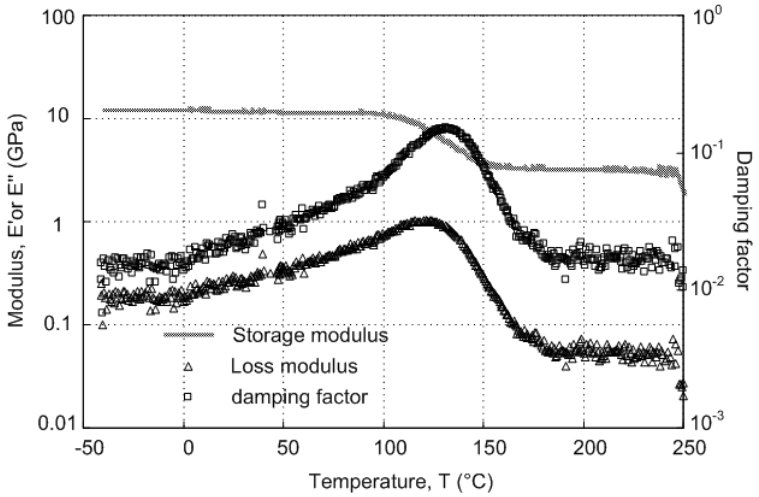

Fig. 1. Changes in E', E'' and tan δ at different temperatures from DMA

The storage modulus, E', loss modulus, E'', and tan δ were obtained as shown in Fig. 1. The storage modulus, which represents the E-modulus in bending of the specimen, was stable at the lower temperature range (below 100°C). When the temperature was increased, the storage modulus dropped rapidly and then reached a plateau at approximately 150°C. Since the experiment was stopped at 250°C, a second decrease during decomposition could not be measured. The loss modulus increased in response to an increase in temperature. However, it dropped rapidly when the temperature exceeded T_g at which point it also levelled off before the decomposition. The damping factor, defined as the ratio of the loss modulus to the storage modulus, behaved similar to the loss modulus as a function of temperature.

3 CHANGE OF POLYMER MATERIAL STATES DURING HEATING

As shown in Fig. 1, the mechanical properties of FRP composites vary significantly when subjected to high temperatures. The variations are, in particular, due to the polymer, whose mechanical properties are dependent on the type of bonds between molecules [18]. The bonds in polymers can be divided into two major groups: the primary bonds and the secondary bonds. The first group includes the strong covalent intra-molecular bonds in the polymer chains and cross-links of thermosets. The dissociation energy of such bonds varies between 50 and 200 kcal/mole. Secondary bonds include much weaker bonds, e.g. hydrogen bonds (dissociation energy: 3-7 kcal/mole), dipole interaction (1.5-3 kcal/mole), and Van der Waals interaction (0.5-2 kcal/mole). Consequently, the secondary bonds can be dissociated much easier.

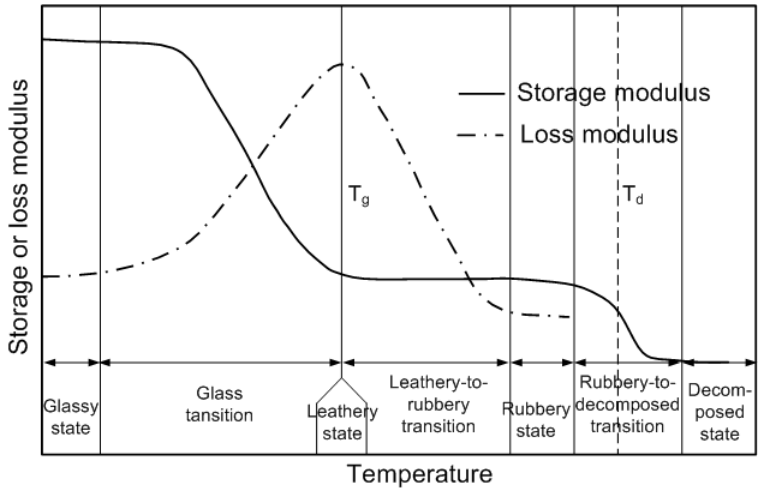

Fig. 2. Definition of different material states and transitions

In the lower temperature range, the material is characterized by intact primary and secondary bonds, therefore corresponding to the highest, almost constant segment of the E-modulus response called the glassy state (Fig. 2). However, when the temperature increases, a material state is reached comprising intact primary bonds and broken secondary bonds, which, in accordance with [18], is referred to as the leathery state. Due to the broken secondary bonds, the E-modulus in the leathery state is much lower than in the glassy state, while the viscosity is much higher. Accordingly, in this transition from glassy to leathery state (generally known as

the glass transition), the viscosity increases, while the E-modulus drops rapidly (see Fig. 2). The reptation theory was proposed by Ashby [18] to explain the steep decrease in the modulus at this transition.

As the temperature is raised further, the polymer chains form entanglement points where molecules, because of their length and flexibility, become knotted together. This state is called the rubbery state [18]. The rubbery state is characterized by intact primary and broken secondary bonds, but in an entangled molecular structure. Due to this kind of molecular structure, the E-modulus in the rubbery state is similar to the E-modulus when the material is in the leathery state, while the viscosities of these two states are different. The rubbery state, because of the entangled molecule chains, obviously exhibits a lower viscosity than the leathery state. For this reason, in the transition from the leathery to the rubbery state, (leathery-to-rubbery transition, see Fig. 2), a plateau is induced in the temperature-dependent storage modulus plot, while the temperature-dependent loss modulus is found to decrease. When even higher temperatures are reached the primary bonds are also broken and the material is decomposed. This is called the rubbery-to-decomposed transition and results in the decomposed state.

Consequently, for the polyester thermosets, four different states (glassy, leathery, rubbery and decomposed) and three transitions (glass transition, leathery-to-rubbery transition, and rubbery-to-decomposed transition) can be defined when the temperature is raised. At each temperature, a composite material can be considered a mixture of materials in different states, with different mechanical properties. The content of each state varies with temperature, thus the composite material shows temperature-dependent properties. The change from one state to another needs to acquire enough energy (activation energy) to form an “activated complex” [19]. This dynamic process can be described by the kinetic theory, thus the Arrhenius equations to estimate the quantity of material in each state can be applied. If the quantity of material in each state is known, the mechanical properties of the mixture can be estimated over the whole temperature range.

This concept can be applied for the E-modulus under tension, compression, bending, or for the shear modulus (G), if the corresponding values for each material state are known (as material constants independent of temperatures). In this work, the temperature-dependent bending E-modulus and the G-modulus are considered. The corresponding kinetic parameters and moduli of different material states are identified based on DMA results, as demonstrated in the next Section.

4 MODELING OF TEMPERATURE-DEPENDENT E-MODULUS

4.1 Formulation of basic equations

Considering the glass transition as a one-step process from the glassy to the leathery state (see Fig. 2), the following equation is obtained based on Arrhenius law:

$$\frac{d\alpha_g}{dt} = A_g \cdot \exp\left(\frac{-E_{A,g}}{RT}\right)\left(1-\alpha_g\right)^n \tag{15}$$

where α_g is the conversion degree of the glass transition, A_g is the pre-exponential factor, $E_{A,g}$ is the activation energy (which is a constant for a specific process), R is the universal gas constant (8.314 J/mol·K), n is the reaction order (that can be taken as 1 in the case of state change), T is the temperature, and t is time. At a constant heating rate β, the following equation is obtained:

$$\frac{d\alpha_g}{dT} = \frac{A_g}{\beta}\exp\left(\frac{-E_{A,g}}{RT}\right)\left(1-\alpha_g\right)^n \tag{16}$$

Similarly, the following equations can be obtained for the leathery-to-rubbery transition and rubbery-to-decomposed transition:

$$\frac{d\alpha_r}{dT} = \frac{A_r}{\beta}\exp\left(\frac{-E_{A,r}}{RT}\right)\left(1-\alpha_r\right) \tag{17}$$

$$\frac{d\alpha_d}{dT} = \frac{A_d}{\beta}\exp\left(\frac{-E_{A,d}}{RT}\right)\left(1-\alpha_d\right) \tag{18}$$

where α_r and α_d are the conversion degrees, A_r and A_d are the pre-exponential factors, $E_{A,r}$ and $E_{A,d}$ are the activation energies, for the leathery-to-rubbery transition and the rubbery-to-decomposed transition, re-

spectively.

Assuming a unit volume of initial material at a specified temperature, the volume of the material at the different states can be expressed as follows:

$$V_g = (1 - \alpha_g) \tag{19}$$

$$V_l = \alpha_g \cdot (1 - \alpha_r) \tag{20}$$

$$V_r = \alpha_g \cdot \alpha_r \cdot (1 - \alpha_d) \tag{21}$$

$$V_d = \alpha_g \cdot \alpha_r \cdot \alpha_d \tag{22}$$

where V denotes the content of the material by volume at the different states and subscripts g, l, r and d denote the states: glassy, leathery, rubbery, and decomposed, respectively.

Assuming that P_g, P_l, P_r, and P_d are the mechanical properties (modulus or viscosity) in the glassy, leathery, rubbery and decomposed states, respectively, the mechanical property of a material composed of different states P_m is determined as:

$$P_m = P_g \cdot (1 - \alpha_g) + P_l \cdot \alpha_g \cdot (1 - \alpha_r) + P_r \cdot \alpha_g \cdot \alpha_r \cdot (1 - \alpha_d) + P_d \cdot \alpha_g \cdot \alpha_r \cdot \alpha_d \tag{23}$$

Considering that the E-modulus of the leathery and rubbery states are almost the same ($E_l = E_r$, see Fig. 2, the leathery and rubbery states are not discernable based solely on the change in E-modulus), the leathery-to-rubbery transition can be neglected. Moreover, after decomposition, the decomposed material no longer has significant structural stiffness. Its modulus, E_d, can be taken as zero and Eq. (23) is reduced to:

$$E_m = E_g \cdot (1 - \alpha_g) + E_r \cdot \alpha_g \cdot (1 - \alpha_d) \tag{24}$$

A constant heating rate is assumed in Eq. (16). In a real fire, however, the heating rate is not constant. Complex heating regimes, with non-constant heating rate, can be considered by transforming the differential form of Eq. (16) into finite difference form and changing the heating rate ($\Delta T/\Delta t$) for each time unit, Δt.

4.2 Estimation of kinetic parameters for glass transition and decomposition

Knowing the degree of the glass transition, α_g, at different heating rates from DMA, the kinetic parameters of the glass transition can be determined by multi-curves methods such as the Kissinger or Ozawa method [20]. When only one heating rate is available (as in this work), the modified Coats-Redfern method can be used [21-22], as demonstrated in the following. Integration of Eq. (16) leads to:

$$\int_0^a \frac{d\alpha_g}{(1-\alpha_g)} = \frac{A_g}{\beta} \cdot \int_\infty^T e^{-E_{A,g}/RT}\, dT \tag{25}$$

As introduced in the Coats-Redfern method [22, 23], the right hand side of Eq. (25) can be written as:

$$\left(A_g RT^2/\beta E_{A,g}\right)\cdot\left(1-2RT/E_{A,g}\right)\cdot\exp\left(-E_{A,g}/RT\right) \tag{26}$$

and the left hand side can be expanded to:

$$\alpha_g + \left(n\alpha_g{}^2/2\right) + n\left(n+1\right)\left(\alpha_g{}^3/6\right) + \ldots \tag{27}$$

In the case of n=1 (see Section 4.1), Eq. (27) is the Taylor series of -ln(1-α_g) since α_g is always less than 1, and the following is obtained:

$$-\ln\left(1-\alpha_g\right) = \left(A_g RT^2/\beta E_{A,g}\right)\cdot\left(1-2RT/E_{A,g}\right)\cdot\exp\left(-E_{A,g}/RT\right) \tag{28}$$

which leads directly to:

$$\ln\left(-\ln\left(1-\alpha_g\right)/T^2\right) = \ln\left(AR/\beta E_{A,g}\right)\cdot\left(1-2RT/E_{A,g}\right) - \left(E_{A,g}/RT\right) \tag{29}$$

Thus, since ln($A_gR/\beta E_{A,g}$)·(1-2$RT/E_{A,g}$) is nearly constant, the quantity ln(-ln(1-α_g)/T^2) is linear with $1/T$ and the corresponding plot should be a straight line with a slope of -$E_{A,g}/R$. As a result, $E_{A,g}$ is obtained from one dataset, at one constant heating rate. Substituting $E_{A,g}$ into Eq. (28), the values of A_g at different α_g are obtained. The required experimental data to determine the kinetic parameters is obtained from DMA, as shown in the following sections.

The kinetic parameters of decomposition can be determined by the same method, as demonstrated in [21]. Since the mass of the material changes when decomposition occurs, the required experimental data is provided by Thermogravimetric Analysis (TGA), which measures the

change of mass as a function of a change in temperature.

4.3 Kinetic parameters of experimental material

In order to estimate the kinetic parameters of glass transition, experimentally obtained conversion degrees of glass transition are necessary, which can be obtained based on the change in the E-modulus obtained from DMA results. If the temperature is far below T_d, the corresponding α_d is zero. Based on Eq. (24), the conversion degree at glass transition, α_g, can be expressed then as:

$$\alpha_g = \frac{E_g - E_m}{E_g - E_r} \tag{30}$$

where E_m is obtained from Eq. (13) (identical to the measured storage modulus) and E_g and E_r can be taken from the initial state and the lower plateau of the curve in Fig. 1, respectively. The degree of glass transition, α_g, was calculated accordingly and the resulting curve is illustrated in Fig. 3. The curve shows that the glass transition mainly occurs between 100 C and 150°C.

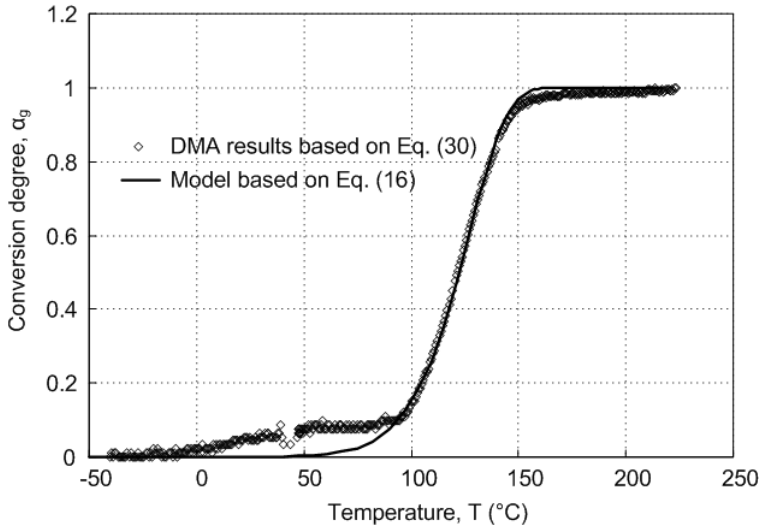

Fig. 3. Conversion degree of glass transition, α_g, for modeling E-modulus

Based on Eq. (29), a plot of $\ln(-\ln(1-\alpha_g)/T^2)$ against $1/T$ gives an almost straight line (correlation factor R^2=0.999) with a slope of $-E_{A,g}/R$, as shown in Fig. 4. The activation energy, $E_{A,g}$, was then calculated as 74.3 kJ/mol (see Table 1). The values of A_g at different α_g were estimated by substitut-

ing $E_{A,g}$ and α_g into Eq. (28). These results are summarized in Table 1. Since the values of A_g are very stable at different α_g, the average value of A_g , (141±1.52)×10^7, is used in the following.

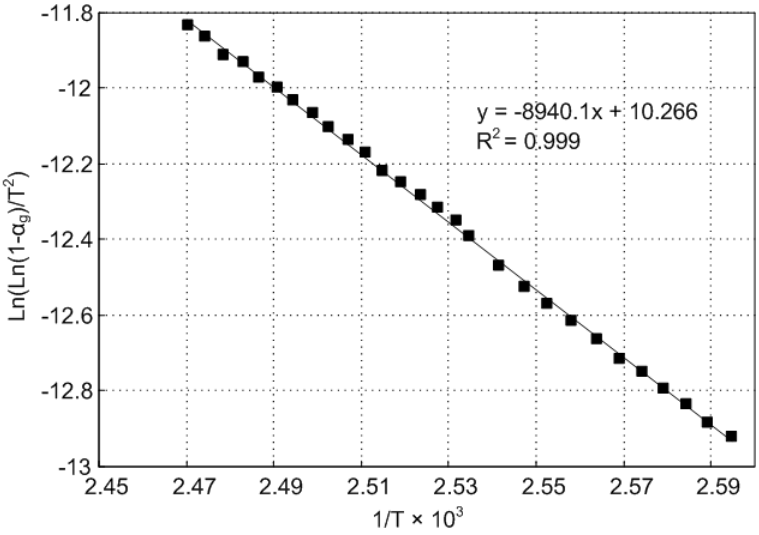

Fig. 4. Determination of $E_{A,g}$ in glass transition for modeling E-modulus

T (°C)	α_g	A_g (×10^{7}min-1)	$E_{A,g}$ (kJ/mol)
95	10%	132.2	74.3
105	20%	134.4	
112	30%	142.1	
118	40%	139.5	
123	50%	143.7	
127	60%	142.5	
132	70%	139.5	

Table 1. Kinetic parameters for modeling E-modulus during glass transition

The kinetic parameters for the decomposition were estimated using the same method and are summarized in Table 2 (for details, see [21]). Substituting these kinetic parameters into Eqs. (16) and (18), the theoretic results of α_g and α_d can be obtained. In Fig. 3 it can be seen that a good agreement between the theoretical values of α_g based on Eq. (16) and the experimental results from DMA was found.

T (°C)	α_d	A_d ($\times 10^5$ min^{-1})	$E_{A,d}$ (kJ/mol)
277	10%	7.6	
295	20%	8.8	
309	30%	8.8	
322	40%	8.7	80.1
332	50%	8.5	
343	60%	8.4	
354	70%	8.1	

Table 2. Kinetic parameters for modeling E-modulus during decomposition

4.4 Temperature-dependent E-Modulus of experimental material

Substituting the theoretical results of α_g and α_d into Eq. (24), and taking E_g=12.3 GPa as the original modulus (modulus of glassy state), E_r=3.14 GPa as the modulus at approximately 250°C (modulus of leathery or rubbery state) from DMA experiments, the temperature-dependent E-modulus can be obtained. A comparison with the DMA data is shown in Fig. 5. A good correspondence was found in the temperature range up to 250°C. Furthermore, it can be seen that the second descending stage, resulting from decomposition, can also be described by the model.

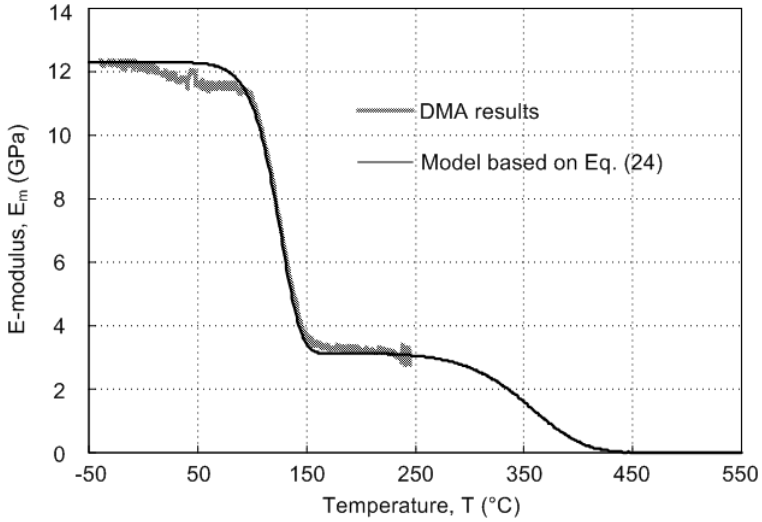

Fig. 5. Comparison of E-modulus between model and DMA data

4.5 Temperature-dependent G-modulus

The same method as described in Section 4.4 can be used to model the temperature-dependent G-modulus. The equations to calculate the conversion degree of glass transition and decomposition degree, together with the corresponding kinetic parameters, are the same as for E-modulus, except that the E-modulus at different states in Eq. (24) is replaced by the corresponding G-modulus.

5 MODELING OF TEMPERATURE-DEPENDENT VISCOSITY

5.1 Formulation of basic equations

As described in Section 3, four different material states can be found when the temperature is increased and the content of each state is obtained from Eqs. (19)-(22). The temperature-dependent viscosity can then be determined from Eq. (23). In this case, since the viscosity in the leathery and in the rubbery state is apparently different (see. Fig. 2), these two states must be separated (unlike that for the modeling of the E-modulus, see Section 4.1), as shown in Eq. (31):

$$\eta_m = \eta_g \cdot (1-\alpha_g) + \eta_l \cdot \alpha_g \cdot (1-\alpha_r) + \eta_r \cdot \alpha_g \cdot \alpha_r \tag{31}$$

It should be noted that decomposition is not considered in Eq. (31), since the temperature range in DMA experiments does not include T_d. Furthermore, when the composite materials are decomposed, it is not appropriate to describe their behavior as visco-elastic.

5.2 Estimation of kinetic parameters for glass transition and leathery-to-rubbery transition

The viscosity in the glassy state, η_g, in Eq. (31) can be obtained from the measured loss modulus according to Eq. 14 (loss modulus at the initial temperature, see Fig. 1), and the viscosity in the rubbery state, η_r, is obtained from the loss modulus at the plateau at approximately 250°C (see Fig. 1). However, the viscosity in the leathery state, η_l, cannot be directly estimated from the loss modulus curve, since two different transitions

(glass transition and leathery-to-rubbery transition) are coupled and materials of several states coexist. Furthermore, it should be noted that these two coupled transitions cannot be distinguished in the conversion degree, α_g, obtained in Section 4 for modeling the temperature-dependent E-modulus. Thus the corresponding kinetic parameters cannot be used directly to describe the change in viscosity. Without the experimental verification of α_r and the value of η_l, the kinetic parameters for these two transitions cannot be estimated. Therefore, as will be seen below, an approximation is made in order to model the temperature-dependent viscosity.

When the viscosity of the material composed of different states reaches its maximum value, the following equation can be obtained by derivation of Eq. (31) with respect to temperature:

$$\frac{d\eta_m}{dT} = \left(\eta_l - \eta_g\right) \cdot \frac{d\alpha_g}{dT} + \left(\eta_r - \eta_l\right) \cdot \frac{d\left(\alpha_g \cdot \alpha_r\right)}{dT} = 0 \tag{32}$$

Considering $\eta_l >> \eta_g$ and $\eta_l >> \eta_r$ gives:

$$\eta_l \cdot \frac{d\alpha_g}{dT} - \eta_l \cdot \frac{d\left(\alpha_g \cdot \alpha_r\right)}{dT} = 0 \tag{33}$$

that is:

$$\frac{d\alpha_g\left(1-\alpha_r\right)}{dT} = \frac{dV_l}{dT} = 0 \tag{34}$$

Equation (34) shows that when the viscosity of the material, η_m, (as a mixture from different states) reaches its maximum value, the content of the leathery state (see Eq. 20) also reaches its maximum value. The content of the material in leathery state is increased during the glass transition, but decreases during the leathery-to-rubbery transition. Consequently, it can be assumed that the glass transition (from glassy to leathery state) occurs before the peak point of η_m is reached (i.e. the peak point of the loss modulus in Fig. 1), and the leathery-to-rubbery transition occurs after the peak point of η_m. Based on this approximation, the peak point of η_m can be considered the viscosity of the material in the leathery state, i.e., η_l in Eq. (31).

By separating the glass transition and the leathery-to-rubbery transi-

tion at the peak point of η_m (see Fig. 2), these two transitions can be decoupled. Accordingly, the kinetic parameters of these two different transitions can be estimated by the same method introduced in Section 4.2.

5.3 Kinetic parameters of experimental material

Taking T_m as the temperature when η_m reaches a maximum value, gives the following:

$$\eta_m = \eta_g \cdot (1-\alpha_g) + \eta_l \cdot \alpha_g \text{ thus } \alpha_g = \frac{\eta_m - \eta_g}{\eta_l - \eta_g} \text{ for } T < T_m \tag{35}$$

$$\eta_m = \eta_l \cdot (1-\alpha_r) + \eta_r \cdot \alpha_r \text{ thus } \alpha_r = \frac{\eta_l - \eta_m}{\eta_l - \eta_r} \text{ for } T \geq T_m \tag{36}$$

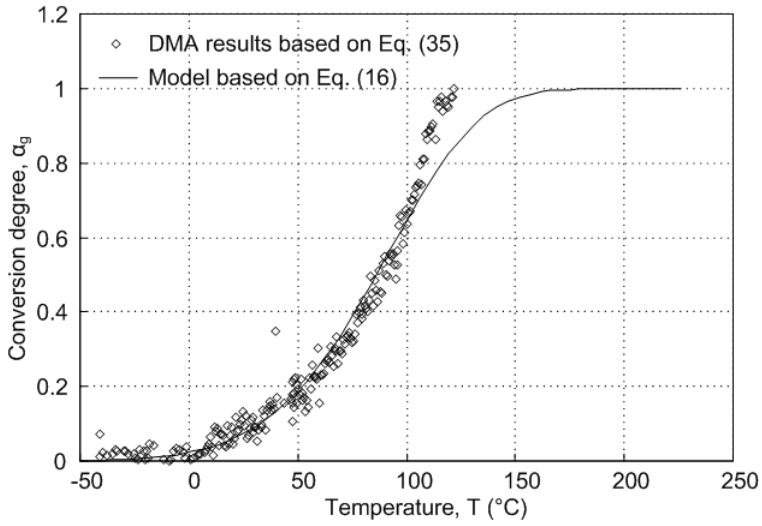

Fig. 6. Conversion degree of glass transition, α_g, for modeling viscosity

Based on Eqs. (35) and (36), the conversion degrees α_g and α_r are calculated from the experimental results as shown in Figs. 6 and 7, respectively. Compared with the α_g obtained from the storage modulus in Section 4 (see Fig. 3 and Eq. 30), both increased with temperature. However, due to the different ways in which the transition from the leathery to rubbery state in the modeling of E-modulus and viscosity is considered, the main change in α_g (from 15% to 95%) is concentrated in the temperature range from 100°C to 150°C (Fig. 3), while over the same temperature range, α_g varies from 60% to 100% (Fig. 6). The different increases in α_g result in a different estimation of the kinetic parameters for the glass transition.

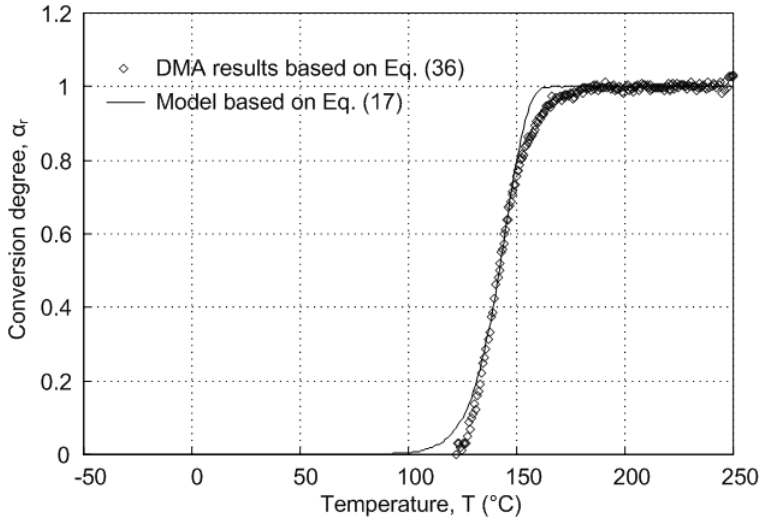

Fig. 7. Conversion degree of transition from leathery to rubbery state, α_r, for modeling viscosity

As introduced in Section 4.2, a plot of $\ln(-\ln(1-\alpha_g)/T^2)$ versus $1/T$ should give a straight line with a slope of $-E_{A,g}/R$. The corresponding plots for the glass and leathery-to-rubbery transitions are shown in Figs. 8 and 9, respectively. The resulting values of $E_{A,g}$ and $E_{A,r}$. were 26.9 kJ/mol and 145.4kJ/mol, respectively. Substituting $E_{A,g}$ and $E_{A,r}$ into Eq. (28), the values of the pre-exponential factor at different conversion degrees are obtained.

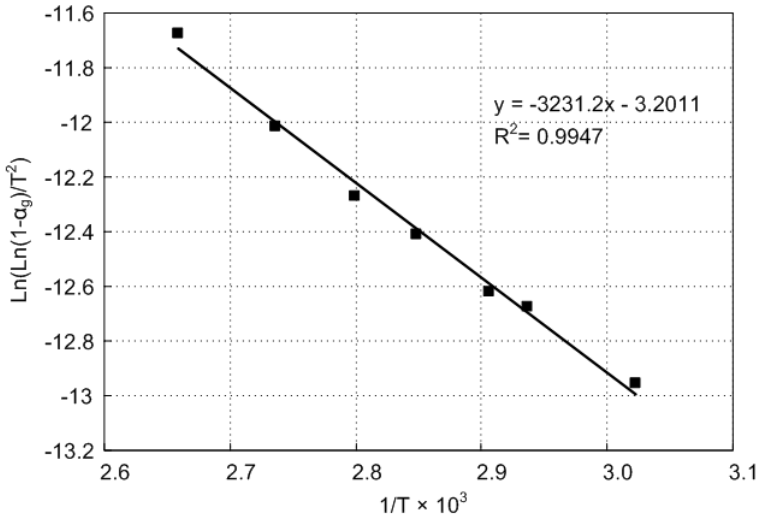

Fig. 8. Determination of $E_{A,g}$ during glass transition for modeling viscosity

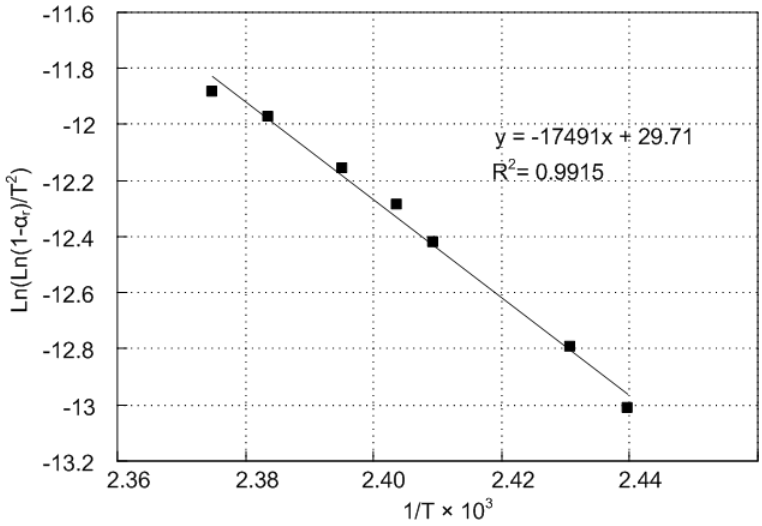

Fig. 9. Determination of $E_{A,r}$ during transition from leathery to rubbery state for modeling viscosity

T (°C)	α_g	A_g (min^{-1})	$E_{A,g}$ (kJ/mol)
58	23%	838.4	
67	31%	846.5	
71	32%	812.5	
78	40%	837.1	26.9
84	45%	822.2	
92	56%	876.3	
103	70%	967.1	

Table 3. Kinetic parameters for modeling viscosity during glass transition

The kinetic parameters for the glass transition are summarized in Table 3, while those for the leathery-to-rubbery transition are given in Table 4 (the experimental results of α_g and α_g are concentrated from 30% to 70%, considering the measurement noise of the loss modulus at the beginning and the end of the curve, see Fig. 1). It was found that the values of the pre-exponential factors, A_g and A_r, are very stable at different conversion degrees, and, for this reason, average values of A_g and A_r , (8.57±0.52)×10^2 and (7.35±0.28)×10^{17}, were used in the following. It should be noted, however, that the kinetic parameters in Table 3 are different from that in Table 1, as discussed previously.

T (°C)	α_r	A_r ($\times 10^{17}$ min^{-1})	$E_{A,r}$ (kJ/mol)
137	31%	7.0	
138	38%	7.5	
142	50%	7.4	
1423	55%	7.7	145.4
144	60%	7.5	
146	67%	7.4	
148	71%	6.9	

Table 4. Kinetic parameters for modeling viscosity during leathery-to-rubbery transition

Substituting the obtained kinetic parameters ($E_{A,g}$ and A_g, $E_{A,r}$ and A_r) into Eqs. (16) and (17), the theoretic conversion degrees were calculated. The results are shown in Figs. 6 and 7 and compare quite well with the experimental values. Some small discrepancies were found at the temperature point T_m (120°C) in Fig. 6, which are due to the assumptions discussed in Section 5.2.

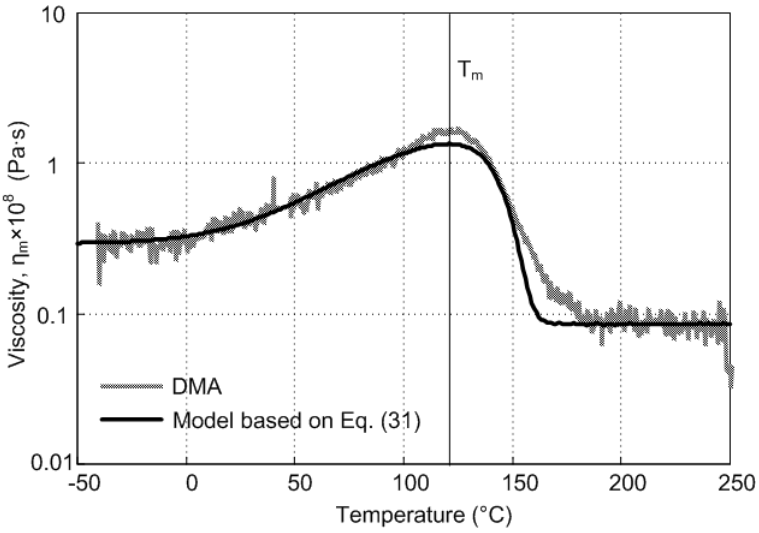

Fig. 10. Comparison of viscosity between theoretical model and DMA

5.4 Temperature-dependent viscosity of experimental material

Substituting the theoretic results of α_g and α_r into Eq. (31), and taking η_g=3.1×10^7, η_l=1.6×10^8, and η_r=8.2×10^6 (based on Fig. 1 and Eq. 14), the

temperature-dependent viscosity can be obtained. A comparison with the DMA data is shown in Fig. 10. The theoretical curve below T_m describes the change in the loss modulus during glass transition from glassy state to leathery state. The theoretical curve beyond T_m describes the change in the loss modulus from leathery to rubbery state. In both cases, a good correspondence can be found, with some discrepancies around T_m, which are likely due to the separation of the two different transitions at T_m.

5.5 Modeling for temperature dependent damping factor

The damping factor is defined as the ratio between the loss modulus and storage modulus (according to Eq. 10). The theoretical values of the damping factor can therefore be obtained by combining Eqs. (24) and (31). The comparison between results from the model and the DMA experiments is shown in Fig. 11. As was the case for the model for temperature-dependent viscosity, a good agreement was found up to a temperature of 250°C.

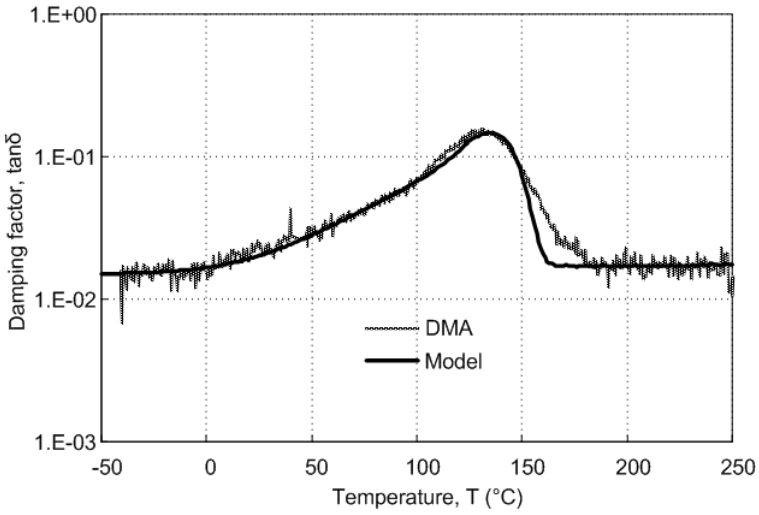

Fig. 11. Comparison of the damping factor between theoretical model and DMA

6 TEMPERATURE-DEPENDENT EFFECTIVE COEFFICIENT OF THERMAL EXPANSION

The true value of the coefficient of thermal expansion, λ_c, for the compo-

sites material can be calculated based on a proportional combination of the coefficients of fiber and matrix (mixture approach) [23]. However, when the temperature is increased, the material in the states after glass transition experiences sudden decreases in the E-modulus and G modulus, as shown in Fig. 5 for the E-modulus. In cross-sections of elements where part of the material remains below the glass transition, the true thermal expansion of the material above the glass transitions does not influence anymore stresses or deformations of the element. To consider these structural effects, a concept of the effective coefficient of thermal expansion is proposed. Contributions of the true thermal expansion of the material after glass transition to the global structural deformation are neglected and, consequently, the effective coefficient of thermal expansion is zero for the material after glass transition. Based on the true coefficient of thermal expansion of the glassy state, λ_c (12.6×10^{-6} K^{-1} [17], in the longitudinal direction), the temperature-dependent effective coefficient of thermal expansion, $\lambda_{c,e}$ is then expressed as follows:

$$\lambda_{c,e} = \lambda_c \cdot \left(1 - \alpha_g\right) \tag{37}$$

The conversion degree of glass transition, α_g, was obtained from Eq. (16). The resulting temperature-dependent effective coefficient of thermal expansion for the experimental GFRP material is shown in Fig. 12.

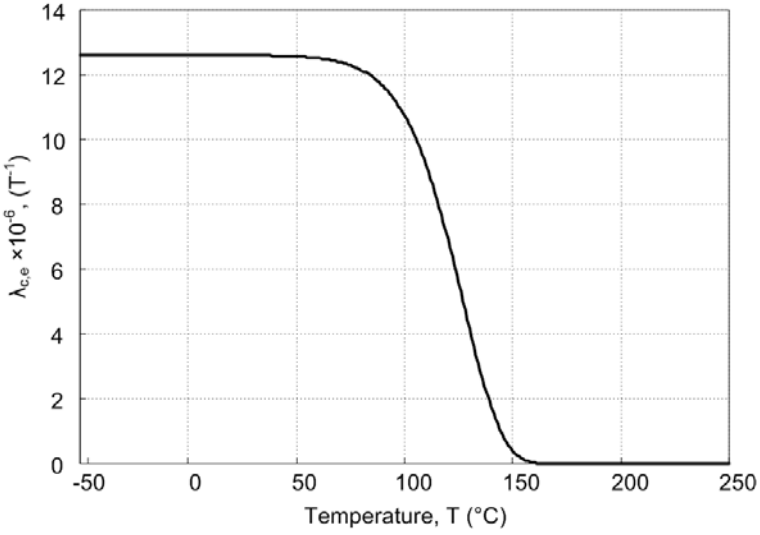

Fig. 12. Temperature-dependent effective coefficient of thermal expansion

7 CONCLUSIONS

New models have been proposed to calculate the temperature-dependent mechanical properties of FRP composites, including the E-modulus, G-modulus, viscosity, and the effective coefficient of thermal expansion. The following conclusions can be drawn:

1. The material state of FRP composites experiences significant changes under elevated and high temperatures. Four different temperature-dependent material states were defined (glassy, leathery, rubbery and decomposed) as well as three different transitions (glass, leathery-to-rubbery, rubbery-to-decomposed).
2. At each temperature, the FRP composites can be considered as a mixture of materials at different states. The quantity of each state at different temperatures can be estimated by kinetic theory and the Arrhenius equations.
3. Considering the material as a mixture and knowing the quantity of each state in the mixture, the material's E-modulus and viscosity can be estimated by the mixture approach. Based on the storage and loss modulus at the different states obtained from DMA experiments, the temperature-dependent E-modulus and viscosity of the material could be derived. The results from the theoretical models compared well with the experimental results from DMA experiments.
4. A concept of an effective coefficient of thermal expansion has been proposed to consider the altered effects of the true coefficient of thermal expansion on the structural behavior after glass transition. The effective coefficient of thermal expansion for the material after glass transition is assumed to be zero, and its quantity below the glass transition can be calculated by kinetic equations.

Based on the mechanical property models for FRP composites proposed herein, further investigations will be conducted on the mechanical responses of cellular GFRP bridge deck elements subjected to mechanical loads and fire.

ACKNOWLEDGEMENT

The authors would like to thank the Swiss National Science Foundation (Grant No. 200020-109679/1) for the financial support of this research.

REFERENCES

1. Keller T, Tracy C, Zhou A. Structural response of liquid-cooled GFRP slabs subjected to fire. Part I: Material and post-fire modeling. *Composites Part A* 2006, 37(9): 1286-1295.

2. Keller T, Tracy C, Zhou A. Structural response of liquid-cooled GFRP slabs subjected to fire, Part II: Thermo-chemical and thermo-mechanical modeling. *Composites Part A* 2006, 37(9): 1296-1308..

3. Chen JK, Sun CT, Chang CI. Failure analysis of a graphite/epoxy laminate subjected to combined thermal and mechanical loading. *Journal of Composite Materials* 1985, 19(5): 216-235.

4. Griffis CA, Nemes JA, Stonesfiser FR, and Chang CI. Degradation in strength of laminated composites subjected to intense heating and mechanical loading. *Journal of Composite Materials* 1986, 20(3): 216-235.

5. Dao M, and Asaro R. A study on the failure prediction and design criteria for fiber composites under fire degradation. *Composites Part A* 1999, 30(2):123-131.

6. Bausano J, Lesko J, and Case SW. Composite life under sustained compression and one-sided simulated fire exposure: characterization and prediction, *Composites Part A* 2006, 37 (7): 1092-1100.

7. Halverson H, Bausano J, Case SW, Lesko JJ. Simulation of response of composite structures under fire exposure. *Science and Engineering of Composite Materials* 2005, 12(1-2): 93-101.

8. Springer GS. Model for predicting the mechanical properties of composites at elevated temperatures. *Journal of Reinforced Plastics and Composites* 1984, 3(1): 85-95.

9. Dutta PK and Hui D. Creep rupture of a GFRP composite at elevated temperatures. *Computers and Structures* 2000, 76(1): 153-161.

10. Gibson, AG, Wu, YS, Evans JT. and Mouritz AP. Laminate theory

analysis of composites under load in fire. J *Journal of Composite Materials* 2006, 40(7): 639-658.

11. Mahieux CA, Reifsnider KL. Property modelling across transition temperatures in polymers: a robust stiffness-temperature model. *Polymer* 2001, 42: 3281-3291.

12. Mahieux CA. A systematic stiffness-temperature model for polymers and applications to the prediction of composite behavior. Ph.D Dissertation, Virginia Polytechnic Institute and State University, 1999.

13. Mahieux CA, Reifsnider KL. Property modeling across transition temperatures in polymers: application to thermoplastic systems. *Journal of Materials Science* 2002, 37: 911-920.

14. Burdette JA. Fire response of loaded composite structures – Experiments and modeling. Master thesis, Virginia Polytechnic Institute and State University, 2001.

15. Gu P, Asaro RJ. Structural buckling of polymer matrix composites due to reduced stiffness from fire damage. *Composite Structures* 2005, 69: 65-75.

16. Ferry JD. Viscoelastic properties of polymers. John Wiley & Sons, Inc., 1980.

17. Tracy C. Fire endurance of multicellular panels in an FRP building system. Ph.D Thesis (No. 3235), Swiss Federal Institute of Technology-Lausanne, Switzerland.

18. Ashby MF, Jones DRH. Engineering materials 2: an introduction to microstructures, processing, and design. Oxford, Pergamon Press, 1997.

19. Holt, Rinehart, and Winston. Modern Chemistry. Harcourt Brace & Company, 1999.

20. Bai Y, Vallée T, Keller T. Modeling of thermophysical properties for FRP composites under elevated and high temperatures. *Composites Science and Technology* 2007, 67(15-16): 3098-3109.

21. Coats AW, Redfern JP. Kinetic parameters from thermogravimetric data. *Nature* 1964; 201: 68-69.

22. Coats AW, Redfern JP. Kinetic parameters from thermogravimetric

data II. *Polymer Letters* 1965, 3: 917-920.

23. Schapery R. Thermal expansion coefficients of composite materials based on energy principles. *Journal of Composite Materials* 1968, 2(3): 380-404.

2.3 Modeling of strength degradation

Summary

When composite materials are exposed to fire, not only is the increased deformation due to stiffness degradation of interest, but also the load-bearing capacity and time-to-failure. Strength degradation therefore becomes another important factor in the safety evaluation of composite materials in fire.

Based on the concepts developed in Sections 2.1 and 2.2, this paper focuses on the modeling of the strength degradation of composites in fire. Compressive, tensile and 10° off-axis tensile tests were conducted on pultruded glass fiber-reinforced polyester composite materials at temperatures ranging from room temperature to 220°C, and the degradation of compressive, tensile and shear strengths was recorded. A composite material at a certain temperature can be considered as being a mixture of materials that are in different states, representing different quantities and strength properties. On the other hand, the morphology of the mixture of different material states influences the effective properties, which can be bounded by the rule and inverse rule of mixture. It was found that the degradation of shear strength is the same as that of the E-modulus, which can be well described by the rule of mixture, while the degradation of nominal compressive strength was well described by the inverse rule of mixture. The failure of specimens in tension is fiber-dominated in a relatively low temperature range; in a high temperature range, shear failure at joints may occur since resin composed of mat layers cannot provide sufficient anchorage for the roving layer, and this failure can therefore be described by the modeling of shear strength degradation.

Reference detail

This paper, accepted for publication in the Journal of Composite Materials, is entitled

"Modeling of strength degradation for fiber-reinforced polyester composites in fire" by Yu Bai and Thomas Keller.

Part of the content of this paper was presented at the 5th International Conference on Composites in Fire (CIF) 10-11 July 2008, Newcastle upon Tyne, UK, entitled

"A kinetic model to predict stiffness and strength of FRP composites in fire" by Yu Bai and Thomas Keller, presented by Yu Bai.

MODELING OF STRENGTH DEGRADATION FOR FIBER-REINFORCED POLYMER COMPOSITES IN FIRE

Yu Bai and Thomas Keller

Composite Construction Laboratory CCLab, Ecole Polytechnique Fédérale de Lausanne (EPFL), BP 2225, Station 16, CH-1015 Lausanne, Switzerland.

ABSTRACT:

A model for predicting composite material strength degradation under elevated and high temperatures is proposed. This model is based on the morphology of the mixture of materials in different states. The degradation of resin-dominated shear strength can be well described by the rule of mixture while the degradation of nominal compressive strength tends to follow the lower bound of strength defined by the inverse rule of mixture. Composite materials under tension may exhibit fiber- or resin-dominated behavior. In a lower temperature range, strength is dominated by the fiber tensile strength, while at higher temperatures, tensile components may exhibit resin-dominated failure in joint regions. The parameters required in the model can be obtained on the basis of kinetic analysis of dynamic mechanical analysis (DMA) results. The fitting of experimental curves of material strength degradation is not necessary. The proposed modeling scheme can easily be incorporated into structural theory to predict mechanical responses and time-to-failure.

KEYWORDS:

Polymer matrix composites; thermomechanical properties; modeling; strength degradation; temperature-dependent

1 INTRODUCTION

The mechanical properties of polymers and fiber-reinforced polymer (FRP) composites degrade significantly during glass transition and decomposition [1]. In order to design safe load-bearing structures incorporating FRP components, the variation in mechanical properties over a broad temperature range, including glass transition and material decomposition, must be known. The stiffness degradation of composites during fire exposure was investigated by Springer in the 1980s [2], McManus et al. in the 1990s [3, 4], and further examined by Gibson et al. in 2004 [5] and Mahieux et al. [6] and Gu and Asaro in 2005 [7], each applying different types of fitting functions to represent experimental data.

Studies on strength degradation are relatively limited in number. Tensile and compression tests were conducted by Feih et al. in 2007 [8] on woven E-glass-fiber and vinylester-resin laminates at temperatures between 20 and 300°C (68 and 572°F). The tensile strength of neat vinylester resin between 20 and 100°C (68 and 212°F) and of fiber bundles between 20°C and 650°C (68 and 1202°F) was also measured. The degradation of fiber and laminate tensile strengths was similar and much slower than that of neat resin. Compressive strength decreased rapidly above 50°C (122°F) and fell to approximately 2% of initial strength above 150°C (302°F). The compressive behavior of slender laminates was further examined by the same authors in [9] in which thermal expansion and mechanical deformation were coupled. Thanks to the good description of stiffness degradation given by the model of Gibson et al. [5], this model was used to fit material strength degradation under elevated temperatures in [8, 9]. In 2004, material compressive strength was measured by Wang et al. [10] from room temperature up to 250°C (482°F). Compact specimens of only 30-mm length were cut from 100×30×4-mm C-channel sections. The pultruded sections consisted of E-glass-fibers embedded in isophthalic polyester resin, a similar material to that used in the present study. They demonstrated that compressive properties at elevated temperatures greatly depend on resin softening and that refined material models are required to describe

the behavior.

In this work, a model for the prediction of stiffness degradation proposed by the authors in 2008 [11] is extended to describe the strength degradation of composites in fire. The model is based on the behavior of the primary and secondary bonds of polymers [12]. The first group includes the strong covalent intra-molecular bonds in polymer chains and cross-links of thermosets. Secondary bonds include much weaker bonds, such as hydrogen bonds, dipole interactions, and Van der Waals interactions, which can be far more easily dissociated. In the lower temperature range (below glass transition), known as the glassy state, materials are characterized by intact primary and secondary bonds. When temperature increases, following glass transition, the leathery state is reached with intact primary bonds and broken secondary bonds. At even higher temperatures, primary bonds are also broken, the material decomposes and only fiber and char material remains. Consequently, at a certain temperature, a composite material can be considered as a mixture of materials in different states, each exhibiting different mechanical properties. In [11], it has been shown that the effective stiffness of the mixture is determined by a) the proportion and the property of the material in each state [11], and b) the morphology of the mixture, which can be quantified by the rule or the inverse rule of mixture [13] for example. This approach is also adopted for the modeling of strength degradation in the following. Compared to existing models, mainly involving the fitting of experimental strength data, the proposed model has a clear theoretic basis since the required parameters are obtained from dynamic mechanical analysis and the direct fitting of strength data is no longer necessary.

Previous experimental investigations showed that the loss of compressive strength occurs mainly because of the resin's glass transition, while tensile strength degradation tends to be fiber-dominated. Shear strength degradation is normally resin-dominated, although the amount of experimental data available is still very limited. To validate the model for all these different cases, tension, shear and compression experiments were

conducted from ambient temperature (20°C/68°F) up to 220°C (428°F), covering the glass transition range during which the main strength loss occurs.

2. EXPERIMENTAL INVESTIGATION

2.1 Shear experiments

In-plane shear strength was measured by means of 10° off-axis tensile experiments, similarly as demonstrated in [14]. Pultruded GFRP laminates of 350-mm length ×30-mm width ×10-mm thickness, consisting of E-glass fibers embedded in an isophthalic polyester resin, were used. Burn-off tests according to ASTM D3171-99 [15] were performed to obtain the fiber mass content of the materials, shown to be 69%. The laminates consisted of two mat layers sandwiching a layer of unidirectional rovings. One mat layer consisted of a chopped strand mat (CSM) stitched together with a woven roving ply [0°/90°]. As reported in [16], the onset of glass transition temperature, $T_{g,onset}$, of this material is approximately 110 °C (230°F) and the onset of decomposition temperature, $T_{d,onset}$, approximately 270°C (518°F).

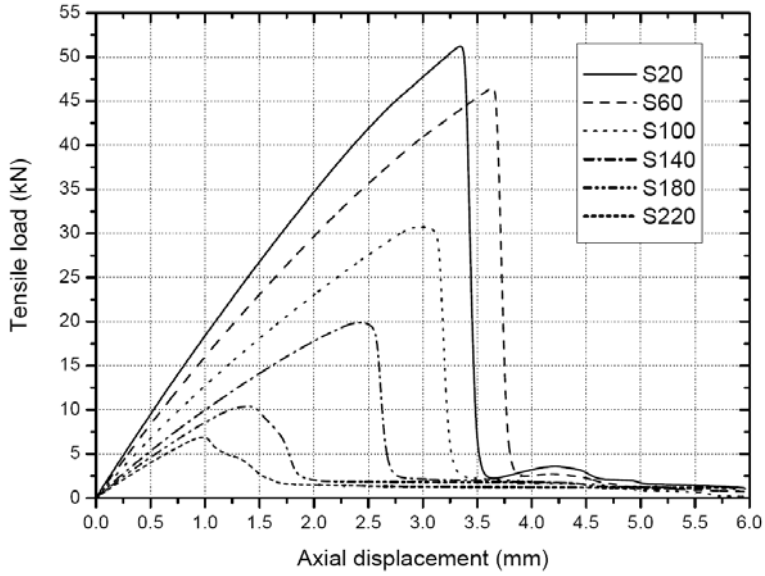

Fig. 1. Load-axial displacement curves for different temperatures from 10° off-axis tensile experiments

Twelve laminates were examined at six temperatures (from 20°C/68°F to 220°C/428°F at 40°C/104°F intervals), two specimens for each tempera-

ture, designated as Sxx, with xx being the temperature. First, the specimens were placed in an environmental chamber (range from -40°C to 250°C, accuracy 2°C), unrestrained to permit free thermal expansion and heated to the target temperature. Uniform through-thickness heating was ensured by the use of a reference specimen equipped with temperature sensors inside the material. As soon as the uniformly distributed target temperature was reached (after almost 50 min for the highest temperature of 220°C/428°F), an Instron Universal 8800 hydraulic machine was used to apply the axial tensile force with a displacement rate of 2 mm/min up to specimen failure.

Strength (MPa)	Glassy	Leathery	Ratio
Shear	26.7	3.5	13.1%
Compressive	344.2	31.5	9.2%
Tensile	326.7	-*	-*

Table 1. Shear, tensile and compressive material strengths at different states (*unavailable due to change of failure mode)

Fig. 2. Failure mode in 10° off-axis tensile experiments at different temperatures

The load-axial displacement curves are summarized in Fig. 1. Stiffness and the ultimate load decreased with increasing temperature. For all temperatures, the load increased linearly with displacement at the beginning, subsequently becoming increasingly non-linear with rising temperature

until ultimate load was reached. The typical failure mode is shown in Fig. 2 and can be classified as shear failure. Failure occurred at approximately 10° off-axis, parallel to the rovings in the homogeneous resin material, without any breaking of fibers (with the exception of the outside mats) and independent of temperature. The failure was more brittle for lower temperatures, as can be seen from the descending part of the curves in Fig. 1. The shear strength, f_s, can be estimated as [14]:

$$f_s = \frac{1}{2} \cdot \sin 2\theta \cdot \sigma_t = 0.171\sigma_t \tag{1}$$

where θ is the off-axis angle (10°) and σ_t is the axial tensile stress at failure. Thus the measured temperature-dependent shear strength was obtained, as shown in Fig. 3. The degradation of shear strength with increased temperature is very pronounced up to 220°C (428°F) and starts stabilizing at only approximately 13.1% of the initial value (see Table 1).

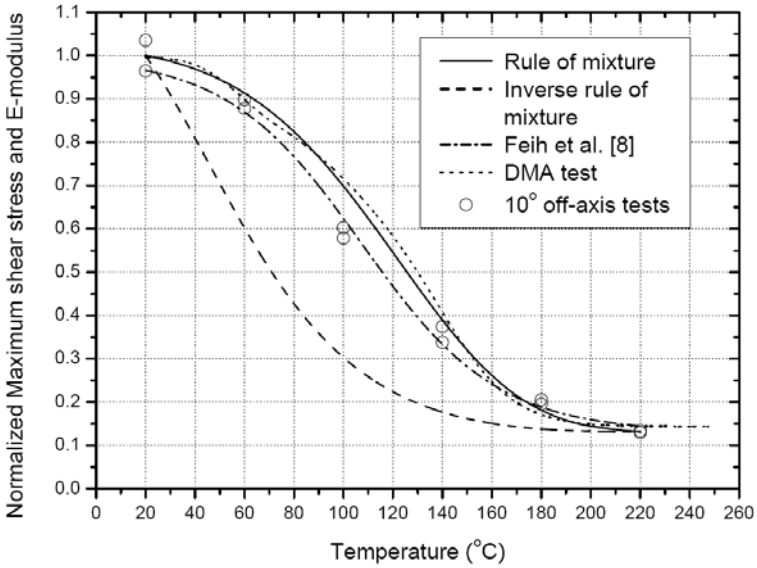

Fig. 3. Temperature-dependent shear strength from 10° off-axis tensile experiments and comparison to modeling results (φ=0.0183, and T_k=107.4 for Feih et al. model)

2.2 Tensile experiments

The GFRP material used for the tensile experiments was the same as that used for the shear experiments. The specimens' axis coincided with the

roving direction however. Their size was 400-mm length×20-mm width×10-mm thickness. The same experimental program was performed as for the shear experiments (two specimens per temperature, designated T*xx*, *xx* being the target temperature). After the target temperature (20-220°C, or 68-428°F) was achieved, the specimens were mechanically loaded in tension up to failure at a displacement rate of 2 mm/min.

Fig. 4. Failure mode in tensile experiments at different temperatures

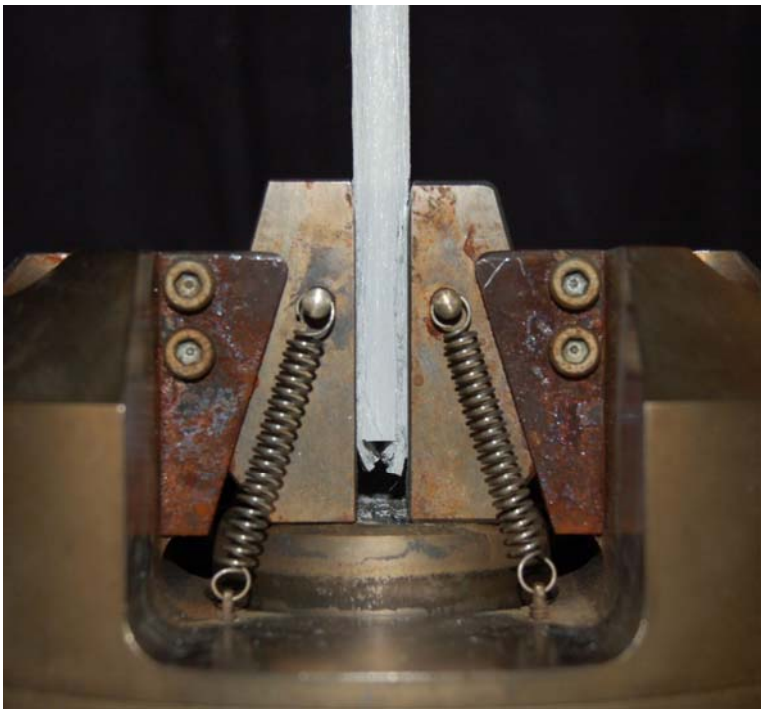

Fig. 5. Clamp shear failure of tensile specimen at high temperature

The failure occurred in two different modes, depending on temperature, as shown in Fig. 4. Up to 100°C (212°F), tensile failure occurred in the roving and mat fibers in the gage region while at higher temperatures, spe-

cimens failed in the clamp region on one side, see Fig. 5. An axial displacement difference between the middle roving layer and outside mat layers was observed due to pulling out of the roving layer. Thus, shear failure occurred in the interface between these two layers, followed by a tensile failure in the mat layers. The roving layer and the clamp region at the other end remained undamaged.

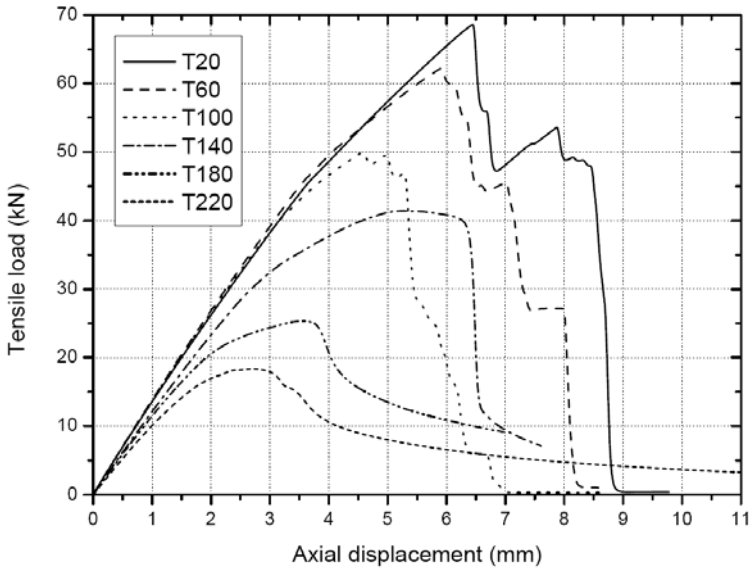

Fig. 6. Load-axial displacement curves for different temperatures from tensile experiments

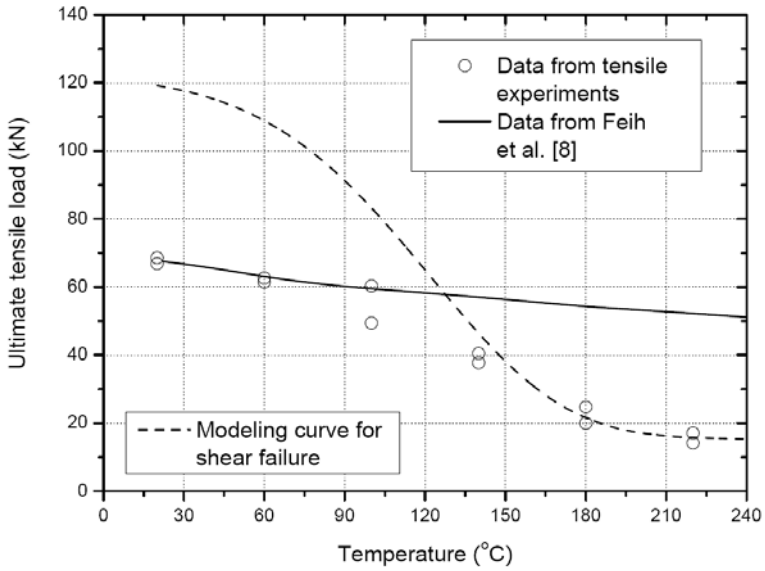

Fig. 7. Temperature-dependent ultimate tensile loads and comparison to modeling results

The load-axial displacement curves for all temperatures are summa-

rized in Fig. 6. The specimens exhibiting tensile failure mode (up to 100°C/212°F) showed an almost linear behavior up to failure (only 16% loss of secant stiffness on average), while those exhibiting shear failure (above 140°C/284°F) showed a highly non-linear response and a less steeply descending branch, similarly as observed for the shear experiments, see Fig. 1.

The ultimate tensile load at different temperatures is shown in Fig. 7. Only a small decrease (less than 18%) occurred when temperature increased from 20°C (68°F) to 100°C (212°F), that is, in the fiber-dominated tensile failure range. At higher temperatures, the ultimate load decreased much faster in the resin-dominated shear failure range and then started to stabilize at 220°C (428°F) at a very low level.

2.3 Compressive experiments

Compressive experiments were conducted on pultruded GFRP tubes of 40/34-mm outer/inner diameter, 3-mm thickness and 300-mm free length. GFRP material from the same pultruder as for the shear and tensile experiments (Fiberline Composites, Denmark) was used. Burn-off tests showed that the tubes comprised two CSM layers on each side and a UD-roving layer in the center; the fiber mass fraction was 64%.

The tubes were tested under concentric compressive load in a fixed-end set-up; the non-dimensional slenderness, $\overline{\lambda}$, was calculated as

$$\overline{\lambda} = \sqrt{\frac{A \cdot f_c(T)}{P_{E,T}}} \tag{2}$$

where A is the area of cross section (348.7 mm^2), $f_c(T)$ is the compressive strength as a function of temperature (see below) and P_E (T) is the global (Euler) buckling load, determined from

$$P_E(T) = \frac{\pi^2 \cdot EI(T)}{(L/2)^2} \tag{3}$$

where $EI(T)$ is the temperature-dependent bending stiffness in the longitudinal (pultrusion) direction and L is the specimen length (300mm). At

ambient temperature, the value of $\bar{\lambda}$ was calculated as 0.45, indicating that the specimens were compact with a reduction factor of almost 1.0. This value did not change significantly with temperature, since both strength and stiffness degraded with increased temperature. The nominal compressive strength was estimated by

$$f_c(T) = \frac{P_U(T)}{A} \tag{4}$$

where $P_U(T)$ is the ultimate load at different temperatures.

The target temperatures were the same as in the shear and tensile experiments. Three specimens were tested at each temperature (designated C*xx*, with *xx* being the temperature). After the target temperature was reached, the axial compressive force was applied with a displacement rate of 1 mm/min up to specimen failure.

Fig. 8. Failure mode in compression experiments at different temperatures

The failure mode at all temperatures is shown in Fig. 8. A local crushing was observed, which did not change significantly with temperature. Since the resin became softer at higher temperatures, the damaged zone was smaller than at lower temperatures (while a similar failure mode observed in [17] at 20°C (68°F) for similar specimens was identified as local buckling).

The load-axial displacement curves are shown in Fig. 9. The linear response up to failure was similar for all temperatures. Only strength and stiffness decreased with temperature. Fig. 10 shows the continuous decrease of nominal compressive strength with increasing temperature (calculated from Eq. (4)) up to 180°C (356°F), where stabilization at only 9.2% of the initial value was reached (see Table 1).

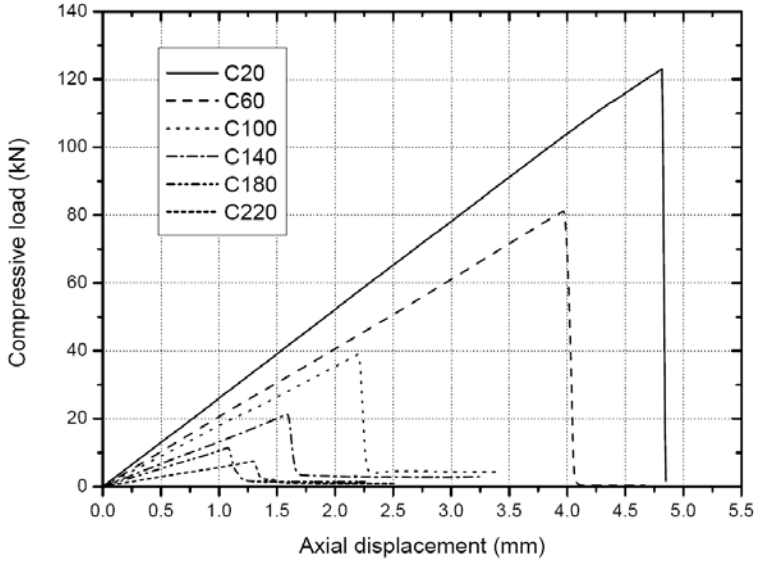

Fig. 9. Load-axial displacement curves for different temperatures from compressive experiments

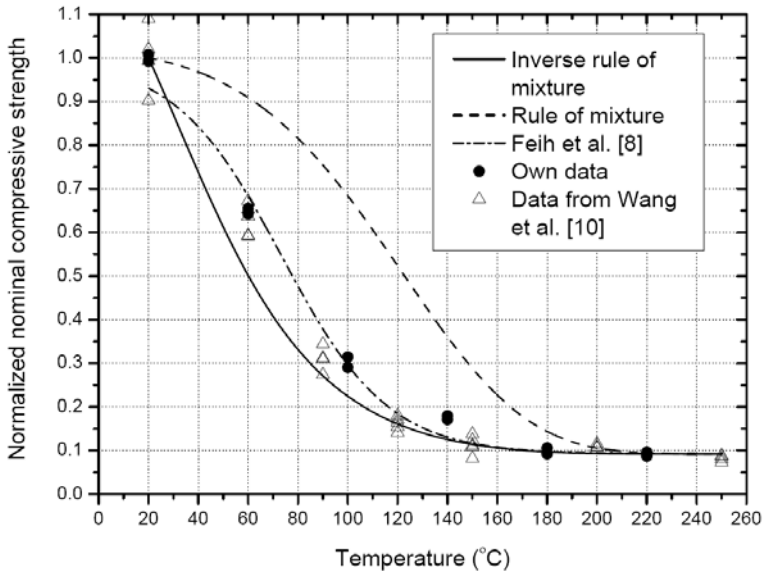

Fig. 10. Temperature-dependent nominal compressive strength (normalized value) and comparison to modeling results (φ=0.0233, and T_k=73.4 for Feih et al. model)

3 MODELING OF TEMPERATURE-DEPENDENT STRENGTH

3.1 Existing models

There are only a few well-established models for predicting strength degradation. Feih et al. [8, 9] expressed the relationship between strength and temperature using the semi-empirical equation:

$$\sigma(T) = \left(\frac{\sigma_0 + \sigma_R}{2} - \frac{\sigma_0 - \sigma_R}{2} \tanh\left(\varphi\left(T - T_k\right)\right) \right) \times R_{rc}(T)^n \tag{5}$$

where φ and T_k are parameters obtained by fitting the experimental data, σ_0 is the strength at ambient temperature and σ_R is the minimum strength (after glass transition and before decomposition), corresponding to the strength in the glassy and leathery states respectively (see Table 1). $R_{rc}(T)^n$ is a scaling function that takes mass loss due to decomposition of the polymer matrix into account, assuming that the resin decomposition process reduces the compressive strength to values below σ_R. The exponent n is an empirical value: n=0 assumes that resin decomposition has no effect on compressive strength, while n=1 assumes a linear relationship between mass loss and strength loss.

This model was used to fit the compressive strength degradation reported in [8] and is further applied for both shear and compressive strength degradation in the following (using n = 0 since decomposition did not occur).

3.2 Proposal of a new model

When subjected to thermal loading, composite materials essentially undergo glass transition and decomposition, which can be described by kinetic theory [11]:

$$\frac{d\alpha_g}{dT} = \frac{A_g}{\beta} \cdot \exp\left(\frac{-E_{A,g}}{R \cdot T} \right) \cdot \left(1 - \alpha_g\right)^{n_g} \tag{6}$$

$$\frac{d\alpha_d}{dT} = \frac{A_d}{\beta} \cdot \exp\left(\frac{-E_{A,d}}{R \cdot T} \right) \cdot \left(1 - \alpha_d\right)^{n_d} \tag{7}$$

where α_g and α_d are the conversion degrees, A_g and A_d are the pre-

exponential factors, $E_{A,g}$ and $E_{A,d}$ the activation energies, n_g and n_d the reaction orders for glass transition and decomposition respectively (the latter three being the kinetic parameters). R is the universal gas constant (8.314 J/mol·K), T is the temperature, and t is time.

Since the decomposition process was not covered by the experiments, only Eq. (6) is applied in the following. The kinetic parameters were identified on the basis of DMA results, see [16]. Subsequently the conversion degree of glass transition was calculated from Eq. (6), see Fig. 11, which shows that all the material was in the leathery state at 220°C (α_g = 1.0). The mechanical properties measured at this temperature level are therefore considered as being representative for the leathery state, while the properties at 20°C (68°F) are considered representative for the glassy state (α_g = 0), as summarized in Table 1.

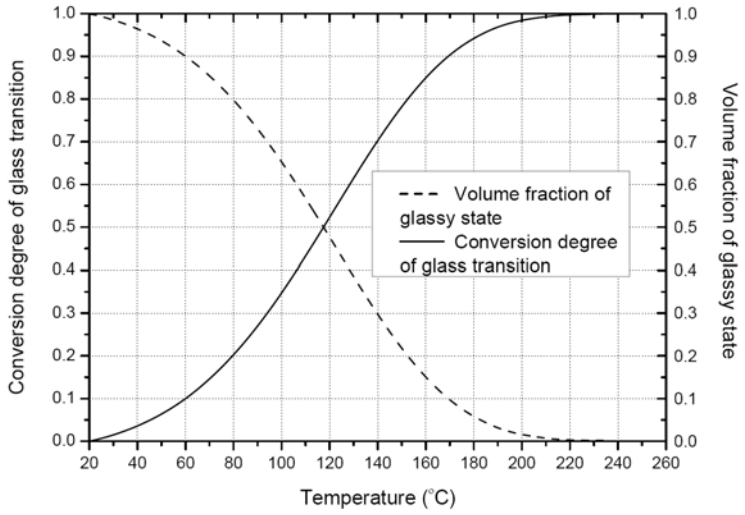

Fig. 11. Temperature-dependent conversion degree of glass transition and volume fraction of glassy state

Once the conversion degrees of glass transition and decomposition are known, the volume fraction of the material in different states can be expressed as:

$$V_g = \left(1 - \alpha_g\right) \tag{8}$$

$$V_l = \alpha_g \cdot \left(1 - \alpha_d\right) \tag{9}$$

$$V_d = \alpha_g \cdot \alpha_d \tag{10}$$

where V_g, V_l and V_d are the volume fractions of the material in the glassy,

leathery and decomposed states.

The volume fraction of the glassy state is calculated from Eq. (8) and shown in Fig. 11. It can be seen that the portion in the glassy state continuously decreases with increasing temperature (with the portion in the leathery state meanwhile increasing accordingly). Focusing in this case on the material before decomposition ($\alpha_d = 0$), the volume fraction of the leathery state can be expressed by

$$V_l = \alpha_g \tag{11}$$

Predicting the effective properties of a two-state (or two-phase) material as a function of the properties of the materials in the individual states has long been a subject of scientific interest [13]. These properties are influenced by many factors, such as geometric features (e.g. shape of constituents or phases) and the spatial distribution of the material in the different states (morphology of mixture). To consider and quantify all these influences is difficult, although complex models have been proposed for some specific cases, such as the mean field approach [18], the differential effective medium scheme [19], and the two-phase self-consistent scheme [20]. However, since the statistic distribution of the different material states and their failure probability at one specified temperature are not known in this instance, none of these models is directly applicable for the glassy and leathery state mixture.

Two simple models, however, can give upper and lower bounds for the effective property of a two-state material [13]: the rule of mixture, Eq. (12), and the inverse rule of mixture, Eq. (13):

$$C_m = C_1 \cdot V_1 + C_2 \cdot V_2 \tag{11}$$

$$\frac{1}{C_m} = \frac{V_1}{C_1} + \frac{V_2}{C_2} \tag{12}$$

where C_m is the effective material property, C_1 and C_2 are the properties, and V_1 and V_2 the volume fractions for the two different states respectively, taking into account that

$$V_1 + V_2 = 1 \tag{13}$$

4 DISCUSSION

4.1 Modeling of temperature-dependent shear strength

Based on the shear strength in the glassy and leathery states (see Table 1) and the volume fraction of each state (see Fig. 11), the modeling curves of the temperature-dependent shear strength (upper and lower bounds) were calculated according to Eqs. (12) and (13) and compared to the experimental results in Fig. 3. The experimental results fall well within the estimated range and are in good agreement with the upper bound (the rule of mixture). In order to compare strength and stiffness degradation, DMA-based results for the same material (E-Modulus obtained in [16]) are also shown in Fig. 3. The comparison shows that stiffness and shear strength degradation are very similar and that the former is also well described by the rule of mixture.

For comparison, the model by Feih et al. [8, 9] was applied to fit the shear strength degradation, see Fig. 3. A good agreement to the experimental results and the rule of mixture curve was found, mainly due to the well-selected fitting parameters. However, these parameters vary with loading type; different values were obtained for compression degradation for example (see below). In the proposed model, the unknown parameters are the material's kinetic parameters according to Eq. (6), which are identified from DMA results, do not need any fitting and are independent of loading type (tension, shear or compression). The proposed model can be applied based on strength information regarding only the two states (glassy and leathery, see Table 1). If the decomposed state is also involved, Eqs. (12) and (13) are still applicable provided that the volume fraction of the decomposed state (V_3, with $V_1+V_2+V_3=1$) is taken into account and assuming that the strength of the decomposed material is zero ($C_3=0$).

4.2 Modeling of temperature-dependent tensile strength

Since the proposed modeling scheme is based on the kinetic processes of the resin, tensile strength at lower temperatures, where fiber failure oc-

curred, cannot be predicted. However, the model is applicable for the resin-dominated clamp shear failure at higher temperatures. The corresponding upper bound curve (rule of mixture) is shown in Fig. 7 and compares well to the experimental results for temperatures above 140°C (284°F).

The tensile strength below 140°C (284°F) compares well to measurements made by Feih et al. [8] on E-glass fiber bundles between 20°C (68°F) and 650°C (1202°F), as shown in Fig. 7 (values calibrated from normalized values), and therefore confirms the fiber-dominant character of the strength decrease. Comparison of the modeling curves of tensile and shear failure shows and confirms that the failure mode changes from fiber- to resin-dominated at around 130°C (266°F), which is in the range of glass transition of the resin. The clamp failure mode is not artificial due to stress concentrations and not specific to the test configuration. At low temperatures, where stress concentrations were much higher (no resin softening), failure occurred in the gage region. Similar failure may also occur in joint regions of tensile elements incorporated in load-bearing structures.

4.3 Modeling of temperature-dependent compressive strength

Based on the same kinetic parameters as those used for shear strength degradation and the material properties of the two different states (see Table 1), the modeling curves for the temperature-dependent nominal compressive strength were calculated from Eqs. (12) and (13) and the results are shown in Fig. 10. The experimental results are again located between the upper and lower bounds, this time however approaching the lower bound (inverse rule of mixture). The normalized nominal compressive strength is therefore smaller than the normalized shear strength at the same temperature level. The experimental results (normalized compressive strengths) from Wang et al. [10] are also shown in Fig. 6. Again, good agreement with the modeling curve for the inverse rule of mixture is found. The reason for the inverse rule of mixture (Eq. (13)) giving better results in compression than the rule of mixture cannot yet be deduced

from the results. Interestingly, the same form of Eq. (13) was obtained to estimate the critical compressive load (or stress) for the combination of two different buckling modes (bending and shear) [21].

Fig. 10 also shows the fitting curve according to Feih et al. [8, 9]. The agreement to the experimental results is very good. However, compared to the shear fitting, the fitting parameters φ and T_k have changed, see corresponding comment in Section 4.1.

5 CONCLUSIONS

A model for predicting composite material strength degradation under elevated and high temperatures is proposed. This model is based on a similar previously proposed model for material stiffness and is validated by means of shear, tensile and compressive experiments on pultruded GFRP specimens at temperatures of up to 220°C (428°F). The modeling results compared well with those obtained from experiments. The following conclusions were drawn:

1. Considering composite materials at a certain temperature as a mixture of materials in different states and knowing the proportion of material in each state in the mixture, upper and lower bounds of mixture strength can be quantified by the rule and inverse rule of mixture, which characterize the morphology of the mixture.
2. The degradation of temperature-dependent resin-dominated shear strength and stiffness (E-modulus) occur similarly and both can be well described by the rule of mixture (upper bound).
3. The degradation of temperature-dependent nominal compressive strength tends to follow the lower bound of strength defined by the inverse rule of mixture. The normalized nominal compressive strength is smaller than the normalized nominal shear strength at the same temperature.
4. When subjected to thermal loading, composite materials under tensile load may exhibit fiber- or resin-dominated behavior. In a lower temperature range (below the onset of glass transition), fiber failure occurs and strength is dominated by the temperature-dependent fiber tensile strength.

At higher temperatures (above the onset of glass transition), tensile components may exhibit resin-dominated failure in joint regions, which can be described by the proposed model. Shear failure occurs between fiber layers in the resin and reduces the anchorage of fibers (roving layer) at mid-depth of the components.

5. The parameters required for the proposed model can be obtained from kinetic analysis of DMA results and have a clear physical basis, making the fitting of experimental curves for material strength degradation unnecessary.

6. The proposed modeling scheme can easily be incorporated into structural theory to predict mechanical responses on the structural level using finite element and finite difference methods. A displacement-based or stress-based failure criterion can be applied and time-to-failure can be predicted.

ACKNOWLEDGEMENT

The authors would like to thank the Swiss National Science Foundation for its financial support (Grant No. 200020-117592/1).

REFERENCES

1. Mouritz, AP, Gibson, AG. Fire properties of polymer composite materials. Springer, 2007.

2. Springer GS. Model for predicting the mechanical properties of composites at elevated temperatures. *Journal of Reinforced Plastics and Composites* 1984, 3(1): 85-95.

3. McManus HL, Springer GS. High temperature thermomechanical behavior of carbon-phenolic and carbon-carbon composites, I. Analysis. *Journal of Composite Materials* 1992, 26(2): 206-229.

4. McManus HL and Chamis CC. Stress and damage in polymer matrix composite materials due to material degradation at high temperatures. NASA technical memorandum 4682.

5. Gibson AG, Wu YS, Evans JT and Mouritz AP. Laminate theory analy-

sis of composites under load in fire. *Journal of Composite Materials* 2006, 40(7): 639-658.

6. Mahieux CA, Reifsnider KL. Property Modelling across transition temperatures in polymers: a robust stiffness-temperature model. *Polymer* 2001, 42: 3281-3291.

7. Gu P, Asaro RJ. Structural buckling of polymer matrix composites due to reduced stiffness from fire damage. *Composite structures* 2005, 69: 65-75.

8. Feih S, Mathys Z, Gibson AG, Mouritz AP. Modeling the tension and compression strengths of polymer laminates in fire. *Composites Science and Technology* 2007, 67: 551-564.

9. Feih S, Mathys Z, Gibson AG, Mouritz AP. Modeling the compression strength of polymer laminates in fire. *Composites Part A* 2007, 38: 2354-2365.

10. Wang YC, Wong PMH, Michael Davies J. An experimental and numerical study of the behavior of glass fiber reinforced plastics (GRP) short columns at elevated temperatures. *Composite Structures* 2004, 63: 33-43.

11. Bai Y, Keller T, Vallée T. Modeling of stiffness of FRP composites under elevated and high temperatures. *Composites Science and Technology* 2008, 68: 3099-3106.

12. Ashby MF, Jones DRH. Engineering materials 2: an introduction to microstructures, processing, and design. Oxford, Pergamon Press, 1997.

13. Beran MJ. Statistical continuum theories. John Wiley, New York 1968.

14. Chamis CC, Sinclair JH. Ten-deg off-axis test for shear properties in fiber composites. *Experimental Mechanics* 1977; 9: 339-346.

15. ASTM D3171-99 Standard Test Method for constituent content of composite materials.

16. Bai Y, Keller T. A kinetic model to predict stiffness and strength of FRP composites in fire. The fifth international conference of Composites in Fire (CIF), Newcastle upon Tyne, UK, 2008.

17. Puente I, Insausti A, and Azkune M. Buckling of GFRP column: an empirical approach to design. *Journal of Composites for Construction* 2006, 10 (6), 529-537.

18. Benveniste Y. A new approach to the application of Mori-Tanaka's theory in composite material. *Mechanics of Materials* 1987, 6: 147.

19. MacLachlan DS, Blaszkiewicz M, and Newnham RE. Electrical Resistivity of Composites. *Journal of the American Ceramic Society* 1990, 73(8): 2187-203.

20. Landauer R. The electrical resistance of binary metallic mixtures. *Journal of Applied Physics* 1952, 23, 7: 779-784.

21. Niu K, Talreja R. Modeling of compressive failure in fiber reinforced composites. *International Journal of Solids and Structures* 2000, 37: 2405-2428.

2.4 Additional experimental investigations of material properties

Summary

Experimental investigations concerning the thermophysical and thermomechanical properties of composite materials under elevated and high temperatures remain scarce, especially for pultruded glass fiber-reinforced polyester (GFRP) composites. In this paper, comprehensive experimental studies were conducted on a different pultruded GFRP composite, supplied by Fiberline, including the mass transfer by Thermogravimetric Analysis (TGA), thermal conductivity by hot disk tests, specific heat capacity by Differential Scanning Calorimetry (DSC), and stiffness by DMA. The results of these experiments were further used to validate the models proposed in Sections 2.1 and 2.2. This paper provides a full set of temperature-dependent thermophysical and thermomechanical properties for a polyester matrix composite and the related kinetic parameters used for the theoretical modeling. This paper also supplies basic material information for the experimental investigation and theoretical analysis of strength degradation in Section 2.3 and time-to-failure in Section 2.8.

Reference detail

This paper was published in Thermochimica Acta 2008, volume 469, pages 28-35, entitled

"Experimental investigations on temperature-dependent thermophysical and mechanical properties of pultruded GFRP composites" by Yu Bai, Nathan L. Post, John J. Lesko, and Thomas Keller.

Part of the content of this paper was presented at the Fourth International Conference on FRP Composites in Civil Engineering (CICE) 22-24 July 2008, Zurich, Switzerland, entitled

"Modeling of thermomechanical properties and responses for FRP composites in fire" by Yu Bai, Thomas Keller and Till Vallée, presented by Yu Bai.

EXPERIMENTAL INVESTIGATIONS ON TEMPERATURE-DEPENDENT THERMOPHYSICAL AND MECHANICAL PROPERTIES OF PULTRUDED GFRP COMPOSITES

Yu Bai[1], Nathan L. Post[2], John J. Lesko[2], and Thomas Keller[1]

[1] Composite Construction Laboratory CCLab, Ecole Polytechnique Fédérale de Lausanne (EPFL), Switzerland.

[2] Material Response Group, Dept. of Engineering Science & Mechanics, Virginia Polytechnic Institute & State University, USA.

ABSTRACT:

The temperature-dependent thermophysical and mechanical properties of a pultruded E-glass fiber-reinforced polyester (GFRP) composite are investigated in this paper. Fitting of theoretical models of the material properties to results of TGA, DSC, hot disk, and DMA experiments demonstrated good agreements. The constants for an Arrhenius representation of the decomposition mass-loss were determined using multi-curve methods. The effective specific heat capacity for the virgin material was found to increase during the decomposition process. A series model based on component volume fraction during decomposition provided an accurate description of the thermal conductivity as a function of temperature as measured by the hot disk method. Models based on the kinetic theory can describe the material degradation during glass transition as indicated by DMA results, while the parameters still need to be accurately identified. This paper provides a full set of temperature dependent physical properties of a polyester matrix composite and demonstrates the applicability of theoretical models to represent the experimental results.

KEYWORDS:

Polymer-matrix composites; thermogravimetry; differential scanning calorimetry; hot disk; dynamic mechanical analysis

1 INTRODUCTION

Fiber-reinforced polymer (FRP) composites have been increasingly used in different fields, such as defense, aerospace, marine and civil engineering. Pultrusion is commonly used to produce FRP profiles with different structural shapes in an economic way. In many applications, these materials must withstand elevated temperatures while maintaining structural integrity. The temperature-dependent thermophysical and mechanical properties of an E-glass/polyester composite material, including the specific heat capacity, thermal conductivity, mass transfer, storage and loss modulus and decomposition behavior are the focus of this paper. Due to the viscoelastic behavior of the polymer matrix in many composites, the physical properties of the composite can change drastically over relatively small changes in temperature [1, 2]. Complicated processes occur at characteristic temperatures including the matrix glass transition and decomposition temperatures. The effective values of physical and mechanical properties are influenced by the chemical changes caused by increased temperature [3-5]. In order to estimate and predict the thermal responses of composite materials, it is necessary to evaluate and model the temperature-dependent thermophysical and thermomechanical properties.

Experimental investigations were conducted by Henderson et al. on glass-filled phenol-formaldehyde (phenolic) resin composite: Temperature-dependent mass loss during decomposition was investigated by thermogravimetric Method (TGA) in 1981 [3]. The multi-curves method (Friedman method) was used to identify the kinetic parameters in the Arrhenius equation. The temperature-dependent effective specific heat capacity (including the decomposition) was studied in 1982 by differential scanning calorimetry (DSC) [4, 5]; and, in 1983, the temperature-dependent thermal conductivity was obtained by the line source technique [6]. In recent work conducted by Lattimer and Ouellette in 2006 [7], the temperature-dependent mass loss, effective specific heat capacity, and thermal conductivity were investigated on glass fiber-reinforced vinyl ester composites (GFRP) from ambient temperature to 800°C. Inverse heat transfer analy-

sis was used to determine the thermophysical properties by specifying the boundary condition of the samples as close to adiabatic as possible. Together with these experimentally obtained temperature-dependent thermophysical properties, a thermal response model was also proposed in their work.

The temperature-dependent mass loss due to decomposition was further investigated for various polymer and composite materials, such as bismaleimide resin by Regnier and Guibe in 1997 [8], DGEBA/MDA system by Lee, Shim and Kim in 2001 [9], etc.

Overall, the reported experimental and modeling work conducted for the thermophysical and thermomechanical properties of GFRP composites manufactured by pultrusion is very limited. This paper provides a complete experimental data set for temperature-dependent thermophysical and mechanical properties of a pultruded GFRP composite. The experimental data was then used to further verify recently developed models for thermophysical and thermomechanical properties [10, 11].

2 DESCRIPTION OF EXPERIMENTAL MATERIALS

The pultruded GFRP laminates (provided by Fiberline A/S, Denmark) investigated in this study consisted of E-glass fibers embedded in an isophtalic polyester resin. The laminates had two different thicknesses (3mm and 6mm). Burn-off tests were performed to obtain the fiber mass content of the materials according to ASTM D3171-99 [12], the volume fraction was calculated considering a glass fiber density of 2.53g/cm^3; the results are summarized in Table 1. Observation of the residual char material after a burn off test showed that the laminate consisted of two mat layers sandwiching a layer of unidirectional roving. The mat layer of the 6mm laminate consisted of a chopped strand mat (CSM) and a woven roving ply [0°/90°], both stitched together, while the 3mm laminate contained only a CSM on each side. Microscopy was further used to obtain the details of the fiber architecture, see Fig. 1. For the 3-mm laminates, the mat and roving layers had an average thickness of 0.6 mm and 1.8 mm, respectively, while

the 6 mm laminates exhibited 1.5 mm and 3.0 mm average thickness for the mat and roving layers respectively. The required sizes of the specimens used in the following experiments were cut or ground from these laminates.

Sample	Fiber volume fraction [%]	Fiber weight fraction [%]
6 mm	35.6	57.6
3 mm	36.1	58.1

Table 1. Fiber volume and weight fraction of pultruded 6mm and 3mm laminates

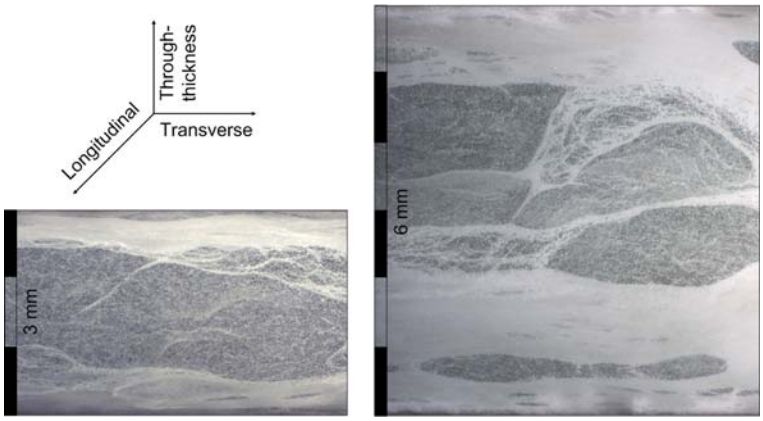

Fig. 1. Material architecture for pultruded 3mm (left) and 6mm (right) laminates by microscope (Fiber is presented in deep color and resin is in light color)

3 EXPERIMENTAL INVESTIGATION

3.1 Temperature-dependent mass change

The Thermogravimetric analysis method is widely accepted as a standard to investigate the mass change of polymer materials, including polymer matrix composites during the decomposition process [13]. The specimens were created by grinding the 6mm laminate into powder using a rasp. The material was taken through the entire laminate thickness to ensure that the fiber and resin contents of powder and laminate were the same. These specimens were analyzed by a TGA Q500 machine from TA Instruments, Inc. The tests were carried out from ambient temperature (25°C) to 700°C

in an air atmosphere with a flow rate of 60 ml/min. Four heating rates (2.5, 5.0, 10.0, and 20.0°C/min) were used. The initial mass of the specimens was 6.0 mg ± 0.3 mg for all runs. The experimental curves of mass fraction (temperature-dependent mass divided by the initial mass) are shown in Fig. 2.

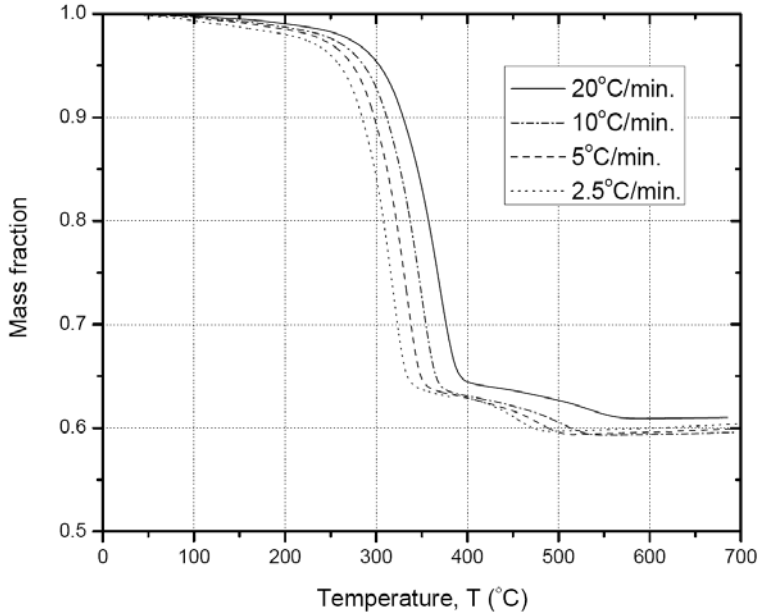

Fig. 2. Temperature-dependent mass fraction at different heating rates from TGA

3.2 Temperature-dependent specific heat capacity

Different methods can be used to obtain the specific heat capacity of the material at different temperatures, such as direct measurement by calorific method (ASTM C351), indirect measurement by transient hot wire method (ASTM C1113), transient line source (ASTM D5930-97), or laser flash (ASTM E1461-01). Differential Scanning Calorimetry (DSC), introduced in ASTM E1269 [14], was used as a direct measurement method in this paper.

For the DSC experiments, powder was ground from the 6 mm laminates. Two specimens of virgin material (13.7 and 12.0 mg) were tested by a DSC analyzer (DSC Q1000, TA instrument, Inc.) from ambient temperature to 300°C under a heating rate of 5°C/min. Small specimen masses

were used in order to reduce the temperature gradients in the material. During testing nitrogen atmosphere at a purge rate of 50 ml/min was maintained to prevent thermo-oxidative degradation. Under the same conditions, two specimens from char material (25.4 and 23.0 mg) obtained after burn-off experiments were tested. The resulting experimental curves for the temperature-dependent specific heat capacity (normalized with respect to the initial mass) of the virgin and char materials are shown in Fig. 3.

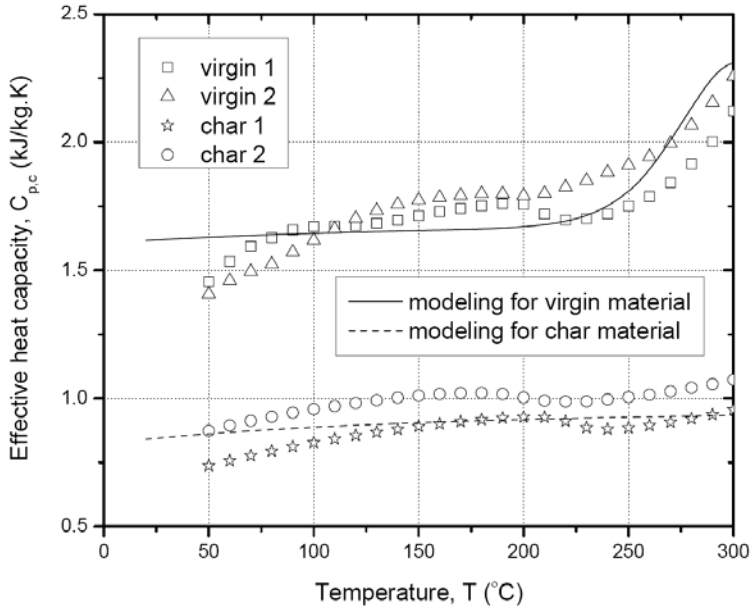

Fig. 3. Effective specific heat capacity on virgin and char materials as a function of temperature (normalized with respect to initial mass of sample) from DSC and modeling

3.3 Temperature-dependent thermal conductivity

For measuring the temperature-dependent thermal conductivity, two different categories of analytical methods are available:

1. Steady heat flux analysis, such as (amongst others) guarded hot plate method (ASTM C177), or comparative longitudinal heat flow (ASTM E1225).

2. Transient heat flux analysis, such as transient hot wire method (ASTM C1113), or transient line source (ASTM D5930-97)

The hot disk method with transient thermal analysis was used in this case. This is an experimental technique developed using the concept of the transient hot strip (THS) technique, first introduced by Gustafsson et al. [15]. The method is accepted as one of the most convenient techniques for studying thermal conductivity [16, 17]. One advantage is that the apparatus employs a comparatively large specimen that allows analyzing the material in its proper structure rather than as a small non-representative coupon.

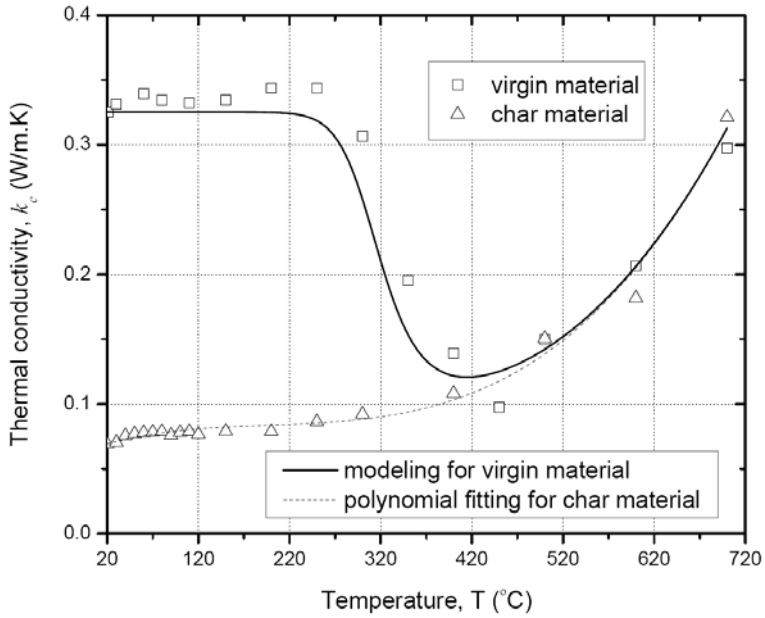

Fig. 4. Temperature-dependent effective thermal conductivity on virgin and char materials from hot disk experiments and modeling

Only the through-thickness thermal conductivity was measured. The specimen used consisted of two 100mm square plates of 6 mm thickness. The hot plate sensor was placed between the two plates and was then heated by an electrical current for a short period of time. The dissipated heat caused a temperature rise in both, the sensor and the surrounding specimen. The average temperature rise of the sensor was measured by recording the change of the electrical resistance. Resistivity changes with temperature and the temperature coefficient of resistivity (TCR) of the sensor material were determined in advance. By comparing the recorded transient temperature rise with that of the theoretical solution from the

thermal conductivity equation, the thermal conductivity was determined. Hot disk experiments (using a Hot Disk Thermal Constants Analyzer, manufactured by Hot Disk Inc.) were repeated three times on each virgin and char specimen at ambient temperature using a Kapton hot plate sensor which provides relatively high accuracy. Experiments at higher temperatures, up to 700°C, were performed on both virgin and char material with a Mika hot plate sensor, which is of lower accuracy. The results from the Mika sensor were then calibrated to the Kapton sensor results at ambient temperature. All of these results are shown in Fig. 4.

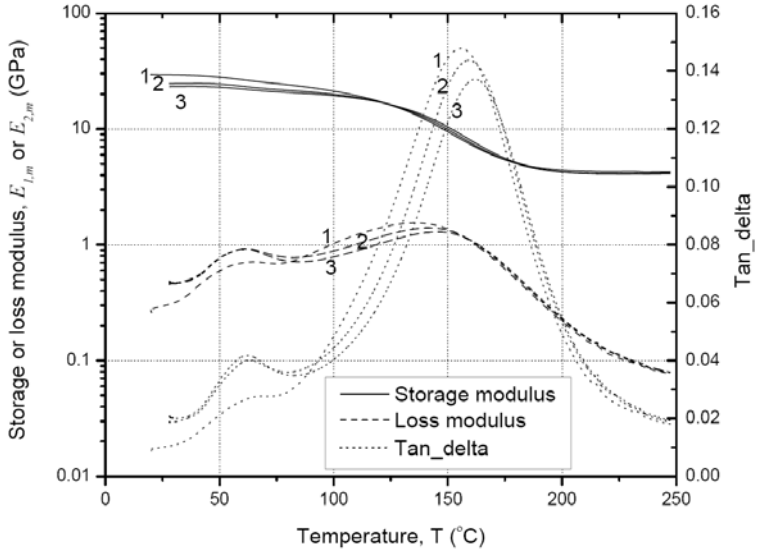

Fig. 5. Temperature-dependent storage modulus, loss modulus and tan-delta in longitudinal direction from three-run DMA (1-3: number of run)

3.4 Temperature-dependent mechanical properties

In order to obtain the temperature dependent elastic and viscoelastic mechanical properties of the material (storage and loss moduli), and to determine the kinetic parameters of the glass transition, DMA was conducted on specimens with 3-mm thickness (see Section 2 for material description). Considering the orthotropic characteristics of the composite materials, two specimens were cut from different directions (longitudinal and transverse, see Fig. 1). The resulting size was 50-mm long × 5-mm wide × 3-mm thick. Cyclic dynamic loads were imposed using a dual cantilever

fixture on a DMA 2980 Dynamic Mechanical Analyzer from TA Instruments, Inc. The detailed procedure is according to ASTM D 5023-99 [18].

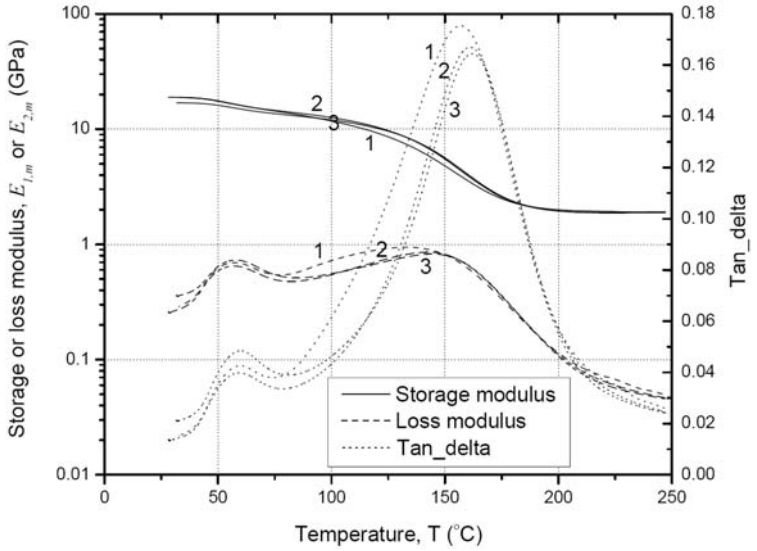

Fig. 6. Temperature-dependent storage modulus, loss modulus and tan-delta in transverse direction from three-run DMA (1-3: number of run)

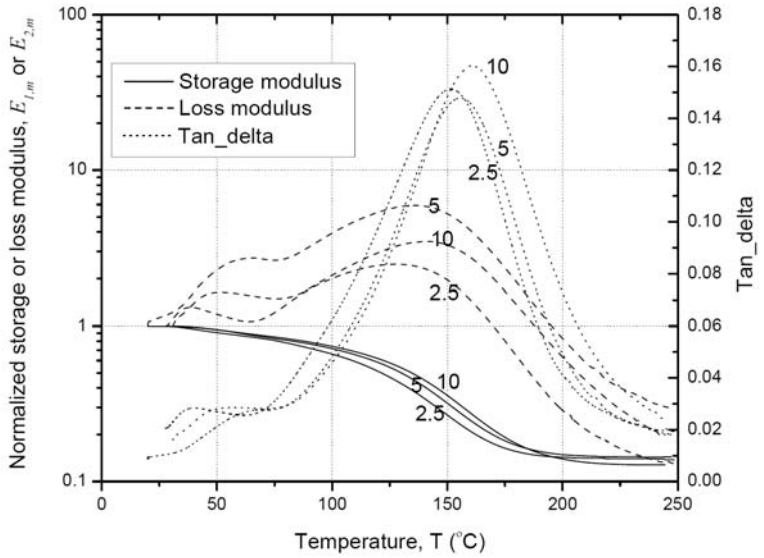

Fig. 7. Storage and loss modulus normalized by the initial values at 25 °C for each specimen, and tan-delta curves in longitudinal direction for three different heating rates (°C/min)

The specimens were ramped from room temperature to 250°C at three different heating rates (2.5, 5 and 10°C/min) and a dynamic oscillation frequency of 1 Hz. The specimen at 5°C/min was cooled to room temperature and heated back to 250°C two more times so that any changes from

postcuring or thermal degradation could be noted. The results from different runs at 5°C/min are shown in Fig. 5 for longitudinal direction (i.e. pultrusion direction) and Fig. 6 for transverse direction; the results for different heating rates for the longitudinal direction are shown in Fig. 7.

4 DISCUSSION AND MODELING

4.1 Temperature-dependent mass transfer

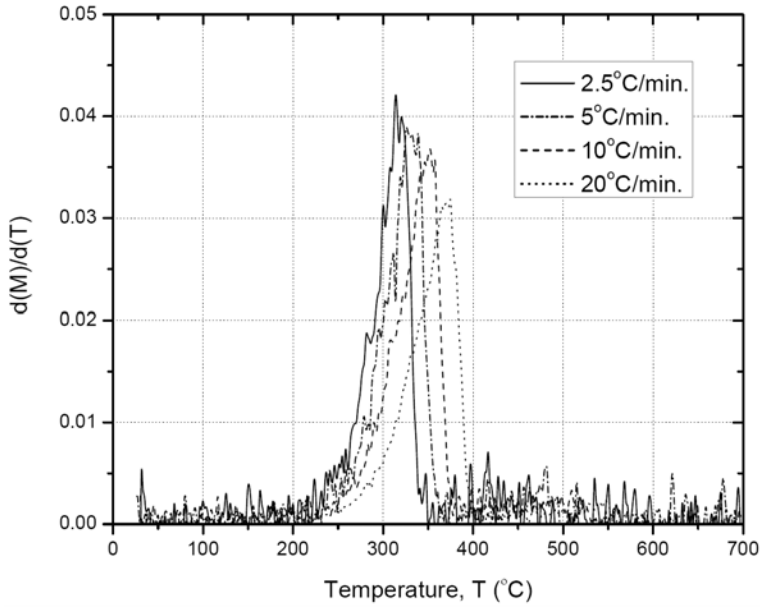

Fig. 8. Derivation curve of temperature-dependent mass for different heating rates

The temperature-dependent mass fraction curves from different heating rates are summarized in Fig. 2. The mass of the material did not change noticeably until the decomposition of the polyester resin started. The onset of decomposition temperature ($T_{d,onset}$) was determined as the temperature at which 5% of the mass was lost, and T_d was determined as the point when the mass decreased at the highest rate, based on the derivative weight curve in Fig. 8. The results from different heating rates are summarized in Table 2. It can be seen that both, T_d and $T_{d,onset}$, increased with the increase of heating rate, because a lower heating rate corresponded to a longer heating time, and thus resulting in a more noticeable decomposition at a same temperature point. The residual mass fractions from all

heating rates are around 60% (see Table 2) of the original material. Thus, considering the fiber mass fraction of 58% obtained by burn-off (see Table 1), most of the residual material in the TGA was glass fiber.

Heating rate [°C/min]	$T_{d,onset}$ [°C]	T_d [°C]	Residual mass [%]
20	304	371	61.0
10	287	353	59.6
5	274	337	59.9
2.5	260	321	60.4

Table 2. Decomposition temperatures $T_{d,\,onset}$, T_d and residual mass from TGA tests at different heating rates

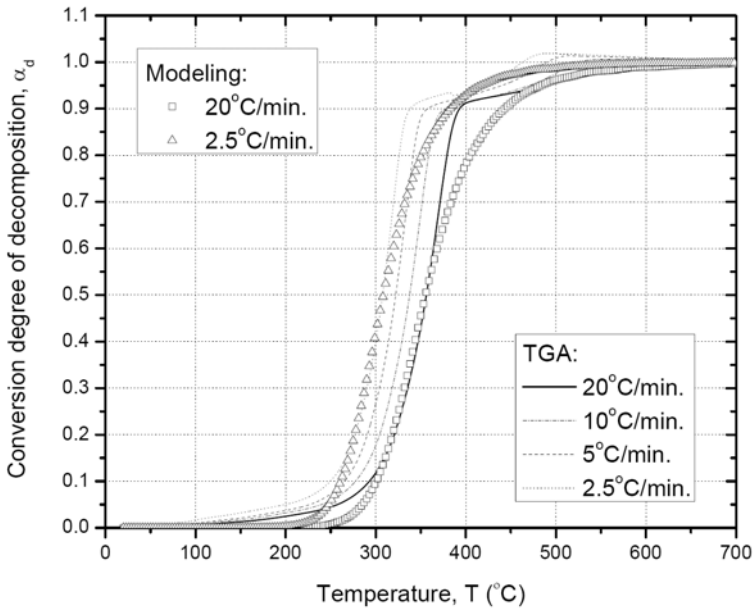

Fig. 9. Conversion degrees of decomposition at different heating rates from TGA; comparison to results from Ozawa method

Simplifying decomposition of resin as one step chemical process, this process can be modeled by the Arrhenius equation:

$$\frac{d\alpha_d}{dT} = \frac{A_d}{\beta} \cdot \exp\left(\frac{-E_{A,d}}{RT}\right) \cdot \left(1-\alpha_d\right)^n \tag{1}$$

where α_d is the conversion degree of decomposition, A_d is the pre-exponential factor, $E_{A,\,d}$ is the activation energy, and n is the reaction order. R is the universal gas constant (8.314 J/mol·K). The Ozawa method [19], as a multi-curve method, was used to identify the kinetic parameters

(A_d , $E_{A,d}$ and n) and the results are summarized in Table 3. Substituting these parameters into Eq. (1), the theoretic conversion degrees of decomposition were obtained in Fig. 9 (only the curves at heating rates 20°C/min and 2.5°C/min are shown for better viewing), which compare well with the experimental results. However, some variations still were found between 350°C and 400°C. Considering that decomposition is a complicated process and different elemental reactions are involved, a single equation can not entirely describe all the concurrent processes. It seems that the decomposition can be better described if separating it as a two-stage process [3]; however, the problem of identifying the kinetic parameters from two coupled processes remains a challenge in such an approach.

Transition	E_A [J/mol]	A(min^{-1})	n
Glass (Ozawa)	118591	2.49×10^{15}	1.89
Glass (Kissinger)	131387	3.24×10^{16}	0.86
Decomposition (Ozawa)	124953	2.72×10^{10}	2.75

Table 3. Kinetic parameters for glass transition and decomposition

4.2 Temperature-dependent heat capacity

As shown in Fig. 3, when the temperature is lower than 250 °C, the increase of the specific heat capacity of the virgin material is very small; in fact, theoretically, the specific heat capacity of pure resin or fibers increases with temperature based on the classic Einstein or Debye model. When the temperature is close to 275°C ($T_{d,onset}$ is 274°C at a heating rate of 5°C/min, see Table 2), the effective heat capacity of the virgin material started to increase faster, because the decomposition process is an endothermic chemical reaction. Similar experimental results also can be found for glass-filled phenol-formaldehyde resin composite in [5], and for E-glass fiber vinyl ester in [7]. The change of the DSC curve of the char material is very small when temperature is increased up to 300°C, since it mainly consisted of glass fibers.

The model for temperature-dependent effective specific heat capacity,

normalized to the initial mass, $C_{p,c}$, and proposed in [10], can be expressed as:

$$C_{p,c} = C_{p,b} \cdot (1 - \alpha_d) + C_{p,a} \cdot \frac{M_e \cdot \alpha_d}{M_i} + \frac{d\alpha_d}{dT} \cdot C_d \quad (2)$$

where $C_{p,b}$ and $C_{p,a}$ is the specific heat capacity of the virgin and decomposed char material in kJ/kg·K. M_i and M_e are the initial and final mass. C_d is the total decomposition heat in kJ/kg, α_d as obtained in Section 4.1.

The modeling curve for true specific heat capacity of char material ($C_{p,a}$) was calculated based on the model in [10], and comparing with the DSC curve on char material in Fig. 3, a good agreement was found. Substituting the theoretic curve of $C_{p,a}$ into Eq. (2), and taking the value at 100°C from the DSC curve of virgin material as $C_{p,b}$, the model curve of the specific heat capacity of the virgin material can be obtained. The comparison with the DSC results on virgin material is shown in Fig. 3. The increase of heat capacity due to decomposition is well described by this model; while there is still a small increment of heat capacity from the initial temperature to around 100°C that remains unaccounted for in the model. This difference could be due to the fact that the true specific heat capacity of pure material (for example, pure polyester) is increasing with temperature or because of measurement inaccuracy in the initial stage of temperature increase. Similar results also can be found in DSC results on E-glass fiber vinyl ester in [7]. Since the highest temperature achieved in the experiments was only 300°C, the decomposition process was not fully covered; the theoretic curve in the higher temperature range should be further confirmed, as well as the total decomposition heat, C_d.

4.3 Temperature-dependent thermal conductivity

The thermal conductivity measured for virgin and char material at room temperature are 0.325±0.004 and 0.069±0.002 W/m·K, respectively. Char material has a much lower thermal conductivity at room temperature since the resin has already decomposed; gaps and voids are left in the composite between the glass fibers that significantly increase the thermal

resistance (shielding effects, see [10]).

The thermal conductivity measured at different temperatures for both virgin and char material are shown in Fig. 4. The thermal conductivity of the char material (mostly glass fibers) increased with the temperature, because the thermal conductivity of glass fibers also increases at these temperatures.

The change of thermal conductivity of the virgin material is comparatively small when temperature is lower than 280°C (i.e. before the decomposition of the resin), while a strong decrease is apparent when the temperature is approaching T_d due to shielding effects of emerging voids [10]. When the resin is fully decomposed, the temperature-dependent thermal conductivity curve approaches and follows that of the char material.

At any specified temperature, the composite material can be considered as a material composed of two phases: the virgin material and the decomposed char material, which are connected in series in the heat flow (through-thickness) direction. The effective thermal conductivity of the composite materials can then be obtained as

$$\frac{1}{k_c} = \frac{V_b}{k_b} + \frac{V_a}{k_a} \tag{3}$$

where V_b and V_a are the volume fractions of the virgin material and decomposed char material, which can be expressed as [10]

$$V_b = 1 - \alpha_d \tag{4}$$

$$V_a = \alpha_d \tag{5}$$

Considering k_b as the thermal conductivity of the virgin material at room temperature (0.325 W/m·K), and k_a as the curve of temperature-dependent thermal conductivity of char material in Fig. 4, the model curve of the virgin (or decomposing) material was obtained. The comparison with the experimental data in Fig. 4 shows a good agreement. It should be noted that the time-dependent temperature progression (a constant heating rate, for example) is necessary to determine the conversion degree of decomposition, α_d, (see Section 4.1). As this information was not available in the high temperature hot disk experiments, the temperature-dependent

α_d obtained at 20°C/min (in Section 4.1) was used in Eqs. (4) and (5) to estimate the volume fractions of the different phases at different temperatures. This comparatively high rate was adopted in view of the rapid heating of the hot disk oven system.

	$T_{g,\,onset}$		T_g	
Run	Longitudinal [°C]	Transverse [°C]	Longitudinal [°C]	Transverse [°C]
1	112	112	156	157
2	116	118	159	161
3	124	123	162	162

Table 4. Glass transition temperature T_g and $T_{g,\,onset}$ by DMA tests from different runs and for different directions

4.4 Temperature-dependent mechanical properties

As shown in Figs. 5 and 6, for both longitudinal and transverse directions, the storage modulus monotonically decreased with the increasing of temperature, with the highest rate of change occurring between 145 to 165°C. The glass transition temperature, T_g (determined by the peak point of the tan-delta curve), and the $T_{g,onset}$ are summarized in Table 4 for different runs of the specimens in different directions. It can be seen that the resulting T_g from the two different directions is very similar, because the temperature effects mainly depend on the polyester resin, which was the same. On the other hand, three-run DMA tests on the same specimen showed that T_g is slightly increased with the number of runs for both directions (see Table 4). The curves of storage and loss modulus from different runs, however, are almost the same, thus post-curing effects were not observed. As also reported by the profile manufacturer, 180°C was reached during the pultrusion process and thus full curing must have been already achieved. It should be noted that a small peak before glass transition was found for the loss modulus and tan-delta curves in all runs and in both directions (see Figs. 5 and 6). This could result from secondary relaxations of

the polymer resin [20] or from additives. DMA results from different heating rates showed similar behavior, as shown in Fig. 7 where the storage and loss modulus were normalized by their initial room temperature values for each specimen. Faster heating rates delay the temperature of glass transition noted by the right shift of the storage modulus curves and the peaks of tan-delta and loss modulus curves.

The glass transition can be modeled by the Arrhenius equations [11]:

$$\frac{d\alpha_g}{dT} = \frac{A_g}{\beta} \cdot \exp\left(\frac{-E_{A,g}}{RT}\right) \cdot \left(1-\alpha_g\right)^n \tag{6}$$

where α_g is the conversion degree, A_g is the pre-exponential factor, $E_{A,g}$ is the activation energy (which is considered as a constant for one specified process) for glass transition. The Ozawa method [19] and Kissinger method [21] were used to determine the kinetic parameters based on the curves from three different heating rates. The corresponding kinetic parameters are summarized in Table 3.

Material state	Storage modulus, E_1 [GPa]	
	Longitudinal	Transverse
Glassy	29.6	18.9
Rubbery	4.26	1.91

Table 5. Storage and loss moduli for different material states in two different directions

Knowing the degree of conversion for the different transitions from Eq. (6), the temperature-dependent storage modulus, $E_{1,m}$ of FRP composite materials can be calculated as:

$$E_{1,m} = E_{1,g} \cdot \left(1-\alpha_g\right) + E_{1,r} \cdot \alpha_g \tag{7}$$

where $E_{1,g}$ and $E_{1,r}$ are the storage moduli in glassy state and rubbery state, respectively. These values are obtained based on the DMA (see Section 3.4) and are summarized in Table 5. It was found that the storage moduli in glassy state obtained by DMA for both longitudinal and transverse directions are very similar to the corresponding values of elastic modulus reported in [22]. The mechanical properties are considered as ze-

ro for the decomposed state.

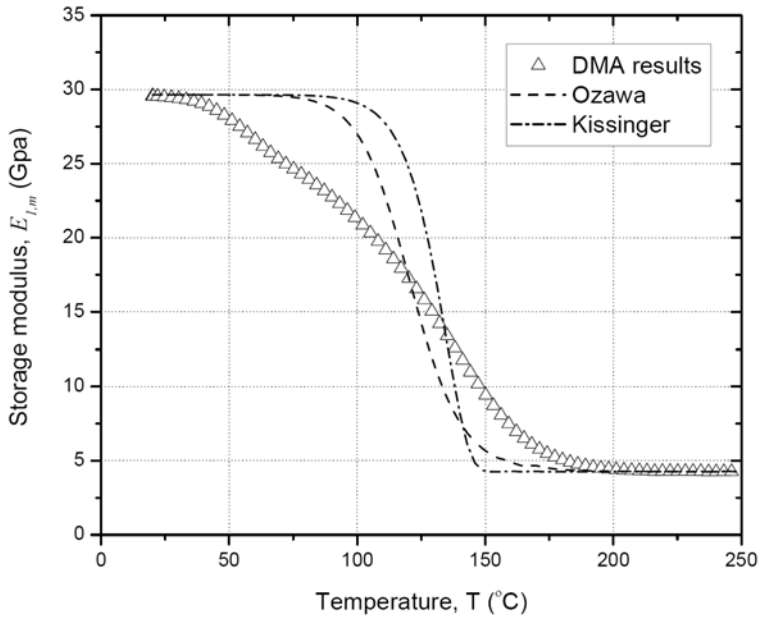

Fig. 10. Comparison of experimental and modeling curves of temperature-dependent storage modulus in longitudinal direction (at 5°C/min)

The modeling curves of temperature-dependent storage-modulus, resulting from the Ozawa and Kissinger methods, are shown in Fig. 10 for the longitudinal direction (at 5°C/min). The discrepancy between the modeling and experimental results could be attributed to the inaccuracy of the methods for the kinetic parameter estimation, or because of the E_A-dependencies induced by multi-step kinetics of the process. Different methods for kinetic parameters identification were discussed and compared in detail in [23-27], and an error analysis was presented in [28]. These methods are mainly used for the kinetic analysis of the decomposition process and seldom for the analysis of glass transition. It is apparent that the application of these methods to obtain kinetic parameters for glass transition requires further investigation.

5 CONCLUSIONS

For the further understanding and application of pultruded GFRP composites under elevated and high temperatures, a series of experiments were conducted to investigate the temperature-dependent thermophysical and

thermomechanical properties, including the mass loss, specific heat capacity, thermal conductivity, and storage and loss modulus. The following conclusions were obtained:

1. The mass of the composite material is stable before T_d. When the decomposition is approaching, the mass starts to decrease rapidly. The Arrhenius equation can be used to model the decomposition process; multi-curves methods were used to identify the kinetic parameters. Further investigations could include characterizing decomposition behavior by multi-stage chemical reactions.

2. The change of specific heat capacity of the composite material is not very significant when the temperature is below T_d. However, the measured value rapidly increases during the decomposition process because additional heat is required for this endothermic chemical reaction. This behavior can be well modeled with the concept of effective specific heat capacity. However, measurements over a higher temperature range would be desirable to cover the whole decomposition process, and to further verify the total decomposition heat.

3. The thermal conductivity of fully decomposed material is much lower than that of virgin material at room temperature. For decomposed material, thermal conductivity was seen to increase with temperature. For virgin material, the effective thermal conductivity is decreased when decomposition occurs, since shielding effects are induced by the emerging voids being filled with gases from the decomposed resin. The effective thermal conductivity can be accurately described by a series model whereby the volume fraction of different phases can be obtained from the decomposition model.

4. The storage modulus of the composite material decreased, while the loss modulus increased, with increasing temperature. The rates accelerate when temperature is approaching T_g. However, when temperature exceeds T_g, the loss modulus starts to decrease. The temperature-dependent mechanical properties show similar behavior in both longitudinal and transverse directions. The Arrhenius equation was used to describe the glass transition. However, the estimation of the kinetic parameters for glass

transition using existing multi-curves methods led to inaccurate results and further investigation is warranted.

ACKNOWLEDGEMENT

The authors would like to acknowledge the support of the Swiss National Science Foundation (Grant No. 200020-117592/1), Fiberline Composites A/S, Denmark for providing the experimental materials, and, John Bausano, Jason Cain and Dr. Aixi Zhou at Virginia Tech for supporting the experiments.

REFERENCES

1. Hilal AS, Abousehly AM, Dessouky, MT, ABD El-hakim AA. Measurement of thermophysical properties of polyester cured with styrene in the range 300-450 K. *Journal of Applied Polymer Science* 1993, 49: 559-563.

2. Tant MR. High Temperature Properties and Applications of Polymeric Materials. Proceedings of the ACS Symposium Series603 1994, San Diego, CA, USA.

3. Henderson JB, Tant MR, Moore GR, Wiebelt JA. Determination of kinetic parameters for the thermal decomposition of phenolic ablative materials by a multiple heating rate method. *Thermochimica Acta* 1981, 44: 253-264.

4. Henderson JB, Wiebelt JA, Tant MR, Moore GR. A method for the determination of the specific heat and heat of decomposition of composite materials. *Thermochimica Acta* 1982, 57: 161-171.

5. Henderson JB. Measurement of the specific heat of a glass-filled polymer composite to high temperatures. *Thermochimica Acta* 1988, 131: 7-14.

6. Henderson JB, Verma YP, Tant MR, Moore GR. Measurement of the thermal conductivity of polymer composites to high temperature using the line source techniques. *Polymer Composites* 1983, 4: 219-224.

7. Lattimer BY, Ouellette J. Properties of composite materials for thermal analysis involving fires. *Composite Part A* 2006, 37: 1068-1081.

8. Regnier N, Guibe C. Methodology for multistage degradation of polyi-

mide polymer. *Polymer Degradation and Stability* 1997, 55: 165-172.

9. Lee LY, Shim MJ, Kim SW. Thermal decomposition kinetics of an epoxy resin with rubber-modified curing agent. *Journal of Applied Polymer Science* 2001, 81: 479-485.

10. Bai Y, Vallée T, Keller T. Modeling of thermo-physical properties for FRP composites under elevated and high temperatures. *Composites Science and Technology* 2007, 67(15-16): 3098-3109.

11. Bai Y, Keller T, Vallée T. Modeling of stiffness for FRP composites under elevated and high temperatures. *Composites Science and Technology* 2008, 68: 3099-3106.

12. ASTM D3171-99 Standard Test Method for constituent content of composite materials.

13. ASTM E1131-03 Standard Test Method for compositional analysis by Thermogravimetry.

14. ASTM E1269-01 Standard Test Method for Determining Specific Heat Capacity by Differential Scanning Calorimetry.

15. Gustafsson SE. Transient plane source techniques for thermal conductivity and thermal diffusivity measurements of solid materials. *Review of Scientific Instruments* 1991, 62: 797-804.

16. Jannot Y, Meukam P. Simplified estimation method for the determination of the thermal effusivity and thermal conductivity using a low cost hot strip. *Measurement Science and Technology* 2004, 15: 1932-1938.

17. Mo P, Hu P, Cao J, Chen Z, Fan H, Yu F. Effective Thermal Conductivity of Moist Porous Sintered Nickel Material. *International Journal of Thermophysics* 2006, 27: 304-313.

18. ASTM D5023-99 Standard Test Method for measuring the dynamic mechanical properties of plastics using three-point bending.

19. Ozawa T. A new method of analysing thermogravimetric data. *Bulletin of the Chemical Society of Japan* 1965, 38(11): 1881-1886.

20. Ashby MF, Jones DRH. Engineering materials 2: an introduction to microstructures, processing, and design. Oxford, Pergamon Press, 1997.

21. Kissinger HE. Reaction kinetics in differential thermal analysis. *Ana-*

lytical Chemistry 1957, 29: 1702-1706.

22. Keller T, Gürtler H. Quasi-static and fatigue performance of a cellular FRP bridge deck adhesively bonded to steel girders. *Composite Structures* 2005, 70(4): 484-496.

23. Brown ME, Maciejewski M, Vyazovkin S, Nomen R, Sempere J, Burnham A, Opfermann J, Strey R, Anderson HL, Kemmler A, Keuleers R, Janssens J, Desseyn HO, Li CR, Tang TB, Roduit B, Malek J and Mitsuhashi T. Computational aspects of kinetic analysis.: Part A: The ICTAC kinetics project-data, methods and results. *Thermochimica Acta* 2000, 355: 125-143.

24. Maciejewski M. Computational aspects of kinetic analysis.: Part B: The ICTAC Kinetics Project – the decomposition kinetics of calcium carbonate revisited, or some tips on survival in the kinetic minefield. *Thermochimica Acta* 2000, 355: 145-154.

25. Vyazovkin S. Computational aspects of kinetic analysis.: Part C. The ICTAC Kinetics Project – the light at the end of the tunnel? *Thermochimica Acta* 2000, 355: 155-163.

26. Burnham AK. Computational aspects of kinetic analysis.: Part D: The ICTAC kinetics projec – multi-thermal-history model-fitting methods and their relation to isoconversional methods. *Thermochimica Acta* 2000, 355: 165-170.

27. Vyazovkin S, Wight CA. Model-free and model-fitting approaches to kinetic analysis of isothermal and nonisothermal data. *Thermochimica Acta* 1999, 340-341: 53-68.

28. Starink MJ. The determination of activation energy from linear heating rate experiments: a comparison of the accuracy of isoconversion methods. *Thermochimica Acta* 2003, 404: 163-176.

2.5 Time dependence of material properties

Summary

Most thermal and mechanical response models for composite materials consider only the temperature dependence of physical and mechanical properties. Based on TGA, DSC and DMA conducted on a GFRP composite material at different heating rates however, it is demonstrated that the thermophysical and thermomechanical properties of composite materials under elevated and high temperatures are not univariate functions of temperature, but also functions of time.

This paper introduces and explains the temperature and time dependence of physical and mechanical properties at elevated and high temperatures. It extends the models proposed in Sections 2.1 and 2.2 to take time effects into account, showing good agreement with experimental results. Based on a finite difference method, complex realistic thermal loading programs such as the ISO fire curve can be considered and are presented in this paper.

Reference detail

This paper, accepted for publication in the Journal of Composite Materials, is entitled

"Time dependence of material properties of composites in fire" by Yu Bai and Thomas Keller.

TIME DEPENDENCE OF MATERIAL PROPERTIES OF FRP COMPOSITES IN FIRE

Yu Bai and Thomas Keller

Composite Construction Laboratory CCLab, Ecole Polytechnique Fédérale de Lausanne (EPFL), BP 2225, Station 16, CH-1015 Lausanne, Switzerland.

ABSTRACT:

Temperature dependence of physical and mechanical properties is considered in most thermal and mechanical response models for composite materials. Based on thermogravimetry analysis (TGA), differential scanning calorimetry (DSC) and dynamic mechanical analysis (DMA) conducted at different heating rates, it is demonstrated that thermophysical and thermomechanical properties are not univariate functions of temperature, but also functions of time. Temperature- and time-dependent models for physical and mechanical properties at elevated and high temperatures are proposed, which show good accordance with experimental results. Based on a finite difference method, complex realistic thermal loading programs such as the ISO fire curve can be taken into account.

KEYWORDS:

Polymer-matrix composites; thermo properties; thermomechanical properties; modeling; temperature- and time-dependent

1 INTRODUCTION

When polymer composites are subjected to elevated and high temperatures, complex physical and chemical processes such as glass transition and decomposition occur, greatly influencing their physical and mechanical properties. Thus, in order to describe the thermal and mechanical responses in the higher temperature range, thermophysical and thermomechanical properties must be considered as variables.

Thermal response models were proposed by Griffis et al. in 1981 [1], in which the effective values of specific heat capacity and thermal conductivity were modeled as stepped functions dependent only on a single variable - temperature. These thermophysical property models were later used by Griffis et al. in 1986 [2], Fanucci in 1987 [3], and Bisby et al. in 2005 [4] amongst others. An extension from purely temperature- to also time-dependent thermophysical property models was proposed by Lattimer and Ouellette [5]. A different thermophysical property model, only dependent on temperature, was introduced by Henderson et al. in 1985 [6]. Here true material properties were considered since the various phenomena (such as decomposition heat, effects of decomposed gases, etc.) were explicitly included in the final governing equations. They were obtained by curve fitting, based on experimental data for original and char material, at different temperatures [7, 8]. This thermophysical property model was later used by Sullivan and Salamon in 1992 [9], Gibson et al. in [10], and Looyeh et al. in [11], amongst others.

Thermomechanical models based on variable mechanical properties for fiber-reinforced polymer (FRP) materials were also developed in the 1980s. The change in E-modulus was described by temperature-dependent functions, based on experimental data obtained from dynamic mechanical analysis (DMA) by Griffis et al. in 1986 [2] and Dao and Asaro in 1999 [12]. Another temperature-dependent model proposed by Gibson et al. in 2004 [13] described the degradation of mechanical properties during glass transition using a *tanh*-function, while the temperature-dependent model developed by Mahieux et al. [14] used Weibull-type functions to describe the

modulus change over the full range of transition temperatures. In all the above models, the E-modulus is a univariate function of temperature.

In other thermomechanical models, such as those introduced by Springer in 1984 [15] and Dutta and Hui in 2000 [16], the change in the E-modulus was empirically related to the mass loss of the material, the latter being estimated by the Arrhenius equation as a time-dependent function. Similarly, Crews and McManus [17] related strength degradation to the percentage of mass loss. However, the effects of glass transition, which caused a significant decrease in mechanical properties but only a small mass loss, were not considered in these models.

A multifactor interaction model was proposed by Chamis and Hopkins in [18] to mathematically describe the time-temperature-stress dependence of thermomechanical properties based on different exponential functions. No clear link to physical mechanisms is provided however. Time- and temperature-dependent E-modulus models can also be established based on steady-state creep theory [19], as demonstrated by Williams, Landel and Ferry's time-temperature equivalence (WLF equation) [20, 21]. However, a modulus/temperature relationship can only be obtained if an accurate modulus vs time prediction scheme is available. A comprehensive review of the time- and temperature-dependent mechanical properties of polymers can be found in [22].

The temperature-dependent effective thermophysical and thermomechanical properties of composite materials from literature [1-3, 12-14] are summarized in Fig. 1. When decomposition occurs, the effective specific heat capacity increases due to the decomposition heat released during this endothermic process. The effective thermal conductivity apparently decreases at this stage since significant thermal resistance results from the decomposed gases (shielding effects). The E-modulus of the composite material obviously decreases when glass transition occurs, and drops further at decomposition. As shown in Fig. 1, each property is determined by only one variable - temperature.

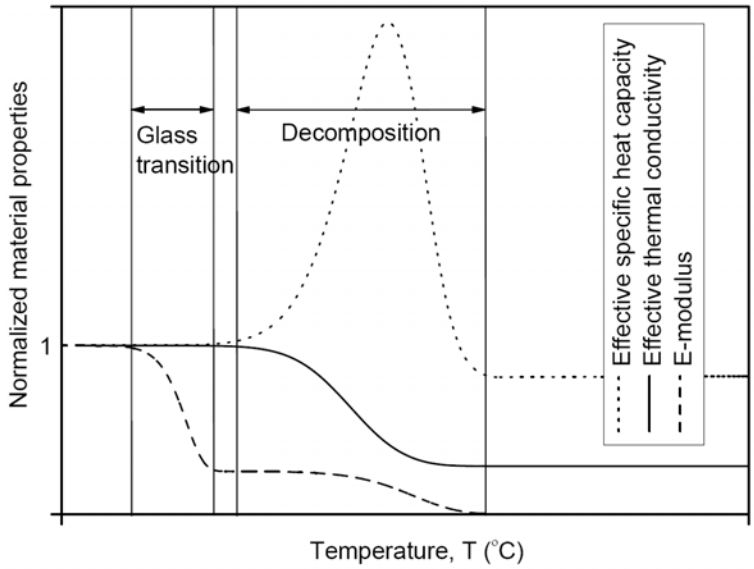

Fig. 1. Temperature-dependent effective specific heat capacity, thermal conductivity and E-modulus for composite materials

The changes in the effective thermophysical and thermomechanical properties are basically determined by the corresponding physical and chemical processes. These processes, being kinetic, are not just univariate functions of temperature. Therefore, and in contrast to true material properties (as used in [6]), effective properties are dependent not only on temperature, but also on time. This can be demonstrated by TGA (thermogravimetry analysis), DSC (differential scanning calorimetry), and DMA experiments at different heating rates, as demonstrated in this paper. It is shown that thermophysical and thermomechanical properties are not univariate functions of temperature, but also functions of time. The time-dependent effects can be incorporated into thermophysical and thermomechanical property models previously proposed by the authors in [23, 24].

2 EFFECTS OF DIFFERENT HEATING RATES ON MATERIAL PROPERTIES

2.1 Material description

In order to investigate the change in material properties at different heating rates, TGA, DSC, and DMA tests were conducted on pultruded glass fiber-reinforced polymer (GFRP) laminates (supplied by Fiberline A/S,

Denmark), which consisted of E-glass fibers embedded in a isophthalic polyester resin (containing low-profile but no fire retardant additives) [25]. Two different laminate thicknesses (3mm and 6mm) were investigated, as shown in Fig. 2, consisting of one roving layer in the middle and one mat layer on each side. The detailed fiber architecture and physical and mechanical properties at ambient temperature (fiber mass fraction, specific heat capacity, thermal conductivity and storage modulus) are reported in [26]. The test specimens were cut or ground from these laminates.

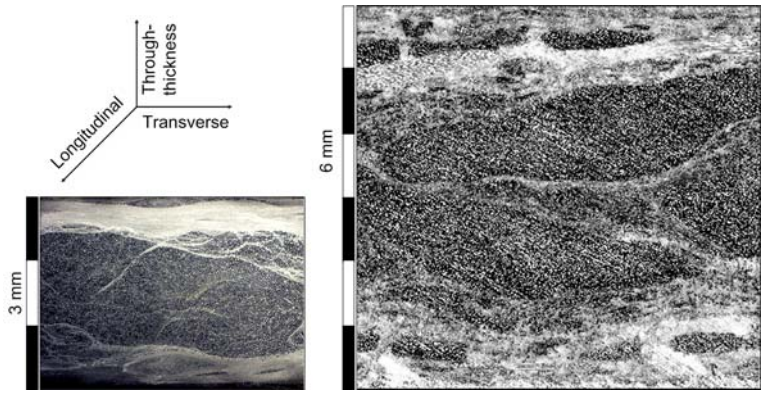

Fig. 2. Material architecture for pultruded 3-mm (left) and 6-mm (right) laminates obtained by microscopy

It should be noted that a generally adopted assumption in TGA, DSC, and DMA experiments is that the temperature in the experimental specimen is uniformly distributed and equal to the temperature measured by the sensor in the experimental devices. This assumption is justified for TGA and DSC because specimens are very small (approximately 20mg) and the defined temperature progression represents the temperature progression of the specimens. The temperature progression of DMA specimens, however, may not precisely correspond to the preset heating rate and be delayed because specimens are comparatively large (50-mm length, 3-mm thickness and 5-mm width for example).

2.2 Influence on mass transfer and decomposition

The decomposition process can be described using TGA. The specimens were obtained by grinding the 6-mm laminate into a powder using a rasp.

The powdery specimen was analyzed by a TGA Q500 from TA Instruments Inc. The tests were carried out at temperatures ranging from 25°C to 700°C. Four different heating rates, 2.5, 5.0, 10.0, and 20.0°C/min were used. The mass of the specimens was 6.0±0.3 mg for all runs. The resulting experimental curves of temperature-dependent mass fraction are shown in Fig. 3. The onset of decomposition temperature, $T_{d,onset}$, was determined as being the temperature at which 5% of the mass was lost [27], and T_d was determined as being the point when the mass decreased at the highest rate (based on the derivative of the curve). Both T_d and $T_{d,onset}$ increased with increasing heating rates, as shown in Table 1.

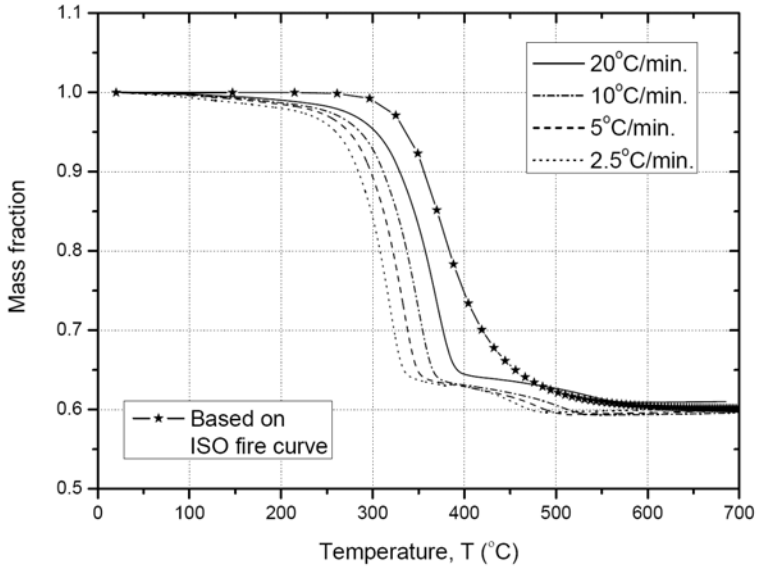

Fig. 3. Mass fraction for different thermal loading programs: curves at constant heating rates from TGA, and modeling curve based on ISO fire curve

Since, at the same temperature, the mass fraction was dependent on the heating rate, it was concluded that the decomposition reaction had progressed to different levels. Therefore, different conversion degrees of decomposition, α_d, were obtained at the same temperature. The conversion degree of decomposition can be calculated as follows:

$$\alpha_d = \frac{M_i - M}{M_i - M_e} \tag{1}$$

where M is instantaneous mass and M_i and M_e are the initial and final

masses respectively. The temperature-dependent α_d for different heating rates is shown in Fig. 4. When $T_{d,onset}$ is reached, α_d started to increase rapidly. A lower heating rate (corresponding to a longer heating time) resulted in a more noticeable decomposition at the same temperature. The discrepancy between different heating rates was small at the initial and final stages of decomposition, while it became more apparent around T_d. At 350°C for example, α_d = 43% was found for 20.0°C/min, while α_d = 91.6 % at 2.5°C/min.

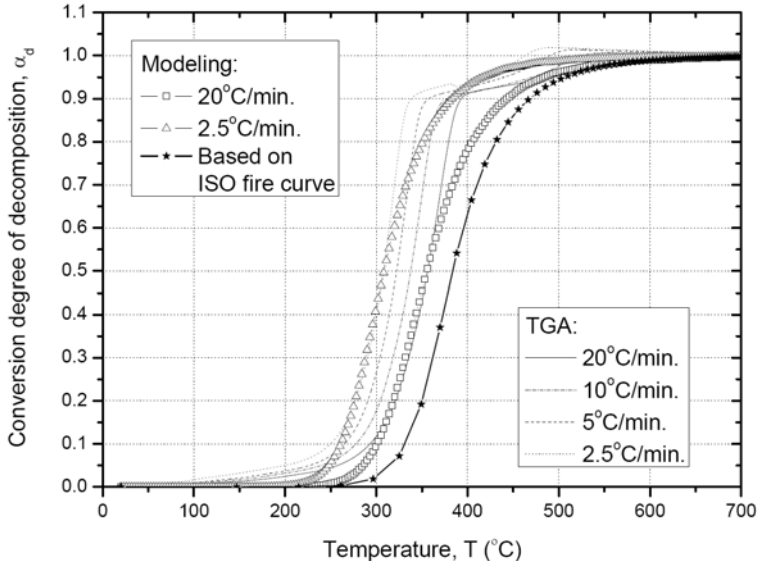

Fig. 4. Conversion degrees of decomposition for different thermal loading programs: curves at constant heating rates from TGA and modeling (only the curves at 2.5 and 20.0°C/min are shown for better viewing), and modeling curve based on ISO fire curve

Heating rate (°C/min)	$T_{g,onset}$ (°C)	T_g (°C)	$T_{d,onset}$ (°C)	T_d (°C)
2.5	108	151	260	321
5.0	112	156	274	337
10.0	117	161	287	353
20.0	-	-	304	371

Table 1. $T_{g,\,onset}$, T_g and $T_{d,\,onset}$, T_d based on DMA and TGA at different heating rates

2.3 Influence on effective specific heat capacity

The same powder ground from the 6-mm-thick laminate as used for TGA was used for the DSC tests. The specimens were tested using a DSC Q1000 analyzer from TA Instruments Inc. at temperatures ranging from 0°C to 300°C at two different heating rates (5.0 and 20.0°C/min). The resulting experimental curves for the two heating rates are shown in Fig. 5. Normalized values are used since the values obtained during the initial stage are often not very accurate and result in a shift of the whole curve. For each heating rate, the effective specific heat capacity was relatively stable before decomposition, with significant increases being caused by the decomposition, which is an endothermic process. Similar results were found in [5] for one heating rate over a wider temperature range however.

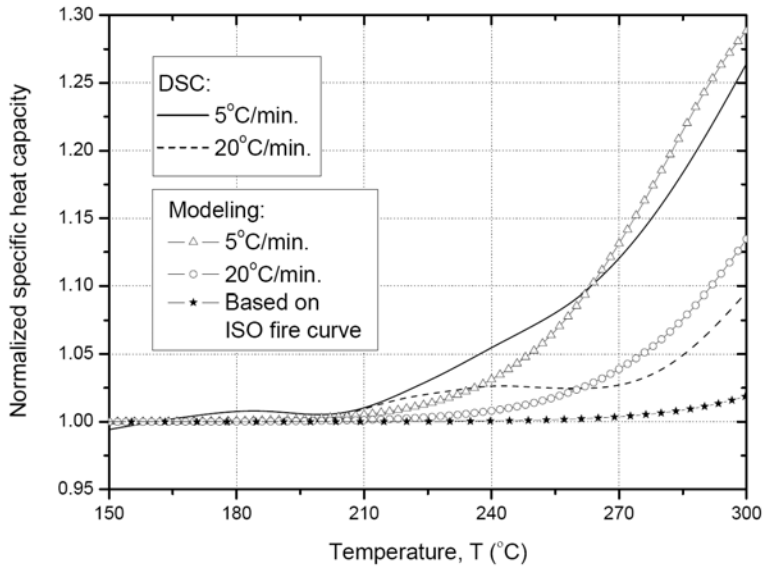

Fig. 5. Effective specific heat capacity for different thermal loading programs: curves at constant heating rates from DSC and modeling, and modeling curve based on ISO fire curve

Comparison of the two different heating rates in Fig. 5 shows that the effective specific heat capacity is not only temperature-dependent. At 300°C for example, the value at a heating rate of 20.0°C/min was 16% lower than at 5.0°C/min. A lower heating rate corresponds to a higher conversion degree of decomposition (see Fig. 4), and thus to a higher effective specific heat capacity during decomposition. Accordingly, in order to accu-

rately take into account the influence of effective specific heat capacity on the modeling of the thermal responses of composites, this time dependence, caused by different heating rates, must be considered.

2.4 Influence on mechanical properties

DMA tests were conducted on specimens 50 mm long × 5 mm wide × 3 mm thick. The specimens were cut from the 3-mm-thick laminates in the longitudinal direction (fiber direction). Cyclic dynamic loads were imposed on a dual cantilever set-up of a DMA 2980 Dynamic Mechanical Analyzer from TA Instruments Inc. The specimens were scanned from ambient temperature (20°C) to 250°C at three different heating rates (2.5, 5.0, 10.0°C/min) using the same dynamic oscillation frequency of 1 Hz. Each specimen was subjected to only one heating program to prevent post-curing effects.

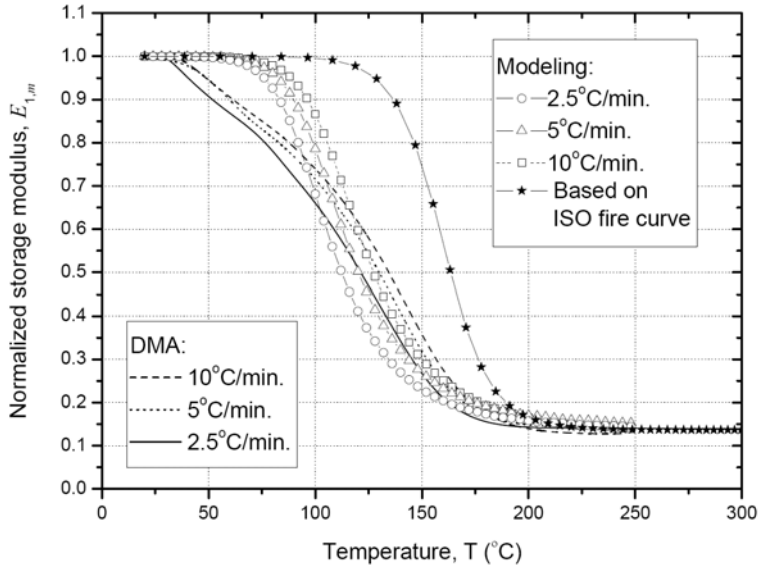

Fig. 6. Normalized storage curves for different thermal loading programs: curves at constant heating rates from DMA and modeling, and modeling curve based on ISO fire curve

The experimental storage modulus, normalized by the initial values to eliminate small discrepancies at the initial temperature, is shown in Fig. 6. During glass transition, the modulus exhibited different values for different heating rates at the same temperature. The discrepancy between different heating rates was relatively small during the initial and final stages,

but increased at the highest process rate (between 100°C and 150°C). A lower heating rate results in a lower value of storage modulus at the same temperature. At 125°C for example, the normalized value was 0.46 at 2.5°C/min in contrast to 0.58 at 10.0°C/min. Accordingly, at 125°C a noticeable modulus underestimation of approximately 26% resulted from the different heating rates.

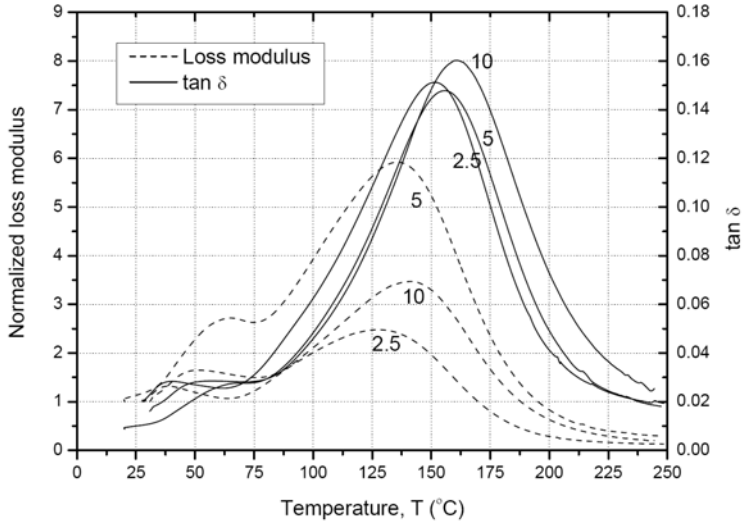

Fig. 7. Normalized loss modulus and tan δ curves at different heating rates from DMA (numbers denote heating rate)

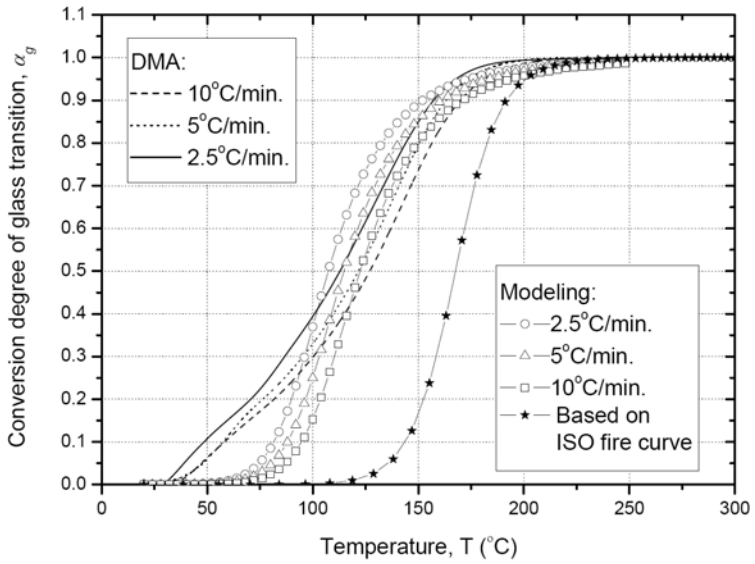

Fig. 8. Conversion degrees of glass transition for different thermal loading programs: curves at constant heating rates from DMA and modeling, and modeling curve based on ISO fire curve

The experimental loss modulus and tan δ curves are summarized in Fig.

7. The peaks of the curves show a right-shift with increasing heating rate. The resulting glass transition temperature, T_g, (determined by the peak point of tan δ) and $T_{g,onset}$ are summarized in Table 1 for different heating rates. Both values increased with increasing heating rate and are therefore time-dependent.

The conversion degree of glass transition, α_g, can be defined as:

$$\alpha_g = \frac{E_g - E}{E_g - E_r} \tag{2}$$

where E_g and E_r are the storage moduli of the material in the glassy and leathery states respectively and E is the instantaneous storage modulus before decomposition. Glass transition is thus considered as a process in accordance with statistical mechanics: an aggregation of a large population of molecules (or other functional units) changes continuously from one state to another (glassy to leathery).

The conversion degrees of glass transition resulting from different heating rates are summarized in Fig. 8. At the same temperature, a higher conversion degree of glass transition was reached at a lower heating rate. It may be concluded that different heating rates can have considerable effects on the mechanical properties of composites and thus on the calculated mechanical responses.

3 TIME-DEPENDENT MATERIAL PROPERTY MODELS

As shown above, composite material properties depend on heating rate and are therefore not only temperature- but also time-dependent. This is significant since, in reality, thermal loading processes are not normally characterized by a constant heating rate, as demonstrated by the ISO-834 fire curve for example:

$$T = T_0 + 345 \cdot \log(8t + 1) \tag{3}$$

where T_0 is the initial temperature and t the time in minutes. The time-dependent temperature curve and corresponding heating rate curve (obtained by derivation of Eq. (3) with respect to t) are shown in Fig. 9. During the first 30 minutes, the temperature is increased by 820°C, and the

heating rate varies from several thousand °C/min to 11 °C/min.

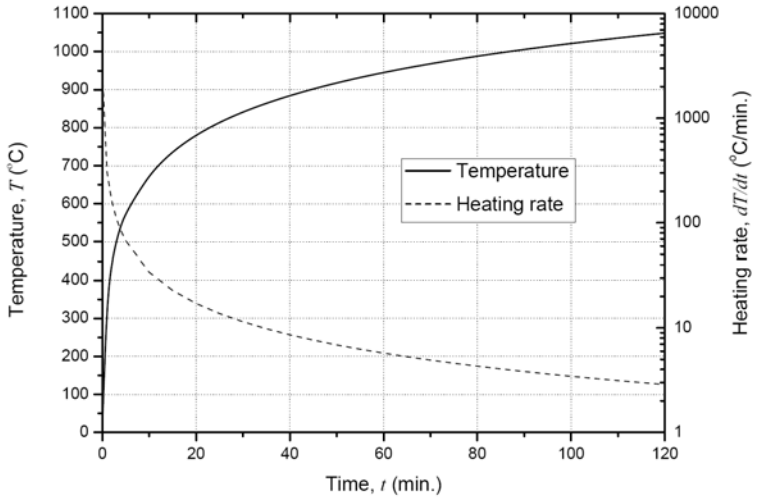

Fig. 9. ISO-834 time-temperature curve and derivation (heating rate)

Previous time-dependent material property models mainly focused on the decomposition process (and are therefore inapplicable for the degradation of thermomechanical properties during glass transition), or were developed as purely mathematical functions not linked to the related physical or chemical processes. Time-dependent thermophysical and thermomechanical property models based on the physical description of both glass transition and decomposition are proposed in the following, and compared with experimental results at different heating rates from the above section.

3.1 Time-dependent conversion degrees of glass transition and decomposition

In order to model the time-dependent physical and mechanical properties, related physical or chemical processes (mainly glass transition and decomposition) must be taken into account. Arrhenius kinetics, well accepted to describe the decomposition process, claim that in order for one material to be transformed into another (or from one state to another), a minimum amount of energy, the activation energy, E_A, is required. At a certain temperature, T, the fraction of molecules having a kinetic energy greater than E_A can be calculated from the Maxwell-Boltzmann distribution of statistical mechanics, and is proportional to $\exp(-E_A/RT)$. This concept is appli-

cable also for glass transition, if it is considered as a process (as stated before) during which a certain activation energy is required for the change in state of the molecules (or other functional units). Therefore, both processes can be described as follows (see [26, 27]):

For the glass transition process:

$$\frac{d\alpha_g}{dt} = A_g \cdot \exp\left(\frac{-E_{A,g}}{RT}\right) \cdot \left(1-\alpha_g\right)^{n_g} \tag{4}$$

For the decomposition process:

$$\frac{d\alpha_d}{dt} = A_d \cdot \exp\left(\frac{-E_{A,d}}{RT}\right) \cdot \left(1-\alpha_d\right)^{n_d} \tag{5}$$

where α_g and α_d are the conversion degrees, A_g and A_d the pre-exponential factors, $E_{A,g}$ and $E_{A,d}$ the activation energies, and n_g and n_d the reaction orders for glass transition and decomposition respectively. R is the universal gas constant (8.314 J/mol·K), T is the temperature, and t is time.

Eqs. (4) and (5) are differential equations with respect to time t that are able to take the effects of complex thermal loading (thermal loading at variable heating rates) into account. Since any thermal loading procedure is also a function of time, and based on a finite difference method, the temperature at each finite time step can be approximated as a constant: at a time step, j, with a constant heating rate β_i, Eqs. (4-5) can be converted to:

$$\frac{\Delta\alpha_{g,j}}{\Delta T_j} = \frac{A_g}{\beta_j} \cdot \exp\left(\frac{-E_{A,g}}{RT_j}\right) \cdot \left(1-\alpha_{g,j}\right)^{n_g} \tag{6}$$

$$\frac{\Delta\alpha_{d,j}}{\Delta T_j} = \frac{A_d}{\beta_j} \cdot \exp\left(\frac{-E_{A,d}}{RT_j}\right) \cdot \left(1-\alpha_{d,j}\right)^{n_d} \tag{7}$$

where $\Delta\alpha_{g,j}$ and $\Delta\alpha_{d,i}$ are the increments of conversion degrees and ΔT_j is the increment of temperature at one time step, j. T_j is the temperature and $\alpha_{g,j}$ and $\alpha_{d,j}$ are the conversion degrees at this time step, which can be approximated in the finite difference algorithm as:

$$\alpha_{g,j} = \alpha_{g,j-1} + \Delta\alpha_{g,j} \tag{8}$$

$$\alpha_{d,j} = \alpha_{d,j-1} + \Delta\alpha_{d,j} \tag{9}$$

The kinetic parameters used in Eqs. (6) and (7) were estimated on the

basis of the experimental results for conversion degrees from constant heating rates [26]. By incorporating these kinetic parameters into Eqs. (6) to (9), the time-dependent conversion degrees of glass transition and decomposition were obtained. The calculated conversion degrees of decomposition were compared with the experimental values for the different heating rates and good agreement was found, as shown in Fig. 4 [26]. The comparison of the conversion degrees of glass transition at different heating rates is shown in Fig. 8. The discrepancies between measured and modeled results may have resulted from the inaccurate identification of kinetic parameters [26] or the temperature progression, which was not precisely represented by the preset heating rate (due to a relatively large specimen size, see Section 2.1).

Based on the time-dependent models expressed by Eqs. (6-9), the conversion degrees for a realistic thermal loading process with variable heating rate can be calculated, as demonstrated for the ISO fire curve (see Fig. 9) in the following. The results are shown in Figs. 4 and 8 for decomposition and glass transition respectively. In Fig. 4, at a specified temperature, the conversion degree of decomposition based on the ISO fire curve is lower than that of any prescribed constant TGA heating rate (2.5 to 20.0°C/min) since the ISO heating rate is greater than 25°C/min in the TGA temperature range up to 700°C, see Fig. 9. Accordingly, at the same temperature level, the mass fraction of the material subjected to the ISO fire curve should be greater than that of the material subjected to the prescribed constant heating rates, as confirmed in Fig. 3. The discrepancies between conversion degrees of glass transition from prescribed constant heating rates and the ISO curve were greater than for decomposition, as shown in Fig. 8. Glass transition occurred within a lower temperature range (less than 250°C, see Fig. 8), whereas the ISO heating rate was very high (greater than 300°C/min, see Fig. 9).

3.2 Time-dependent function for effective specific heat capacity

The true specific heat capacity is related to the quantity of energy required

to raise the temperature of a specified mass of material to a specified temperature level. For composites, this property can be estimated using the mixture approach. For the effective specific heat capacity, the energy change during decomposition (i.e. decomposition heat) must be taken into account. The rate of energy absorbed for decomposition is determined by the reaction rate, i.e. the decomposition rate given by Eq. (5). The resulting time-dependent function for the effective specific heat capacity, $C_{p,j}$, at time step j, can be expressed as [23]:

$$C_{p,j} = C_{p,b} \cdot \left(1 - \alpha_{d,j}\right) + C_{p,a} \cdot \frac{M_e \cdot \alpha_{d,j}}{M_i} + \frac{\Delta\alpha_{d,j}}{\Delta T_j} \cdot C_d \tag{10}$$

where $C_{p,b}$ and $C_{p,a}$ are the specific heat capacities of the virgin and decomposed char material. M_i and M_e are the initial mass of virgin material and final mass of char material, and C_d is the total decomposition heat. Since α_d was obtained as a time-dependent function applicable for different heating rates, the effective specific heat capacity is also a time-dependent function.

The normalized effective heat capacity was calculated for different heating rates based on Eq. (10) and, as shown in Fig. 5, the modeling results corresponded reasonably well to the DSC data. Some differences were found between modeling and experiments, especially at the initial stage, which may result from inaccurate measurements of DSC or an increase of the true specific heat capacity of the material.

Modeling results from complex thermal loading, as represented by the ISO fire curve, are also shown in Fig. 5. The increase of the calculated effective specific heat capacity is very slow compared to that resulting from the prescribed constant heating rates because the conversion degree of decomposition also increased very slowly compared to the value resulting from the prescribed constant heating rates (see Fig. 4) in this temperature range (less than 300°C).

3.3 Time-dependent function for effective thermal conductivity

Since the change in effective thermal conductivity is almost insignificant

before decomposition (see Fig. 1), the composite material at any specific temperature can be considered as being composed of two states: the virgin (un-decomposed) material and the decomposed char material. The two states are connected in series in the heat flow direction (through-thickness direction). The effective thermal conductivity, $k_{c,j}$, at time step j can then be obtained as follows [23]:

$$\frac{1}{k_{c,j}} = \frac{V_{b,j}}{k_b} + \frac{V_{a,j}}{k_a} \tag{11}$$

$$V_{b,j} = 1 - \alpha_{d,j} \tag{12}$$

$$V_{a,j} = \alpha_{d,j} \tag{13}$$

where k_b and k_a are the true thermal conductivities of the virgin and decomposed material respectively. V_b and V_a are the volume fractions of virgin and decomposed material calculated from the conversion degree of decomposition according to Eqs. (12) and (13). The effective thermal conductivity (from Eq. (11)) is a time-dependent function and is particularly sensitive to different heating rates within the 200°C to 460°C temperature range, as shown in Fig. 10. The lower heating rate resulted in a lower value of effective thermal conductivity (at the same temperature) because of the higher conversion degree of decomposition at the lower heating rate (see Fig. 4) and, correspondingly, an increased shielding effect. For all heating rates, an increase was observed above 420°C because of the increase of V_a (thermal conductivity of decomposed material, mainly glass fibers) in this temperature range.

Figure 10 also shows the resulting effective thermal conductivity for the complex thermal loading according to the ISO fire curve. The curve lies above those of the prescribed constant heating rates (2.5-20.0°C/min) due to the higher ISO heating rates in this temperature range (200-460°C, see Fig. 9). Hot disk experiments were conducted on the same material up to 700°C in [26]. Although it was not possible to control the heating rate in the hot disk oven, Fig. 10 shows that the experimental curve follows a similar tendency to that of the modeling curves. The ISO-based curve is the closest to the experimental curve as a result of the comparatively high rate

observed during the heating process in the hot disk oven.

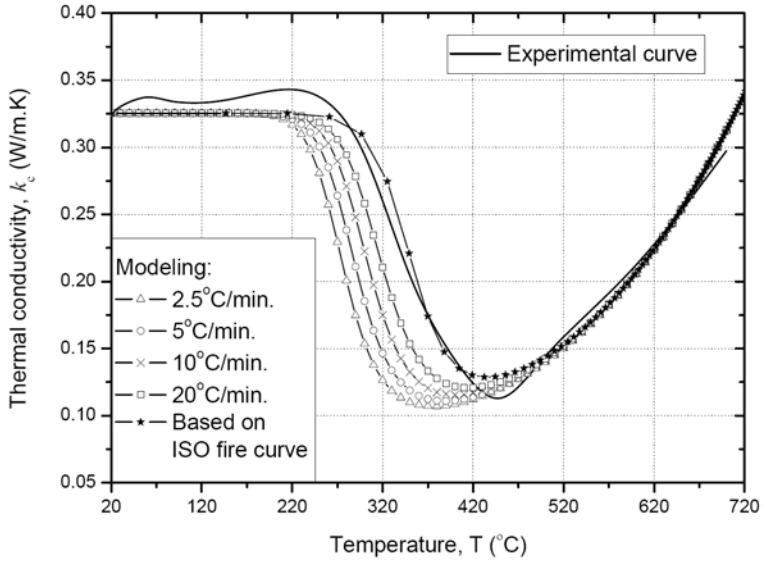

Fig. 10. Effective thermal conductivity for different thermal loading programs: modeling curves for constant heating rates and ISO fire curve, and hot disk experimental curve

3.4 Time-dependent function for storage modulus

Composite materials exposed to elevated and high temperatures undergo glass transition and decomposition, as modeled in Section 3.1. The time-dependent storage modulus can be estimated when the proportion of the material in each different state at any particular time is known. Assuming that the volume of the initial material is unit at the initial temperature (i.e. initial time), the volume fraction, V, of the material in different states at a specified time step, j, can be expressed as follows [24]:

$$V_{g,j} = 1 - \alpha_{g,j} \tag{14}$$

$$V_{r,j} = \alpha_{g,j} - \alpha_{g,j} \cdot \alpha_{d,j} \tag{15}$$

$$V_{d,j} = \alpha_{g,j} \cdot \alpha_{d,j} \tag{16}$$

where subscripts g, r and d denote the glassy, rubbery, and decomposed states respectively. Since the storage modulus of the material in the decomposed state is zero, the time-dependent normalized storage modulus, $E_{1,j}$, at a specified time step, t_j, can be expressed as:

$$E_{1,j} = V_{g,j} + \frac{E_r}{E_g} \cdot V_{r,j} \tag{17}$$

The normalized storage modulus was calculated at different heating rates and compared reasonably well with the experimental DMA data, as shown in Fig. 6. At the same temperature, smaller values were obtained for lower heating rates due to a higher conversion degree of glass transition (see Fig. 8). This effect was more pronounced for the ISO fire curve, which shows a very high heating rate in the glass transition temperature range (see Fig. 9). A smaller decrease in modulus was found, therefore, during glass transition, as shown in Fig. 6. This result demonstrates that stiffness degradation, described by one single variable temperature-function to simulate fire effects, may be overestimated. The degradation process is obviously influenced by the heating rate.

4 CONCLUSIONS

Time and temperature dependence of the thermophysical and thermomechanical properties of FRP composite materials were investigated based on TGA, DSC and DMA, conducted at different heating rates. The following conclusions could be drawn:

1. The changes in the thermophysical and thermomechanical properties of composite materials under elevated and high temperatures are the result of complex physical and chemical processes and are thus not simply univariate functions of temperature, but also depend on time. The experimental results demonstrated that, depending on the heating rate (and therefore time), significant differences in thermophysical and thermomechanical properties can be obtained at the same temperature.
2. The related physical and chemical changes can be modeled by kinetic theory that and the effects of different heating rates on the effective material properties can be taken into account. Modeling and experimental results compared well.
3. Based on a finite difference method, complex thermal loading programs can be taken into account in the models, e.g. the ISO fire curve, which

shows very high heating rates at the beginning, i.e. in the temperature range of the glass transition and decomposition of most resins used in FRP composites. An underestimation of the E-modulus, mass fraction and effective thermal conductivity and an overestimation of effective specific heating capacity may result if lower constant heating rates are used in the modeling.

4. The temperature- and time-dependent material property models can easily be incorporated into classic heat transfer and beam theory in order to calculate thermal and mechanical responses.

ACKNOWLEDGEMENT

The authors wish to acknowledge the financial support provided by the Swiss National Science Foundation (Grant No. 200020-117592/1), and Fiberline, Denmark for supplying the experimental materials.

REFERENCES

1. Griffis CA, Masumra RA, Chang CI. Thermal response of graphite epoxy composite subjected to rapid heating. *Journal of Composite Materials* 1981, 15: 427-442.

2. Griffis CA, Nemes JA, Stonesfiser FR, Chang CI. Degradation in strength of laminated composites subjected to intense heating and mechanical loading. *Journal of Composite Materials* 1986, 20(3): 216-235.

3. Fanucci JP. Thermal response of radiantly heated kevlar and graphite/epoxy composites. *Journal of Composite Materials* 1987, 21(2): 129-139.

4. Bisby LA, Green MF, Kodur VKR. Modeling the behavior of fiber reinforced polymer-confined concrete columns exposed to fire. *Journal of Composite Construction* 2005, 9(1): 15-24.

5. Lattimer, BY, Ouellette J. Properties of composite materials for thermal analysis involving fires. *Composite Part A* 2006, 37: 1068-1081.

6. Henderson JB, Wiebelt JA, Tant MR. A model for the thermal response of polymer composite materials with experimental verification. *Journal of*

Composite Materials 1985, 19(6): 579-595.

7. Henderson JB, Verma YP, Tant MR, Moore GR. Measurement of the thermal conductivity of polymer composites to high temperature using the line source techniques. *Polymer Composites* 1983, 4(4): 219-224.

8. Henderson JB, Wiebelt JA, Tant MR, Moore GR. A method for the determination of the specific heat and heat of decomposition of composite materials. *Thermochimica Acta* 1982, 57: 161-171.

9. Sullivan RM, Salamon NJ. A finite element method for the thermochemical decomposition of polymeric materials - I. Theory. *International Journal of Engineering Science* 1992, 30(4): 431-441.

10. Gibson AG, Wu YS, Chandler HW, Wilcox JAD. A model for the thermal performance of thick composites laminates in hydrocarbon fires. *Revue de l'Institute du Pétrol* 1995, 50(1): 69-74.

11. Looyeh MRE, Rados K, Bettess P. Thermomechanical responses of sandwich panels to fire. *Finite Elements in Analysis and Design* 2001, 37(11): 913-927.

12. Dao M, and Asaro R. A study on the failure prediction and design criteria for fiber composites under fire degradation. *Composites Part A* 1999, 30(2): 123-131.

13. Gibson, A.G., Wu, Y-S., Evans, J.T. and Mouritz, A.P. Laminate theory analysis of composites under load in fire. *Journal of Composite Materials* 2006, 40(7):639-658.

14. Mahieux CA, Reifsnider KL. Property Modelling across transition temperatures in polymers: a robust stiffness-temperature model. *Polymer* 2001, 42: 3281-3291.

15. Springer GS. Model for predicting the mechanical properties of composites at elevated temperatures. *Journal of Reinforced Plastics and Composites* 1984, 3(1): 85-95.

16. Dutta PK and Hui D. Creep rupture of a GFRP composite at elevated temperatures. *Computers and Structures* 2000, 76(1):153-161.

17. Crews LK and McManus HL. Modeling the Effects of High Temperature Exposure on the Mechanical Material Properties of Graphite/Epoxy.

Proceedings of the 13th Annual Technical Conference on Composite Materials, 1998.

18. Chamis CC and Hopkins DA. Thermoviscoplastic nonlinear constitutive relationships for structural analysis of high temperature metal matrix composites. NASA TM 87291, 1985.

19. Ashby MF and Jones DRH. Engineering materials 2: an introduction to microstructures, processing, and design. Oxford, Pergamon Press, 1997.

20. Williams ML, Landel RF, and Ferry JD. The temperature dependence of relaxation mechanisms in amorphous polymers and other glass-forming liquids. *Journal of the American Chemical Society* 1955, 77: 3701-3707.

21. Sullivan JL. Creep and physical aging of composites. *Composites science and technology* 1990, 39: 207-232.

22. Mahieux CA. A systematic stiffness-temperature model for polymers and applications to the prediction of composite behavior. Ph.D. Dissertation, Virginia Polytechnic Institute and State University, 1999.

23. Bai Y, Vallée T, Keller T. Modeling of thermo-physical properties for FRP composites under elevated and high temperatures. *Composites Science and Technology* 2007, 67: 3098-3109.

24. Bai Y, Keller T, Vallée T. Modeling of stiffness for FRP composites under elevated and high temperatures. *Composites Science and Technology* 2008, 68: 3099-3106.

25. Fiberline Composites. Fiberline design manual, Kolding, Denmark, 2003.

26. Bai Y, Post NL, Lesko JJ, Keller T. Experimental investigations on temperature-dependent thermo-physical and mechanical properties of pultruded GFRP composites. *Thermochimica Acta* 2008, 469: 28-35.

27. Fox DM, Gilman JW, De Long HC, Trulove PC. TGA decomposition kinetics of 1-butyl-2,3-dimethylimidazolium tetrafluoroborate and the thermal effects of contaminants. *The Journal of Chemical Thermodynamics* 2005, 37(9): 900-905.

2.6 Modeling of thermal responses

Summary

The thermophysical property models for composite materials under elevated and high temperatures were developed in Section 2.1. Integrating these material property models into the heat transfer governing equation, a one-dimensional model was proposed in this paper to predict the thermal responses of FRP composites up to a high temperature range.

An implicit finite differential method was used to solve the governing equation. The progressive change in thermophysical properties – including decomposition degree, mass transfer, specific heat capacity, and thermal conductivity – was determined using the proposed model, and obtained in both the time and space domains. Several sets of boundary conditions were considered in the model, including prescribed temperature or heat flow, heat convection and/or radiation. The results obtained using different boundary conditions were compared to experimental data obtained from structural fire endurance experiments on cellular FRP panels with and without liquid cooling. For each scenario, the calculated and measured time-dependent temperature progressions at different material depths were in good agreement.

Reference detail

This paper was published in Composites Science and Technology 2008, volume 68, pages 47-56, entitled

"Modeling of thermal responses for FRP composites under elevated and high temperatures" by Yu Bai, Till Vallée and Thomas Keller.

Part of the content of this paper was presented at the first Asia-Pacific Conference on FRP in Structures (APFIS) 12-14 December 2007, Hong Kong, entitled

"Modeling of thermophysical properties and thermal responses for FRP composites in fire" by Yu Bai, Till Vallée and Thomas Keller, presented by Yu Bai.

MODELING OF THERMAL RESPONSES FOR FRP COMPOSITES UNDER ELEVATED AND HIGH TEMPERATURES

Yu Bai, Vallée Till and Thomas Keller

Composite Construction Laboratory CCLab, Ecole Polytechnique Fédérale de Lausanne (EPFL), BP 2225, Station 16, CH-1015 Lausanne, Switzerland.

ABSTRACT:

Based on temperature-dependent thermophysical property models developed previously, a one-dimensional model was proposed to predict the thermal responses of FRP composites in time and space domain, up to high temperatures. An implicit finite differential method was used to solve the governing equation. The progressive change in thermophysical properties – including decomposition degree, mass transfer, specific heat capacity, and thermal conductivity – was determined using the proposed model. Several sets of boundary conditions were considered in the model, including prescribed temperature or heat flow, heat convection and/or radiation. The results obtained using different boundary conditions were compared to experimental data of structural fire endurance experiments on cellular FRP panels with and without liquid-cooling. For each scenario, calculated and measured time-dependent temperature progressions at different material depths were in good agreement.

KEYWORDS:

Polymer-matrix composites; modeling; pultrusion; thermal responses

1 INTRODUCTION

The increased use of fiber-reinforced polymer (FRP) composites in major load-bearing structures brings many challenges to material scientists and structural engineers. One of these challenges is the understanding and prediction of the behavior of FRP composites under elevated (20-200°C) and high (>200°C) temperatures. For FRP composite materials, it has been reported that the material state and properties of a polymer composite remain stable below the glass transition temperature, T_g, of its resin. However, when the temperature reaches T_g, significant changes in the material state and properties occur. When the temperature of the resin approaches the decomposition temperature, T_d, it starts decomposing and produces various other phases (smoke, liquids, incombustible and combustible gases). In structural design, both structural and non-structural members must provide enough fire ignition prevention and fire resistance to prevent fire and smoke from spreading and structural collapse. For example, in practice, a 90 (60) minute fire design time (F90 (F60)) is required for residential buildings with three or more floors, and a fire load of more than 1000 (500) MJ/m^2 [1]. Significant research has been conducted to improve the fire performance of FRP composites materials under elevated and high temperatures, including the use of flame-retardant intumescent coating [2, 3] or a liquid cooling system [4, 5]. First, however, in order to understand the structural behavior on the level of systems, the thermal response of FRP composites under elevated and high temperature must be understood and predicted.

Griffis et al. in 1981 [6] developed a model to predict the thermal response of graphite epoxy composites. The one-dimensional model used a finite difference method to solve the energy equation subjected to uniform and constant heat flux boundary conditions. Stepped temperature-dependent effective thermal properties were used in this model. The resulting temperature profiles agreed well with measured values for graphite epoxy plates. The same thermophysical property models was later used by Chen et al. in 1981 [7], Griffis et al. in 1986 [8], Chang in 1986 [9],

and Milke and Vizzini in 1991 [10]. McManus and Coyne in 1982 [11] developed a thermochemical model coupled with a mechanical model in a numerical computer code named the TRAP model. Assembling similar thermophysical property models as in [8], validation of the thermochemical portion of the TRAP was performed on carbon and aramid fiber-reinforced epoxy composites by Fanucci in 1987 [12]. The agreement between predicted and experimental results was reasonably good.

Different temperature-dependent thermophysical property models were introduced by Henderson et al. in 1985 [13, 14]. The concept of an effective material property was once again discussed, though not used, because the various phenomena were explicitly treated in the final governing equations. The temperature-dependent properties were obtained by curve fitting based on the experimental data of the original and charred materials at different temperatures [15, 16]. These material properties were assembled into a thermchemical model, and a finite difference method was used to solve the governing equations. Comparison of predicted and experimental results obtained by heating a glass fiber-reinforced phenolic composite by radiant electrical heaters revealed only small discrepancies.

In 1984 Springer [17] presented a thermochemical model in conjunction with a thermomechanical model. The temperature-dependent thermophysical property models were similar to the one used in Henderson's work. Validation was performed by comparing predictions to the experimental data on graphite epoxy composites from Pering [18]. McManus and Springer later presented an updated model in 1992 [19, 20]. The approach was also similar to Henderson's work, though it was specifically developed for carbon fiber-reinforced phenolic composites. In 1992 Sullivan and Salamon [21, 22] introduced a further thermochemical model in which the simulated phenomena were basically the same as in the McManus and Springer models, and the material property models were similar to that of Henderson's work. A model for the thermomechanical behavior of glass epoxy composites was developed by Dimitrienko in 1997 [23] in which a similar heat capacity model was used as in Henderson's work, while a more com-

plicate thermal conductivity model was employed.

A model similar to Henderson's work was used in the thermochemical model introduced by Gibson et al. in 1995. In this work, the thermochemical model was coupled with a thermomechanical model [24]. Further development of this model can be followed in publications up to 2004 by the collaborative efforts of Gibson et al. [25-28], Davies et al. [29], Dodds et al. [30], Looyeh et al [31, 32], Lua and O'Brian [33], and Samatnta et al [34]. Over that period, validation was performed on glass fiber-reinforced polyester, vinylester, and phenolic laminates where the agreement between predicted and measured temperatures was good.

Different temperature-dependent thermophysical property models were developed and introduced by the authors in [35]. Furthermore, experimental comparative studies were conducted on cellular panels of glass fiber-reinforced polyester composites [4, 5]. The property models were assembled in the final governing equation presented in the present paper. The thermal responses obtained from the mathematical models will be compared to experimental results.

2 DESCRIPTION OF THE EXPERIMENTAL WORK

Structural fire endurance experiments were performed on cellular GFRP slabs (DuraSpan® 766 slab system from Martin Marietta Composites) [4, 5]. The E-glass fibers that were used had a softening temperature, T_s, of approximately 830 °C, while the glass transition temperature, T_g, and decomposition temperature, T_d, of the non-fire retarded isophthalic polyester resin were found to be 117 °C and 300 °C, respectively. Detailed material parameters and fiber fractions are given in Table 1.

Mass Transfer Model		Ref.
Activition energy, E_A	77878 J/mol	[35]
Pre-exponential factor, A	316990 Min^{-1}	[35]
Reaction order, n	1.08	[35]
Gas constant, R	8.314 J/mol·K	[35]
Density of material before decomposition, ρ_b	1870 kg/m^3	[4, 5]
Density of material after decomposition, ρ_a	1141 kg/m^3	[4, 5]
Initial fiber mass fraction, m_f	0.61	[4, 5]
Initial resin mass fraction, m_m	0.39	[4, 5]
Specific Heat Capacity		
Initial specific heat capacity of fiber, $C_{p,f}$	840 J/kg·K	[35]
Initial specific heat capacity of resin, $C_{p,m}$	1686 J/kg·K	[35]
Specific heat capacity of material before decomposition, $C_{p,b}$	1170 J/kg·K	[37]
Specific heat capacity of material after decomposition, $C_{p,a}$	Eq. (34)	[35]
Decompostion heat, C_d	234 kJ/kg	[13]
Thermal Conductivity		
Initial thermal conductivity of fiber, k_f	1.1 W/m·K	[31, 34]
Initial thermal conductivity of resin, k_m	0.2 W/m·K	[31, 34]
Thermal conductivity of gases, k_g	0.05 W/m·K	[38]
Thermal conductivity of material before decomposition, k_b	0.35 W/m·K	[37]
Thermal conductivity of material after decomposition, k_a	0.1 W/m·K	[37]
Initial fiber volume fraction, V_f	0.52	[4, 5]
Initial resin volume fraction, V_m	0.48	[4, 5]

Table 1. Material properties and parameters for specimens SLC01, SLC02 and SLC03

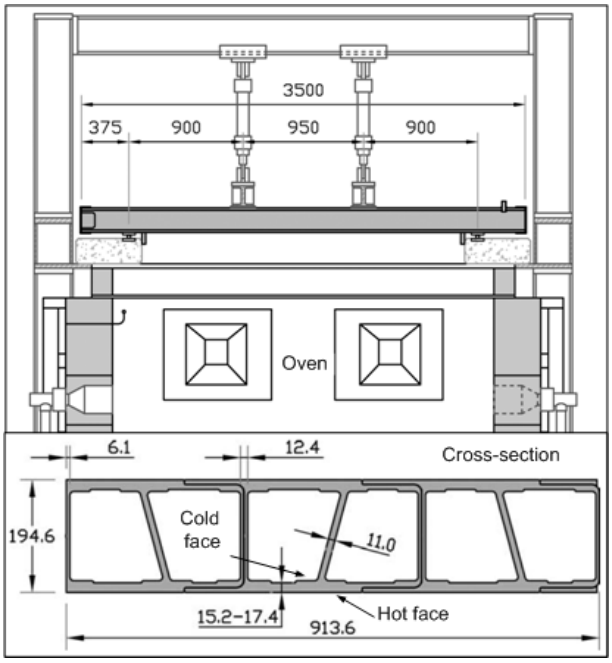

Fig. 1. Experimental specimen and setup

The temperature progressions at different face sheet depths and temperature profiles at different times throughout the experiments were measured with thermocouples. The experiments on the liquid-cooled specimens were stopped after 90 minutes (SLC01) and 120 minutes (SLC02) without structural failure, whereas the non-cooled specimen failed after 57 minutes in the compressed upper face sheet. More details about the experimental set-up and results can be found in [5].

3 MODELING ASSUMPTIONS

3.1 Decoupling of different actions

When exposed to high temperatures and fire, FRP composites experience complex changes in material states involving the interaction of thermal, chemical, physical, mechanical, and structural phenomena. Modeling and predicting all the coupled responses of FRP structures is therefore a complex task. By treating independently only one or two of these phenomena in each model, however, the task becomes more reasonable. The thermal phenomena (heat transfer, temperature distribution, etc.) are mainly determined by thermophysical or chemical properties of the material and thermal boundary conditions, while the mechanical and structural phe-

nomena are dependent on the mechanical properties of the material (which are greatly influenced by temperature) and mechanical boundary conditions. Consequently, the effects of physical and chemical phenomena can be considered in the modeling of thermophysical or thermochemical properties. By assembling these material property models, the thermal phenomena can be described based on the governing equation of heat transfer. Finally the mechanical and structural responses can be obtained from the temperature-dependent mechanical properties and the structural model.

3.2 Chemical reactions

Complex reactions are involved in the material state changes of FRP materials under elevated and high temperature. For simplification, it is convenient to describe this process in four stages [36]:

1. Heating: Energy is transferred to the material up to T_d (decomposition temperature of resin);
2. Decomposition: The chemical bonds of the polymer are progressively broken and decomposition products are formed (residual char, various liquids, smoke, incombustible and combustible gases);
3. Ignition: Ignition occurs when a sufficient concentration and proper form of the fuel source mixes with an oxidizing agent at the proper temperature;
4. Combustion: The exothermic reaction between the combustible gases and the oxygen.

In order for combustion to begin, the fuel source must meet with an adequate supply of an oxidizing agent (normally oxygen in air) and an adequate energy source to heat the fuel to its ignition temperature. Furthermore, the fuel and the oxidizing agent must be present in the right state (only gases combust) and concentrations. Adequate energy must also be available to break the covalent bonds within the compound and release the free radicals that eventually react with the oxidizing agent. More in-depth discussion of the combustion of polymers can be found in [36].

In this paper, only the first two stages – heating and decomposition – are considered. Moreover, one single Arrhenius equation is assumed in the decomposition process with one set of kinetic parameters [35].

3.3 Effects of pyrolysis gases and decomposition heat

The thermal response of a material is largely influenced by the pyrolysis gases and decomposition heat. One way to consider these effects is to introduce them into the final governing equations of the thermal response model, as was done in the models proposed by e.g. Henderson [13, 16] and Gibson [24, 25]. Another possibility is to consider these effects in the "effective" thermophysical properties, such as in the models in [7-12].

The specific heat capacity of a mixture (composite material) is determined by the properties of the different phases and their mass fraction, while the effective specific heat capacity includes the energy needed for additional chemical or physical changes. Consequently, the decomposition heat can be considered a part of the effective specific heat capacity [35]. The effects due to pyrolysis gases on the specific heat capacity are negligible, since most gases can escape from the material, and thus the mass fraction of the remaining gases is very small.

The thermal conductivity of a mixture is determined by the properties of the different phases and their volume fraction [35]. Consequently, the effect due to pyrolysis gases on the thermal conductivity is prominent, since the volume of residual gases is nearly equal to the volume of decomposed resin, and gases always have a very small thermal conductivity (for example 0.03 W/m·K for dry air). Considering that the volume of decomposed resin (i.e. the volume of remaining gases) can be obtained through the decomposition model, the effects of pyrolysis gases also can be considered in the effective thermal conductivity model.

In this paper, effective material properties are used. Furthermore, instead of linearly interpolating discontinuous curves as was done in previous work [7-12], continuous functions dependent on temperature (obtained in [35]) are used. The prediction of material properties from these

models are further verified in this paper.

3.4 One dimensional heat transfer

When subjected to a uniformly distributed fire on one side, the heat transfer through the thickness direction of a plate is dominant as compared to that in the in-plane directions. Three main zones can be defined through the thickness of an FRP laminate during decomposition [37]:

1. A char and gas zone, where most of the resin material has burnt away ($T > T_d$)
2. A pyrolysis zone, in which resin is in decomposition ($T_g < T < T_d$)
3. A virgin material zone, which represents that part of the material that remains unchanged ($T < T_g$)

The load resistance capacity and post-fire performance of the laminate are largely dependent on the size of the virgin zone, which is mainly determined by the temperature profile in the through-thickness direction. Consequently, the problem of describing the temperature change in the experimentally investigated GFRP slabs can be simplified to a one dimensional problem (in the face sheet thickness direction).

4. THERMAL RESPONSE MODEL

4.1 Material property models

The temperature dependent thermophysical properties – including mass (density), thermal conductivity and specific heat capacity – developed in [35] are summarized in Eq. (1) to Eq. (4):

$$\rho_c = (1-\alpha)\cdot\rho_b + \alpha\cdot\rho_a \tag{1}$$

$$\frac{1}{k_c} = \frac{(1-\alpha)}{k_b} + \frac{\alpha}{k_a} \tag{2}$$

$$C_{p,c} = C_{p,b}\cdot f_b + C_{p,a}\cdot f_a + \frac{d\alpha}{dT}\cdot C_d \tag{3}$$

$$\frac{d\alpha}{dt} = A\exp\left(\frac{-E_A}{RT}\right)(1-\alpha)^n \tag{4}$$

where ρ_c, k_c, and $C_{p,c}$ are the density, thermal conductivity and specific heat capacity for the FRP composite, respectively, over the whole temperature range, E_A is the activation energy for the decomposition reaction, A is the pre-exponential factor, n is the reaction order, T denotes temperature and t denotes time, and R is the gas constant (8.314 J/mol·K). Subscripts b and a denote the material before and after decomposition, α is the temperature dependent decomposition degree as determined by the decomposition model in Eq. (4). The factors k_b and k_a can be estimated using a series model, $C_{p,a}$ and $C_{p,b}$ can be estimated by the Einstein model and mixture approach, and mass fractions f_a and f_b can be estimated using the decomposition model. C_d is the decomposition heat, i.e. the energy change during decomposition. The rate of energy absorbed for decomposition is determined by the reaction rate, i.e. the decomposition rate, which is obtained by the decomposition model (Eq. 4). Detailed information for obtaining these parameters can be found in [35].

4.2 Governing equation for heat transfer

Assuming one-dimensional heat transfer, the following governing Eq. (5) is obtained by considering that the net rate of heat flow should be equal to the rate of internal energy increase and the heat flow is given by the Fourier law related to temperature gradients:

$$\frac{\partial}{\partial x}\left(k_c \frac{\partial T}{\partial x}\right) = C_{p,c}\rho \frac{\partial T}{\partial t} \tag{5}$$

Substituting the temperature and time dependent material properties (Eqs. 1-4) into Eq. (5), a non-linear partial differential equation is obtained. A finite difference method can be used to solve this equation considering given boundary conditions. Temperature responses can then be calculated along the time and space axis.

4.3 Boundary conditions

Different kinds of boundary conditions can be considered in the thermal response model: prescribed temperature or heat flow boundary conditions

as expressed in Eqs. (6) and (7), respectively [38]:

$$T(x,t)\big|_{x=0,L} = T(t) \tag{6}$$

$$-k_c \frac{\partial T(x,t)}{\partial x}\bigg|_{x=0,L} = q(t) \tag{7}$$

where x denotes the spatial coordinates in one dimension, $x = 0$ and L define the space coordinate at the boundaries, *T(t)* and *q(t)* describe the specified time-dependent temperature and heat flux at the boundaries. By discretizing the space and time domains, Eqs. (6) and (7) are transformed to Eqs. (8) to (11) in finite difference forms:

$$T_{0,j} = T(j) \tag{8}$$

or

$$T_{N,j} = T'(j) \tag{9}$$

$$-k_c \frac{T_{1,j} - T_{0,j}}{\Delta x} = q(j) \tag{10}$$

or

$$k_c \frac{T_{N-1,j} - T_{N,j}}{\Delta x} = q'(j) \tag{11}$$

where 0 and N denote the first and the last element number, i.e. the element at boundaries, j is the time step, and Δx denotes the length of one element. *T(j), T'(j)* and *q(j), q'(j)* denote the temperature and heat flux at time step, j, at two different boundaries, respectively.

Compared with the boundary conditions for prescribed temperature and heat flow, heat convection and radiation are more general cases. The equation of heat convection is given by Newton's law of cooling [38]:

$$-k_c \frac{\partial T(x,t)}{\partial x}\bigg|_{x=0,L} = h\left(T_\infty - T\big|_{x=0,L}\right) \tag{12}$$

In finite difference form:

$$-k_c \frac{T_{1,j} - T_{0,j}}{\Delta x} + h \cdot T_{0,j} = h \cdot T_\infty \text{ (heat flow into material)} \tag{13}$$

or

$$k_c \frac{T_{N,j} - T_{N-1,j}}{\Delta x} + h' \cdot T_{N,j} = h' \cdot T'_\infty \text{ (heat flow out of material)} \tag{14}$$

where h and h' denote the convection coefficients at the two different boundaries, respectively, T_∞ and T'_∞ are the ambient temperatures at the two different boundaries.

Heat transfer through radiation is calculated using the Stefan-Boltzmann law, where the net heat transfer, q_r, is expressed according to Eq. (15):

$$q_r = \varepsilon_r \cdot \sigma_r \cdot \left(T_\infty^4 - T^4 \big|_{x=0,L} \right) \tag{15}$$

In finite difference form:

$$-k_c \frac{T_{1,j} - T_{0,j}}{\Delta x} + \varepsilon_r \cdot \sigma_r \cdot T^4{}_{0,j} = \varepsilon_r \cdot \sigma_r \cdot T_\infty^4 \tag{16}$$

or

$$k_c \frac{T_{N,j} - T_{N-1,j}}{\Delta x} + \varepsilon_r \cdot \sigma_r \cdot T^4{}_{N,j} = \varepsilon_r \cdot \sigma_r \cdot T'^4{}_\infty \tag{17}$$

where ε_r is the emissivity of the solid surface, σ_r is the Stefan-Boltzmann constant (5.67×10^{-8} W·m^{-2}K^{-4}) [38].

In the case of heat transferred through both radiation and convection, Eqs. (18) and (19) are obtained by combining Eqs. 13-14 and 16-17:

$$-k_c \frac{T_{1,j} - T_{0,j}}{\Delta x} + h \cdot T_{0,j} + \varepsilon_r \cdot \sigma_r \cdot T_{0,j}^4 = h \cdot T_\infty + \varepsilon_r \cdot \sigma_r \cdot T_\infty^4 \tag{18}$$

$$k_c \frac{T_{N,j} - T_{N-1,j}}{\Delta x} + h' \cdot T_{N,j} + \varepsilon_r \cdot \sigma_r \cdot T_{N,j}^4 = h' \cdot T'_\infty + \varepsilon_r \cdot \sigma_r \cdot T'^4_\infty \tag{19}$$

The above equations will be used to model the boundary conditions of the experiments (liquid cooled and non-cooled boundaries) in Section 5.

4.4 Solution of governing equation

The governing equation, Eq. (5), is a partial differential equation with non-linear, time and temperature-dependent material properties, and general boundary conditions. One approach to solving this equation is to discretisize the space and time domain through transformation into finite difference form, and to solve the subsequent system of algebraic equations for the temperature field. An explicit method and implicit method can be formulated in finite difference methods. For the first method, the tempera-

ture at node i in time step j+1 can be determined explicitly by the previous time step, j. The algebraic system is easy to solve since each single equation can be solved directly without coupling to the other equations, however, the explicit approach does not always lead to a stable solution, and consequently it was not used here. The implicit algorithm, where the spatial derivative is evaluated at the current time step, is stable, but requires simultaneous solution of the spatial node equations. Hence, for a space domain with n spatial nodes, n simultaneous equations are necessary and need to be solved at the same time.

For each spatial node, i, and at each time step, j, the governing equation can be expressed in the finite difference form using the implicit method as shown in Eq. (20):

$$\rho_{i,j-1} C_{p,(i,j-1)} \frac{T_{i,j} - T_{i,j-1}}{\Delta t} = k_{c,(i,j-1)} \frac{T_{i-1,j} + T_{i+1,j} - 2T_{i,j}}{(\Delta x^2)} + \frac{k_{c,(i,j-1)} - k_{c,(i-1,j-1)}}{\Delta x} \cdot \frac{T_{i,j} - T_{i-1,j}}{\Delta x} \tag{20}$$

For n spatial nodes, n coupled algebraic equations are obtained (the first one (i=1) and the last one (i=N) are determined by boundary conditions). Based on the material properties at the previous time step j-1 ($\rho_{i,j-1}$, $C_{p,(i,j-1)}$ and $k_{c,(i,j-1)}$), the temperature profile at time step j can be calculated by solving these n coupled algebraic equations.

The temperature-dependent material properties are expressed in the finite difference form as shown in Eqs. (21) to (25):

$$\alpha_{i,j} = \alpha_{i,j-1} + \Delta t \cdot A \exp\left(\frac{-E_A}{R T_{i,j-1}}\right)\left(1 - \alpha_{i,j-1}\right)^n \tag{21}$$

$$\rho_{i,j} = \left(1 - \alpha_{i,j}\right) \cdot \rho_b + \alpha_{i,j} \cdot \rho_a \tag{22}$$

$$\frac{1}{k_{c,(i,j)}} = \frac{\left(1 - \alpha_{i,j}\right)}{k_b} + \frac{\alpha_{i,j}}{k_a} \tag{23}$$

$$f_{i,j} = \frac{M_i \cdot \left(1 - \alpha_{i,j}\right)}{M_i \cdot \left(1 - \alpha_{i,j}\right) + M_f \cdot \alpha_{i,j}} \tag{24}$$

$$C_{i,j} = C_{p,b} \cdot f_{i,j} + C_{p,a} \cdot \left(1 - f_{i,j}\right) + \frac{\alpha_{i,j} - \alpha_{i,j-1}}{T_{i,j} - T_{i,j-1}} \cdot C_d \tag{25}$$

Substituting the temperature at the time step *j* into Eq. (21) to (25), the material properties are obtained and then serve as the input for the next time step *j+1*.

5 APPLICATION AND DISCUSSION

5.1 Basic model

The thermal response model developed in Section 4 was applied to the experimental specimens SLC02 (liquid-cooled) and SLC03 (non-cooled) to determine the progression of temperature and thermophysical properties in the lower face sheet up to two hours for SLC02 (end of experiment) and 60 minutes for SLC03 (failure after 57 minutes). For calculation, the average 16.3 mm thick lower face sheet of the experimental specimen was discretisized into 17 elements in the thickness direction (thus the length of one element was almost 1 mm) and into 60 or 120 time steps (thus the duration of one time step was 1 minute). At the two sides of the lower face sheet, the boundary conditions of the heat transfer were defined for the hot face (exposed to fire) and the cold face (exposed to water cooling or air environment), as shown in Fig.1. The initial values (before starting of the burners) of all the parameters used in the above equations were taken as the value at room temperature (20°C) and are summarized in Table 1.

5.2 Non-cooled specimen SLC03

In the non-cooled specimen, the heat was transferred by both radiation and convection from the furnace air environment to the hot face. The boundary conditions according to Eq. (18) can therefore be used for this case. The temperature of the oven was controlled by a computer, which read the furnace temperature from internal thermocouples and adjusted the intensity of the burners to follow the ISO-834 temperature curve as close as possible. Accordingly, T_∞ in Eq. (18) was assumed as the temperature of the ISO curve, as defined by Eq. (26) ([39], t in minutes):

$$T_\infty - T_0 = 345 \cdot \log(8t + 1) \tag{26}$$

The convection coefficient, h, for the hot face was taken from Eurocode 1, Part 1.2 [40] for real building fires as $h = 25$ W/m²·K.

The cold face of the specimens was exposed to ambient air in the open cells of the specimens. Equation (19) was used to model the heat transferred through radiation and convection between the cold face and room environment, assuming T'_∞ as room temperature (20°C) for the cold face. The temperature-dependent convection coefficient, h', for the cold face was determined according to Eq. (27), based on hydromechanics [41]:

$$h' = 0.14 \cdot k_g \left(P_r \cdot \frac{g \cdot \beta}{\upsilon} \left(T_{sur} - T'_\infty \right) \right)^{1/3} \tag{27}$$

where k_g is the thermal conductivity of air (0.03 W/m·K), g is the acceleration due to gravity (9.81 m/s²), β is the volumetric coefficient of thermal expansion of air (3.43×10^{-3} K^{-1}), υ is the kinematic viscosity of air (1.57×10^{-5} m²/s), T_{sur} is the temperature of the outer surface (cold face), T_∞ is the ambient temperature (room temperature), P_r is the Prandtl number defined by hydromechanics, which is 0.722 in the present case [41]. The temperature-dependent emissivity, ε_r, was assumed to vary linearly from 0.75 to 0.95 in the temperature range of 20°C to 1000°C [41].

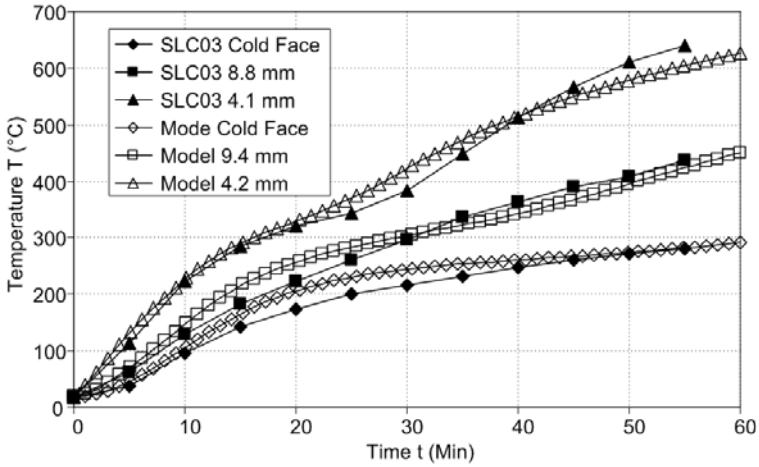

Fig. 2. Time-dependent temperature of non-cooled specimen SLC03 and results from model (distances in legend indicate depth from hot face)

A comparison of the temperature progression at different depths between experimental and computed values is shown in Fig. 2. The slightly different depths between model and experiment resulted from the discreti-

sized depth in the model. The temperature is well predicted, even after 60 min of heating and at the locations near the hot face. Figure 3 shows the comparison of temperature profiles at different times. The good correspondence between experimental results and model also indicates that the boundary conditions described by Eqs. (18) and (19) and the convection coefficients were well estimated.

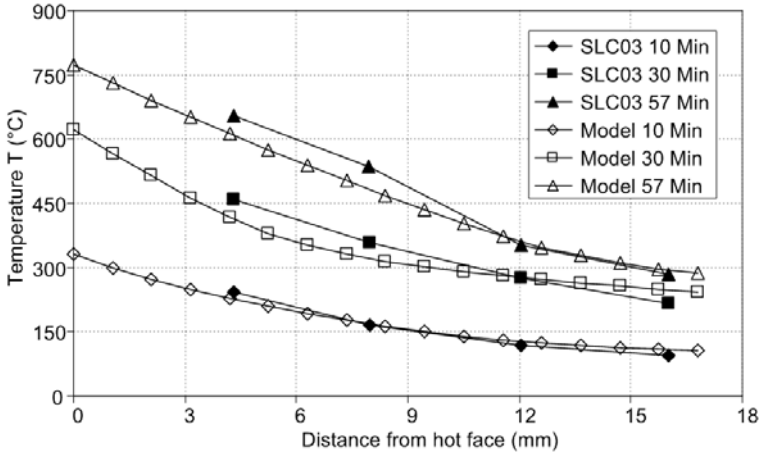

Fig. 3. Temperature profiles of non-cooled specimen SLC03 and results from model

The temperature field shown in Fig. 4 illustrates how the temperature increases with heating time and distance from the cold face. After having been subjected to the ISO fire curve up to 60 min, the temperature at almost all locations lay above 300 °C; even at the cold face this temperature point was also nearly reached. Thus, decomposition probably had already started at the cold face, considering that T_d is about 300 °C. This could be further verified by the decomposition degree plot in Fig. 5, which shows that the decomposition degree was 24.8% at the cold face. The progressive changes in material properties resulting from the model are illustrated in Figs. 6 to 8, for density, thermal conductivity, and specific heat capacity. The decrease in density due to decomposition of resin, shown in Fig 6, and the corresponding decomposition degree of 100% in Fig. 5, indicate that the hot face was fully decomposed after almost 17 minutes. At this time, the thermal conductivity, shown in Fig. 7, dropped to 0.1 W/m·K, the value for the thermal conductivity after decomposition (k_a) (see Table 1). Since

decomposition also occurred at the cold face, the density and thermal conductivity decreased, as shown in Figs. 6 and 7. Figure 8 illustrates the time (or temperature) dependent effective specific heat capacity. The contribution of the decomposition heat to the specific heat capacity is marked by the peak in the plot. Again, this plot indicates that the decomposition at the cold face had already started.

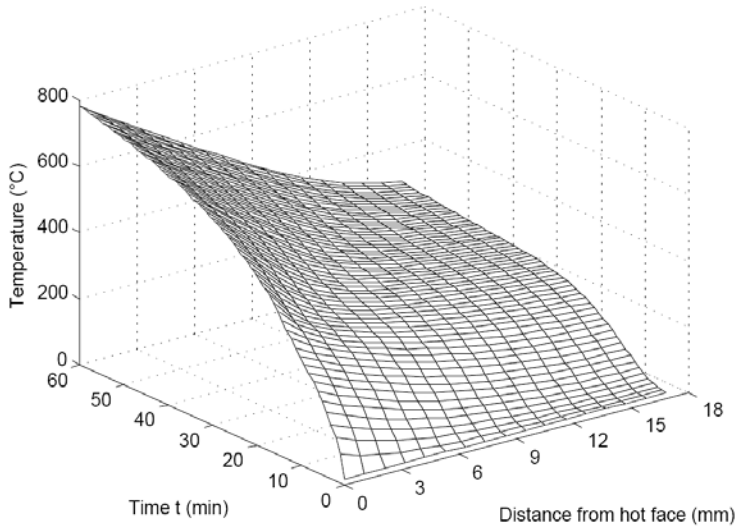

Fig. 4. Temperature field of non-cooled specimen SLC03

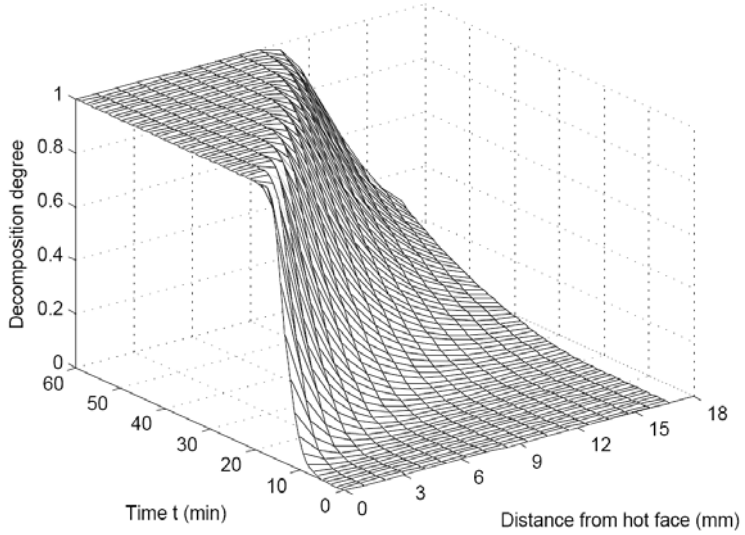

Fig. 5. Decomposition degree of non-cooled specimen SLC03

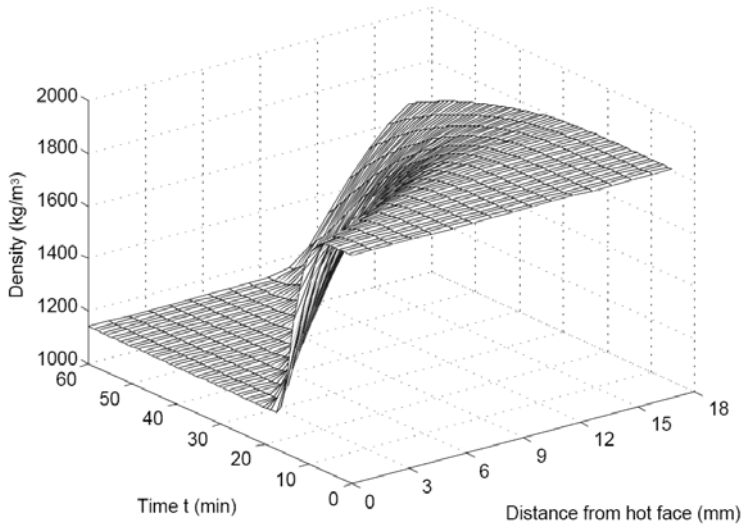

Fig. 6. Density of non-cooled specimen SLC03

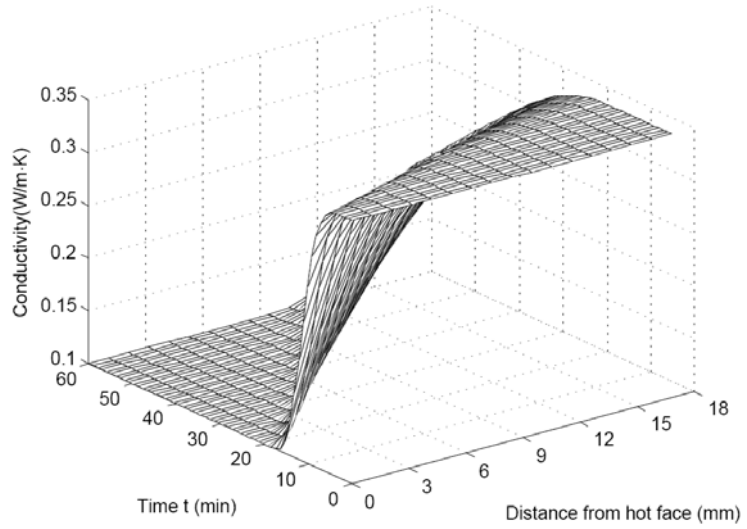

Fig. 7. Effective thermal conductivity of non-cooled specimen SLC03

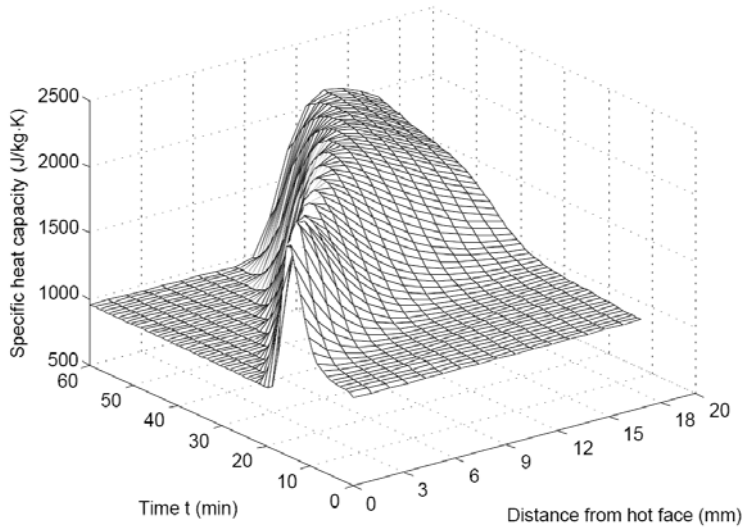

Fig. 8. Effective specific heat capacity of non-cooled specimen SLC03

5.3 Liquid-cooled specimen SLC02

For the liquid-cooled specimen, the boundary condition on the hot face was the same as for SLC03. At the cold face, water was continuously supplied through a calibrated and certified digital flow rate meter before entering the specimens. In this case, convection was the dominant mechanism of heat transfer process, so that Eq. (14) was used for the boundary condition. The value of $h' = 230$ W/m²·K was discussed and determined in [41] based on hydromechanics, which directly served as input for this model. The same emissivity of the heat radiation as that assumed for specimen SLC03 was taken.

The computed temperature field is shown Fig. 9 and again the heating curves at different depths are plotted along the time axis. The time dependent temperature curve at the hot face developed similarly to the non-cooled specimen due to the same thermal loading (boundary condition). However, due to the liquid-cooled boundary condition on the cold face, the temperature gradients were much steeper and the temperature at the cold face remained below 60°C. From the comparison of measured and computed through-thickness temperatures at different time steps a good agreement was found, as illustrated in Fig. 10. The only exception was the 4.1 mm curve above 80 minutes, however, it is thought that the offset of this curve at this time is more likely linked to a measurement problem than to a significant change in the element behavior. Figure 11 shows the comparison of the temperature profiles through the thickness. Again, measured and computed curves compare well. In the curves at 60 min and 120 min (both experiment and model), a change in the slope is seen at distances of about 6-8 mm from the hot face. At those times and distances, the temperatures reached the decomposition temperature of around 300°C. Towards the hot face, decomposed gases reduced the thermal conductivity and a steeper slope of the gradients resulted. On the other hand, due to the liquid-cooling effect, the temperatures towards the cold face remained below 300°C and the observed flattening resulted due to the higher thermal conductivity. This conclusion is further confirmed by the decomposi-

tion degree plot in Fig. 12, where almost half of the depth (from 8mm to the cold face) exhibited no decomposition. As a result, density and thermal conductivity almost showed no change in this region, as shown in Figs. 13 and 14 respectively. While the region near the hot face fully decomposed (see Fig. 12), a sharp decrease of density and thermal conductivity occurred (see Figs. 13 and 14). Figure 15 shows the effective specific heat capacity plot. The locations of the rises in the field due to the decomposition heat are in agreement with the locations of the sharp changes in the plots in Figs. 12-14.

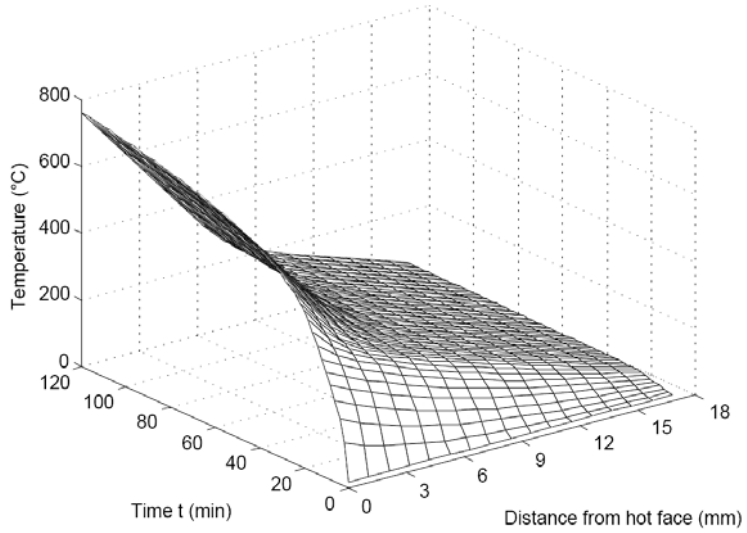

Fig. 9. Temperature field of liquid-cooled specimen SLC02

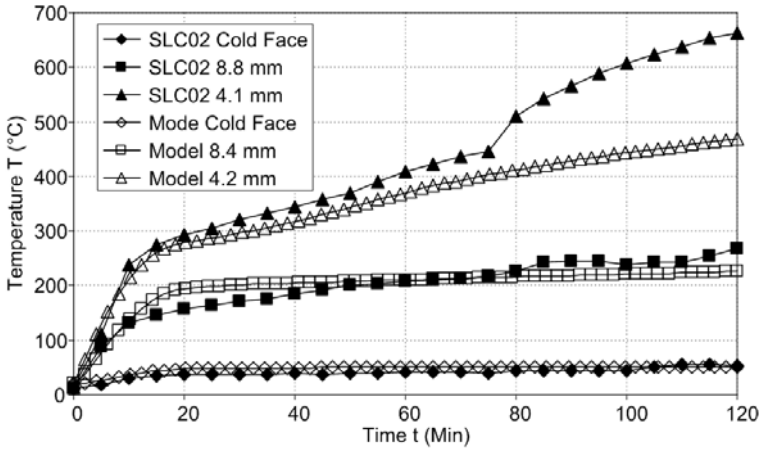

Fig. 10. Time-dependent temperature of liquid-cooled specimen SLC02 and results from model (distances in legend indicate depth from hot face)

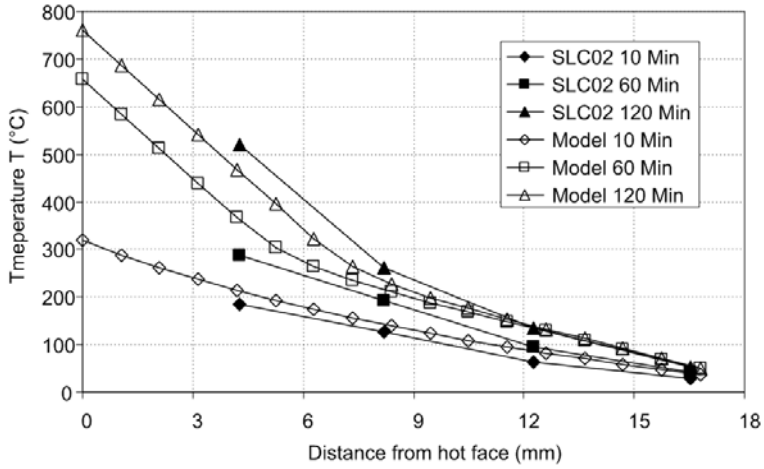

Fig. 11. Temperature profiles of liquid-cooled specimen SLC02 and results from model

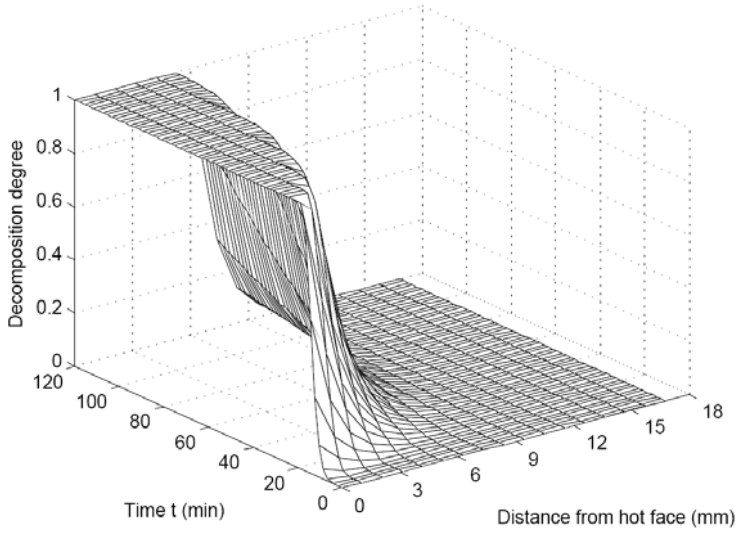

Fig. 12. Decomposition degree of liquid-cooled specimen SLC02

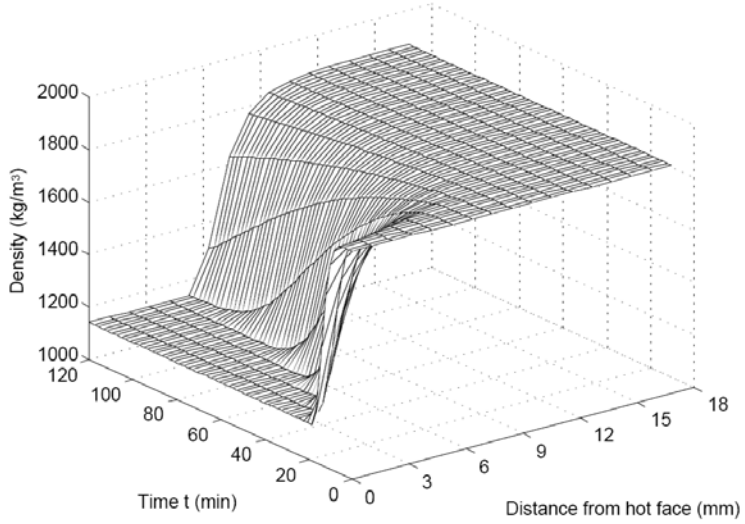

Fig. 13. Density of liquid-cooled specimen SLC02

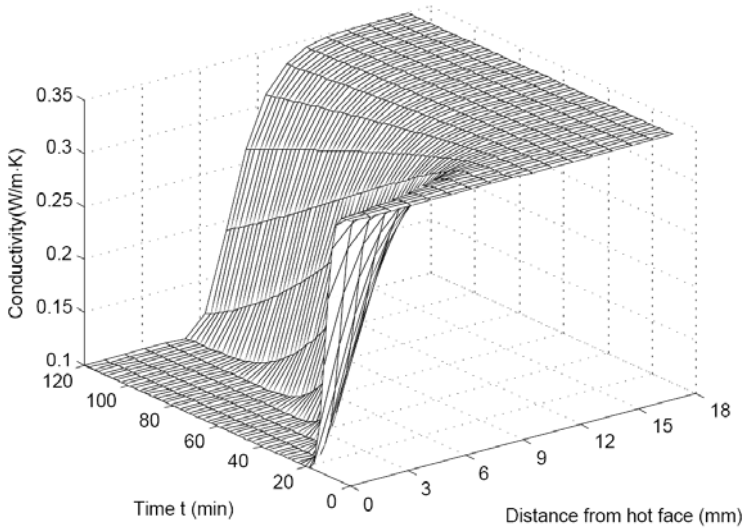

Fig. 14. Effective thermal conductivity of liquid-cooled specimen SLC02

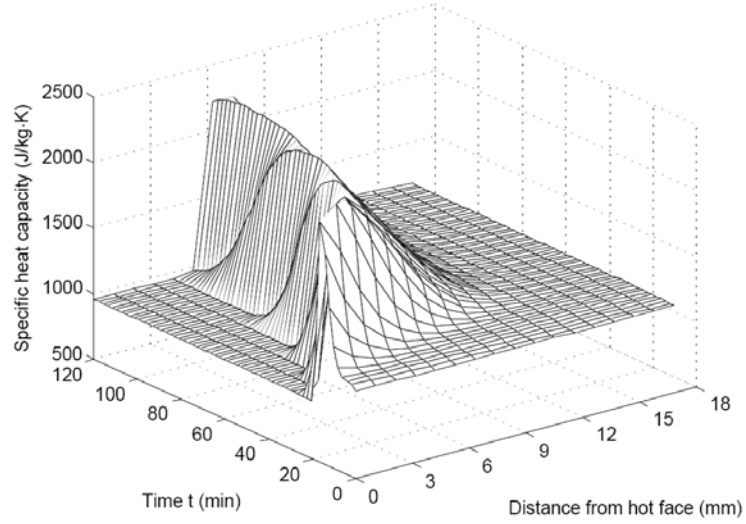

Fig. 15. Effective specific heat capacity of liquid-cooled specimen SLC02

6 CONCLUSIONS

A one-dimensional thermal response model was developed to predict the temperature of FRP structural elements subjected to fire. Different experimental scenarios were conducted on cellular GFRP slabs with different boundary conditions, in which the heating time lasted up to 60, 90 and 120 minutes, following the ISO-834 fire curve. The results from the experimental scenarios were compared to the results from the models including the time-dependent temperature progression at different depths and temperature profiles at different time steps. A good agreement was found and

the following conclusions were drawn:

1. The one-dimensional thermal response model can be used to predict the temperature responses of FRP composites in both time and space domain.
2. Complex boundary conditions can be considered in this model, including prescribed temperature or heat flow, as well as heat convection and/or radiation.
3. The numerical results are stable, since an implicit finite difference method was used to solve the governing differential equation.
4. The temperature-dependent thermophysical properties including decomposition degree, density, thermal conductivity and specific heat capacity can be obtained in space and time domain using this model.
5. Complex processes such as endothermic decomposition, mass loss, and delamination effects can be described based on effective material properties over the whole time and space domain.

Although the experimental verification was based on polyester resin reinforced with E-glass fiber, this model can be further applied in other kinds of composite materials, if the necessary material parameters are determined.

ACKNOWLEDGEMENT

The authors would like to acknowledge the support of the Swiss National Science Foundation (Grant No. 200020-109679/1).

REFERENCES

1. SIA 183. SN 520 183 - La protection contre l'incendie dans les construction. Swiss Society of Engineers and Architects, Zurich.
2. Hörold S. Phosphorus flame retardants in thermoset resins. *Polymer Degradation and Stability* 1999, 64: 427-431.
3. Porter D, Metcalfe E, Thomas MJK. Nanocomposite fire retardants – A review. *Fire and Materials* 2000, 24: 45-52.
4. Keller T, Zhou A, Tracy C, Hugi E, Schnewlin P. Experimental study on the concept of liquid cooling for improving fire resistance of FRP struc-

tures for construction. *Composites Part A* 2005, 36(11): 1569-1580.

5. Keller T, Tracy C, Hugi E. Fire endurance of loaded and liquid-cooled GFRP slabs for construction. *Composites Part A* 2006, 37(7): 1055-1067.

6. Griffis CA, Masumra RA, Chang CI. Thermal response of graphite epoxy composite subjected to rapid heating. *Journal of Composite Materials* 1981, 15: 427-442.

7. Chen JK, Sun CT, Chang CI. Failure analysis of a graphite/epoxy laminate subjected to combined thermal and mechanical loading. *Journal of Composite Materials* 1985, 19(5): 216-235.

8. Griffis CA, Nemes JA, Stonesfiser FR, Chang CI. Degradation in strength of laminated composites subjected to intense heating and mechanical loading. *Journal of Composite Materials* 1986, 20(3): 216-235.

9. Chang CI. Thermal effects on polymer composite structures. *Theoretical and Applied Fracture Mechanic*s 1986, 6(2): 113-120.

10. Milke JA, Vizzini AJ. Thermal response of fire exposed composites. *Journal of Composites Technology and Research* 1991, 13(3): 145-151.

11. McManus LN, Coyne DC. TRAP4-A digital computer program for calculating the response of mechanically and thermally loaded aircraft structures to the thermal radiation of a nuclear explosion or high energy laser. TM-141, 1982, Kaman Avidyne Technical Memorandum.

12. Fanucci JP. Thermal response of radiantly heated kevlar and graphite/epoxy composites. *Journal of Composite Materials* 1987, 21(2): 129-139.

13. Henderson JB, Wiebelt JA, Tant MR. A model for the thermal response of polymer composite materials with experimental verification. *Journal of Composite Materials* 1985, 19(6): 579-595.

14. Henderson JB, Wiecek TE. A mathematical model to predict the thermal response of decomposing, expanding polymer composites. *Journal of Composite Materials* 1987, 21(4): 373-393.

15. Henderson JB, Verma YP, Tant MR, Moore GR. Measurement of the thermal conductivity of polymer composites to high temperature using the line source techniques. *Polymer Composites* 1983, 4(4): 219-224.

16. Henderson JB, Wiebelt JA, Tant MR, Moore GR. A method for the determination of the specific heat and heat of decomposition of composite materials. *Thermochimica Acta* 1982, 57: 161-171.

17. Springer GS. Model for predicting the mechanical properties of composites at elevated temperatures. *Journal of Reinforced Plastics and Composites* 1984, 3(1): 85-95.

18. Pering GA, Farrell PV, Springer GS. Degradation of tensile and shear properties of composites exposed to fire or high temperatures. *Journal of Composite Materials* 1980, 14: 54-68.

19. McManus LN, Springer GS. High temperature thermo-mechanical behavior of carbon-phenolic and carbon-carbon composites, I. *Journal of Composite Materials* 1992, 26(2): 206-229.

20. McManus LN, Springer GS. High temperature thermo-mechanical behavior of carbon-phenolic and carbon-carbon composites, II. Results. *Journal of Composite Materials* 1992, 26(2): 230-251.

21. Sullivan RM, Salamon NJ. A finite element method for the thermochemical decomposition of polymeric materials: I. Theory. *International Journal of Engineering Science* 1992, 30(4): 431-441.

22. Sullivan RM, Salamon NJ. A finite element method for the thermochemical decomposition of polymeric materials: II. Carbon Phenolic Laminates. *International Journal of Engineering Science* 1992, 30(7): 939-951.

23. Dimitrienko YI. Thermo-mechanical behavior of composite materials and structures under high temperatures: 1. Materials. *Composites Part A* 1997, 28(5): 453-461.

24. Gibson AG, Wu YS, Chandler HW, Wilcox JAD. A model for the thermal performance of thick composites laminates in hydrocarbon fires. *Revue de l'Institute du Pétrol* 1995, 50(1): 69-74.

25. Gibson AG, Wright PNH, Wu YS, Mouritz AP, Mathys Z and Gardiner CPG. Models for the residual mechanical properties of polymer composites after fire. *Plastics, Rubber and Composites* 2003, 32(2): 81-90.

26. Gibson AG, Wright PNH, Wu YS, Mouritz AP, Mathys Z and Gardiner CPG. Integrity of polymer composites during and after fire. *Journal of*

Composite Materials 2004, 38(15): 1283-1308.

27. Gibson AG, Wu YS, Evans JT and Mouritz AP. Laminate theory analysis of composites under load in fire. *Journal of Composite Materials* 2006, 40(7): 639-658.

28. Gibson AG, Wright PNH, Wu YS, Mouritz AP, Mathys Z, Gardiner CP. Fire integrity of polymer composites using the two layer model. Proc. of the Int. SAMPE Symposium. Long Beach 2004.

29. Davies JM, Dewhurst DW. The fire performance of GRE pipes in empty and dry, stagnant water filled, and flowing water filled conditions. Proc. of the Int. Conf. on Composites in Fire, Newcastle upon Tyne 1999, 69-84.

30. Dodds N, Gibson AG, Dewhurst D, Davies JM. Fire behaviour of composite laminates. *Composites Part A* 2000, 31(7): 689-702.

31. Looyeh MRE, Bettess P. A finite element model for the fire-performance of GRP panels including variable thermal properties. *Finite Elements in Analysis and Design* 1998, 30(4): 313-324.

32. Looyeh MRE, Rados K, Bettess P. Thermomechanical responses of sandwich panels to fire. *Finite Elements in Analysis and Design* 2001, 37(11): 913-927.

33. Lua J, O'Brien J. Fire simulation of woven fabric composites with temperatures and mass dependent thermal-mechanical properties. 3rd Int. Conf. on Composites in Fire. Newcastle upon Tyne 2003.

34. Samanta A, Looyeh MRE, Jihan S, McConnachie J. Thermo-mechanical assessment of polymer composites subjected to fire. Engineering and Physical Science Research Council & the Robert Gordon University, 2004, Aberdeen, UK.

35. Bai Y, Vallée T, Keller T. Modeling of thermo-physical properties for FRP composites under elevated and high temperatures. *Composites Science and Technology* 2007, 67: 3098-3109.

36. Hilado CJ. Flammability Handbook for Plastics, Technomic Publishing Co., Inc., Lancaster, PA, USA, 1990.

37. Keller T, Tracy C, Zhou A. Structural response of liquid-cooled GFRP slabs subjected to fire. Part I: Material and post-fire modeling. *Composites*

Part A 2006, 37(9): 1286-1295.

38. Özisik MN. Basic Heat Transfer, Robert E. Krieger Publishing Company, Malabar, FL, USA, 1977.

39. ISO. Fire Resistance Tests-Elements of Building Construction. International Standard ISO-834, Geneva, 1975.

40. European Committee for Standardization (CEN). Eurocode 1: Actions on Structures: Part 1.2: Actions on Structures Exposed to Fire. Revised Edited Document, 2002.

41. Keller T, Tracy C, and Zhou A. Structural response of liquid-cooled GFRP slabs subjected to fire. Part II: Thermo-chemical and thermo-mechanical modeling. *Composites Part A* 2006, 37(9): 1296-1308.

2.7 Modeling of mechanical responses

Summary

The thermomechanical property models for composite materials subjected to elevated and high temperatures were developed in Section 2.2. Integrating these material property models into a structural theory, a thermomechanical model is presented in this paper to predict the time-dependent deflections of cellular FRP slab elements subjected to mechanical loads and fire from one side. The temperature information required for the thermomechanical property models was calculated using the thermal response model in Section 2.6.

The model comprises mechanical property sub-models for the E-modulus, viscosity and coefficient of thermal expansion. Two different thermal boundary conditions were investigated – with and without liquid cooling of the slab elements in the cells. A finite difference method was used to calculate the deflection at each time step. Deflections caused by stiffness degradation due to the glass transition and decomposition of the resin dominated those caused by viscosity and thermal expansion. The predicted total deflections compared well with the measured results obtained from realistic fire scenarios over a test period of up to two hours.

Reference detail

This paper, submitted to Composites Part A: Applied Science and Manufacturing and currently accepted pending minor revisions, is entitled

"Modeling of mechanical responses for FRP composites under elevated and high temperatures" by Yu Bai, Thomas Keller and Till Vallée.

Part of the content of this paper was partially introduced in the Fourth International Conference on FRP Composites in Civil Engineering (CICE) 22-24 July 2008, Zurich, Switzerland, entitled

"Modeling of thermomechanical properties and responses for FRP composites in fire" by Yu Bai, Thomas Keller and Till Vallée, presented by Yu Bai.

MODELING OF MECHANICAL RESPONSE OF FRP COMPOSITES IN FIRE

Yu Bai and Thomas Keller

Composite Construction Laboratory CCLab, Ecole Polytechnique Fédérale de Lausanne (EPFL), BP 2225, Station 16, CH-1015 Lausanne, Switzerland.

ABSTRACT:

A thermomechanical model is presented for predicting the time-dependent deflections of cellular FRP slab elements subjected to mechanical loading and fire from one side. The model comprises temperature-dependent mechanical property sub-models for the E-modulus, viscosity and coefficient of thermal expansion. Two different thermal boundary conditions were investigated: with and without liquid-cooling of the slab elements in the cells. A finite difference method was used to calculate the deflection at each time step. Deflections resulting from stiffness degradation due to glass transition and decomposition of the resin dominated over those resulting from viscosity and thermal expansion. The predicted total deflections compared well with the measured results over a test period of up to two hours. The failure mode of the non-cooled specimen could be explained.

KEYWORDS:

Polymer-matrix composites; thermomechanical properties; pultrusion; viscoelasticity

1 INTRODUCTION

Investigations on modeling of the thermal and mechanical responses of fiber-reinforced polymer (FRP) composites subjected to fire can be traced back to initial efforts by the defense and aerospace industries. The focus has since shifted from mainly carbon fiber composites to glass fiber-reinforced polyester, vinylester, and phenolic composites used for marine and civil applications.

The mechanical responses (stress, strain, displacement and strength) of FRP composites under elevated and high temperatures are affected significantly by their thermal exposure [1]. On the other hand, mechanical responses almost have no influence on the thermal responses of these materials. As a result, the mechanical and thermal responses can be decoupled. This can be done by, in a first step, estimating the thermal responses and then, based on the modeling of temperature-dependent mechanical properties, predicting the mechanical responses of the FRP composites.

Thermomechanical models for FRP materials were first developed in the 1980s. One of the first thermomechanical models for FRP materials was introduced by Springer in 1984 [2], where the degradation of mechanical properties was empirically related to the mass loss. In 1985, Chen et al. [3] added a mechanical model to the thermochemical model presented by Griffis in 1981 [4]: mechanical properties at several specified temperature points were assembled into a finite element formulation. Griffis et al. [5] introduced an updated version of Chen's model in 1986, whereby an extrapolation process was used to obtain the data in the higher temperature range.

In 1992, McManus and Springer [6, 7] presented a thermomechanical model that considered the interaction between mechanically-induced stresses and pressures created by the decomposition of gases within the pyrolysis front. Again, temperature-dependent mechanical properties were determined at several specified temperature points as stepped functions. The issue of degradation of material properties at elevated temperatures was considered in Dao and Asaro's [8] thermomechanical model in 1999.

The degradation curves used in the model were, once again, obtained by curve fitting of limited experimental data. Later in 2000, Dutta and Hui [9] devised a simple empirical model for temperature or time dependent mechanical properties. In this model, the ratio of moduli at two different temperatures was determined by the density and temperature at these two points.

In 1999, a theoretical model for a temperature-dependent modulus was developed by Mahieux et al. [10, 11]. In this model, Weibull functions were used to describe the change in modulus over the full temperature range including the glass transition temperature. Experimental validation was conducted on six different polymers. In each case, the degradation of the modulus during glass transition was successfully described by the model. A further application of this model to predict the mechanical responses of composites can be found in Burdette et al. [12].

Gibson et al. [13] developed a thermomechanical model by combining their thermochemical model with Mouritz's two-layer post-fire mechanical model (a fully degraded region that is simplified as having little or no residual mechanical properties, and an unaffected region that is simplified as having the same properties as before the fire exposure, [14]). A remaining resin content (RRC) criterion was successfully used to identify the border between two different layers. In 2004, Gibson et al. [15] then presented an upgraded version by adding a new mechanical model. A function that assumes the relaxation intensity is normally distributed over the transition temperature was used to fit the temperature-dependent E-modulus. Furthermore, in order to consider the resin decomposition, each mechanical property was modified by a power law factor. Predictions of mechanical responses based on the thermomechanical models were also performed by Bausano et al. [16] and Halverson et al. [17]. Mechanical properties were correlated to temperatures through Dynamic Mechanical Analysis (DMA); but no special temperature-dependent mechanical property models were developed.

The above-mentioned thermomechanical models only consider material

elastic behavior, viscoelastic behavior of FRP composites at elevated and high temperatures has seldom been investigated. Boyd et al. [18] reported on compression creep rupture tests performed on uni-directional laminates of E-glass/vinylester composites subjected to a combined compressive load and one sided heating. Models were developed to describe the thermo-viscoelasticity of the material as a function of time and temperature. In their work, the temperature-dependent mechanical properties were determined by fitting the Ramberg-Osgood equations. The viscoelastic effects were considered by the generalized Maxwell-Voigt equations; and the temperature profiles were estimated by a transient 2D thermal analysis in ANSYS® 9.0.

The objectives of this paper is to validate the material property models recently proposed by the authors in [19] on the structural level and, based on the modeling results, to understand the complex thermomechanical responses (including both elasticity and viscosity) of FRP load-bearing structures subjected to fire. Conversion degrees in both time and space domain of the related chemical and physical transitions are calculated. Subsequently the time- and temperature-dependent elastic and viscoelastic displacements are obtained and compared to experimental results from cellular FRP panels subjected to mechanical loads and fire from one side [20]. The additional deflections due to thermal expansion are also considered and the failure modes are discussed.

2 MODELING OF TEMPERATURE-DEPENDENT MECHANICAL PROPERTIES

Structural fire endurance experiments were performed on cellular GFRP slab elements (DuraSpan® 766 slab system from Martin Marietta Composites) as shown in Fig. 1. A detailed description of the experimental set-up and results is given in [20]. The pultruded composite material consisted of E-glass fibers (volume fraction 48%) embedded in an isophthalic polyester resin. The mechanical properties at ambient temperature of the cellular deck components (upper and lower face sheets and internal webs) are

summarized in Table 1. The glass transition temperature, T_g, of the material was 117°C and the decomposition temperature, T_d, 300°C [19].

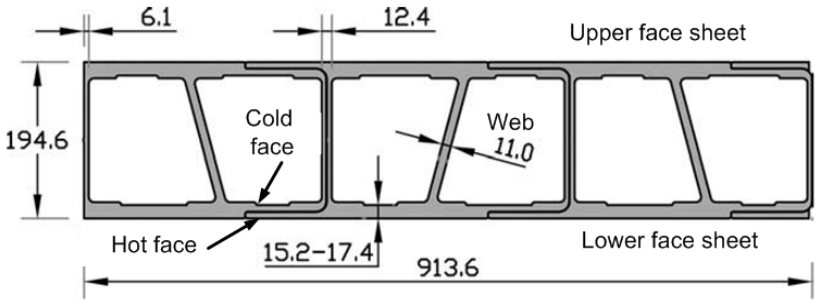

Fig. 1. Cross section of DuraSpan specimens used for fire endurance experiments

Property	Face sheets	Webs	Total
E_x (GPa)	21.24	17.38	-
G_{xy} (MPa)	5580	7170	-
λ_c ($\times 10^{-6}$ K^{-1})	-	-	12.6
η_m (GPa·hour)	-	-	82.4
A (mm^2)	15350	11480	42180
Height (mm)	15.2-17.4	161	194.6
Width (mm)	913.6	71.3	913.6

Table 1. Mechanical properties and geometric parameters of DuraSpan deck

2.1 Temperature-dependent E-modulus

To describe the change in E-modulus with temperature, the related physical and chemical processes that occur during glass transition and decomposition must be understood. Different kinetic models can be used to describe the conversion degree of each process [19, 21]:

$$\frac{d\alpha_g}{dT} = \frac{A_g}{\beta} \cdot \exp\left(\frac{-E_{A,g}}{RT}\right) \cdot \left(1-\alpha_g\right)^{n_g} \tag{1}$$

$$\frac{d\alpha_r}{dT} = \frac{A_r}{\beta} \cdot \exp\left(\frac{-E_{A,r}}{RT}\right) \cdot \left(1-\alpha_r\right)^{n_r} \tag{2}$$

$$\frac{d\alpha_d}{dT} = \frac{A_d}{\beta} \cdot \exp\left(\frac{-E_{A,d}}{RT}\right) \cdot \left(1-\alpha_d\right)^{n_d} \tag{3}$$

where α_g, α_r and α_d are the conversion degrees; A_g, A_r and A_d the pre-exponential factors; $E_{A,g}$, $E_{A,r}$ and $E_{A,d}$ the activation energies; and n_g, n_r and n_d the reaction orders for glass transition, leathery-to-rubbery transition and decomposition respectively. R is the universal gas constant; T is the temperature; t is time; and β is the heating rate. Complex thermal loading history can be taken into account by varying β within a finite difference algorithm.

By adopting a simple mixture approach, the temperature-dependent E-modulus, E_m, can be expressed as follows (taking into account the fact that the E-moduli in the leathery and rubbery states are almost the same [19]):

$$E_m = E_g \cdot \left(1-\alpha_g\right) + E_r \cdot \alpha_g \cdot \left(1-\alpha_d\right) \tag{4}$$

where E_g is the E-modulus in the glassy state (for initial values for face sheets and webs, see Table 1) and E_r is the E-modulus in the leathery and rubbery states, defined as being 5.8 GPa [19]. After decomposition, the material is considered as having no structural stiffness. Based on a value of β = 5°C/min (the same as for DMA), the temperature-dependent E-modulus results are shown in Fig. 2a. The stiffness degradation due to glass transition compares well to the DMA results given in [19], and the drop due to decomposition is also described by the model.

2.2 Temperature-dependent viscosity

The temperature-dependent viscosity, η_m, can be obtained by the same method as that used for the modeling of a temperature-dependent E-modulus. However, since the viscosities in the leathery and rubbery states are different [19], the following Eq. (5) is derived:

$$\eta_m = \eta_g \cdot \left(1-\alpha_g\right) + \eta_l \cdot \alpha_g \cdot \left(1-\alpha_r\right) + \eta_r \cdot \alpha_g \cdot \alpha_r \tag{5}$$

where η_g, η_l and η_r are the viscosities in the glassy, leathery and rubbery states. In order to obtain the viscosity in the glassy state (initial value at room temperature), creep tests at room temperature were performed on

the same DuraSpan slab elements, as shown in Fig. 2d [22], and a value of η_g = 82.4 GPa·hour was obtained (for calculation procedure, see Section 3.5). The values of η_l and η_r were adjusted proportionally to the viscosity results obtained from DMA [19]. The resulting temperature-dependent viscosity is shown in Fig. 2c. In agreement with the DMA results, an increase in viscosity before T_g (due to the glassy-to-leathery transition), and a decrease after T_g (due to the leathery-to-rubbery transition) are obtained.

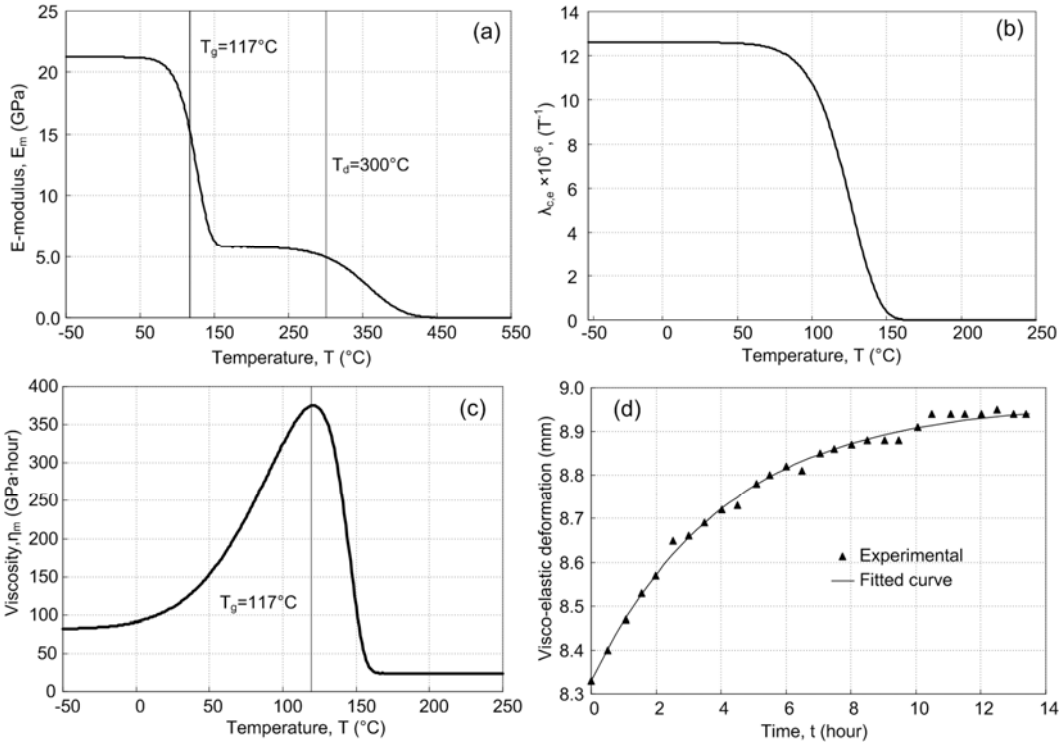

Fig. 2. Thermomechanical properties: (a) E-modulus, (b) effective coefficient of thermal expansion, (c) viscosity; (d) viscoelastic response (at ambient temperature)

2.3 Temperature-dependent effective coefficient of thermal expansion

As shown above, the E-modulus decreases towards zero after glass transition. In cross sections of elements where part of the material remains below glass transition, the true thermal expansion of the part of the material above glass transition therefore no longer influences the stresses or deformations of the element. Any contributions of the true thermal expan-

sion of the material above glass transition to the global structural deformation can therefore be disregarded. To take this structural effect into account, an effective coefficient of thermal expansion (CTE), $\lambda_{c,e}$, is applied as follows [19]:

$$\lambda_{c,e} = \lambda_c \cdot (1 - \alpha_g) \tag{6}$$

where λ_c is the true coefficient of thermal expansion in the glassy state (see Table 1). The relationship given in Eq. (6) is shown in Fig. 2b.

3 MODELING OF EXPERIMENTAL RESULTS

3.1 Experimental set-up and results

Three full-scale specimens were fabricated, designated SLC01, SLC02 and SLC03, with identical configurations and dimensions, as shown in Fig. 1. Specimens SLC01 and SLC02 were liquid-cooled during mechanical and thermal loading by slowly circulating water in the cells (1.25 and 2.5 cm/s), while specimen SLC03 was not cooled [20].

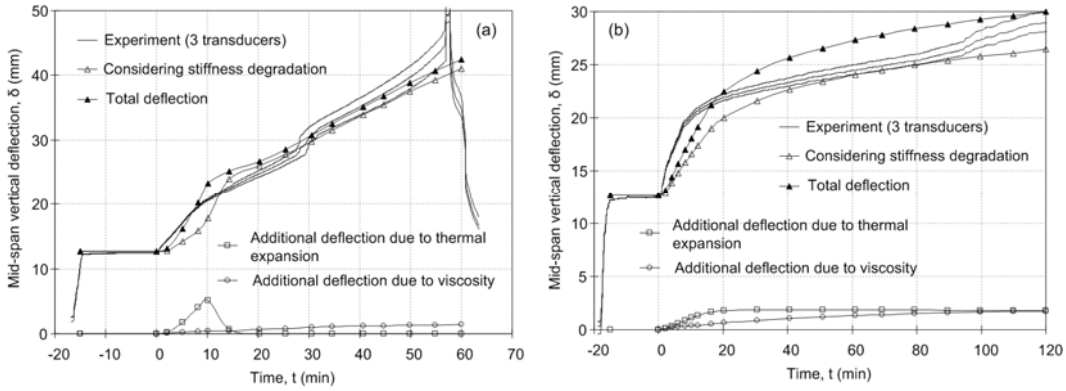

Fig. 3. Experimental deflections and model: (a) non-cooled SLC03, (b) liquid-cooled SLC02

The specimens were subjected to serviceability loads in a four-point bending configuration (span 2.75 m, loads 2×92 kN). After 15 minutes (time t=0), thermal loading according to the ISO-834 fire curve was applied from the underside. At t=57 min, the non-cooled specimen SLC03 failed, while the liquid-cooled specimens SLC01/ SLC02 continued to sustain the load up to 90/120 min, when the experiments were stopped. The experimental mid-span deflection curves, discussed in [20], are shown in

Fig. 3 and will be compared to the corresponding results from thermomechanical modeling in the following. Due to the similar behavior of specimens SLC01 and SLC02, reference is made only to the results obtained for the latter.

3.2 Thermochemical model for thermal responses

Models describing the temperature-dependent thermophysical properties of FRP composites (density, thermal conductivity, and specific heat capacity) under elevated and high temperatures were proposed in [21]. By combining these models, a one-dimensional thermochemical model was developed (and experimentally validated) to predict the change in temperature in the lower face sheet of the specimens [23].

3.3 Thermomechanical model for stiffness degradation

Assuming the specimen as a simply-supported beam loaded by two loads, P, beam theory can be used to calculate the elastic mid-span deflection, δ_E:

$$\delta_E = \frac{aP}{GA} + \frac{PL^3}{24EI}\left(\frac{3a}{L} - \frac{4a^3}{L^3}\right) \tag{7}$$

where L is the span, a the distance between one load and the support, A the cross-sectional area of the webs, G the shear modulus, and I the moment of inertia of the section. The first term on the right side of Eq. (7) is the deflection due to shear and the second is deflection due to bending. Since the E-modulus at ambient temperature varies over the cross section (see Table 1), the stiffness of the slab element, EI, was calculated as the sum of the stiffnesses of the individual components:

$$EI = E_w I_w + E_{ufs} I_{ufs} + E_{lfs} I_{lfs} \tag{8}$$

where subscripts *ufs*, *w*, and *lfs* designate the upper face sheet, web and lower face sheet respectively. The additional deflections due to thermal expansion and viscosity are not yet taken into account (see Sections 3.4 and 3.5). Based on Eq. (7), the initial deflection before thermal loading was calculated as 13.1 mm (8% above the experimental value). Of this, 0.6 mm (or 7.6%) was due to shear deformation and 12.1 mm (92.4%) due to bend-

ing deformation.

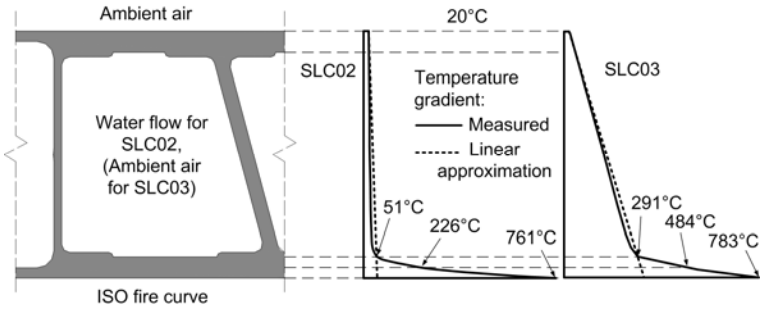

Fig. 4. Temperature gradient at 120 min for liquid-cooled SLC02 and at 57 min for non-cooled SLC03

The temperature in the upper face sheets of all specimens and the temperature of the webs of the cooled specimens remained below the glass transition temperature, see Fig. 4 and [23]. Consequently, the E-modulus of these components was assumed to remain unchanged. The temperature in the lower part of the webs of the non-cooled specimen, however, exceeded T_g. Nevertheless, constant E- and G-moduli were also assumed for the webs of the non-cooled specimens in order to simplify the model. A sensitivity analysis showed only a small underestimation of deflections at the final stage. The lower face sheets of all specimens, however, exhibited steep temperature gradients throughout the entire fire exposure and the corresponding E-modulus, E_{lfs}, could not be assumed to remain unchanged.

By discretizing the lower face sheet into 17 layers of almost 1-mm thickness and the time domain into 60 time steps (thus 1 min per time step for SLC03 and 2 min for SLC02), the calculation process for the mid-span deflections for each time step is as follows:

1. The temperature of each layer is calculated using the thermochemical model [21, 23].
2. Based on the available temperature and estimated kinetic parameters, the conversion degrees are calculated for each layer, as shown in Fig. 5a and 5b for α_g (the corresponding conversion degrees of decomposition are shown in [23]).
3. The E-modulus is estimated using Eq. (4), as shown in Fig. 5c and 5d.
4. The stiffness, EI, of the whole cross section is calculated using Eq. (8).

5. Incorporating *EI* obtained at each time step into Eq. (7), the time-dependent mid-span deflection is calculated, as shown in Fig. 3 for SLC03 and SLC02 (curves labeled "considering stiffness degradation").

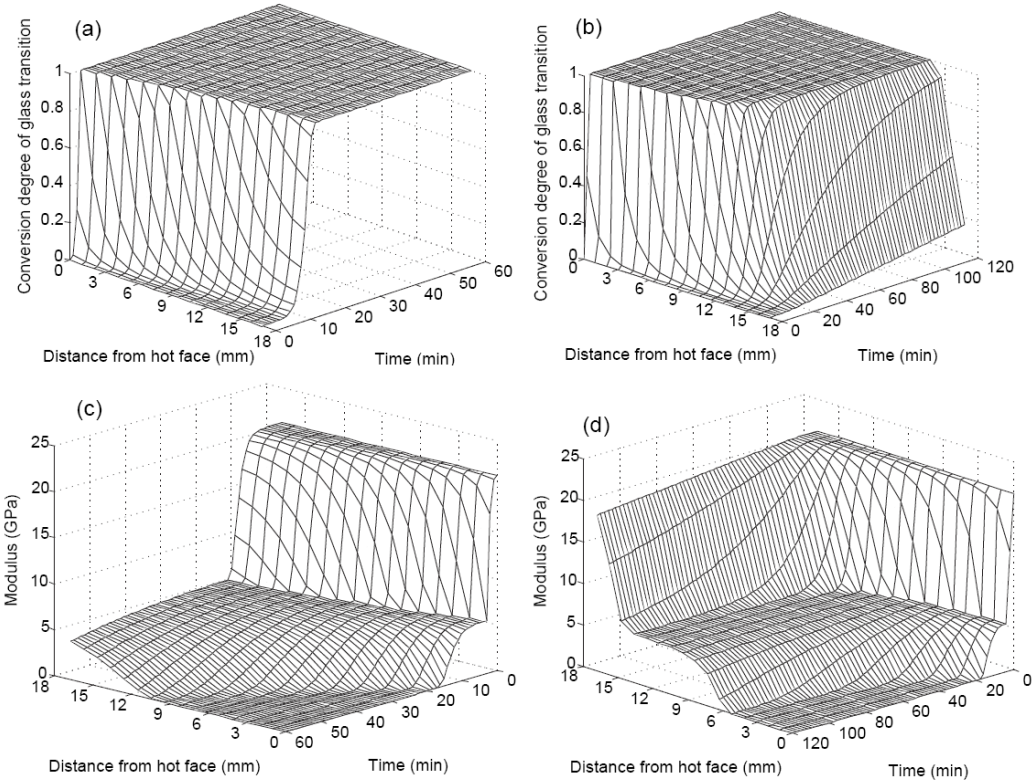

Fig. 5. Conversion degree of glass transition and resulting modulus degradation through lower face sheet: (a) and (c) non-cooled SLC03, (b) and (d) liquid-cooled SLC02

3.4 Model extension: effects of thermal expansion

The deflection curves resulting from stiffness degradation, shown in Fig. 3, persistently underestimate the experimental results for both specimens, especially at the beginning stage. The underestimation was partially attributed to the non-consideration of thermal expansion, particularly at the beginning, when most of the material had not yet reached glass transition. Since only the lower face sheets of the specimens were subjected to thermal loading, the temperature gradient between the upper and lower face sheets caused an additional deflection in the downward direction, which contributed to the increase in total deflection. The temperature gradient

through the depth of the cross section, h, at time step t_i is given by $(\Delta T/h)_{t_i}$ and the additional deflection, $\delta_T(t_i)$, at time step t_i can be approximated by:

$$\delta_T(t_i) = \frac{\lambda_{c,e}(t_i) \cdot L^2}{8} \cdot \left(\frac{\Delta T}{h} \right)_{t_i} \tag{9}$$

The effective coefficient of thermal expansion, $\lambda_{c,e}$, is calculated on the basis of the obtained temperature field and Eq. (6). Figure 6 shows the corresponding distribution through the lower face sheets of both slab elements. The effective CTE value is zero in most parts for both cases because glass transition has already occurred. The temperature gradient was therefore assumed to be linear and to have the same slope as that of the web, as shown in Fig. 4. Based on this approximation, the additional deflections due to thermal expansion were estimated at different time steps and are shown in Fig. 3 for both slabs. A noticeable deflection from thermal expansion is particularly observed during the first 15 min for the non-cooled slab. The subsequent contributions to total deflection are negligible. The contribution to the total deflection of the liquid-cooled slab is constant but small over the entire duration.

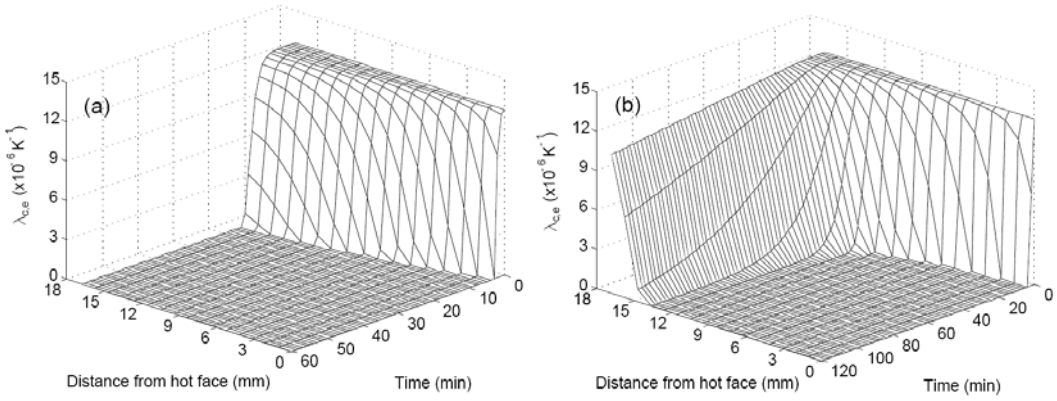

Fig. 6. Effective coefficient of thermal expansion through lower face sheet: (a) non-cooled SLC03 and (b) liquid-cooled SLC02

3.5 Model extension: effects of viscosity

The viscoelastic behavior of a composite material can be described as being an association of a number of dashpots, *j,* and a number of springs, *i,* in series or parallel [24, 25]. The governing equation of the system motion

can be expressed as:

$$\sum_j p_j \frac{\partial^j \sigma}{\partial t^j} = \sum_i q_i \frac{\partial^i \varepsilon}{\partial t^i} \tag{10}$$

where σ denotes the stress and ε denotes the strain; t is the time and p_j and q_i are coefficients determined by the E-modulus of the springs and the viscosity of the dashpots as well as the structure of the system. If at each time step σ is approximated as a constant, and only the first derivation of the strain is taken into account, Eq. (10) can be simplified to:

$$p_0 \cdot \sigma = q_0 \cdot \varepsilon + q_1 \cdot \dot{\varepsilon} \tag{11}$$

Eq. (11) is a first-order differential equation of ε with respect to time t, the solution being expressed as:

$$\varepsilon = \frac{p_0 \cdot \sigma}{q_0} + \left(C_0 - \frac{p_0 \cdot \sigma}{q_0} \right) \cdot \exp\left(-\frac{t}{q_1/q_0} \right) \tag{12}$$

where the constant C_0 can be considered as the initial strain at t=0, which is determined by the initial elastic stiffness, $(p_0 \cdot \sigma)/q_0$ is the strain when $t=\infty$ and q_1/q_0 is the relaxing time, expressed as the ratio between the viscosity (η_m) and the E-modulus (E_m).

In order to estimate the deflection due to viscoelasticity, Eq. (11) was considered as part of the finite difference framework presented in Section 3.3. Based on Euler's beam theory (disregarding shear deformation, as discussed in Section 3.3), and considering the stress-strain relationship in Eq. (11), the following was obtained:

$$M = \int y \cdot \sigma dA = \int \left(\frac{q_0 \cdot \varepsilon}{p_0} + \frac{q_1 \cdot \dot{\varepsilon}}{p_0} \right) \cdot y dA = -w'' \int \frac{q_0}{p_0} y^2 dA - \dot{w}'' \int \frac{q_1}{p_0} y^2 dA \tag{13}$$

where M is the bending moment and y is the coordinate in the depth direction. In discretized form (as described in Section 3.3), Eq. (13) can be expressed as:

$$w'' \sum \left(\frac{q_0}{p_0} I \right) + \dot{w}'' \sum \left(\frac{q_1}{p_0} I \right) = -M \tag{14}$$

where $w=w(x, t)$ is the deflection function dependent on x (space axis along the span) and t (time axis) and I is the time-dependent moment of inertia. Assuming that the additional deformation due to viscosity in each time

step is small compared to the previously determined elastic deformation, I for each layer can be assumed as being the same as in Section 3.3.

With regard to the four-point bending set-up, Eq. (14) can be transformed as follows:

$$K_1 \cdot w + K_2 \cdot \dot{w} = f(x) \tag{15}$$

where

$$f(x) = \frac{Pax}{6L}\left(L^2 - x^2 - a^2\right) + \frac{P(L-a)}{6L}\left[\frac{L}{L-a}(x-a)^3 + \left(2La - a^2\right)x - x^3\right] \tag{16}$$

$$K_1 = \sum\left(\frac{q_0}{p_0} I\right) \tag{17}$$

$$K_2 = \sum\left(\frac{q_1}{p_0} I\right) \tag{18}$$

f (x) is a function of the space coordinate, x, which is independent of time, t, while K_1 and K_2 are time-dependent parameters, which were obtained from the temperature-dependent E-modulus and viscosity, see Section 2.1 and 2.2. It should be noted that the initial value of viscosity obtained by curve fitting in Section 2.2 was based on this model.

Eq. (15) can be solved for time step t_i as follows:

$$w(x,t_i) = \frac{f(x)}{K_{1,t_{i-1}}} + C_1 \cdot \exp\left(-\frac{K_{1,t_{i-1}} \cdot \Delta t}{K_{2,t_{i-1}}}\right) \tag{19}$$

where C_1 is a constant determined by the initial condition and Δt is the time interval. Assuming that the initial condition for time step t_i is the deflection at the previous time step t_{i-1}, gives:

$$w(x,t_i) = \frac{f(x)}{K_{1,t_{i-1}}} + \left(w(x,t_{i-1}) - \frac{f(x)}{K_{1,t_{i-1}}}\right) \cdot \exp\left(-\frac{K_{1,t_{i-1}} \cdot \Delta t}{K_{2,t_{i-1}}}\right) \tag{20}$$

The deflection increment due to viscoelasticity can then be expressed as:

$$\Delta\delta_{V,t_i} = -\frac{K_{1,t_{i-1}} \cdot \Delta t}{K_{2,t_{i-1}}}\left(w(x,t_{i-1}) - \frac{f(x)}{K_{1,t_{i-1}}}\right) \cdot \exp\left(-\frac{K_{1,t_{i-1}} \cdot \Delta t}{K_{2,t_{i-1}}}\right) \tag{21}$$

where $w(x, t_0)$ is the elastic deflection as determined in Section 3.3. The additional deflection due to viscosity effects at each time step was computed by Eq. (21) and is shown in Fig. 3 for both specimens. Furthermore,

the changes in viscosity in all the layers in the whole time domain are obtained and shown in Fig. 7.

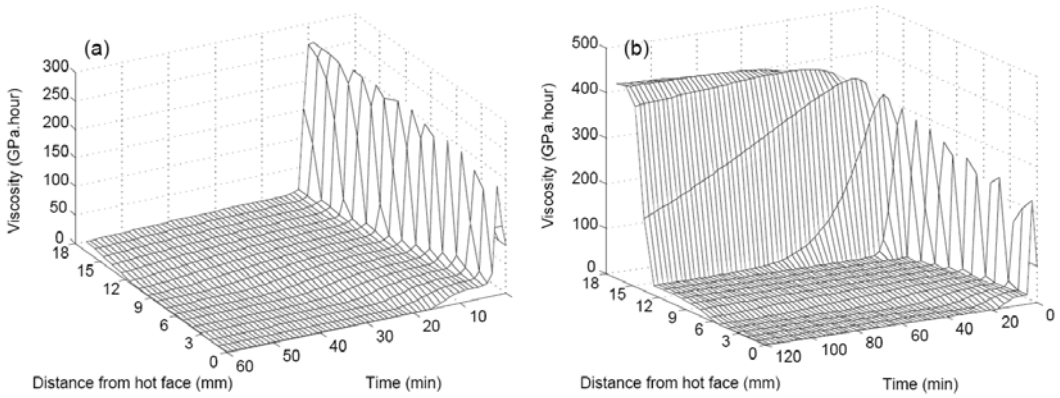

Fig. 7. Viscosity through lower face sheet: (a) non-cooled SLC03 and (b) liquid-cooled SLC02

4 DISCUSSION

4.1 Modeling of temperature- and time-dependent E-modulus, CTE and viscosity

4.1.1 Non-cooled specimen SLC03

Figure 5c shows the time-dependent E-modulus through the lower face sheet of the non-cooled specimen SLC03. The stiffness rapidly decreased to E_r (5.8 GPa, rubbery state) due to the glass transition that occurred through the whole depth within the first 15 minutes (see the conversion degree of glass transition in Fig. 5a). Decomposition at the hot face started after 10 min (at approximately 311°C, see [20, 23]), associated with a total loss of stiffness. At the cold face, however, even after 60 min of heating, the material was not fully decomposed. Consequently, the cold face almost still exhibited the E_r stiffness.

Figure 6a shows the time-dependent effective coefficient of thermal expansion, which decreased to zero through the whole lower face sheet after only 15 min since full glass transition was then achieved (see Fig. 5a). The time-dependent viscosity is shown in Fig. 7a. At each depth through the lower face sheet, viscosity first increased due to the glassy-to-leathery

transition and then decreased due to the leathery-to-rubbery transition. Since higher temperatures were attained earlier close to the hot face, viscosity also decreased earlier than in the cold face region.

4.1.2 Liquid-cooled specimen SLC02

The time-dependent E-modulus through the lower face sheet of the liquid-cooled specimen SLC02 is shown in Fig. 5d. At the hot face, the decrease in the modulus was similar to that of the non-cooled specimen. At the cold face, however, only a slight decrease occurred due to the low conversion degree of glass transition even after 120 min (see Fig. 5b). The remaining E-modulus was 88% of the initial value.

Figure 6b shows the time-dependent effective coefficient of thermal expansion. For the elements close to the hot face of the lower face sheet, the coefficient quickly decreased to zero, similarly to that of the non-cooled specimen SLC03 (see Fig. 6a). However, in contrast to SLC03, the decrease in the coefficient for elements far from the hot face was small due to the small conversion degree of glass transition (see Fig. 5b).

The time-dependent viscosity is shown in Fig. 7b. Close to the hot face of the lower face sheet, viscosity changed similarly to that of SLC03 due to the same thermal loading. For elements closer to the cold face, however, viscosity remained high because the leathery-to-rubbery transition had not yet occurred.

The beneficial effect of liquid-cooling was confirmed and quantified by these results: at the cold face, the stiffness was almost retained and the effective coefficient of thermal expansion and viscosity decreased only slightly compared to the non-cooled specimen.

4.2 Modeling of temperature- and time-dependent deflections

4.2.1 Non-cooled specimen SLC03

The E-modulus of the non-cooled specimen was highly degraded due to thermal loading, resulting in a progressive increase in deflection at mid-

span, as shown in Fig. 3a. However, when only the stiffness degradation was considered, an underestimation of the measured deflections resulted, especially during the first 15 minutes of thermal loading.

The additional deflection due to thermal expansion (Eq. 10), also shown in Fig. 3a, mainly occurred within the first 15 min – the period during which the glass transition process in the lower face sheet was not yet completed (see Figs. 5a and 6a). After glass transition, the effective coefficient of thermal expansion was zero, see Section 2.3. This explained the discrepancy, especially during the first 15 minutes, between the experimental results and the model results, which did not take thermal expansion into account.

The estimated deflection due to viscosity, also shown in Fig. 3a, increased continuously but remained small, the final deflection being only 1.6 mm at t = 57 minutes. The total deflection curve was obtained by adding together all the contributors (stiffness degradation, thermal expansion, and viscosity) and good agreement with experimental results was found, as shown in Fig. 3a. As mentioned in Section 3.3, a slight underestimation occurred during the last 10 min of fire exposure due to the constant stiffness assumption for the webs.

4.2.2 Liquid-cooled specimen SLC02

Similarly to SLC03, the deflection curve of SLC02, resulting from pure stiffness degradation, remained below the experimental deflection curve throughout the fire exposure, as shown in Fig. 3b. However, as seen in Fig. 5b, due to the liquid-cooling effects the conversion degree of glass transition at the cold face of the lower face sheet remained low at 120 min and consequently an additional deflection due to thermal expansion occurred throughout the experiment. The additional deflection due to viscosity was also small, reaching only 1.8 mm at 120 min (see Fig. 3b). The total deflection revealed a slight overestimation of the measured results in the middle part of the experiment, but matched the final value well (Fig. 5b).

Compared with specimen SLC03, the deflection of SLC02 due to stiff-

ness degradation increased much more slowly and the additional deflection due to thermal expansion lasted longer because of the liquid-cooling effect. The deflection due to viscosity was similar in both specimens (1.35 mm at 60 min for SLC02 compared to 1.55mm at 57 min for SLC03).

4.3 Failure analysis

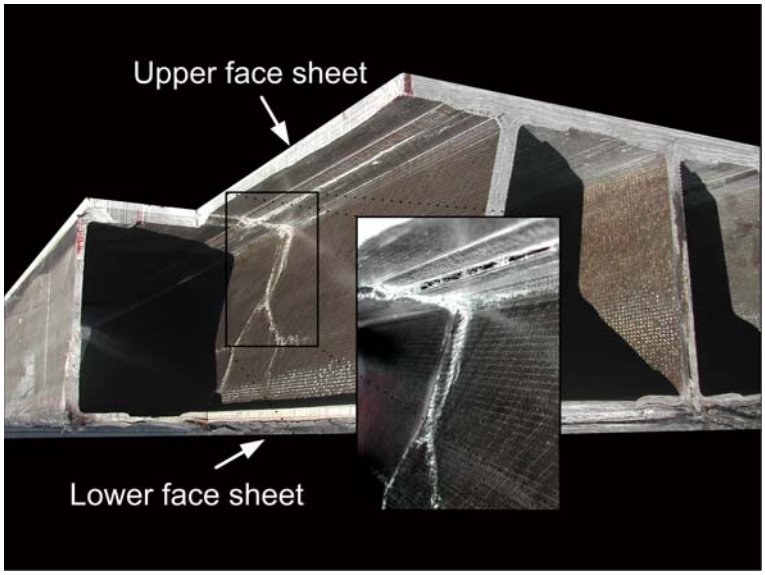

Fig. 8 Failure mode of non-cooled specimen SLC03

Specimen SLC01/02 did not fail after 90/120 min, when experiments were stopped. The non-cooled specimen SLC03, however, failed after 57 min. Post-fire inspection showed delamination cracks at the web-flange junctions and local buckling at the compressed upper face sheet and webs, see Fig. 8 and [20]. In order to understand the failure mode, the shear stress at the web-flange junction was calculated as follows:

$$\tau_{yx} = \frac{dM}{dx} \cdot \frac{\int_A E(y) \cdot y \cdot dA}{b \cdot EI_{eff}} = Q \cdot \frac{\int_A E(y) \cdot y \cdot dA}{b \cdot EI} \tag{23}$$

where Q is the shear force, y the distance to the neutral axis, and b the specimen width. Incorporating the E-modulus distribution at the final time step of specimens from Fig. 5c and 5d into Eq. (22), the shear stress at the web-flange junction was calculated as 24.1 MPa for SLC03 (taking into account a 59% loss of the webs above 150° where the material is in the rubbery state, see Fig. 2) and 8.1 MPa for SLC02 (no loss). The shear

strength measured on the same material was reported to be in the range of 15 to 23 MPa [26], which explains why failure occurred at the web-flange junctions of SLC03, and why no failure occurred for SLC01/02.

5 CONCLUSIONS

Temperature-dependant material property models based on kinetic theory were combined to form a thermomechanical response model, which was validated through experimental results obtained from the exposure of full-scale FRP slab elements to mechanical loading and fire for up to two hours. In particular, the following conclusions were drawn:

1. When subjected to elevated and high temperatures, FRP composites undergo complex material changes, such as glass transition, leathery-to-rubbery transition and decomposition. As kinetic processes, these transitions can be modeled by kinetic theory, thus allowing the conversion degree of different transitions and the quantity of the material in different states to be ascertained.
2. Since the material content in each state at any specified temperature is known, the temperature-dependent mechanical properties, including E-modulus, viscosity, and the effective coefficient of thermal expansion, can be determined using a simple mixture approach.
3. By combining the temperature-dependent mechanical properties, and based on the finite difference method, beam theory can then be used to predict the temperature- and time-dependent deflections of beam or slab elements subjected to mechanical and thermal loadings.
4. During fire exposure, stiffness degradation, thermal expansion and material viscosity led to an increase in the deflections of cellular slab elements, with stiffness degradation predominating. The additional bending deflection due to thermal expansion contributed to the total deflection mainly when the material was in glassy state.
5. Since different thermal boundary conditions can be considered in the model, the benefit of liquid-cooling, which reduces stiffness degradation and increases fire resistance time, could be quantified.

6. The ultimate failure of the non-cooled FRP specimen was initiated when shear strength was exceeded at the web-flange junction on the specimen side opposite to that exposed to fire due to partial loss of the webs, while the liquid-cooled specimen did not fail during 90 and 120 min since the entire webs remained in the glassy state.

ACKNOWLEDGEMENT

The authors would like to thank the Swiss National Science Foundation (Grant No. 200020-109679/1) for supporting this project.

REFERENCES

1. Mouritz, AP, Gibson, AG. Fire properties of polymer composite materials. Springer, 2007.

2. Springer GS. Model for predicting the mechanical properties of composites at elevated temperatures. *Journal of Reinforced Plastics and Composites* 1984, 3(1): 85-95.

3. Chen JK, Sun CT, Chang CI. Failure analysis of a graphite/epoxy laminate subjected to combined thermal and mechanical loading. *Journal of Composite Materials* 1985, 19(5): 216-235.

4. Griffis CA, Masumra RA, Chang CI. Thermal response of graphite epoxy composite subjected to rapid heating. *Journal of Composite Materials* 1981, 15: 427-442.

5. Griffis CA, Nemes JA., Stonesfiser FR, and Chang CI. Degradation in strength of laminated composites subjected to intense heating and mechanical loading. *Journal of Composite Materials* 1986, 20(3): 216-235.

6. McManus LN, Springer GS. High temperature thermomechanical behavior of carbon-phenolic and carbon-carbon composites, I. Analysis. *Journal of Composite Materials* 1992, 26(2): 206-229.

7. McManus LN and Springer GS. High temperature thermomechanical behavior of carbon-phenolic and carbon-carbon composites, II. Results. *Journal of Composite Materials* 1992, 26(2): 230-251.

8. Dao M and Asaro R. A study on the failure prediction and design crite-

ria for fiber composites under fire degradation. *Composites Part A* 1999, 30(2): 123-131.

9. Dutta PK and Hui D. Creep rupture of a GFRP composite at elevated temperatures. *Computers and Structures* 2000, 76(1): 153-161.

10. Mahieux CA, Reifsnider KL. Property Modeling across transition temperatures in polymers: a robust stiffness-temperature model. *Polymer* 2001, 42: 3281-3291.

11. Mahieux CA, Reifsnider KL. Property modeling across transition temperatures in polymers: application to thermoplastic systems. *Journal of Materials Science* 2002, 37: 911-920.

12. Burdette JA. Fire response of loaded composite structures – Experiments and Modeling. Master thesis 2001, Virginia Polytechnic Institute and State University.

13. Gibson AG, Wright PNH, Wu YS, Mouritz AP, Mathys Z and Gardiner CPG. Integrity of polymer composites during and after fire. *Journal of Composite Materials* 2004, 38(15): 1283-1308.

14. Mouritz AP and Mathys Z. Post-Fire Mechanical Properties of Glass-Reinforced Polyester Composites. *Composites Science and Technology* 2001, 61: 475-490.

15. Gibson AG, Wu YS, Evans JT and Mouritz AP. Laminate theory analysis of composites under load in fire. *Journal of Composite Materials* 2006, 40(7): 639-658.

16. Bausano J, Lesko J, and Case SW. Composite life under sustained compression and one-sided simulated fire exposure: characterization and prediction, *Compos Part A* 2006, 37(7): 1092-1100.

17. Halverson H, Bausano J, Case S, Lesko J. Simulation of response of composite structures under fire exposure. *Science and Engineering of Composite Materials* 2005, 12(1-2): 93-101.

18. Boyd SE, Case SW, Lesko JJ. Compression creep rupture behavior of a glass/vinyl ester composite subject to isothermal and one-sided heat flux conditions. *Composites Part A* 2007, 38: 1462-1472.

19. Bai Y, Keller T, Vallée T. Modeling of stiffness of FRP composites un-

der elevated and high temperatures. *Composites Science and Technology* 2008, 68: 3099-3106.

20. Keller T, Tracy C, and Hugi E. Fire endurance of loaded and liquid-cooled GFRP slabs for construction. *Composites Part A* 2006, 37/7: 1055-1067.

21. Bai Y, Vallée T, Keller T. Modeling of thermo-physical properties for FRP composites under elevated and high temperatures. *Composites Science and Technology* 2007, 67 (15-16): 3098-3109.

22. Keller T, Schollmayer M. Plate bending behavior of a pultruded GFRP bridge deck system. *Composite Structures* 2004, 64: 285-295.

23. Bai Y, Vallée T, Keller T. Modeling of thermal responses for FRP composites under elevated and high temperatures. *Composites Science and Technology* 2008, 68 (1): 47-56.

24. Hauger G, Wriggers S. Technische Mechanik 4: Elemente der Höheren Mechanik, Numerische Methoden. Springer, 1995. (in German).

25. Ferry JD. Viscoelastic properties of polymers. John Wiley & Sons, Inc., 1980.

26. Keller T, Schollmayer M. Through-thickness performance of adhesive joints between FRP bridge decks and steel girders. *Composite Structures* 2009, 87(3): 232-241.

2.8 Modeling of time-to-failure

Summary

The time-to-failure of a structure or its components is an important issue for structural safety considerations. Based on the strength degradation models for composite materials under elevated and high temperatures developed in Section 2.3, in this paper the time-to-failure is predicted for GFRP tubes under both thermal and mechanical loading in compression. Temperature responses were again calculated using the thermal response model presented in Section 2.6.

The GFRP tubes were fixed in a climate chamber, subjected to a compressive load at a prescribed level, and thermal loading was then increased up to final failure or the prescribed duration time. A water-cooling system was designed for pultruded GFRP components with closed cross section, in which different thermal boundary conditions were achieved with water cooling at different flow rates or without water cooling. Experimental results showed that the time-to-failure was increased with the increase of flow rate, but decreased with the increase of load level. The experimental results, including temperature responses and time-to-failure, could be well predicted for each experimental scenario.

The experiments presented in this paper also demonstrated that the proposed water-cooling system can enable GFRP compressive elements to resist thermal loading for a satisfactory time duration.

Reference detail

This paper, accepted for publication in Composite Structures, is entitled

"Pultruded GFRP tubes with liquid-cooling system under combined temperature and compressive loading" by Yu Bai and Thomas Keller.

PULTRUDED GFRP TUBES WITH LIQUID COOLING SYSTEM UNDER COMBINED TEMPERATURE AND COMPRESSIVE LOADING

Yu Bai and Thomas Keller

Composite Construction Laboratory CCLab, Ecole Polytechnique Fédérale de Lausanne (EPFL), BP 2225, Station 16, CH-1015 Lausanne, Switzerland.

ABSTRACT:

An active fire protection system, liquid cooling, was applied to pultruded GFRP tubes subjected to combined thermal and mechanical loading in order to maintain material temperature below the critical glass transition temperature. The use of an appropriate flow rate enabled endurance times of up to three hours at full serviceability loads to be achieved, even in the most severe scenario of compressive loading. Building code requirements concerning fire exposure – normally for a fire endurance of up to two hours – can therefore be met. The experimental results evidenced not only the temperature- but also the time-dependency of the load-bearing capacity. Previously proposed thermal response and strength degradation models were further validated by the experiments. Since the applied models were derived from kinetic theory, the experimentally observed time-dependence could be well described.

KEYWORDS:

Polymer-matrix composites; pultrusion; compression; thermal loading; water cooling

1 INTRODUCTION

Load-bearing structures composed of fiber-reinforced polymer (FRP) composite components are vulnerable to fire exposure [1-5]. Elevated temperatures just above the glass transition of the resin (at 100-150°C) may lead to structural collapse if structural behavior is resin-dominated, i.e. if components are subjected to shear or compressive loading [6-8]. To fulfill the requirements of structural safety, functionality and integrity, passive or active fire protection is therefore required [9, 10].

Passive fire protection methods for FRP materials include the addition of retardant agents to the resin material (such as aluminum trihydroxide, antimony oxide, magnesium hydroxide [11]), the use of inherently fire retardant resins [12], or the application of protective layers onto the FRP component surfaces (e.g. intumescent coatings [13]). The function of these methods is to make FRP components less likely to burn, less sensitive to other burning objects, or less dangerous when they eventually burn, due to low toxic gas emission and flame spread. Most of these methods, however, offer only limited effectiveness with regard to the structural aspect. They cannot prevent the dangerous resin from softening at comparatively low temperatures, or at least only do so in a very limited way. Passive protection methods may thus be insufficient in many cases and have to be complemented (or replaced) by active methods. Active protection methods normally incorporate an automated detection of fire in its early stage and then suppress the fire (e.g. by sprinkler systems) and/or dissipate heat (e.g. using liquid-cooling systems) [14].

The concept of internal liquid cooling involves circulating a liquid through critical components in order to remove heat, a technique frequently used in car engines, rocket nozzles, etc. Liquid cooling is also applied in engineering structures, e.g. for fire protection of the steel skeletons of buildings since the 1960s [15]. Applications for FRP structural components, however, are very limited. The fire performance of glass fiber-reinforced epoxy pipes filled with stagnant water was evaluated by Marks et al. in 1986 [16] and a similar investigation was conducted by Davies et al. on a

glass-epoxy pipe system filled with stagnant or flowing water [17]. A three-minute endurance time of an empty pipe was increased to approximately 10 minutes using stagnant water. In the flowing condition, however, no endurance limit was found during a two-hour exposure. Keller et al. applied an internal water-cooling system in cells of full-scale E-glass fiber-reinforced polyester panels (DuraSpan bridge deck system) subjected to serviceability loading in a four-point bending setup and ISO-834 fire from the underside, which was in tension [18]. Modest water flow rates of 0.2 to 5.0 cm/s (as found in under-floor heating systems) were used and demonstrated to be effective in maintaining structural resistance and stiffness for up to two hours (when experiments were stopped).

Since GFRP components subjected to compression are expected to be more vulnerable than components subjected to bending (with fire on tension side) due to early resin softening and subsequent fiber buckling, water-cooled GFRP tubes were examined under compression in this study. Different load levels and water flow rates were investigated and the experimental results, including temperature responses and time-to-failure, were used to further validate thermochemical and thermomechanical models proposed by the authors in [19, 20].

2 EXPERIMENTAL INVESTIGATION

2.1 Description of materials and specimens

Pultruded GFRP tubes with a 40/34-mm outer/inner diameter and 3-mm thickness, supplied by Fiberline A/S, Denmark, were used for the experimental investigation. The specimens consisted of E-glass fibers embedded in an isophthalic polyester resin, comprising two chopped strand mats (CSM) on the inner and outer sides with a UD-roving layer in the center. The fiber mass and volume fractions were 63.8% and 42.5% respectively. The onset of glass transition temperature, $T_{g,onset}$, and decomposition temperature, $T_{d,onset}$, was approximately 110°C and 270°C respectively ([5], a similar material being used from the same pultruder).

The non-dimensional slenderness, $\bar{\lambda}$, was calculated according to Eq. (1):

$$\bar{\lambda} = \sqrt{\frac{A \cdot f_c}{P_E}} \tag{1}$$

where A is the area of cross section (348.7 mm^2) and f_c is the nominal compressive strength (344.2±20.3 MPa [8]) at room temperature. P_E is the global (Euler) buckling load (580 kN), determined from:

$$P_E = \frac{\pi^2 \cdot (EI)}{(L/2)^2} \tag{2}$$

where EI is the bending stiffness (1.3×10^9 N·mm^2) and L is the specimen length (300 mm, tube ends were fully fixed). The resulting slenderness was 0.45, which corresponded to a compact component exhibiting a reduction factor of almost 1.0.

2.2 Thermal response experiments

To obtain through-thickness temperature profiles, temperature sensors had to be placed at different depths in slots cut into the tubes. To prevent this damage from exerting a negative influence on structural endurance, temperature and mechanical response measurements were separated and made on different specimens. Temperature response experiments were first performed for three scenarios: without water cooling (non-cooled), with water cooling at a low flow rate (8 cm/s), and with water cooling at a high flow rate (20 cm/s). The flow rates used were slightly higher than those in the experiments on the panels [18] due to the much smaller tube depth (tubes 3 mm vs panel face sheets 15.2-17.4 mm). The Reynolds numbers were 2770 for 8 cm/s and 6920 for 20 cm/s, indicating that the flow was transitional for low rate and turbulent for high rate. However, due to the short tube length and corresponding effects of water inlet and outlet (see below), no stable flow was achieved in the tube. One tube specimen was investigated for each scenario, designated TN, TC1, and TC2, see Table 1. In each specimen, six temperature sensors were embedded in two groups at different positions in the through-thickness direction at ap-

proximately 0.5 mm (designated 0-1 mm), 1.5 mm (1-2 mm), and 2.5 mm (2-3 mm) from the outer surface.

	TN	TC1	TC2	MN1-1/2	MN2-1/2	MC1-1/2	MC2-1/2	MC3-1	MC4-1
Load level (kN/% of SLS load)	0/0	0/0	0/0	68/100	34/50	68/100	68/100	51/75	34/50
Fire protection	no	yes	yes	no	no	yes	yes	yes	yes
Flow rate (cm/s)	-	8	20	-	-	8	20	20	20
Increase in water temperature (°C)	-	5.6	2.1	-	-	-	-	-	-
Failure time for specimens 1/2 (min)	-	-	-	6.8/ 7.4	13.6/ 12.4	72.1/ 71.8	157.3/ 170.0	> 525	> 250
Predicted time-to-failure (min)				6.3	11.2	63.4	178.6	340	850

Table 1. Parameters for thermal response and structural endurance experiments

The same experimental setup was used as for the subsequent endurance experiments, although without applying a mechanical load, see Fig. 1. The specimens were placed in free mode in the environmental chamber of a 100-kN Instron universal 8800 hydraulic machine (range and accuracy of the chamber: -40°C to 250°C, ±2°C). Water was supplied by the fire plumbing of the test laboratory, and the flow rates were controlled by the water volume passing within unit time. As shown in Fig. 1, the water passed through the inlet, flowed through the specimen, and then through the outlet. The thermal loading was applied when the outlet water temperature reached a constant value (i.e. when thermal equilibrium was achieved between the water temperature at the inlet (10°C) and the ambient temperature of the specimen). A heating rate of approximately 5°C/min was applied until a through-thickness uniformly distributed target temperature of 220°C was attained, which was selected as being between glass transition and decomposition temperatures. The temperature progressions of the chamber and the temperature sensors were recorded.

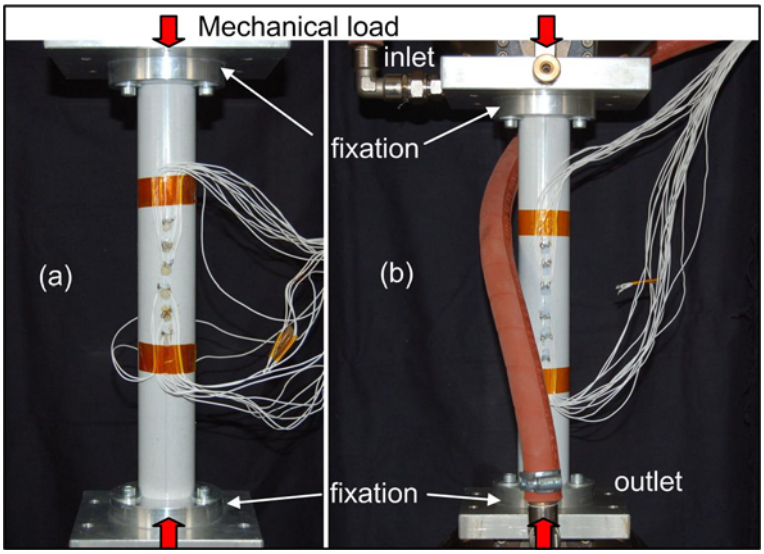

Fig. 1. Experimental setup for thermal response experiments (unloaded) and structural endurance experiments: (a) non-cooled, (b) water-cooled

2.3 Structural endurance experiments

Since the tubes used in the structural endurance experiments were not

equipped with temperature sensors (see Section 2.2), only the chamber temperature was recorded and it was assumed that through-thickness temperature progression was similar to that in the thermal response experiments. The tubes were fully fixed, see Fig. 1, and therefore exhibited a buckling length of $L/2$. Six scenarios were investigated, including different combinations of compressive load levels and water flow rates as summarized in Table 1 (two specimens per scenario for scenarios MN1/2 and MC1/2, one specimen for scenarios MC3/4).

In each scenario, the specimen was first loaded in a load-control mode to a prescribed level: 100%, 75%, 50% of SLS (serviceability limit state) load, see Table 1. The load was then kept constant during the subsequent thermal loading process. The SLS-load, P_{SLS}, was determined as follows:

$$P_{SLS} = \frac{f_c \cdot A}{\gamma_M \cdot \gamma_F} = 68 \text{ kN} \tag{3}$$

$$\gamma_M = \gamma_{M,1} \cdot \gamma_{M,2} \cdot \gamma_{M,3} = 1.26 \tag{4}$$

where γ_M is the resistance factor, which can be assumed according to Eq. (4) and [21] as being composed of: $\gamma_{M,1}$=1.15 (properties derived from tests), $\gamma_{M,2}$=1.1 (pultruded material), and $\gamma_{M,3}$=1.0 (short-term loading). The load factor was assumed as being γ_F=1.4.

After the load level was reached, water was circulated at the same flow rates as those used in the thermal response experiments, see Table 1. Thermal loading was then applied (set as time t=0) according to the predefined temperature-time curve (see Section 2.2) until ultimate failure occurred or the prescribed time duration was reached.

3 EXPERIMENTAL RESULTS

3.1 Thermal response experiments

The non-cooled specimen, TN, exhibited similar temperature progressions at different depths because of similar thermal boundary conditions on the outer and inner surfaces, as shown in Fig. 2. The through-thickness temperatures increased in parallel to the chamber temperature up to the pre-

scribed value of 220°C.

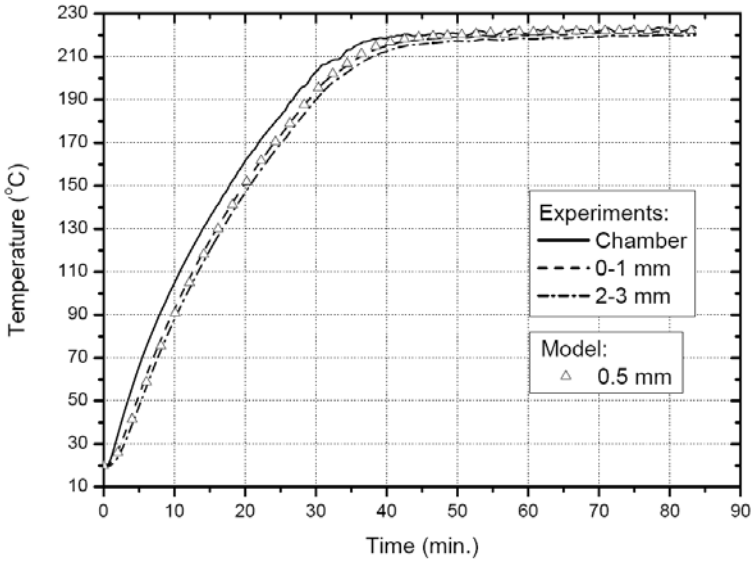

Fig. 2. Time-dependent chamber temperature and through-thickness temperature progression for non-cooled specimen TN

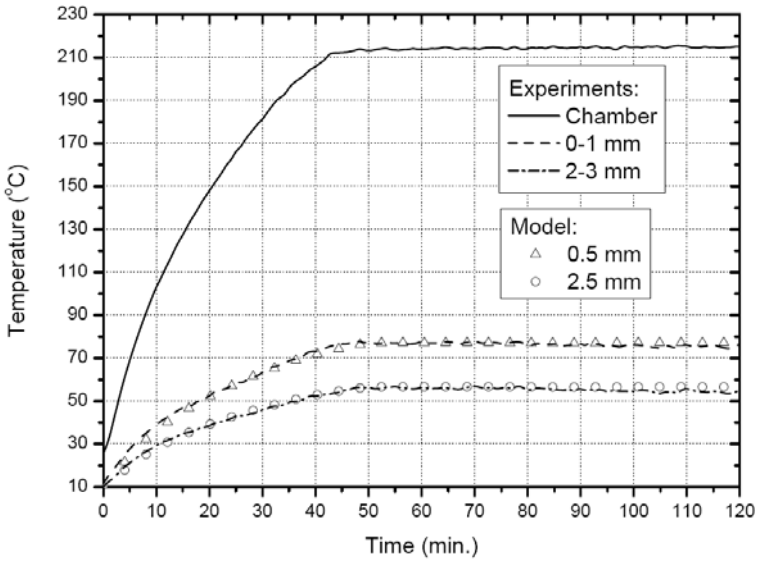

Fig. 3. Time-dependent chamber temperature and through-thickness temperature progression for water-cooled specimen at low flow rate (TC1)

The through-thickness temperature progression of the water-cooled specimen at low flow rate, TC1, is shown in Fig. 3. The water cooling caused a steep temperature gradient in the through-thickness direction. After approximately 50 minutes a steady state was reached with a hot face temperature of approximately 77°C (clearly below $T_{g,onset}$), while the cold face temperature remained approximately 57°C. The water temperature at

the outlet increased 5.6 °C compared to the inlet temperature of 10°C. The temperature progression in the chamber was similar to that in the non-cooled experiment with a slightly lower (3°C) target temperature.

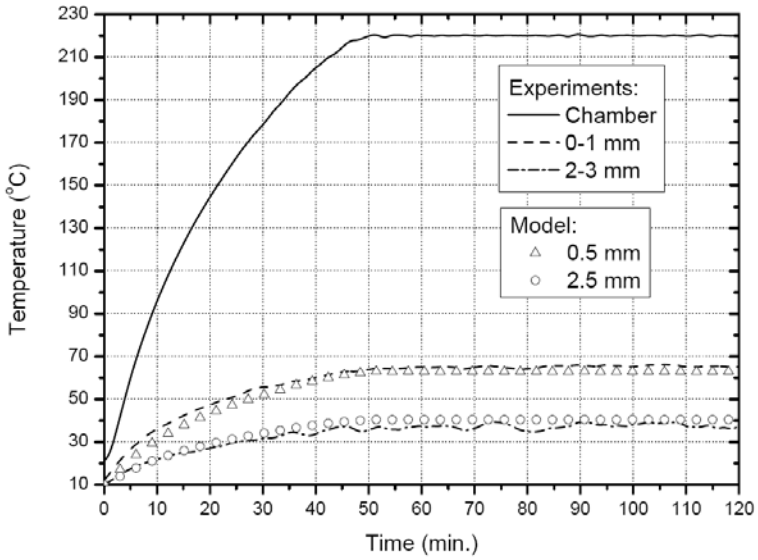

Fig. 4. Time-dependent chamber temperature and through-thickness temperature progression for water-cooled specimen at high flow rate (TC2)

The high rate water-cooled specimen, TC2, behaved similarly to the low rate TC1, although the steady state temperatures were much lower (15°C on average) compared to TC1: approximately 65°C at the hot face and 38°C at the cold face, see Fig. 4. The water temperature increased by only 2.1°C. The chamber temperature progression was similar to that in the non-cooled scenario and varied only within the accuracy of the chamber.

3.2 Structural endurance experiments: MN1 and MN2

Scenarios MN1 and MN2 involved specimens without water cooling subjected to 100% and 50% SLS-loads, see Table 1. The axial displacements were -3.1 mm (MN1) and -1.7 mm (MN2) after mechanical loading (negative sign indicates shortening of specimen). The displacement increase during the subsequent thermal loading process is shown in Fig. 5 (displacements do not include those from mechanical loading and start with 0-value at t=0). A continuous increase in axial displacements was observed for both load levels because of stiffness degradation due to thermal expo-

sure, which was more dominant than thermal elongation. Specimens MN1 failed after 7.1 mins (average) of thermal loading, while specimens MN2 resisted for slightly longer (13.0 mins on average) because of the lower load level. A local crushing of the compact FRP tubes under compression was observed, see failure mode shown in Fig. 6(a). At failure, the average through-thickness temperatures were approximately 67°C and 112°C for MN1 and MN2 respectively (see Fig. 2).

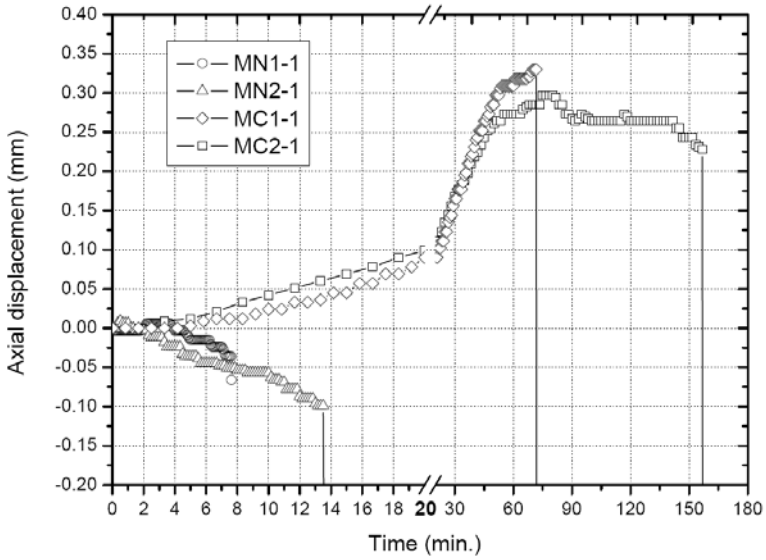

Fig. 5. Time-dependent vs axial displacement curves for non-cooled and water-cooled specimens (positive values indicate elongations)

3.3 Structural endurance experiments: MC1 and MC2

Water-cooled specimens were subjected to 100% SLS loading in these scenarios, while low (MC1) and high (MC2) flow rates were applied (see Table 1). Mechanical loading resulted in axial displacements of -3.0 mm (MC1) and -3.1 mm (MC2), similar to those in the non-cooled specimens (MN1). During the thermal loading process, thermal elongation exceeded compression strain, as shown in Fig. 5, since stiffness degradation was low due to water cooling. The thermal elongation in both scenarios stabilized after approximately 60 min of thermal exposure because a stable temperature distribution was achieved (see Figs. 3 and 4). Shortly afterwards, MC1 specimens failed (after 72 min on average at 65°C average through-

thickness temperature), while a slight decrease in elongation was observed for MC2 specimens up to failure after 164 min (on average, at 54°C average temperature, see Figs. 3 and 4). The slight decrease in elongation may be attributed to creep effects during the extended loading period.

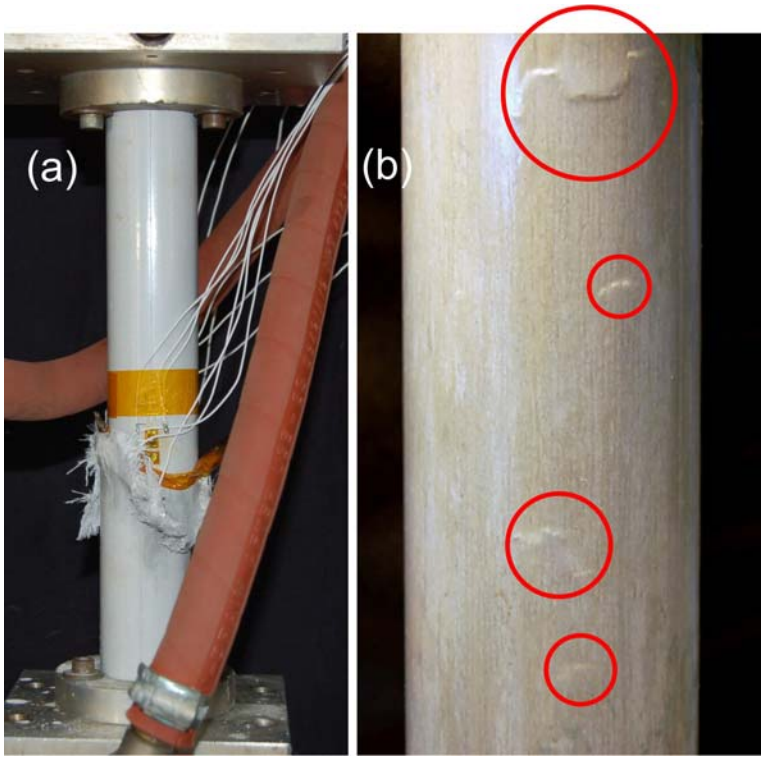

Fig. 6. Failure modes: (a) specimen MN2-2, (b) failure initiation in specimen MC3-1

3.4 Structural endurance experiments: MC3 and MC4

Specimens were subjected to 75% (MC3) and 50% (MC4) SLS loads and water cooled at high flow rate, see Table 1. After mechanical loading, axial displacements were -2.3 mm (MC3) and -1.6 mm (MC4). The time-dependent axial displacement curves of these two scenarios behaved similarly to those of MC1/2 because of a similar water-cooling effect.

Specimens in scenarios MC3/4 did not fail within the planned experiment duration. After cooling, the surfaces of specimens MC4 did not exhibit any damage, while failure initiation (a form of wrinkling) was apparent on specimens MC3 subjected to the higher compressive load, see Fig. 6(b). The residual compressive strength measured at ambient temperature was

231 MPa (MC4) and 299 MPa (MC3), corresponding to 68% and 88% of the nominal compressive strength respectively (see Section 2.1).

4 MODELING AND DISCUSSION

4.1 Temperature responses

The thermal response model proposed in [20] was used to predict temperature progression in the specimens and for further validation. Assuming a one-dimensional heat transfer in the through-thickness direction, specimens were discretized into 6 layers (thus a 0.5-mm thickness for each layer), and the temperature responses were calculated at each time step by solving the heat transfer governing equation using a finite difference method. Based on the temperature measurements, convection heat transfer coefficients of 120 and 230 W/m^{2}K were obtained for low and high flow rate respectively.

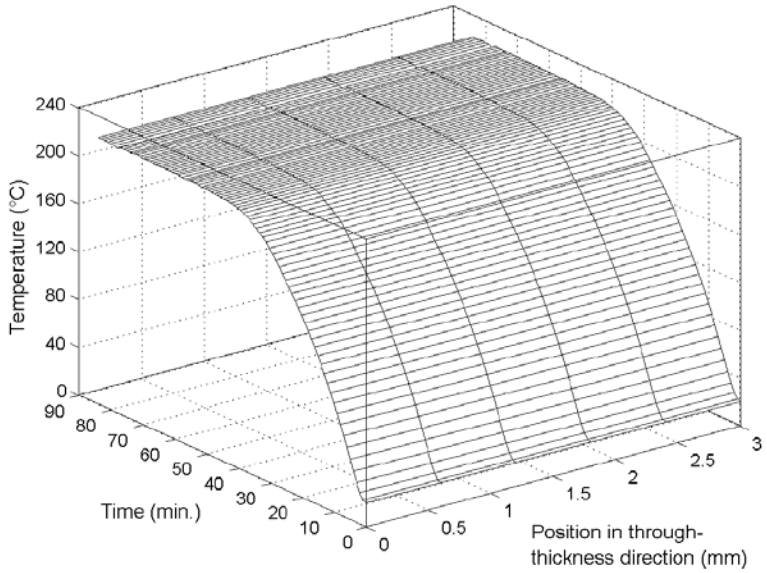

Fig. 7. Temperature field for non-cooled specimens (TN and MN1/2, position in through-thickness direction denotes distance from outer hot surface)

The calculated temperature field up to 220°C for the non-cooled specimen TN (representative for scenarios MN1/2) is shown in Fig. 7. The temperature progression is illustrated along the time and temperature axes, while the temperature gradient in the through-thickness direction is illu-

strated along the position and temperature axes. The temperature gradient was found to be very small. The temperature progression at 0.5 mm distance from the outer (hot) surface was extracted and compared with the experimental results and a good agreement was found, see Fig. 2.

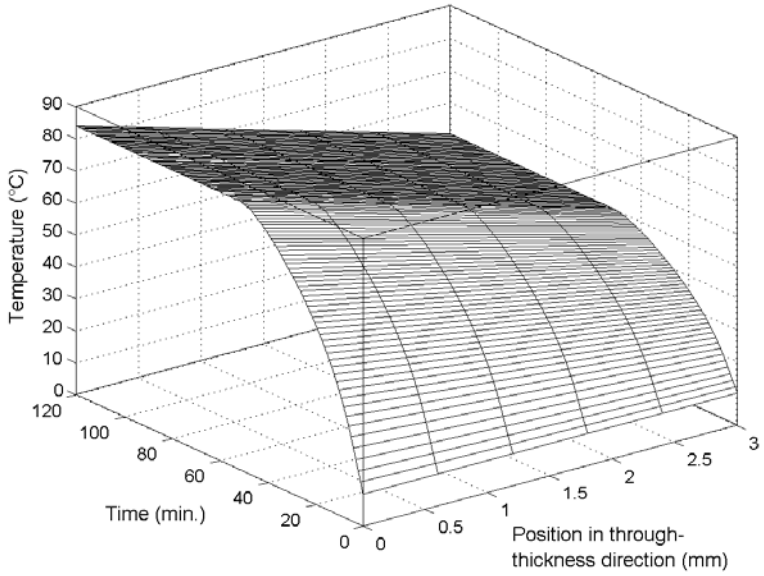

Fig. 8. Temperature field for water-cooled specimens at low rate (TC1 and MC1, position in through-thickness direction denotes distance from outer hot surface)

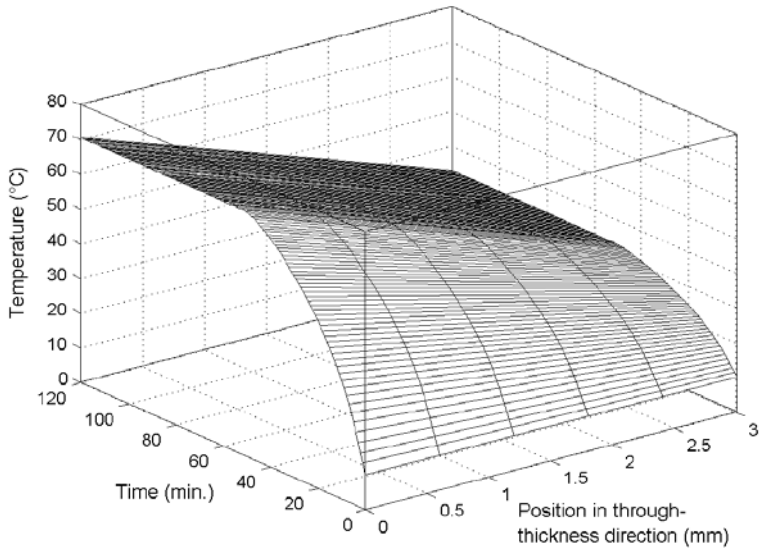

Fig. 9. Temperature field for water-cooled specimens at high rate (TC2 and MC2-4, position in through-thickness direction denotes distance from outer hot surface)

The calculated temperature fields for the two water-cooled specimens

TC1 and TC2 are shown in Fig. 8 (low rate) and Fig. 9 (high rate), the former being representative for scenario MC1 and the latter for MC2-4. The gradient at the high rate was significantly higher than that at the low rate. The temperature progressions at 0.5-mm and 2.5-mm distances from the hot face were again extracted and compared to the experimental results shown in Figs. 3 and 4 and again a very good agreement was found.

4.2 Strength degradation

A model for predicting the compressive strength degradation of FRP materials in fire was applied as proposed in [8] for further validation. Similarly to a previously developed model for stiffness degradation [22], it assumes that an FRP material at a certain temperature can be modeled as a mixture of materials that are in different states (glassy, leathery and decomposed). The strength of the mixture is determined by the quantity and strength of the material in each state according to an inverse rule of mixture, as expressed by Eq. (5):

$$\frac{1}{f_{c,m}} = \frac{(1-\alpha_g)}{f_{c,g}} + \frac{\alpha_g \cdot (1-\alpha_d)}{f_{c,l}} \tag{5}$$

where $f_{c,m}$ is the temperature-dependent nominal compressive strength of the mixture, $f_{c,g}$ and $f_{c,l}$ are the nominal compressive strengths in the glassy and leathery states, the former being the value at ambient temperature and the latter the value after glass transition and before decomposition, (9.2% of $f_{c,g}$ [8]). α_g and α_d are the conversion degrees for glass transition and decomposition respectively calculated on the basis of kinetic theory, as demonstrated in [20, 22]. The decomposed state is considered as having neither stiffness nor strength. Applying the temperature responses from the previous section, this model was directly used to estimate the strength of each layer at each time step. The resulting strength degradation is shown in Figs. 10-12 for the different scenarios.

Fig. 10 shows the through-thickness strength distribution at each time step for the non-cooled specimens (MN1 and MN2, see Table 1). The time-dependent strength degradation can be identified by selecting a specific

position (layer) in the through-thickness direction. The strength rapidly and almost uniformly decreased in the thickness direction to 9.2% of the initial value (leathery state) during the first 30 mins and then remained constant, while the corresponding temperature increased to around 195°C (see Figs. 2 and 7).

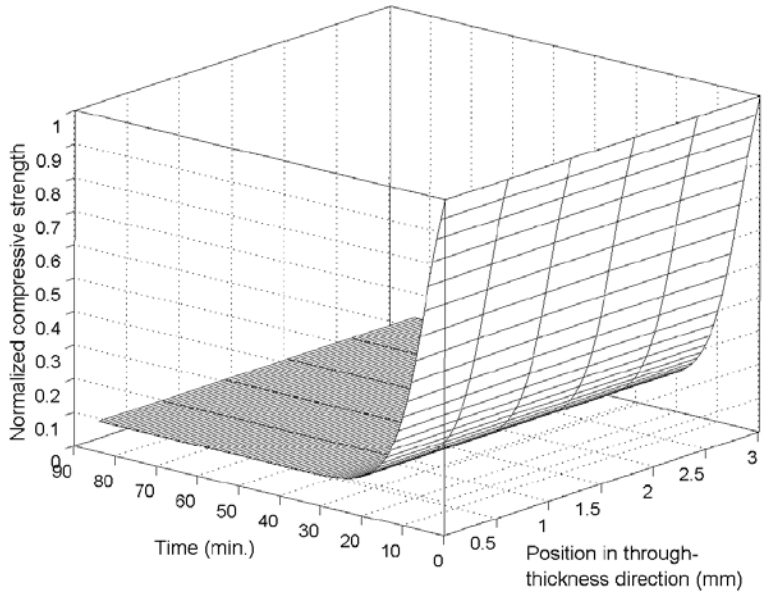

Fig. 10. Strength degradation for non-cooled specimens (MN1/2, position in through-thickness direction denotes distance from outer hot surface)

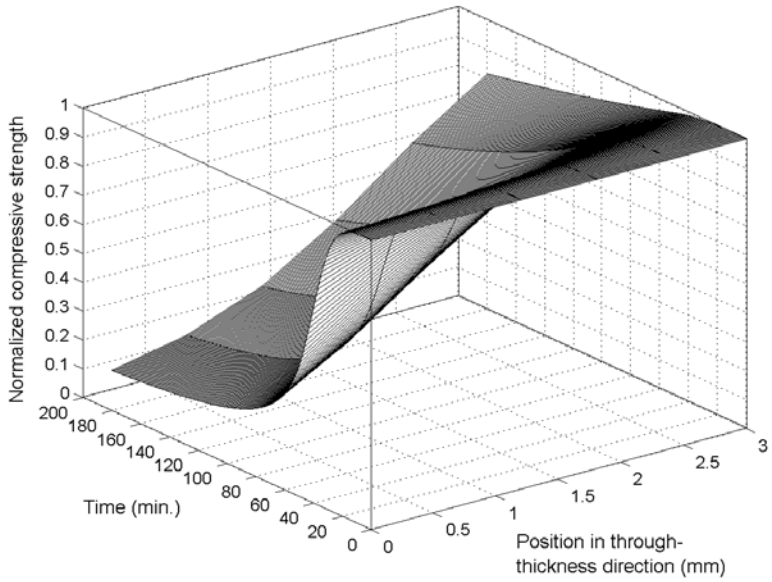

Fig. 11. Strength degradation for water-cooled specimens at low rate (MC1, position in through-thickness direction denotes distance from outer hot surface)

The through-thickness strength distribution for specimens with water cooling applied at a low rate (MC1) is shown in Fig. 11. Compared to Fig. 10, strength decreased much more slowly in all layers because of the water-cooling effect. At the inner cold surface, strength decreased only approximately 20% after 180 mins of thermal loading, while at the outer hot surface strength decreased to 14% of the initial value after 180 mins.

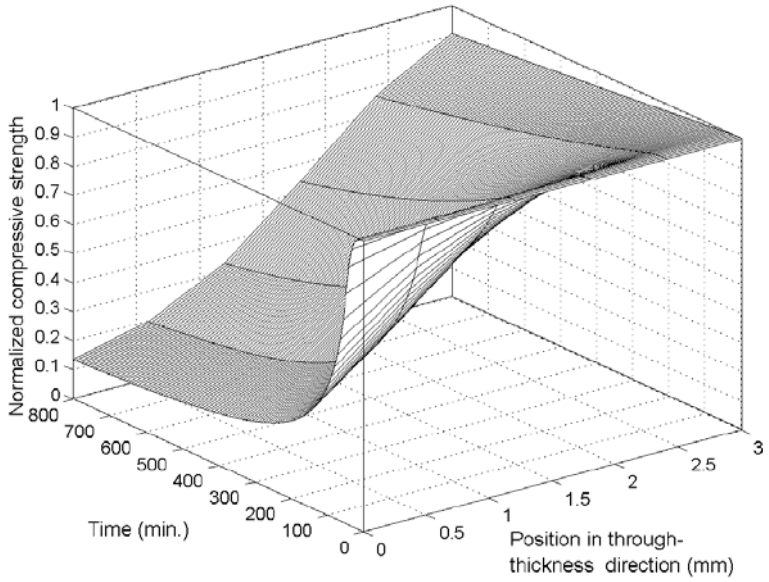

Fig. 12 Strength degradation for water-cooled specimens at high rate (MC2-4, position in through-thickness direction denotes distance from outer hot surface)

The water-cooling effect became more obvious for specimens at a high flow rate (MC2-4), as shown in Fig. 12. At the inner surface, strength decreased only approximately 3% after 180 mins and 10% after 800 mins, while a decrease to 28% was observed at the outer surface after 180 mins and to 13% after 800 mins.

It may seem surprising that the strength in the water-cooling cases decreased although temperatures remained clearly below the onset of the glass transition temperature of the resin (77/65°C for MC1/2-4 vs $T_{g,onset} \approx$ 110°C). However, DMA measurements (from which $T_{g,onset}$ was deduced) evidenced a storage modulus reduction as from 20°C [5, 8]. Furthermore, compressive strength measurements [8, 23] (which may be more sensitive to temperature than stiffness) showed a strength decrease of up to 35% be-

tween 20°C and 60°C. A further increase in strength degradation may occur due to time effects during long-lasting exposure, see next section. In accordance with these observations, the beginning of the glass transition process ($\alpha_g = 0$) in the model was set as low as 20°C.

4.3 Time-to-failure

In analogy with Eq. (5), the time-dependent ultimate load, $P_u(t)$, can be obtained as follows:

$$P_u(t) = A \cdot \left(\sum_{i=1}^{n} \frac{A_i}{A \cdot f_{c,i}(t)} \right)^{-1} \tag{6}$$

where n is number of layers, $f_{c,i}(t)$ is the strength of the i^{th} layer at time t, and A_i and A are the cross sectional area of the i^{th} layer and the total cross section respectively. The resulting time-dependent ultimate loads for non-cooled and water-cooled specimens at low and high rates are shown in Fig. 13 (values normalized by the ultimate load at ambient temperature, 120 kN).

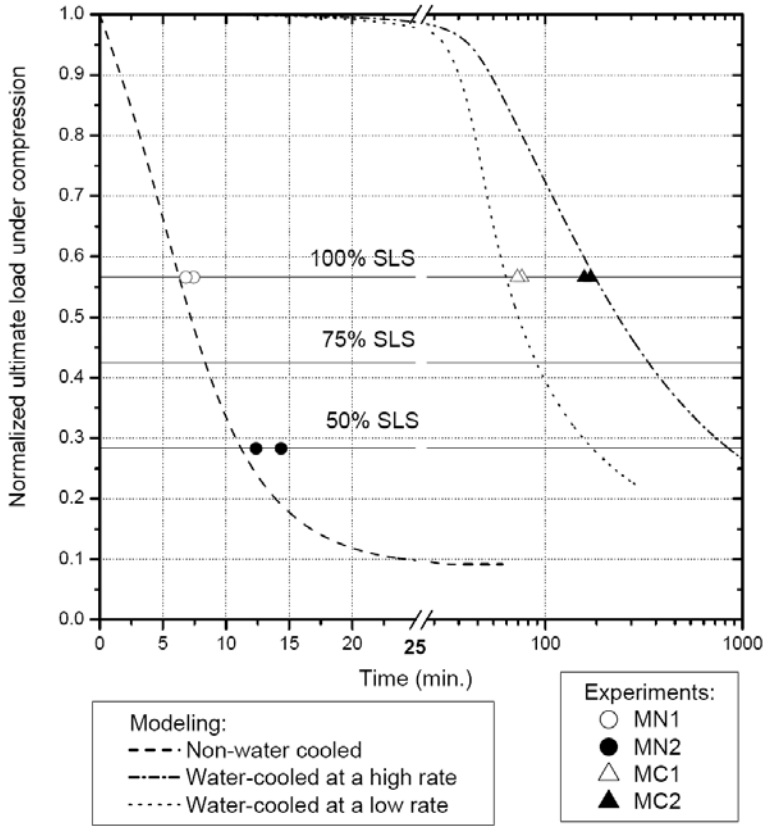

Fig. 13 Time-to-failure prediction and comparison to experimental results

A far greater decrease in load-carrying capacity was found for the scenarios without water cooling, where the ultimate load decreased to the SLS-load level (corresponding to 56.6% of the ambient ultimate load) after 6.3 mins of thermal loading, and further decreased to 50% of the SLS-load level (28.3% of ambient ultimate load) after 11.2 mins. When compared to the experimental results (scenarios MN1/2), good agreement was found between the measured and predicted ultimate loads, see Table 1 and Fig. 13. A slight underestimation of the time-to-failure of 14% resulted (average for all four specimens), which was, however, on the safe side.

The decrease in the ultimate load of the water-cooled specimens (low and high rates) began only after 30 mins at which point the non-cooled specimens had already lost 81% of their capacity, see Fig. 13. Compared to the water-cooling system used for full-scale GFRP panels in [18], where results were not sensitive to flow rate, the higher flow rate considerably improved the performance in this case. This different behavior was primarily attributed to the material thicknesses in the heat flow direction: only 3 mm in this case vs 15.2-17.4 mm in [18]. When compared to the experimental results obtained for scenarios MC1/2, the modeling time-to-failure again showed good agreement (average difference of 11%, see Table 1 and Fig. 13).

It should be noted that, for these two scenarios, temperatures in the through-thickness direction had already stabilized after 56 mins of thermal loading (see Figs. 3 and 4), long before time-to-failure was reached (72.0 and 163.7 mins, average values for MC1/2). This demonstrates that the strength degradation of composite material at elevated and high temperatures is not only temperature-dependent, but also time-dependent, i.e. the load-carrying capacity continuously decreases with time even at a constant elevated temperature.

For scenarios MC3 and 4, the specimens did not fail after 525 mins and 250 mins of thermal loading, the former in contrast to the modeling results, which predicted a time-to-failure of 340 mins, see Fig. 13. Predictions of the time-to-failure at low load levels and low temperatures are

very sensitive to small inaccuracies in the prediction of the load decrease, as can be seen from Fig. 13. Specimen MC3, however, must have been close to global failure as indicated by the local wrinkling observed and considerable reduction in post-heating ultimate load (68% of ambient ultimate load). Specimen MC4 already showed an ultimate load reduction of 88% after 250 mins, representing 29% of the predicted time-to-failure (860 mins).

5 CONCLUSIONS

An active fire protection system, liquid cooling, was applied to pultruded GFRP tubes subjected to combined thermal and mechanical loading in order to maintain material temperature below the critical glass transition temperature. The experimental time-to-failure resulting from different experimental scenarios, comprising different flow rates and load levels, compared well to the corresponding modeling results. The following conclusions were drawn:

1. The experiments demonstrated that the endurance of FRP structural components subjected to combined thermal and mechanical loading can be effectively improved by the application of a water-cooling system. The use of an appropriate flow rate enables endurance times of up to three hours at full serviceability loads to be achieved, thus easily satisfying requirements concerning fire exposure in building codes, even in the worst scenario of compressive loading.

2. While for components with higher wall thickness (> 15 mm) no significant dependence of endurance on flow rate was observed, a high sensitivity resulted for lower wall thicknesses (of approximately 3 mm. The rate of heat transfer could be increased by increasing the GFRP-water contact surface, e.g. by adding fins inside the tube.

3. The experimental results evidenced not only the temperature-dependence but also an obvious time-dependence (at constant elevated or high temperature) of the load-bearing capacity of FRP components. Since the models were derived from kinetic theory, this observed time-

dependence could be well described.

4. The previously proposed thermal response and strength degradation models were further validated by these experiments. A potential application of these models is the prediction of the time-to-failure for FRP composites on the structural level by their incorporation into structural theory and finite difference or finite element methods.

ACKNOWLEDGEMENT

The authors would like to thank the Swiss National Science Foundation for its financial support (Grant No. 200020-117592/1), and Fiberline Composites, Denmark for providing the experimental materials.

REFERENCES

1. Mouritz, AP, Gibson, AG. Fire properties of polymer composite materials. Springer, 2007.

2. Chen JK, Sun CT, Chang CI. Failure analysis of a graphite/epoxy laminate subjected to combined thermal and mechanical loading. *Journal of Composite Materials* 1985, 19(5): 216-235.

3. Griffis CA, Nemes JA, Stonesfiser FR, Chang CI. Degradation in strength of laminated composites subjected to intense heating and mechanical loading. *Journal of Composite Materials* 1986, 20(3): 216-235.

4. Gu P, Asaro RJ. Structural buckling of polymer matrix composites due to reduced stiffness from fire damage. *Composite Structures* 2005, 69: 65-75.

5. Bai Y, Post NL, Lesko JJ and Keller T. Experimental investigations on temperature-dependent thermo-physical and mechanical properties of pultruded GFRP composites. *Thermochimica Acta* 2008, 469: 28-35.

6. Kim J, Lee SW, Kwon S. Time-to-failure of Compressively Loaded Composite Structures Exposed to Fire. *Journal of Composite Materials* 2007, 41: 2715-2735.

7. Feih S, Mathys Z, Gibson AG, Mouritz AP. Modeling the tension and compression strengths of polymer laminates in fire. *Composites Science*

and Technology 2007, 67: 551-564.

8. Bai Y, Keller T. Modeling of strength degradation for fiber reinforced polymer composites in fire. *Journal of Composite Materials*, in press.

9. Gibson AG, Wright PNH, Wu YS, Mouritz AP, Mathys Z and Gardiner CPG. Integrity of polymer composites during and after fire. *Journal of Composite Materials* 2004, 38(15): 1283-1308.

10. Buchanan AH. Structural design for fire safety. Chichester: Wiley 2002.

11. Fire FL. Combustibility of plastics. Van Nostrand Reinhold, New York, USA 2000.

12. Grand AF, Wilkie CA. Fire retardancy of polymeric materials. Marcel Dekker, Inc., Basel.

13. Allen B. Intumescent coating solutions in fire scenarios. 2nd International Conferences on Composites in Fire, Newcastle upon Tyne, UK, 2001.

14. Cote A. Fire protection handbook. 19th ed., National fore protection association, MA, USA, 2003.

15. Dallaire G. Kansas city bank tower features water-filled columns, exposed spandrels. *Civil Engineering* 1976, 1: 58-62.

16. Marks PR. The fire endurance of glass-reinforced epoxy pipes. Proceedings of the 2nd International Conference on Polymers in a Marine Environment, London, UK, 1987.

17. Davies JM, Dewhurst DW. The fire performance of GRE pipes in empty and dry, stagnant water filled, and flowing water filled conditions. Proceedings of International Conference on Composites in Fire, Newcastle upon Tyne, UK, 1999.

18. Keller T, Tracy C, and Hugi E. Fire endurance of loaded and liquid-cooled GFRP slabs for construction. *Composites Part A* 2006, 37(7): 1055-1067.

19. Bai Y, Vallée T, Keller T. Modeling of thermo-physical properties for FRP composites under elevated and high temperatures. *Composites Science and Technology* 2007, 67(15-16): 3098-3109.

20. Bai Y, Vallée T, Keller T. Modeling of thermal responses for FRP composites under elevated and high temperatures. *Composites Science and*

Technology 2008, 68(1): 47-56.

21. EuroComp. Structural design of polymer composites, EuroComp design code and handbook, edited by J. L. Clarke. E&FN SPON, London, 1996.

22. Bai Y, Keller T, Vallée T. Modeling of stiffness of FRP composites under elevated and high temperatures. *Composites Science and Technology* 2008, 68: 3099-3106.

23. Wong PMH, Davies MJ, Wang YC. An experimental and numerical study of the behavior of glass fiber reinforced plastics (GRP) short columns at elevated temperatures. *Composite Structures* 2004, 63: 33-43.

2.9 Modeling of post-fire stiffness

Summary

It was found that an FRP load-bearing structure may retain a certain percentage of its strength and stiffness after fire exposure. Post-fire mechanical models allow evaluation of the damage and estimation of the residual capacity of the structure or its components.

A new model is proposed in this paper to estimate the post-fire stiffness of FRP composites after different fire-exposure times. The model considers the E-modulus recovery of the material after cooling from temperatures ranging between glass transition and decomposition during the fire (i.e. leathery or rubbery state), as indicated by the two DMA tests conducted on the same specimen. Since the content of each state can be estimated using the thermomechanical models in Section 2.2, the post-fire stiffness can therefore be evaluated.

Furthermore, based on the proposed models, the through-thickness temperature gradients and remaining resin contents (RRC) can be calculated, which were frequently used in previous two- or three-layer post-fire models from literature. Post-fire stiffness estimated by the new model and refined two- and three-layer post-fire models based on temperature or RRC criteria was compared with experimental results. Good agreement between the calculated and measured post-fire stiffness of two full-scale cellular GFRP panels subjected to mechanical and thermal loading was found for realistic fire-exposure times of up to 2 hours.

Reference detail

This paper was published in Composites Part A: Applied Science and Manufacturing 2007, volume 38, pages 2142-2153, entitled

"Modeling of post-fire stiffness of E-glass fiber-reinforced polyester composites" by Yu Bai and Thomas Keller.

MODELING OF POST-FIRE STIFFNESS OF E-GLASS FIBER REINFORCED POLYESTER COMPOSITES

Yu Bai and Thomas Keller

Composite Construction Laboratory CCLab, Ecole Polytechnique Fédérale de Lausanne (EPFL), BP 2225, Station 16, CH-1015 Lausanne, Switzerland.

ABSTRACT:

A new model is proposed to estimate the post-fire stiffness of FRP composites after different fire exposure times. The model considers the E-modulus recovery of the material if cooled down from temperatures between glass transition and decomposition during the fire. Furthermore, based on this model, the through-thickness temperature gradients and remaining resin contents (RRC) can be calculated. Post-fire stiffness estimated by the new model and refined two- and three-layer post-fire models based on temperature or RRC criteria was compared with experimental results. A good agreement of calculated and measured post-fire stiffness of two full-scale cellular GFRP panels subjected to mechanical and thermal loading was found for fire exposure times up to two hours.

KEYWORDS:

Polymer-matrix composites; modeling; pultrusion; post-fire properties

1 INTRODUCTION

Fiber-reinforced polymer (FRP) composites have been successfully used in space, marine, and civil applications. One of the major advantages of FRP composites is their high strength-to-weight ratio at ambient temperatures (less than 100°C). A disadvantage of these materials, however, is that their stiffness and strength decrease significantly at raised temperatures that reach the range of glass transition [1, 2]. Models for temperature-dependent thermophysical and thermomechanical material properties were proposed by the authors in [3, 4]. Assembling these material properties, thermochemical and thermomechanical models were developed to predict the thermal and mechanical responses of FRP composites under elevated and high temperatures [5, 6]. Nevertheless, after being subjected to a fire, it was found that a certain percentage of the strength and stiffness of an FRP load-carrying structure may remain. Post-fire mechanical models allow the evaluation of the damage and to estimate the remaining capacity of the structure or its components.

One of the first formal investigations into the post-fire mechanical properties of FRP materials was performed by Pering et al. in 1980 [7]. Carbon fiber-reinforced epoxy laminates were exposed to fire on both sides by gas-fueled burners for up to 15 minutes. The loss of mass over time was approximated as a single-step Arrhenius reaction. An empirical correlation was then made between the rate of char formation and the remaining shear strength and stiffness, while the remaining tensile strength and stiffness were correlated to the loss of mass. Based on Pering's work, Springer presented a more generalized analytical model in 1984 [8]; the mechanical portion of the model was, however, only validated on cellulose materials. In 1993, Sorathia et al. [9] exposed small coupons of thermoplastic and thermosetting matrix composites to low heat fluxes in a cone calorimeter for up to 20 minutes. A temperature-limit criterion was proposed for the determination of post-fire mechanical properties. Thereby, the portion of the material that does not exceed this critical temperature during fire exposure was considered to retain virgin mechanical properties.

From 1999 to 2004, Gardiner, Mouritz, and Mathys [10-15] developed an approach for determining the residual mechanical properties of fire damaged glass-reinforced polyester, vinylester, and phenolic composites. Validation was performed on mostly small-scale specimens using a cone calorimeter, although Gardiner has also used kerosene pool fires for larger specimens. The approach involves the discretization of the material into two layers: a fully degraded region that is simplified as having little or no residual mechanical properties, and an unaffected region that is simplified as having the same properties as before the fire exposure. An empirical correlation was made between the depth of the fully degraded char layer, the duration of exposure, and the time at that charring first occurred.

The key issue in the existing discretized post-fire stiffness models is the determination of the border between the different layers. Initially, model calibration was carried out by physically measuring this depth [13]. This method was further developed through empirical equations related to post-ignition fire exposure time [15], by experimentally studying the through-thickness temperature profile [1], and by the use of a pulse-echo instrument and a percentage remaining resin content (RRC) criterion [16]. Empirical data fitting resulted in a RRC criterion, which stipulates that the regions where less than 80% of the resin remains are considered degraded [16]. An experimental investigation was conducted by Keller et al. [17] where large-scale specimens were subjected to true flaming heat, with exposure times lasting up to 120 minutes. Two- and three-layer models were developed to predict post-fire stiffness and a good agreement was found with the experimental results. The border between different layers was determined by characteristic temperature points: glass transition temperature, T_g, for the two-layer model and the onsets of glass transition and decomposition temperatures, $T_{g,onset}$ and $T_{d,onset}$, for the three-layer model [1].

From the previous research it is seen that information from the fire damaged specimens such as measured temperature profiles or remaining resin contents is necessary for estimating the post-fire stiffness. Based on

the thermochemical and thermomechanical models developed in [5, 6], the predicted temperature profiles and the degree of decomposition can be used to evaluate the post-fire stiffness using either a temperature or RRC criterion, thus information from fire damaged specimens is not necessary. Furthermore, based on two DMA tests performed on the same specimen, a new post-fire stiffness model is proposed considering the stiffness recovery of material that was between the glass transition and decomposition state during fire. The results from the models are compared with the post-fire stiffness obtained from the aforementioned experiments on two cellular FRP panels [17], which were damaged by fire exposure up to 120 minutes.

2 EXPERIMENTAL INVESTIGATION

2.1 Experimental description

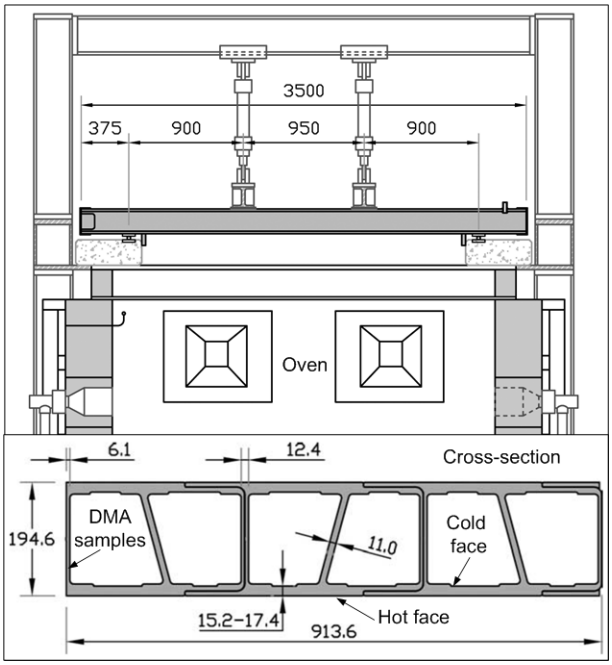

Fig. 1. Experimental specimen and setup

In a series of fire endurance experiments, three full-scale GFRP slab specimens (SLC01, SLC02, and SLC03) were fabricated and tested to study their response when subjected to both sustained serviceability level structural loads and the ISO-834 fire condition (see Fig. 1). The cellular slab specimens, assembled from three pultruded dual-cell sections, were 3500 mm in length, 913.6 mm in width, and 194.6 mm in depth each, as shown

in Fig. 1. The mechanical properties of the E-glass fiber/polyester material and the geometric parameters are summarized in Table 1. The specimens were loaded in a four-point bending arrangement. Liquid-cooling was used to improve the fire performance of the slabs. The SLC01 experiment was conducted at a flow rate of $2m^3$/hr water in the cells, the SLC02 experiment was conducted at $1m^3$/hr, while the SLC03 experiment was carried out without liquid-cooling as a reference. Structural tests were conducted for specimens SLC01 and SLC02 before and after the fire experiments to examine their pre-fire and post-fire structural behavior. Post-fire mechanical tests were not conducted on the non-cooled specimen SLC03 because the specimen failed after 57 minutes of fire exposure. Detailed information about the experimental set-up can be found in [17, 18].

Property	Face sheets	Webs	Total
E_x (GPa)	21.24	17.38	-
G_{xy} (MPa)	5580	7170	-
A (mm^2)	15350	11480	42180
Height (mm)	15.2-17.4	161	194.6
Width (mm)	913.6	71.3	913.6

Table 1. Mechanical properties and geometric parameters of cellular GFRP specimens

2.2 Time-dependent thermal responses

The measured temperature profiles through the lower face sheet of the liquid-cooled panel of specimen SLC02 at different times are shown in Fig. 2. With increasing time, the hot face temperature increased and gradients became steeper, while the cold face temperature remained almost unchanged due to liquid-cooling. Figure 3 shows the temperature profiles of the non-cooled specimen SLC03. The temperature increase at the hot face was similar to that of specimen SCL02. However, due to the absence of liquid-cooling, the cold face temperature also increased and the gradients remained less steep. The flow rate did not markedly influence the results,

thus the thermal responses of specimen SCL01 was similar to that of specimen SLC02. Detailed results of the thermal responses of the specimens can be found in [5, 17]. The temperature gradients were directly used to determine the borders of different layers in the discretized post-fire stiffness models presented in [1].

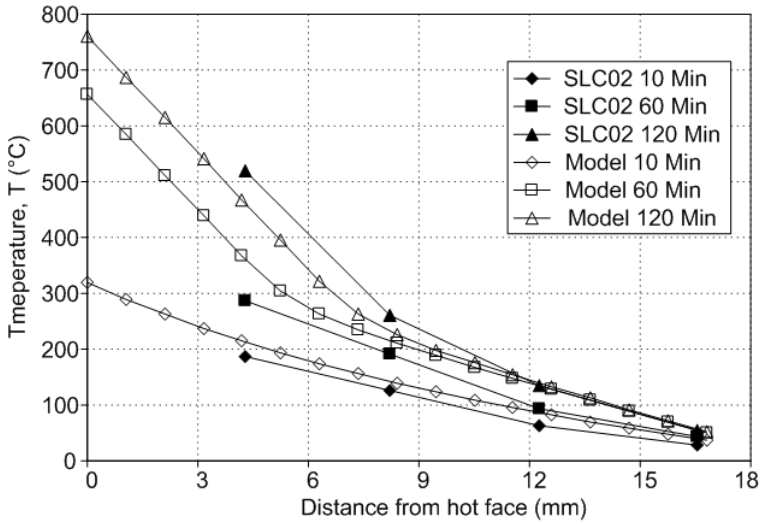

Fig. 2. Temperature profiles through lower face sheet of liquid-cooled specimen from model and experiments

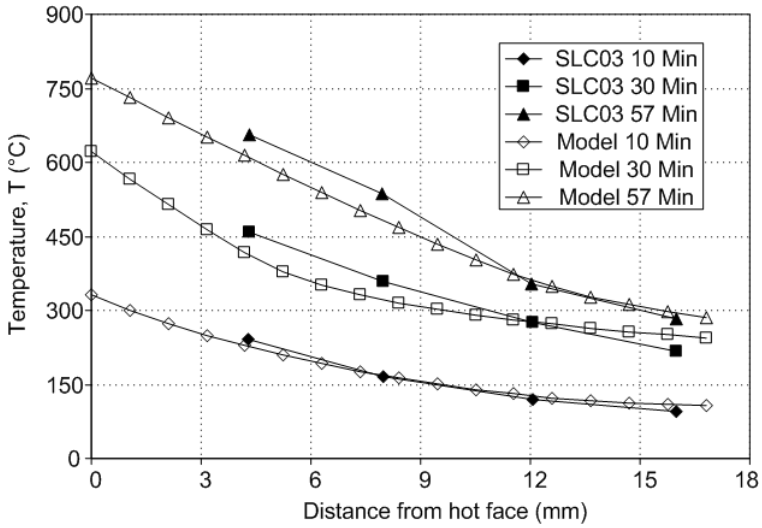

Fig. 3. Temperature profiles through lower face sheet of non-cooled specimen from model and experiments

2.3 Time-dependent mechanical responses

The time-dependent deflections at mid-span of all specimens during fire

exposure are illustrated in Fig. 4. After the ignition of the burners, the deflections increased sharply in the first fifteen minutes for all specimens. While the liquid-cooled specimen SLC 01/02 stabilized thereafter, the non-cooled specimen (SLC03) continued to deflect much faster than the others. At 57 mins, the non-cooled specimen SLC03 failed in the upper compressed face sheet, while experiments SLC 01/02 could be continued up to the planed 90/120 mins. The time-dependent deflection curves for SLC01/02 were almost the same due to the similar liquid-cooling effects.

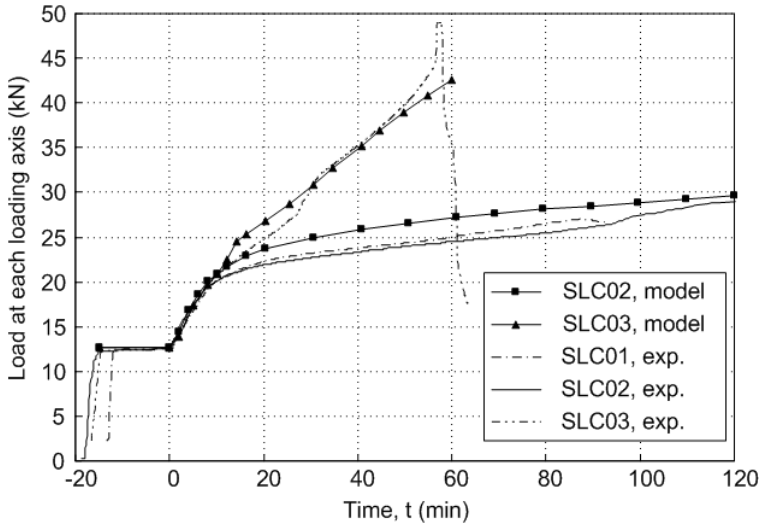

Fig. 4. Time-dependent deflections during fire exposure from model and experiments

2.4 Load-deflection responses from pre-fire, fire exposure and post-fire experiments

Pre-fire load-bearing experiments up to serviceability loads were performed on all specimens in the same four-point-configuration. Figure 5 shows the corresponding load-deflection responses of specimens SLC01/02, which survived the fire experiments. Furthermore, Fig. 5 illustrates the measured load-deflection relationship at the end of fire exposure (90/120 mins for SLC01/02), extracted from Fig. 4. After cooling down of specimens SLC01/02, both were loaded up to the maximum capacity of the jacks. The responses again are shown in Fig. 5. From Fig. 5, it can be seen that the stiffness of each specimen decreased due to the fire exposure; however,

approximately one third of the stiffness loss was recovered after the specimens had cooled down.

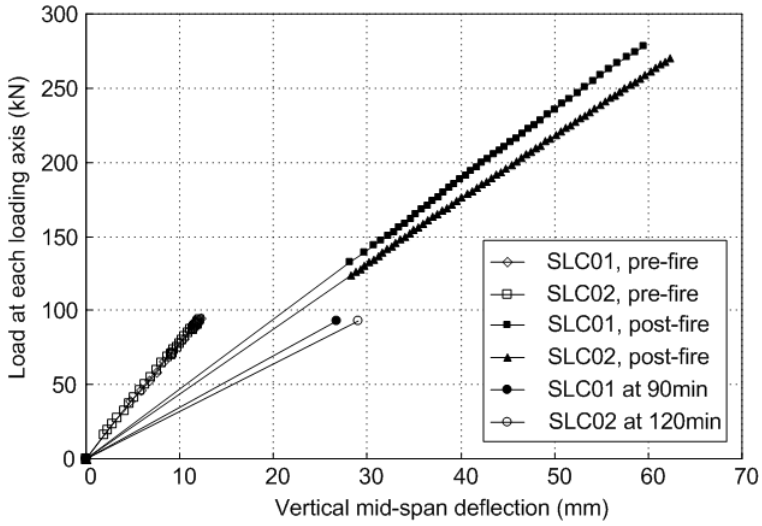

Fig. 5. Load-deformation relationship from pre-fire, fire-exposure and post-fire experiments

2.5 Stiffness from pre-fire, fire exposure and post-fire experiments

From the measured deflections, the bending stiffness (*EI*) of the panels was calculated using Equation (1) for the four-point bending setup:

$$\delta = \frac{aP}{GA} + \frac{PL^3}{24EI}\left(\frac{3a}{L} - \frac{4a^3}{L^3}\right) \quad (1)$$

where P is the applied load per loading point, L is the clear span of the slab (2.75 m) and a is distance of the loading points from the supports (0.90 m). A is the cross-sectional area of the webs, G is the shear modulus. Considering that shear stiffness was mainly given by the webs, which were not subjected to obvious temperature change (below $T_{g,onset}$ during fire endurance experiments), the value of G during and after fire was assumed to not deviate from the pre-fire value given in Table 1.

The resulting stiffness from pre-fire, fire exposure and post-fire experiments are summarized in Table 2. The fire-exposure stiffnesses of SLC01/02 were similar (7% lower for SLC02), even though fire exposure of SLC02 lasted 30 minutes longer (33% longer). This result, again, pointed out the effectiveness of liquid-cooling. However, the two specimens lost

56% of pre-fire stiffness on average during fire exposure. The post-fire experiments also showed a similar bending stiffness for SLC01/02, with an average reduction of 38% compared to the pre-fire stiffness. It is interesting to note that the post-fire stiffness differed by the same 7% between SLC01 and SLC02 as observed for the fire exposure stiffness. The average post-fire stiffness was 38% higher than the average stiffness during fire exposure and highlighted an important recovery of stiffness after cooling down.

Load per axis	Measured mid-span deflection		Resulting bending stiffness	
P [kN]	SLC01 δ [mm]	SLC02 δ [mm]	SLC01 EI [kN·m²]	SLC02 EI [kN·m²]
92 (pre-fire)	12.4	12.4	5460	5460
92.9 (fire-exposure)	26.8	29.0	2528(-54%)*	2336(-57%)*
270 (post-fire)	57.7	62.3	3500 (-36%)*	3250 (-40%)*

Table 2. Results from pre-fire, fire-exposure and post-fire experiments (* comparison of stiffness is based on pre-fire data)

2.6 E-modulus recovery quantified by DMA tests

In order to further investigate the stiffness recovery of composite materials, DMA tests were conducted on samples cut from specimen webs not exposed to an increase in temperature during the experiment (for locations see Fig. 1). The sample size was 52-mm long × 10-mm wide × 3-mm thick. Cyclic dynamic loads were imposed on a three-point-bending set-up of a Rheometric Solids Analyzer at the Laboratory of Polymer and Composite Technology, EPFL. The specimen was scanned from 0°C to 200°C (higher than the T_g, but lower than the T_d), with a heating rate of 5°C/min and a dynamic oscillation frequency of 1 Hz. Under the same test conditions as noted above, the same test specimen was scanned a second time. The corresponding results are shown in Fig 6.

After the specimen had cooled down from the first run, a shift in the

loss modulus and tan δ was observed for the second run curves, which indicated an increase in the glass transition temperature, T_g, of about 12°C (determined by the peak of the tan-δ curve). The temperature-dependent storage modulus curve from the second run (representing the E-modulus of the material), however, was similar to that of the first run. After the first run, where the material was heated up to temperatures between glass transition and decomposition, the E-modulus recovered almost to its initial value (88% of initial value based on Fig. 6). These results are in agreement with a post-curing investigation reported in [19]: the fiber dominated properties, such as E-modulus, are not greatly affected by the post-curing process.

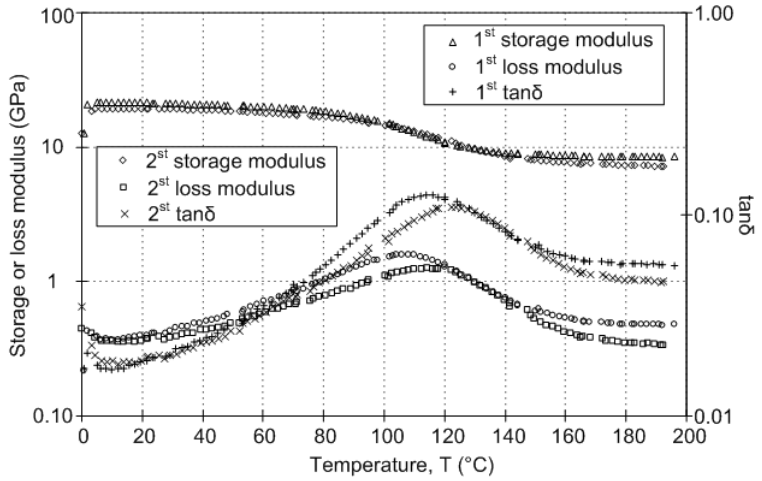

Fig. 6. Results from two DMA tests on same specimen material

Based on the thermal and mechanical response models presented in [5, 6] and the information gained on E-modulus recovery from DMA, a new model for the prediction of post-fire stiffness is proposed in the following.

3 MODELING OF POST-FIRE STIFFNESS

3.1 Thermal response model

By finite element and finite difference methods, the governing equation of one-dimensional heat transfer can be expressed for each spatial node of the lower face sheet, i, and each time step, j, as follows [5]:

$$\begin{aligned}&\rho_{i,j-1}\cdot C_{p,(i,j-1)}\frac{T_{i,j}-T_{i,j-1}}{\Delta t}\\&=k_{c,(i,j-1)}\frac{T_{i-1,j}+T_{i+1,j}-2T_{i,j}}{\Delta x^2}+\frac{k_{c,(i,j-1)}-k_{c,(i-1,j-1)}}{\Delta x}\cdot\frac{T_{i,j}-T_{i-1,j}}{\Delta x}\end{aligned} \tag{2}$$

where ρ, k_c, and C_p are the time-dependent density, thermal conductivity and specific heat capacity for the material, T denotes the temperature and t denotes the time. Subscript i and j denote the layer number at different thicknesses through the lower face sheet and the time step, respectively. Δt is the time interval of two adjacent time steps, Δx is the thickness of one layer.

The time-dependent material properties are expressed in the finite difference form as shown in Eqs. (3) to (7) according to [5]:

$$\alpha_{d,(i,j)}=\alpha_{d,(i,j-1)}+\Delta t\cdot A\cdot\exp\left(\frac{-E_{A,d}}{R\cdot T_{i,j-1}}\right)\left(1-\alpha_{d,(i,j-1)}\right)^n \tag{3}$$

$$\rho_{i,j}=\left(1-\alpha_{d,(i,j)}\right)\cdot\rho_b+\alpha_{d,(i,j)}\cdot\rho_a \tag{4}$$

$$\frac{1}{k_{c,(i,j)}}=\frac{\left(1-\alpha_{d,(i,j)}\right)}{k_b}+\frac{\alpha_{d,(i,j)}}{k_a} \tag{5}$$

$$f_{i,j}=\frac{M_i\cdot\left(1-\alpha_{d,(i,j)}\right)}{M_i\cdot\left(1-\alpha_{d,(i,j)}\right)+M_f\cdot\alpha_{d,(i,j)}} \tag{6}$$

$$C_{i,j}=C_{p,b}\cdot f_{i,j}+C_{p,a}\cdot\left(1-f_{i,j}\right)+\frac{\alpha_{d,(i,j)}-\alpha_{d,(i,j-1)}}{T_{i,j}-T_{i,j-1}}\cdot C_d \tag{7}$$

where $E_{A,d}$ is the activation energy for the decomposition process, A is the pre-exponential factor, n is the reaction order, and R is the gas constant (8.314 J/mol·K), subscripts b and a denote the material before and after decomposition, α_d is the temperature-dependent conversion degree of decomposition as determined by the chemical kinetic model in Eq. (3), C_d is the decomposition heat, M_i and M_f are the initial and final mass. Thermal conductivity, k_b and k_a, can be estimated using a series model, $C_{p,a}$ and $C_{p,b}$ can be estimated using the Einstein model and mixture approach. Detailed information for obtaining these parameters can be found in [3].

For n spatial nodes, n coupled algebraic equations were obtained. Based on the material properties at the previous time step, *j-1* ($\rho_{i,j-1}$, $C_{p,(i,j-1)}$

and $k_{c,(i,j-1)}$), the temperature profile at time step j can be calculated by solving these n coupled algebraic equations. The temperature gradient was extracted from the model and compared with the experiments in Figs. 2 and 3 for SLC03 and SLC02, respectively. A good agreement was found between the model and the experimental results. The calculated temperature gradient can be directly used to estimate the post-fire stiffness based, for example, on the temperature criterion (see Section 4.4).

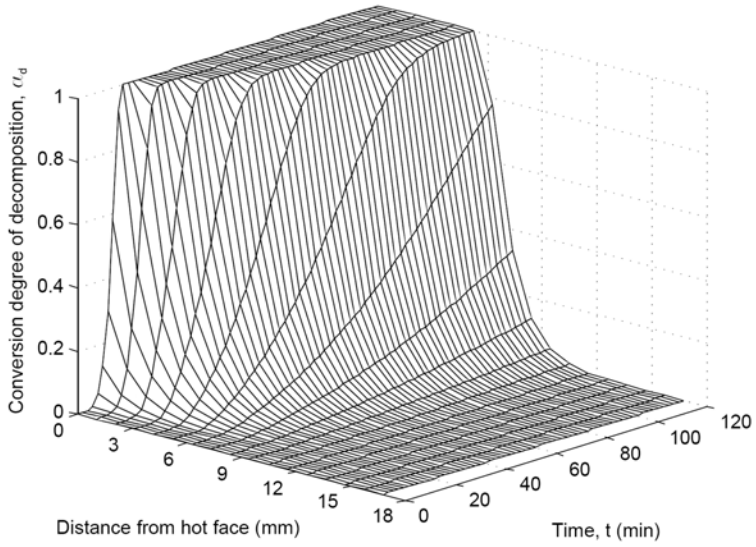

Fig. 7. Conversion degree of decomposition through lower face sheet of liquid-cooled specimen

A more accurate "Remaining Resin Content (RRC)" model was proposed in [16] to determine the boundary of different layers. An effective cutoff point between undamaged material and char was taken as RRC=80%. However, in previous research, the RRC was obtained by a pulse-echo instrument applied on the tested specimens (otherwise, a visual inspection was used to determine the boundary of different layer). In fact, based on [3], the RRC can be expressed as follows:

$$\mathrm{RRC} = V_m / V_{m0} = 1 - \alpha_d \tag{8}$$

where V_{m0} is the initial resin volume fraction, V_m is the time-dependent resin volume fraction. The time-dependent decomposition degree, α_d, was calculated according to Eq. (3) and is illustrated in Fig. 7 and 8 for SLC02 and SLC03, respectively. Substituting the value of α_d at the final time step of fire-exposure into Eq. (8), the RRC can be obtained. These simulated

data can be further used to predict the post-fire stiffness based on the RRC without information from tested specimens (see Section 4.4).

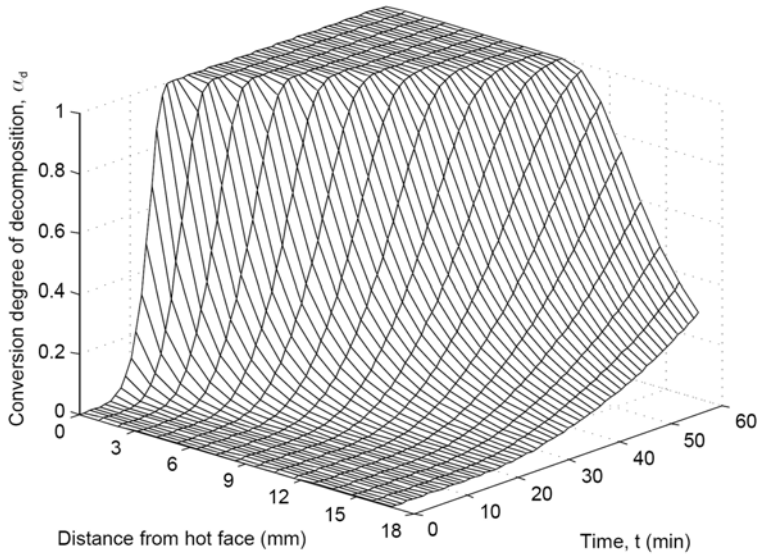

Fig. 8. Conversion degree of decomposition through lower face sheet of non-cooled specimen

3.2 Mechanical response model

Different material states (glassy, leathery, rubbery, and decomposed) can be found when composite materials are subjected to elevated and high temperatures. The material at different temperatures can be considered as a mixture of materials in different material states. The mechanical properties of the mixture are determined by the content and the property of each state [4]. Consequently, the time-dependent E-modulus, E_m, can be expressed as:

$$E_m = E_g \cdot (1 - \alpha_g) + E_r \cdot \alpha_g \cdot (1 - \alpha_d) \tag{9}$$

where E_g is the modulus of the glassy state, E_r is the modulus of the leathery or rubbery state (the moduli of these two states being almost identical, see [4]), α_g and α_d are the conversion degree of glass transition and decomposition, which can be estimated by kinetic theory and Arrenhius equations as introduced in [3, 4].

By discretizing the time domain into 60 time steps (thus 1 min per time step for SLC03 and 2 mins for SLC02), the calculation process for each

time step can be summarized as follows:

1. The conversion degrees of glass transition and decomposition (α_g and α_d) are calculated for each element, as shown in Figs. 7 and 8 for α_d of SLC03 and SLC02, and in Figs. 9 and 10 for α_g of SLC02 and SLC03, respectively.

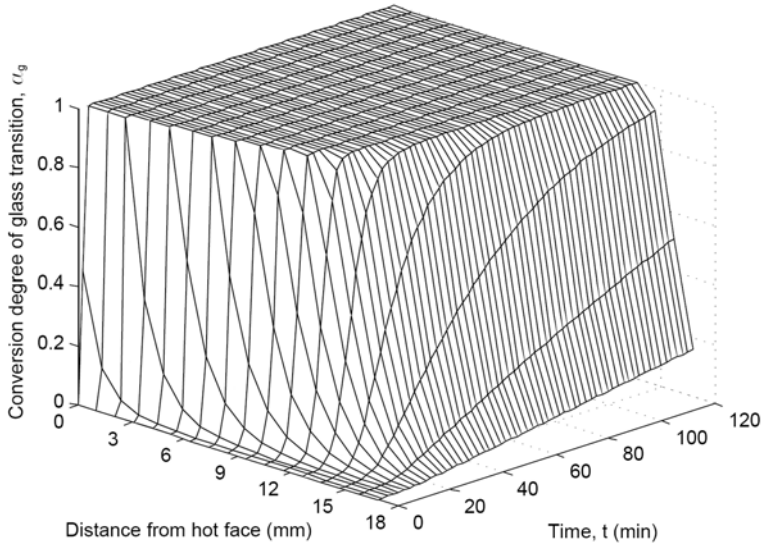

Fig. 9. Conversion degree of glass transition through lower face sheet of liquid-cooled specimen

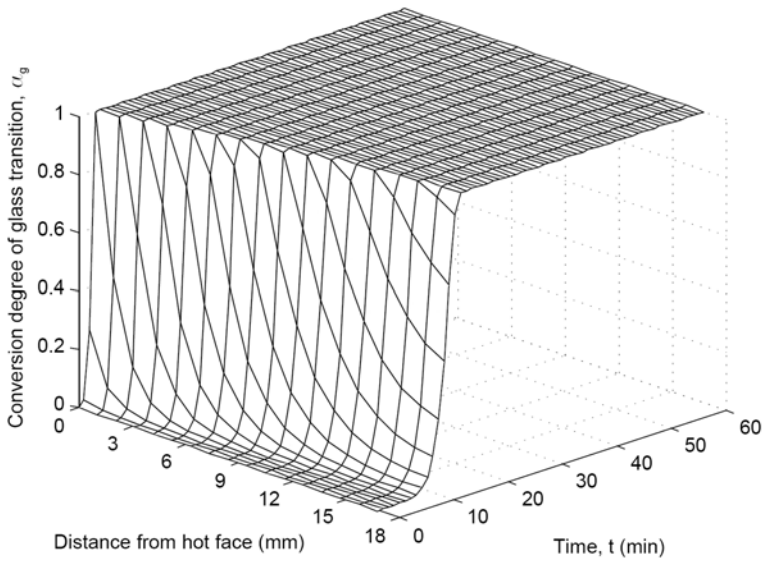

Fig. 10. Conversion degree of glass transition through lower face sheet of non-cooled specimen

2. The E-modulus is estimated from Eq. (9), as presented and discussed in [6].

3. The neutral axis of the section is determined and the moment of inertia of each part is calculated based on beam theory. The stiffness, *EI*, of the

cross section is then calculated as the sum of the stiffnesses of the individual components.

4. Substituting *EI* obtained at each time step into Eq. (1), the time-dependent mid-span deflection is calculated.

The comparison between the mechanical responses from the model and structural fire endurance tests is shown in Fig. 4. A good agreement was found in both cases. As a result, the corresponding α_g and α_d were further verified. The conversion degree of glass transition and decomposition will be used to evaluate the post-fire stiffness of the structure in the following.

3.3 Post-fire stiffness model

Figure 5 and Table 2 reveal that a significant recovery of stiffness occurs after fire (that is, the post-fire stiffness is higher than the stiffness during fire exposure). Furthermore, based on the two DMA tests performed on the same specimen, it was found that, if cooled down from temperatures between glass transition and decomposition, the E-modulus can recover almost to its initial value (see Fig. 6). In the modeling of the post-fire stiffness, the decomposed material (with the content α_d) has no stiffness, while the material after glass transition but before decomposition (with the content α_g) experiences a recovery. Thereby, for the modelling of the post-fire stiffness, Eq. (9) can be transformed to:

$$\begin{aligned} E_m &= E_g \cdot (1-\alpha_g) + E_g' \cdot \alpha_g \cdot (1-\alpha_d) \\ &= E_g - \alpha_g \cdot (E_g - E_g') - \alpha_d \cdot \alpha_g \cdot E_g' \end{aligned} \tag{10}$$

where E_g' is the E-modulus of the material after recovery, which was taken as 88% of E_g (initial value, see Section 2.6).

Substituting the conversion degree of glass transition (Fig. 9, 10), and the conversion degree of decomposition (Fig. 7, 8) from each time step of the fire endurance experiments into Eq. (10), the post-fire E-modulus was calculated through the thickness of the lower face sheet over a range of fire exposure times, as is shown in Fig. 11 for the liquid-cooling scenario and in Fig. 12 for the non-cooling scenario. Following the procedure presented in Section 3.2 for the calculation of *EI* during fire exposure, the

post-fire stiffness of the entire cross section was then obtained for a range of fire exposure times, as shown in Fig. 13, for the liquid-cooling and the non-cooling scenarios.

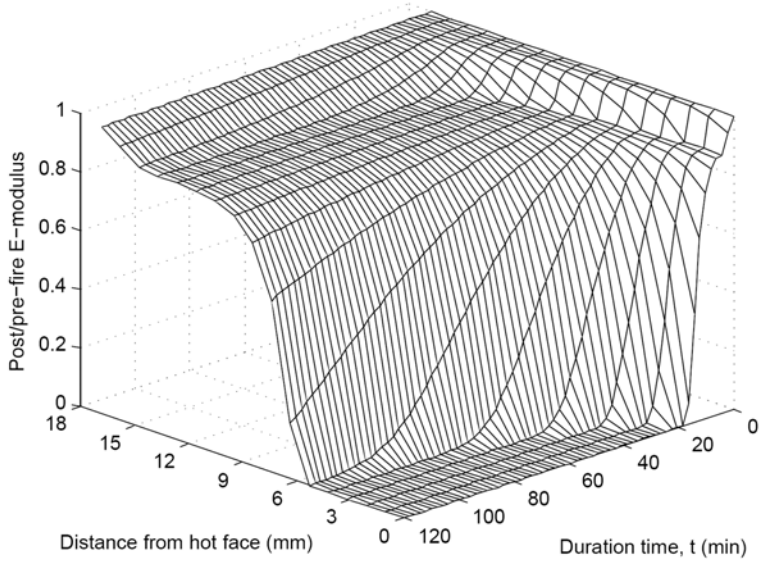

Fig. 11. Post-fire E-modulus through lower face sheet of liquid-cooled specimen after different fire exposure times

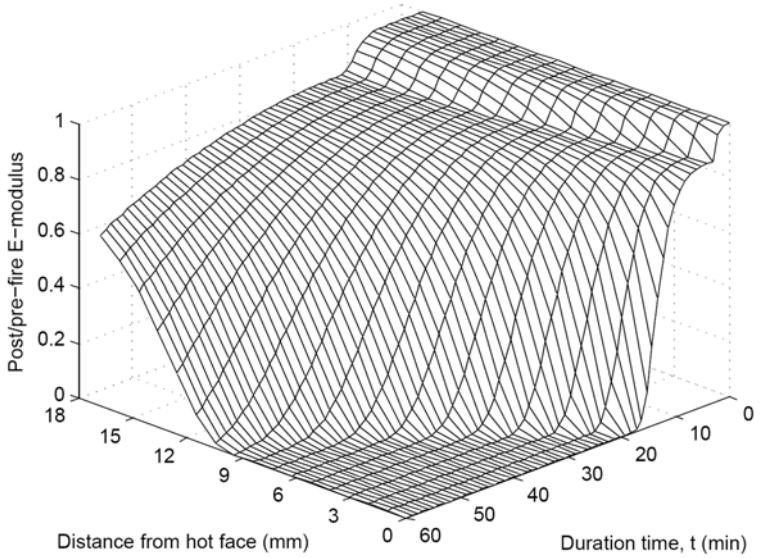

Fig. 12. Post-fire E-modulus through lower face sheet of non-cooled specimen after different fire exposure times

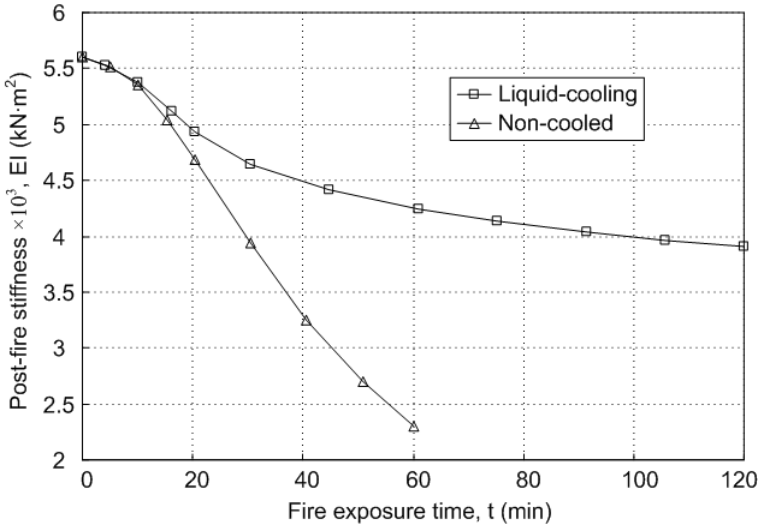

Fig. 13. Post-fire stiffness of liquid-cooled and non-cooled specimens after different fire exposure times

4 DISCUSSION

4.1 Discussion of post-fire E-modulus from new model

As defined by Eq. (10), the post-fire E-modulus was determined from the conversion degrees of glass transition and decomposition. Through the thickness of lower face sheet, α_g and α_d increased towards the hot face over time (see Figs.7-10) and, accordingly, the post-fire E-modulus decreased with increasing fire exposure time as shown in Figs. 11 and 12. The post-fire stiffness thereby is still much higher than the stiffness during the fire exposure, since E_g' in Eq. (10) is much higher than E_r in Eq. (9) (see [6]).

Considering that specimen SLC01 behaved similar to SLC02 (see Fig. 2), the post-fire E-modulus distribution through the thickness of the lower face sheet for SLC01 and SLC02 can be represented by the corresponding curves at 90 mins and 120 mins extracted from Fig. 11. The post-fire E-modulus distribution through the thickness of the lower face sheet for SLC03 can be obtained by extracting the corresponding curve at 57 mins from Fig. 12. These three curves are compared in Fig. 14. Because the conversion degrees of glass transition and decomposition had very similar distributions at 90 mins and 120 mins (see Fig. 7 for α_d and Fig. 9 for α_g), the distribution of the post-fire E-modulus after 90 minutes of fire exposure

for SLC01 and 120 minutes of fire exposure for SLC02 were also similar (see Fig. 14). Due to a longer fire exposure time for SLC02, slightly higher conversion degrees of glass transition and decomposition were found from Figs. 7 and 9, thus corresponding to a slightly lower post-fire modulus in Fig. 14.

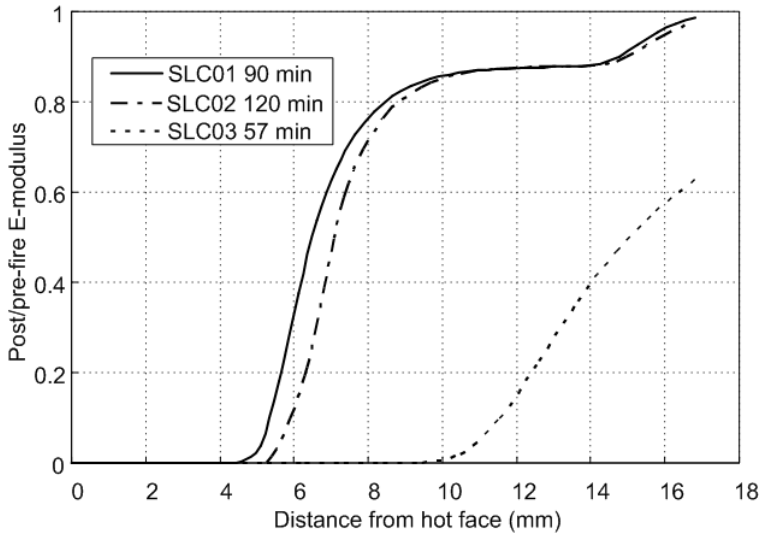

Fig. 14. Ratio post/pre-fire E-modulus through lower face sheet for all specimens

On the other hand, without liquid-cooling effects, the conversion degrees of glass transition and decomposition at 57 mins near the hot face were apparently higher (see Figs. 8 and 10), corresponding to a much lower post-fire E-modulus for SLC03 from 5mm to the cold face, as shown in Fig. 14. From the hot face to approximately 5mm depth of all the specimens, the post-fire E-moduli were the same and equal to zero, because full glass transition and decomposition were achieved in this range (see Fig. 7-10).

4.2 Comparison post-fire stiffness from new model and experimental

As shown in Fig. 13, the post-fire stiffness calculated from the model decreased over the fire exposure time, which was also demonstrated experimentally in [10-15]. After a short fire exposure time (about 10 mins), for both slabs, liquid-cooled and non-cooled, the post-fire stiffness decreased

much faster. While the post-fire stiffness of the liquid-cooled specimen stabilized after the first 10 minutes, the post-fire stiffness of the non-cooled specimen continued to decrease at almost the same rate. The post-fire stiffness at 90 mins and 120 mins can be extracted from the curve of the liquid-cooling scenario and compared with SLC01 and SLC02, respectively, see Table 3. It was found that the experimental post-fire stiffness based on basic beam theory was overestimated by 15.2% for SLC01, and 20.1% for SLC02.

EI (kNm²)	Experimental	Calculated	Calculated*
SLC01 90 mins	3500	4033(+15.2%)	3427(-2%)
SLC02 120 mins	3250	3903(+20.1%)	3306(+2%)

(.)= 100 × (experimental - calculated) / experimental

*: considering effects of shear modulus loss

Table 3. Comparison between post-fire stiffness from proposed model based on Eq. 10 and experiments

The result can be improved, if the change of the post-fire G-modulus of the lower face sheet is considered. In fact, a post-fire G-modulus change can be assumed to occur proportionally to the E-modulus change shown in Fig. 14, since the change of post-fire mechanical properties results from the change of material states [4]. The decrease of the G-modulus of the lower face sheet thereby induced a partial composition action between the upper parts of the cross section (webs and upper face sheet) and the lower face sheet. The calculation in Section 4.2 did not take into account of these effects of partial composition action. Consideration of partial composition action between different layers in its entirety is a difficult task and is not the main objective in this work. A simplified approach considers that, due to the loss of the G-Modulus, the material with less than 80% of the initial G-modulus (following the RRC criterion) is mechanically disconnected from the remaining section, while the material with more than 80% of initial G-modulus is in full composition action with the other layers. The results of this refined model are summarized in Table 3 and are in good

agreement with the experimental data. However, it should be noted that a higher cut-off point results in a lower estimation of the post-fire stiffness. A still acceptable underestimation of 9.1% for SLC01 and 14.1% for SLC02 can be found assuming that material with less than 50% of the initial G-modulus is mechanically disconnected from the remaining section.

4.3 Comparison results from new and refined discretized models

As introduced above, existing post-fire stiffness models are obtained by discretizing the post-fire specimen into two or three different layers (virgin/undamaged, partially degraded (3-layer model), fully degraded layers). The temperature profiles of specimen SLC02 at 120 mins were extracted from the model together with the corresponding remaining resin content (calculated based on Eq. 8 and Fig. 7), as shown in Fig. 15 (SLC01 results are similar). The corresponding temperature and RRC criteria are also illustrated in Fig. 15 to determine the borders of different layers. The temperature criterion considers that the degraded region has no stiffness and the virgin region has initial stiffness. A partially degraded layer is added for the three-layer model, exhibiting 30% of the pre-fire modulus [1]. The RRC criterion considers that regions with less than 80% of the remaining resin have no stiffness (only two-layer model).

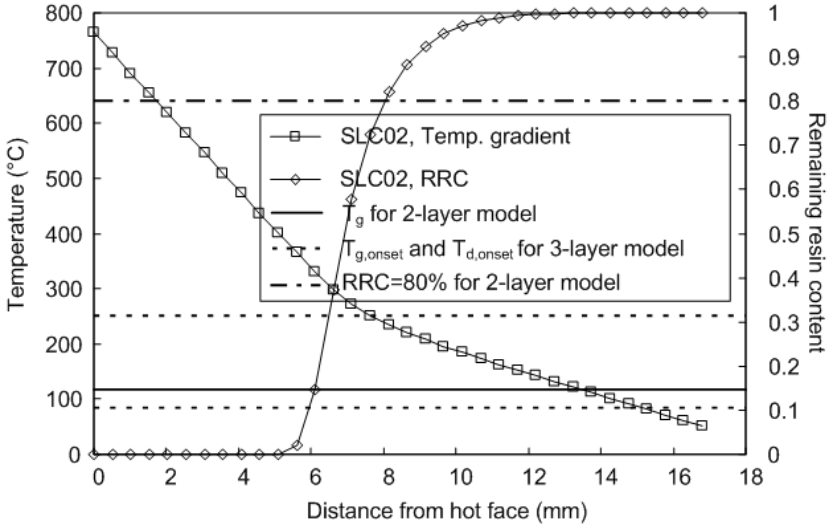

Fig. 15. Temperature profile and RRC of SLC02 with corresponding criteria for two- and three-layer models

The resulting post-fire E-modulus distributions through the lower face sheet based on these criteria are illustrated in Fig. 16. Compared with the continuous curve of the post-fire E-modulus obtained by the new model (extracted from Fig. 14), stepped distributions have resulted from the discretized models due to the two- or three-layer assumption. As shown in Fig. 16, the thickness of the virgin layer (with 100% E-modulus) estimated by the two-layer model with the RRC criterion was 4.5 mm thicker than that estimated by the temperature criterion. As a result, the post-fire bending stiffness estimated from the RRC criterion is higher than that estimated from the temperature criterion, as also confirmed by Table 4. Based on the distribution of the post-fire E-modulus through the lower face sheet, the calculated post-fire bending stiffness (*EI*) is summarized in this Table (also considering the loss of G-Modulus). For SLC02, the temperature criterion based the two-layer model gave an underestimation of the post-fire bending stiffness of around 8%, while a 7% overestimation was obtained based on the RRC criterion. However, all the results based on the predicted data for SLC01 and SLC02 compared well with the experimental results (less than 10% deviation).

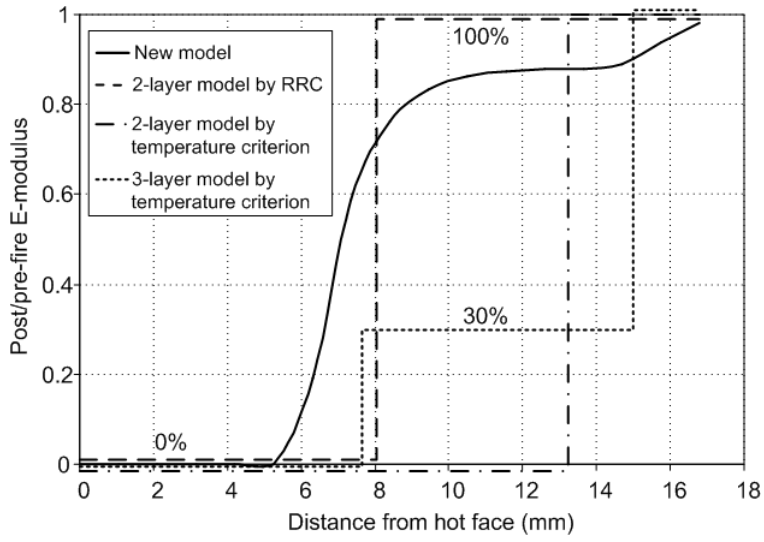

Fig. 16. Ratio post/pre-fire E-modulus through lower face sheet determined by different models

It should be noted that the post-fire stiffness was estimated without any information from the fire damaged specimens; the only inputs in-

cluded the initial material properties (the values at room temperature), the thermal and mechanical boundary conditions, and the fire exposure time. This implies that the post-fire behavior can be estimated before the fire exposure (assuming a sustainable time, as prescribed for different forms of structures in many codes), or can be pre-designed based on the functionality and importance of the structure.

EI (kN·m²)	SLC01, 90 mins	SLC02, 120 mins
2-layer model, temperature criterion	3530 (+1%)	2990 (-8%)
2-layer model, RRC	3611 (+3%)	3487 (+7%)
3-layer model, temperature criterion	3380 (-3%)	3060 (-6%)

(.)= 100 × (experimental - calculated) / experimental

Table 4. Comparison between post-fire stiffness from existent discretized models based on predicted data and from experiments

5 CONCLUSIONS

A new model and refined discretized models were developed to predict the post-fire stiffness of FRP composites. Results from the models compared well with results from full-scale fire experiments on cellular GFRP slabs subjected to mechanical and thermal loading up to 120 minutes. The following conclusions can be drawn:

1. Based on two DMA tests performed on the same specimen, an important recovery of the E-modulus was found and quantified for the portion of the material heated up to the range between glass transition and decomposition. It appears that with higher temperatures in this range, the capacity of recovery decreases. This result, however, must be further confirmed.

2. Considering the E-modulus recovery of the material before decomposition, the post-fire E-modulus of the composite material can be calculated. The post-fire stiffness of structural components can then be evaluated.

3. Based on the proposed thermal and mechanical response models, predicted temperature profiles and the conversion degrees of decomposition can be used to estimate the post-fire stiffness from existing two- and three-layer models. The borders between different layers can be determined by either a temperature criterion or a remaining resin content (RRC) criterion.

4. The post-fire stiffness of composite materials can be effectively characterized by the new proposed model under different thermal boundary and even real fire conditions, and after different fire exposure times. Furthermore, continuous through thickness distributions of the post-fire E-modulus can be obtained, instead of stepped curves in existing discretized models.

5. Based on the proposed models, the post-fire stiffness of FRP composite materials can be evaluated without information from the fire damaged specimens and before fire exposure. As a result, the post-fire behaviour can be pre-designed based on the functionality and importance of the structure.

ACKNOWLEDGEMENT

The authors would like to thank the Swiss National Science Foundation for financial support (Grant No. 200020-117592/1), and Mr. François Bonjour at the Laboratory of Polymer and Composite Technology, Ecole Polytechnique Fédérale de Lausanne for conducting the DMA tests.

REFERENCES

1. Keller T, Tracy C, Zhou A. Structural response of liquid-cooled GFRP slabs subjected to fire. Part I: Material and post-fire modeling. *Composites Part A* 2006, 37(9): 1286-1295.

2. Keller T, Tracy C, Zhou A. Structural response of liquid-cooled GFRP slabs subjected to fire, Part II: Thermo-chemical and thermo-mechanical modeling. *Composites Part A* 2006, 37(9): 1296-1308.

3. Bai Y, Vallée T, Keller T. Modeling of thermo-physical properties for

FRP composites under elevated and high temperatures. *Composites Science and Technology* 2007, 67(15-16): 3098-3109.

4. Bai Y, Keller T, Vallée T. Modeling of stiffness for FRP composites under elevated and high temperatures. *Composites Science and Technology* 2008, 68: 3099-3106.

5. Bai Y, Vallée T, Keller T. Modeling of thermal responses for FRP composites under elevated and high temperatures. *Composites Science and Technology* 2008, 68(1): 47-56.

6. Bai Y, Keller T. Modeling of mechanical responses of FRP composites in fire. *Composites Part A*, under review.

7. Pering GA, Farrell PV, and Springer GS. Degradation of tensile and shear properties of composites exposed to fire or high temperatures. *Journal of Composite Materials* 1980, 14, 54-68.

8. Springer GS. Model for predicting the mechanical properties of composites at elevated temperatures. *Journal of Reinforced Plastics and Composites* 1984, 3(1): 85-95.

9. Sorathia U, Beck C, and Dapp T. Residual strength of composites during and after fire exposure. *Journal of Fire Sciences* 1993, 11(3): 255-269.

10. Gibson AG, Wright PNH, Wu YZ, Mouritz AP, Mathys Z, and Gardiner CP. Modelling Residual Mechanical Properties of Polymer Composites After Fire. *Plastics, Rubber and Composites* 2003, 32(2): 81-90.

11. Mouritz AP and Mathys Z. Post-Fire Mechanical Properties of Marine Polymer Composites. *Composite Structures* 1999, 47: 643-653.

12. Mouritz AP. Post-Fire Properties of Fibre-Reinforced Polyester, Epoxy and Phenolic Composites. *Journal of Materials Science* 2002, 37: 1377-1386.

13. Mouritz AP. Mechanical Properties of Fire Damaged Glass-Reinforced Phenolic Composites. *Fire and Materials* 2000, 24: 67-75.

14. Mouritz AP. Simple Models for Determining the Mechanical Properties of Burnt FRP Composites. *Materials Science and Engineering* 2003, A359: 237-246.

16. Mouritz AP and Mathys Z. Post-Fire Mechanical Properties of Glass-

Reinforced Polyester Composites. *Composites Science and Technology* 2001, 61: 475-490.

17. Gardiner CP, Mathys Z, and Mouritz AP. Post-Fire Structural Properties of Burnt GRP Plates. *Marine Structures* 2004, (17): 53-73.

18. Keller T, Tracy C, and Hugi E. Fire endurance of loaded and liquid-cooled GFRP slabs for construction. *Composites Part A* 2006, 37(7): 1055-1067.

19. Tracy C. Fire endurance of multicellular panels in an FRP building system. Ph.D. Thesis (No. 3235), Swiss Federal Institute of Technology-Lausanne, Switzerland, April 2005.

20. Cain JJ, Post NL, Lesko JJ, Case SW, Lin YN, Riffle JS, Hess PE. Post-curing effects on marine VARTM FRP composite material properties for test and implementation. *Journal of Engineering Materials and Technology* 2006, 128(1): 34-40.

CHAPTER 3

Summary

3 Summary

Complex physical and chemical processes such as the glass transition and decomposition are involved when a composite material is subjected to elevated and high temperatures. During these processes, material states undergo significant changes, as described by kinetic theory. At a certain temperature, a composite material was considered as being a mixture of materials that are in different states, and the quantity of material in each state could be estimated. The thermophysical and thermomechanical properties of the mixture were quantified by adopting appropriate distribution functions, for example the rule and inverse rule of mixture. In this way, not only were the effects of a certain temperature considered, but also the thermal loading history, i.e. the models for thermophysical and thermomechanical properties are not univariate functions of temperature, but also functions of time.

Incorporating the thermophysical property sub-models into a heat transfer governing equation, the thermal responses were calculated by an implicit finite difference method in order to achieve stable numerical results. Different thermal boundary conditions were considered in the heat transfer governing equation, including prescribed temperature or heat flow, heat convection and/or radiation.

Integrating the thermomechanical property sub-models within a structural theory, the mechanical (elastic and/or viscoelastic) responses were described using a finite element method. Based on the modeling results for the time-dependent displacement and load-bearing capacity, the time-to-failure of a structure or its components could be predicted in accordance with a predefined failure criterion (displacement-based or stress-based). In addition, the post-fire stiffness was predicted by considering the modulus recovery of the material after cooling from temperatures ranging between glass transition and decomposition during the fire.

3.1 Original contributions

New thermophysical and thermomechanical property models with clear physical and chemical backgrounds were proposed. They consider the progressive changes in the states of composite materials under elevated and high temperatures, in which four different states (glassy, leathery, rubbery and decomposed) and three transitions (glass transition, leathery-to-rubbery transition, and decomposition) were defined when the temperature is raised. The proposed models are capable of describing the continuous changes in material properties, whereas stepped or empirical modeling functions based on experimental observations were used in previous research. Complex processes such as endothermic decomposition, mass loss, and shielding effects can also be described based on the concepts of effective material properties in the proposed models. The proposed material property models were developed from kinetic theory as not only temperature-dependent but also time-dependent functions and cover both glass transition and decomposition, therefore the effects of the complex and full-range thermal loading history can be modeled.

Based on the proposed material property models, thermal response and mechanical response models were developed and validated by full-scale fire endurance experiments with realistic fire exposure of up to 120 mins. The proposed models are therefore capable of describing the progressive changes in material properties and responses that occur during the extended excessive heating and/or fire exposure of large-scale FRP structures. Based on the strength degradation model, the time-dependent load-bearing capacity and the time-to-failure can be predicted. Since time effects were considered in the material property models, the time-to-failure was not predicted simply as the highest temperature achieved, but the time when a pre-defined failure criterion (either displacement-based or stress-based) was met. The proposed modeling scheme thus assists performance-based structural fire design, which can be considered as an integral part of structural design.

Different from the discrete two- or three-layer post-fire stiffness models

developed previously in literature, a new model was developed to describe the continuous changes in the post-fire stiffness of FRP composite materials subjected to different durations of fire exposure. As this model does not require any information from the fire-damaged specimens, it can be used to evaluate and design post-fire behavior before fire exposure, based on the functionality and importance of the structure. The through-thickness temperature gradients and remaining resin contents (RRC) can be calculated with this new model, which also enables the temperature gradient-based or RRC-based criterion previously proposed in literature to be used for structural post-fire stiffness assessment.

3.2 Further investigations and future prospects

3.2.1 Further investigations

Like every model, the proposed modeling system has certain limitations and requires further investigation, particularly with regard to the following:

- One-dimension simplification
- Assumption of decoupling of thermal and mechanical responses
- Accurate identification of kinetic parameters
- Reliability and physical justification of an adopted statistical distribution function
- Universality of time dependence

The models were developed based on the one-dimensional assumption, i.e. the heat flow in the through-thickness direction. Further work should contribute towards developing the system to cover two and three dimensions. This would require using more complicated governing equations for both heat transfer analysis and mechanical analysis in two or three dimensions.

It was assumed in the modeling that mechanical responses have almost no influence on the thermal responses of these materials. However, some mechanical processes can change the effective values of thermophysical properties, for example thermal conductivity can be significantly reduced

by gaps resulting from delamination. Another assumption in the modeling is that the decomposed gases produced in thermal processes can freely escape and therefore no pore pressure is considered in the mechanical processes. The applicability of such assumptions in different situations needs further validation.

The accuracy of the modeling results is largely dependent on the kinetic parameters used in kinetic theory. Although many approaches for the estimation of these parameters have been proposed since the 1960s, these methods are mainly used for the kinetic analysis of the decomposition process and seldom for the analysis of glass transition. The application of these methods to obtain kinetic parameters for glass transition requires further investigation.

In the modeling of stiffness and strength degradation, two simple statistical distribution functions were used: the rule and inverse rule of mixture. The rule of mixture can give a good description of stiffness and shear strength degradation, while the inverse rule better describes compressive strength degradation. No physical mechanism was found to explain such a discrepancy however. The roles of statistical rules in different situations still requires clarification.

The time dependence of stiffness and strength degradation was experimentally demonstrated and analytically modeled for FRP materials under elevated and high temperatures over several hours. This gave rise to the following questions: does such behavior resulting from the transition from the glassy to the leathery state exist at an even lower temperature and last for a longer time? If so, how low could this temperature be, what is the extent of this behavior, and how long would it last? How is this behavior different from or correlated with material viscosity? To answer these questions, more specific experimental investigations are necessary.

3.2.1 Future prospects

The proposed modeling system offers promising possibilities for future work in the following domains:

It was found that an FRP load-bearing structure may retain a certain percentage of its strength and stiffness after fire exposure. A post-fire stiffness model was proposed in Section 2.9, while post-fire strength modeling remains to be examined. It appears that the concepts used for the modeling of post-fire stiffness are also applicable for strength modeling; future work should include the identification of an appropriate distribution function for different material states in post-fire strength modeling and related experimental validations. The subject of post-fire reparation (reparation of FRP structures after fire exposure) has not yet been adequately addressed.

The proposed modeling approaches provided a good description of the time dependence of the mechanical properties of composite materials under elevated and high temperatures over several hours, which could probably also be extended to include lower temperature ranges and longer time durations.

The proposed modeling system was not developed for a specific composite material and should therefore be applicable for composite materials or polymers in general. The modeling of the decomposition process based on kinetic theory has been found to be well accepted and verified for different types of composite materials and polymers, while investigations aimed at integrating such a decomposition model into the modeling of other thermophysical properties (such as effective thermal conductivity and specific heat capacity) remain scarce. Kinetic theory was first used to model stiffness degradation and validated by DMA conducted on E-glass fiber polyester composites, but validation on other kinds of composites or even polymers is still necessary. The same can be said for the experimental demonstration and modeling of time effects, which were also only based on E-glass fiber polyester composites.

The improvement of the fire resistance of FRP structures represents a long-term objective for material scientists and structural engineers. One way of achieving this is to enhance the material itself, for example by improving its glass transition temperature as much as possible, and the oth-

er way is to design acceptable passive (fire-protective layers or coatings for example) and/or active (water-cooling system for example) fire protection techniques. The understanding gained and modeling of the behavior of FRP composites under elevated and high temperatures carried out in this thesis are expected to benefit both of them.

Curriculum Vitæ

Family, First Name:	**Bai**, **Yu**
Date of Birth:	May 26th, 1979
Nationality:	P. R. China
Email:	yu.bai@gmail.com

Education

Sep. 2004-Feb. 2009	*School of Architecture, Civil and Environmental Engineering, École Polytechnique Fédérale Lausanne (EPFL), Switzerland*. **PhD** candidate in Civil Engineering,
Sep. 2001-Jul. 2004	*Department of Civil Engineering, Tsinghua University, Beijing, China.* **Master** in Civil Engineering
Sep. 1997-Jul. 2001	*Department of Civil Engineering, Tsinghua University, Beijing, China.* **Bachelor** in Structure Engineering

Work experience

Feb. 2009-	*Composite Construction Laboratory, EPFL, Switzerland*. Postdoctoral researcher
Sep. 2004-Feb. 2009	*Composite Construction Laboratory, EPFL, Switzerland*. Teaching and research assistant
May. 2007-Jul. 2007	*Material Response Group, Department of Engineering Science and Mechanics, Virginia Polytechnic Institute and State University, USA.* Visiting scholar
Sep. 2001-Jul. 2004	*Department of Civil Engineering, Tsinghua University, Beijing, China.* Teaching and research assistant

Peer reviewed journals

23 **Y. Bai** and T. Keller. Modeling of mechanical response of FRP composites in fire. *Composites Part A*, accepted pending minor revisions.

22 **Y. Bai**, T. Vallée, T. Keller. Delamination of pultruded glass fiber-reinforced polymer composites subjected to axial compression. *Composite Structures*, accepted pending minor revisions.

21 **Y. Bai** and T. Keller. Pultruded GFRP tubes with liquid cooling system under combined temperature and compressive loading. *Composite Structures*, in press.

20 **Y. Bai** and T. Keller. Modeling of strength degradation for fiber-reinforced polymer composites in fire. *Journal of Composite Materials*, in press.

19 **Y. Bai** and T. Keller. Time dependence of material properties of FRP composites in fire. *Journal of Composite Materials*, in press.

18 **Y. Bai** and T. Keller. Shear failure of pultruded FRP composites under axial compression. *ASCE Journal of Composites for Construction*, in press.

17 Z. Guo, L. Jin, F. Li, and **Y. Bai**. (2009). Applications of the rotating orientation XRD method to orientated materials. *Journal of Physics D: Applied Physics*, 42: 012001 (4pp).

16 J. Nie, **Y. Bai**, and C. S. Cai. (2008). New connection system for confined concrete columns and beams. I: experimental study. *ASCE Journal of Structural Engineering*, 134 (12): 1787-1799.

15 **Y. Bai**, J. Nie, and C. S. Cai. (2008). New connection system for confined concrete columns and beams. II: theoretical modeling. *ASCE Journal of Structural Engineering*, 134 (12): 1800-1809.

14 **Y. Bai** and T. Keller. (2008). Modal parameter identification for a GFRP pedestrian bridge. *Composite Structures*, 82 (1): 90-100.

13 **Y. Bai**, T. Vallée, and T. Keller. (2008). Modeling of thermal responses for FRP composites under elevated and high temperatures. *Composites Science and Technology*, 68 (1): 47-56.

12 **Y. Bai**, N. L. Post, J. J. Lesko, and T. Keller. (2008). Experimental investigations on temperature-dependent thermophysical and mechanical properties of pultruded GFRP composites. *Thermochimica Acta*, 469: 28-35.

11 **Y. Bai**, T. Keller, and T. Vallée. (2008). Modeling of stiffness of FRP composites under elevated and high temperatures. *Composites Science and Technology*, 68: 3099-3106.

10 **Y. Bai** and L. Jin. (2008). Characterization of frequency dependence for glass transition temperature by Vogel-Folcher relationship. *Journal of Physics D: Applied Physics*, 41: 152008 (4pp).

09 T. Keller, **Y. Bai**, and T. Vallée. (2007). Long-term performance of a glass fiber reinforced polymer truss bridge. *ASCE Journal of Composites for Construction*, 11 (1): 99-108.

08 **Y. Bai**, T. Vallée, and T. Keller. (2007). Modeling of thermophysical properties for FRP composites under elevated and high temperatures. *Composites Science and Technology*, 67 (15-16): 3098-3109.

07 **Y. Bai** and T. Keller. (2007). Modeling of post-fire stiffness of E-glass fiber-reinforced polyester composites. *Composites Part A*, 38 (10): 2142-2153.

06 J. Nie, J. Zhao, **Y. Bai**, and R. Liu. (2006). Seismic behavior of discontinuous concrete filled steel tube ring connection. *Journal of Harbin Institute of Technology*. 37. (In Chinese)

05 J. Nie, **Y. Bai**, S. Li, J. Zhao, and Y. Xiao. (2005). Analyses on composite column with inside concrete filled steel tube under axial compression. *China Civil Engineering Journal*, 38 (9): 9-13. (In Chinese)

04 J. Nie, **Y. Bai**, S. Li, and Y. Xiao. (2005). Effective restrained radius of

confined concrete. *Journal of Tsinghua University (Science and Technology)*, 45 (3): 289-292. (In Chinese)

03 J. Nie, **Y. Bai**, S. Li, and Y. Xiao. (2005). Calculation method for confined concrete with multiple lateral hoopings. *Industrial Construction*, 35 (12): 43-46. (In Chinese)

02 J. Nie, J. Zhao, and **Y. Bai**. (2005). Bearing capacity of axially compressed core columns having concrete-filled steel tubes. *Journal of Tsinghua University (Science and Technology)*, 9: 3-6. (In Chinese)

01 J. Nie, **Y. Bai**, and S. Li. (2004). Experimental study on discontinuous connection of concrete filled tube. *Building Structure*, 12. (In Chinese)

Conference papers

06 **Y. Bai** and T. Keller. (2008). A kinetic model to predict stiffness and strength of FRP composites in fire. The fifth international conference of Composites in Fire (CIF), Newcastle upon Tyne, UK.

05 **Y. Bai**, T. Keller, and T. Vallée. (2008). Modeling of thermomechanical properties and responses for FRP composites in fire. The fourth International Conference on FRP Composites in Civil Engineering (CICE), Zurich, Switzerland.

04 **Y. Bai**, T. Vallée, and T. Keller. (2007). Dynamic behavior of an all-FRP pedestrian bridge. The first Asia-Pacific Conference on FRP in Structures (APFIS), Hong Kong, China.

03 **Y. Bai**, T. Vallée, and T. Keller. (2007). Modeling of thermophysical properties and thermal responses for FRP composites in fire. The first APFIS, Hong Kong, China.

02 T. Keller, **Y. Bai**, and T. Vallée. (2007). Long-term performance of the Pontresina GFRP pedestrian bridge. The third International Conference on Durability and Field Applications of FRP Composites for Construction (CDCC), Québec, Canada.

01 A. Zhou, **Y. Bai**, and T. Keller. (2005). Dynamic characteristics of

bridge superstructures with FRP composite structural elements. The third International Conference of Composites in Construction (CCC), Lyon, France.

Appendix A

Experimental investigations concerning strength degradation

Summary

In order to investigate the degradation of the shear, tensile and compressive strengths of FRP composites under elevated and high temperatures, 10° off-axis tensile, tensile and compressive experiments were performed as presented in Sections A.1, A.2 and A.3 respectively. Some of the information included in this appendix may be a repetition of that which appeared in Section 2.3 of the thesis, but this is intentional for information purposes.

A.1 Shear strength

A.1.1 Experiments

10°C off-axis tensile experiments were performed to measure the in-plane shear strength of pultruded GFRP laminates (E-glass fibers embedded in an isophthalic polyester resin, supplied by Fiberline, Denmark). The specimens were cut from a large plate (10-mm thickness) to 350-mm length×30-mm width, and with the same thickness.

Fig. 1. 10° off-axis tensile experiment setup for in-plane shear strength

A total of twelve laminates were tested at six temperatures: 20°C, 60°C, 100°C, 140°C, 180°C and 220°C. Two specimens were examined for each temperature, designated S*xx*, with *xx* representing temperature. First, the laminates were clamped and heated to the target temperature in an environmental chamber (temperature range from -40°C to 250°C, accuracy ±2°C) as shown in Fig. 1, placed in a free mode (load change within ±0.2kN) to avoid thermal stresses caused by thermal expansion. Uniform heating was ensured by the use of a reference specimen (see Fig. 1) equipped with temperature sensors inside the material. When the target temperature was reached in each scenario, an Instron Universal 8800 hydraulic machine (max. 100 kN) was used to apply the axial tensile force at a displacement rate of 2 mm/min up to specimen failure.

A.1.2 Instrumentation

Since only the maximum load is of interest in this study, no strain gages were used for the mechanically tested specimens. The through-thickness temperature progressions were measured by three temperature sensors (PT100, Distrelec) embedded in the reference specimen: first, three holes of 1-mm radius and 8-mm depth were drilled from one side as shown in Fig. 2, the temperature sensors were then inserted and the holes filled with epoxy.

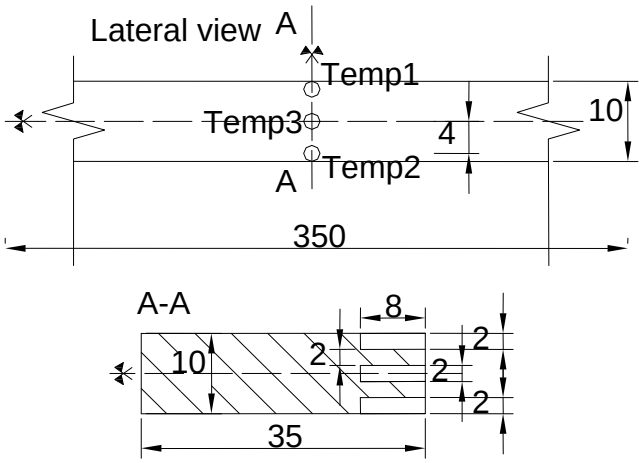

Fig. 2. Disposition of temperature sensors in temperature reference specimen

A.1.3 Results

The load-axial displacement curves are summarized in Fig. 3 for all the scenarios.

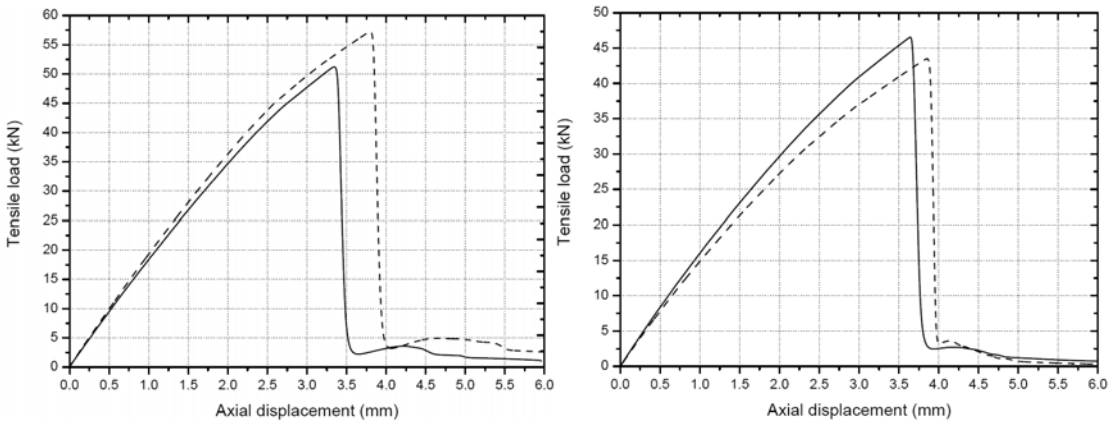

(a) S20

(b) S60

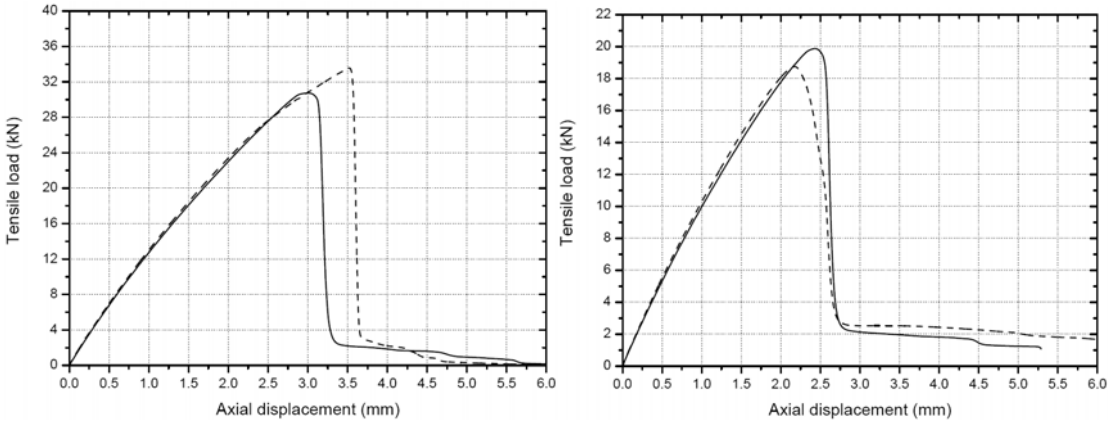

(c) S100

(d) S140

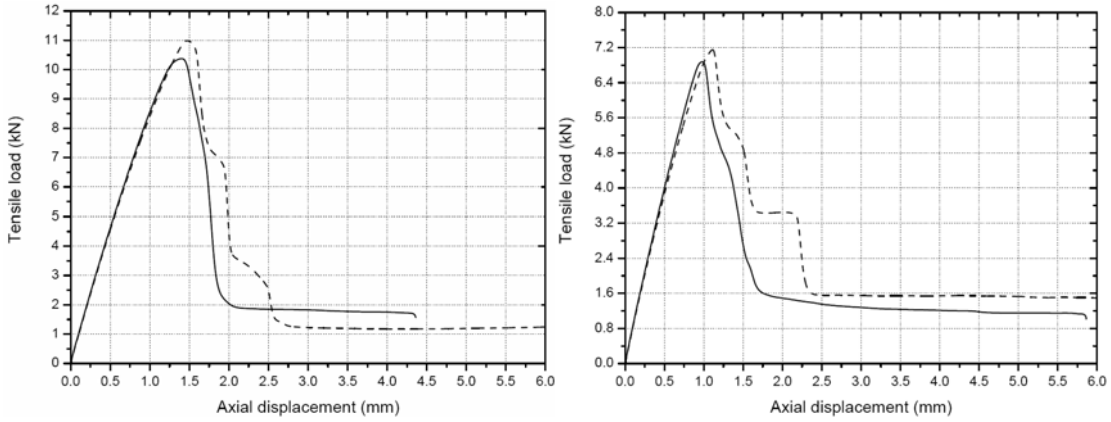

(e) S180

(f) S220

Fig. 3. Load-axial displacement curves for different scenarios from 10° off-axis tensile experiments (S*xx*-1: solid line; S*xx*-2: dashed line)

The ultimate load and corresponding displacement were identified from Fig. 3 for each specimen, as summarized in Table 1.

Specimen	Ultimate load [kN]	Displacement [mm]	Shear strength [MPa]
S20-1	51.2	3.3	25.8
S20-2	57.3	3.8	27.7
S60-1	46.6	3.6	23.5
S60-2	43.5	3.8	24.0
S100-1	30.7	3.0	15.5
S100-2	33.6	3.5	16.1
S140-1	19.9	2.4	10.0
S140-2	18.8	2.2	9.0
S180-1	10.4	1.4	5.2
S180-2	11.0	1.5	5.5
S220-1	6.9	1.0	3.5
S220-2	7.2	1.1	3.6

Table 1. Ultimate load, displacement and shear strength for different scenarios from 10° off-axis tensile experiments

The temperatures measured from the reference specimen for each scenario are summarized in Fig. 4.

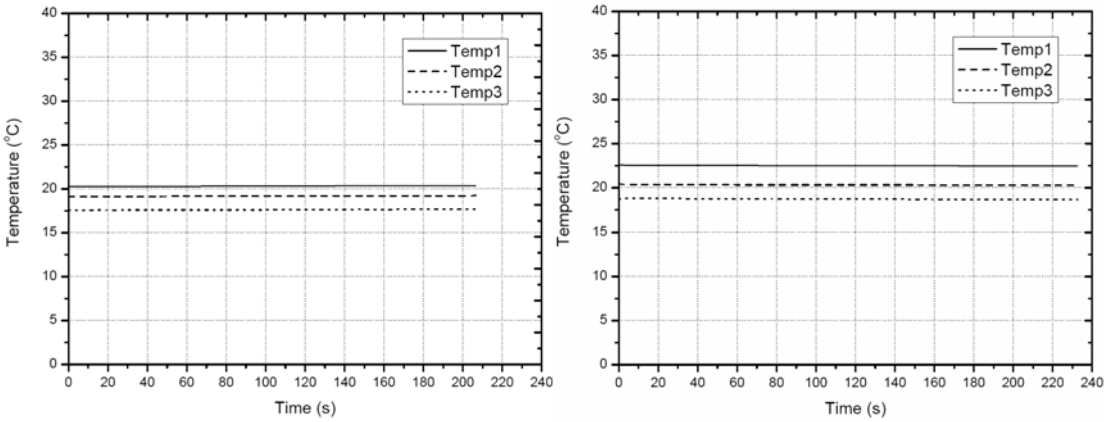

(a) S20-1 (b) S20-2

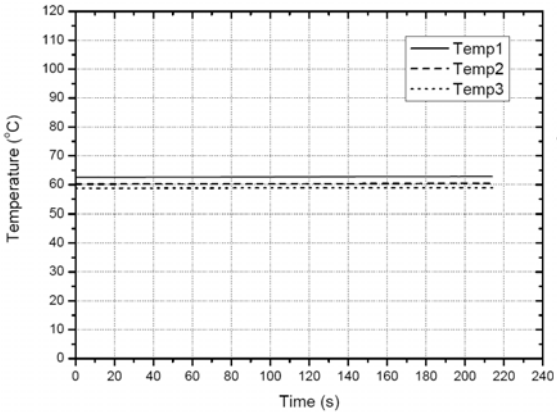

(c) S60-1

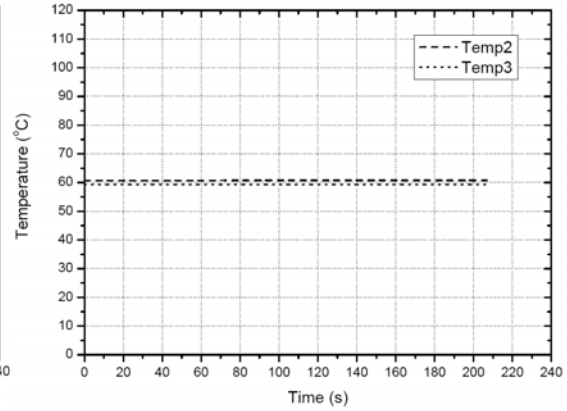

(d) S60-2

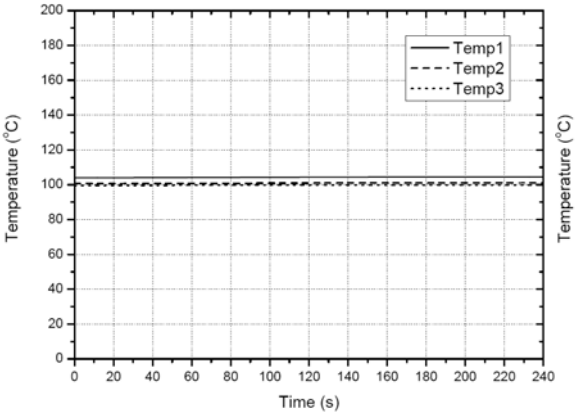

(e) S100-1

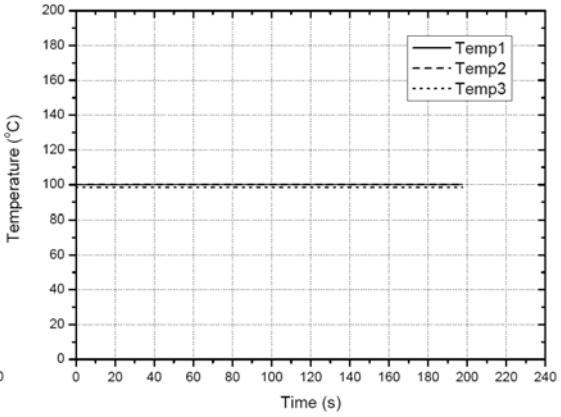

(f) S100-2

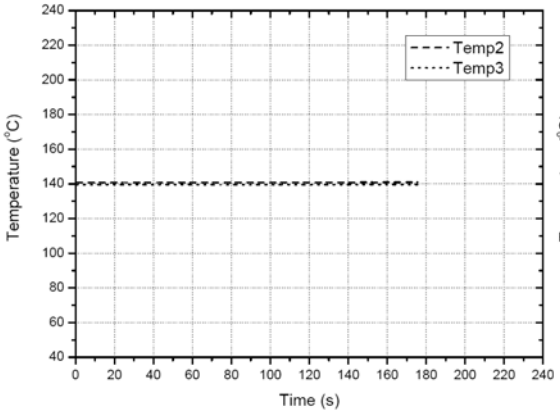

(g) S140-1

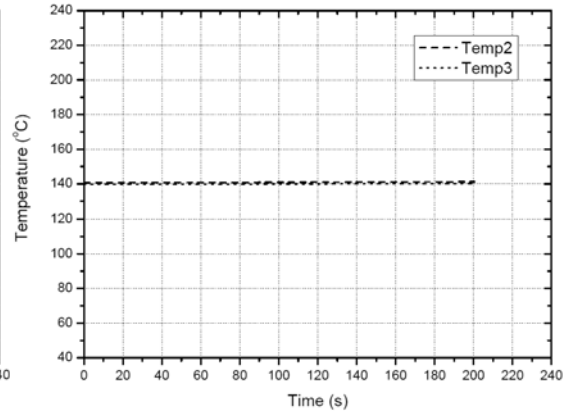

(h) S140-2

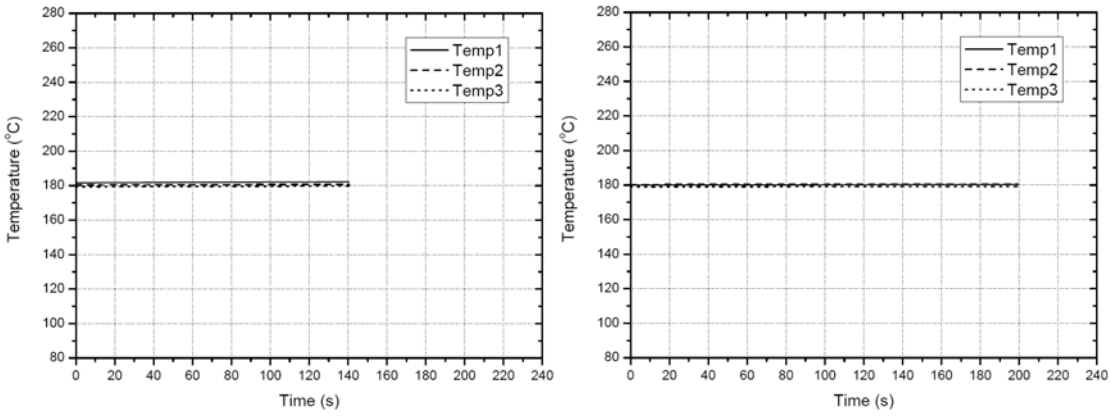

(i) S180-1 (j) S180-2

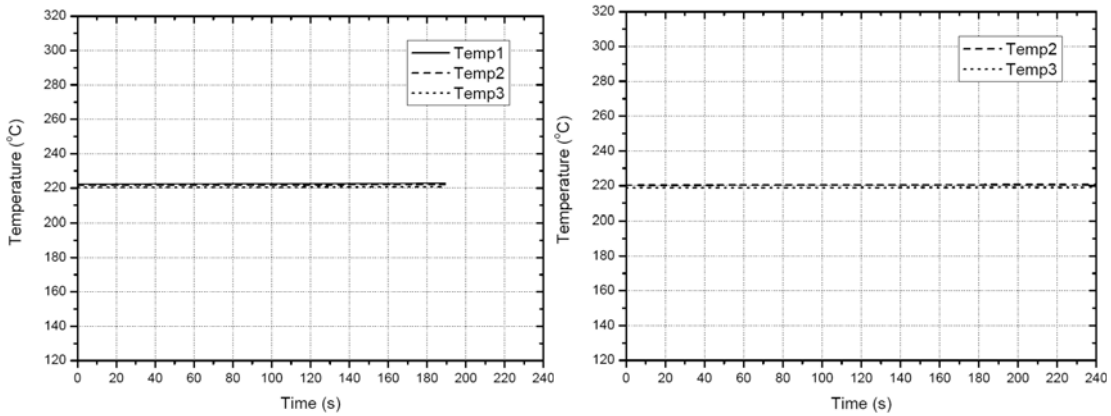

(k) S220-1 (l) S220-2

Fig. 4. Temperature measurements from reference specimen for each scenario of 10° off-axis tensile experiments

The failure mode for each scenario is shown in Fig. 5.

(a) S20-1 (b) S20-2 (c) S60-1

(d) S60-2

(e) S100-2

(f) S140-1

(g) S140-2

(h) S180-1

(i) S180-2

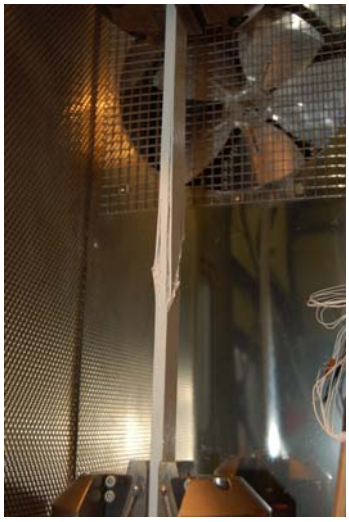

(j) S220-1

(k) S220-2

(l) Frontal view of typical damaged specimens

Fig. 5. Failure mode in 10° off-axis tensile experiments at different temperatures

The shear strength, f_s, can be estimated as follows:

$$f_s = \frac{1}{2} \cdot \sin 2\theta \cdot \sigma_t = 0.171\sigma_t \tag{1}$$

where θ is the off-axis angle (10°) and σ_t is the axial tensile stress at failure. Thus the measured temperature-dependent shear strength was obtained, as shown in Fig. 6.

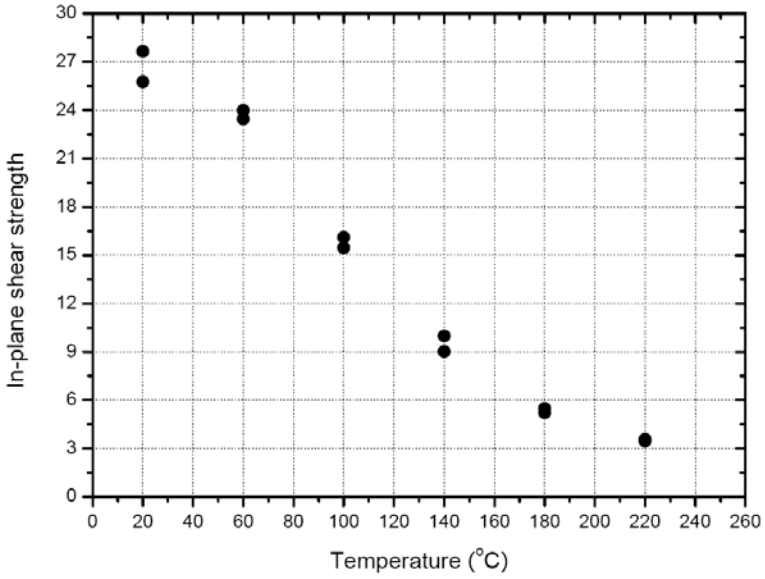

Fig. 6. Temperature-dependent shear strength from 10° off-axis tensile experiments

A.2 Tensile strength

A.2.1 Experiments

The GFRP material used for the tensile experiments was the same as that used for the shear experiments. The specimens' axis coincided with the roving direction however. Their dimensions were 400-mm length×20-mm width×10-mm thickness. The same experimental program was performed as for the shear experiments (two specimens per temperature, designated T*xx*, *xx* being the target temperature) as shown in Fig. 7. After the target temperature (20-220°C) was achieved, the specimens were mechanically loaded in tension up to failure at a displacement rate of 2 mm/min.

Fig. 7. Tensile experiment setup for tensile strength

A.2.2 Instrumentation

The same as that used in the shear experiments (A.1.2).

A.2.3 Results

The load-axial displacement curves are summarized for all the scenarios in Fig. 8.

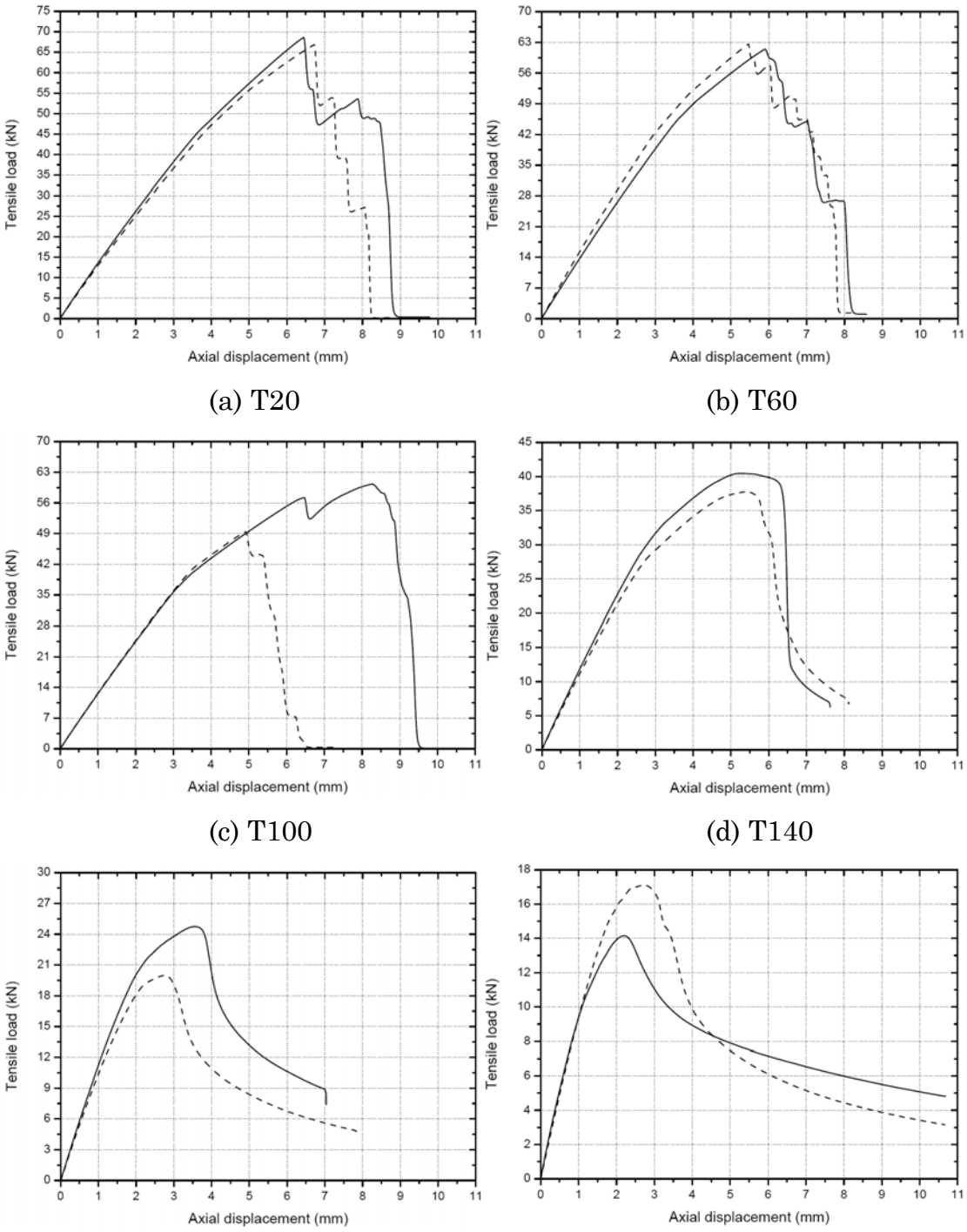

(a) T20 (b) T60

(c) T100 (d) T140

(e) T180 (f) T220

Fig. 8. Load-axial displacement curves for different temperatures from tensile experiments (T*xx*-1: solid line; T*xx*-2: dashed line)

The ultimate load and corresponding displacement were identified from Fig. 8 for each specimen, as summarized in Table 2.

Specimen	Ultimate load [kN]	Displacement [mm]
T20-1	68.6	6.5
T20-2	66.8	6.7
T60-1	61.4	5.9
T60-2	62.6	5.5
T100-1	60.3	8.3
T100-2	49.4	4.9
T140-1	40.5	5.2
T140-2	37.7	5.4
T180-1	24.7	3.6
T180-2	20.0	2.8
T220-1	14.1	2.2
T220-2	17.1	2.8

Table 2. Ultimate load and displacement for different scenarios from tensile experiments

The temperatures measured from the reference specimen for each scenario are summarized in Fig. 9.

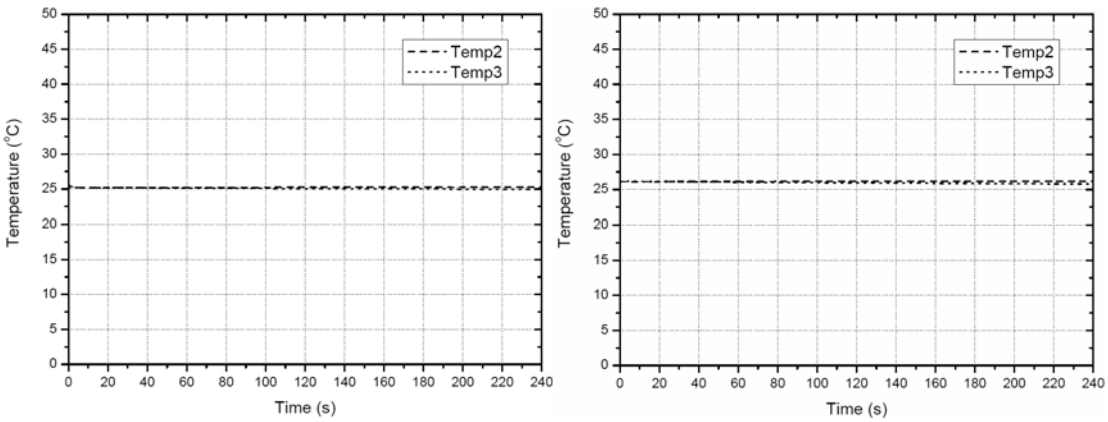

(a) T20-1 (b) T20-2

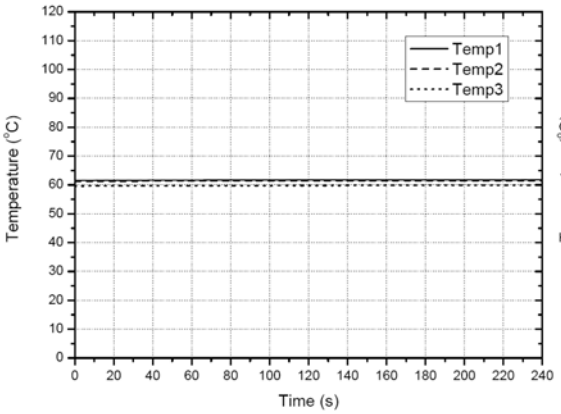

(c) T60-1

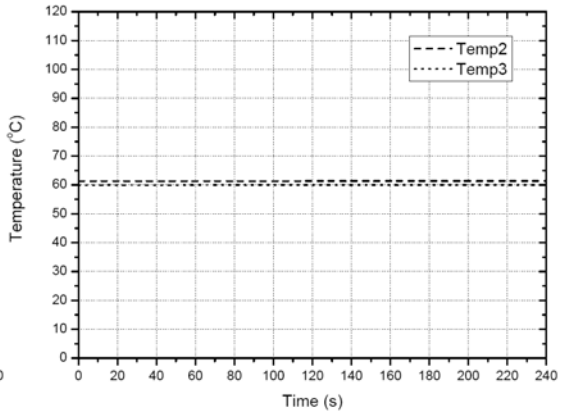

(d) T60-2

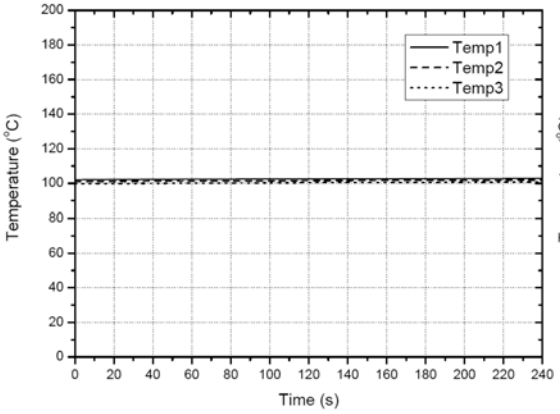

(e) T100-1

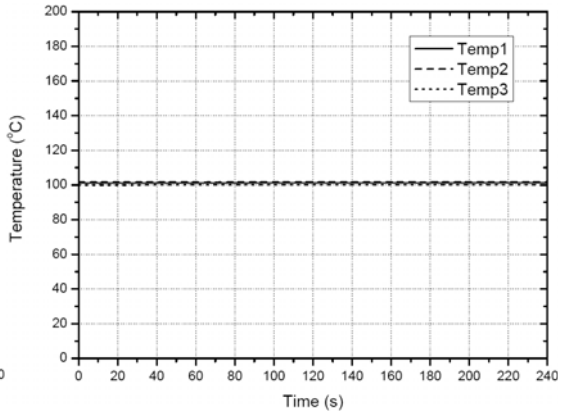

(f) T100-2

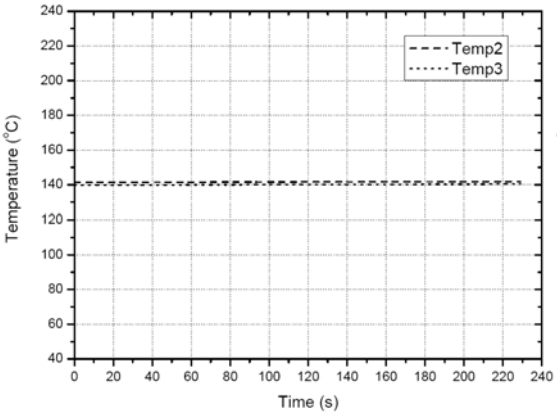

(g) T140-1

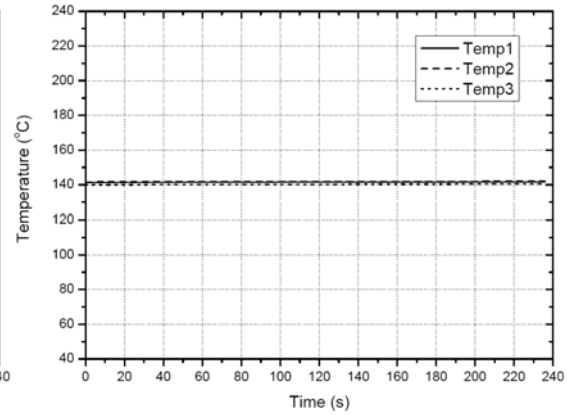

(h) T140-2

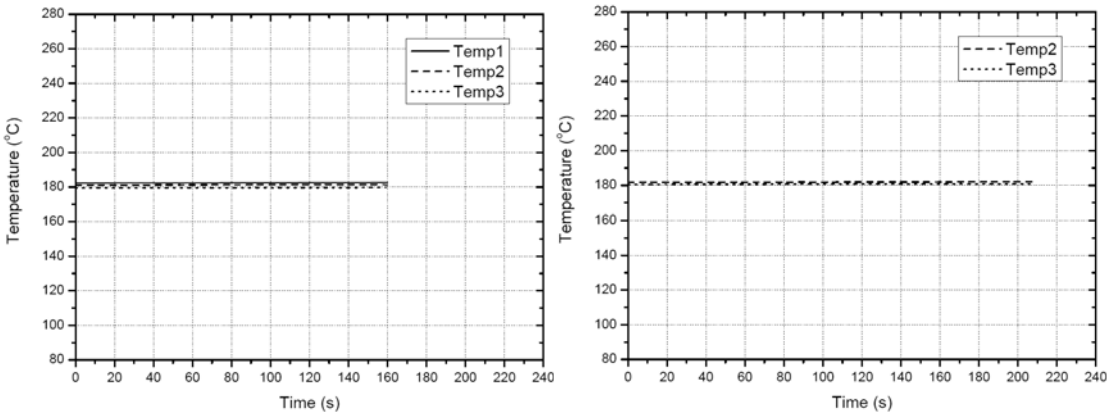

(i) T180-1 (j) T180-2

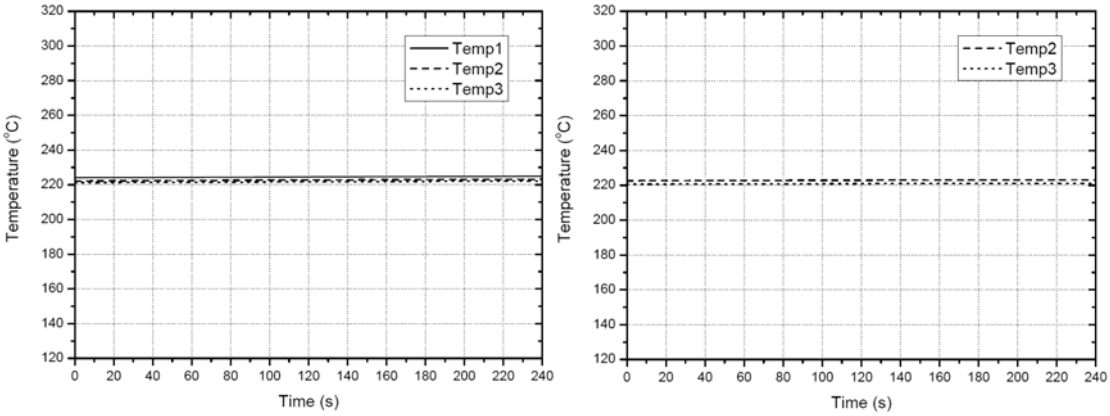

(k) T220-1 (l) T220-2

Fig. 9. Temperature measurements from reference specimen for each scenario of tensile experiments

The typical failure modes are shown in Figs. 10-12 for all the scenarios.

(a) T20-1 (b) T20-2 (c) T60-1

(d) T60-2 (e) T100-1 (f) T100-2

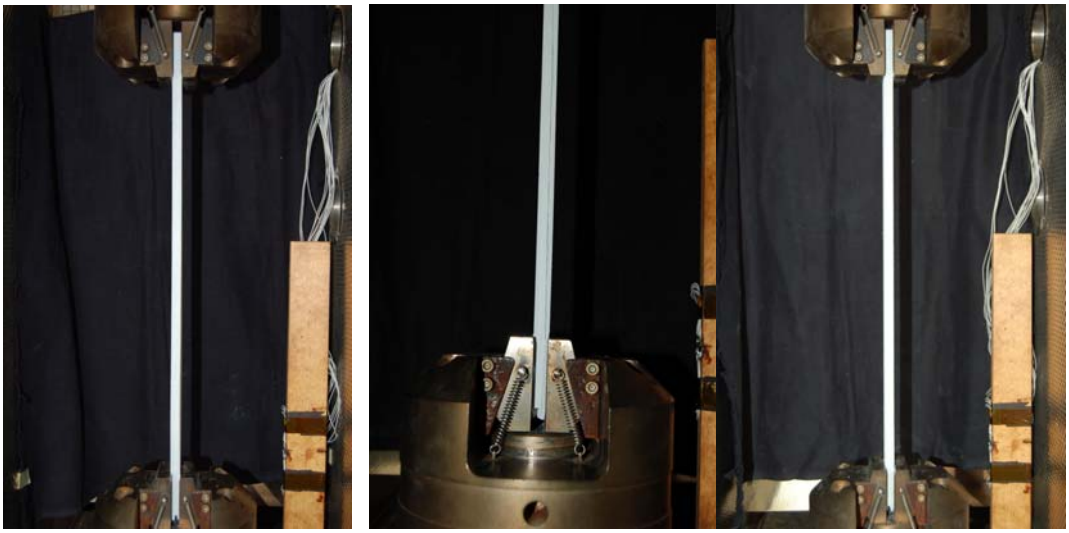

(g) T140-1 (h) T140-2 (i) T180-1

(j) T180-2 (k) T220-1 (l) T220-2

Fig. 10. Failure modes at different temperatures in tensile experiments

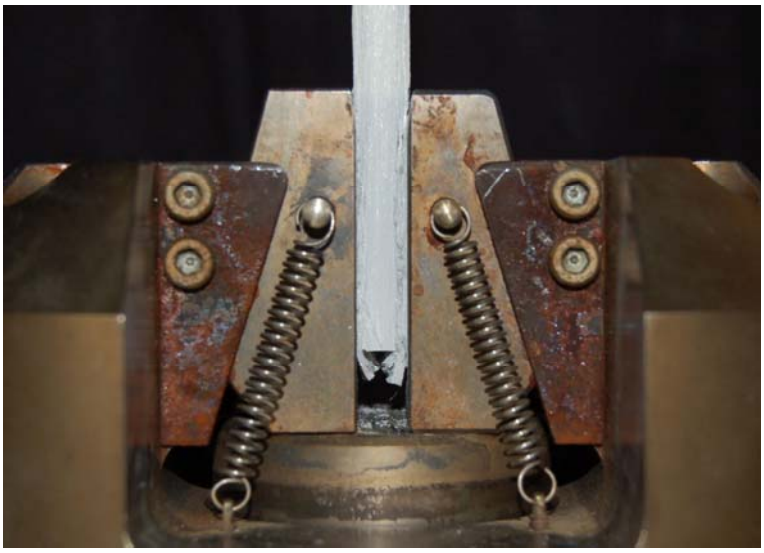

(a) T140-1

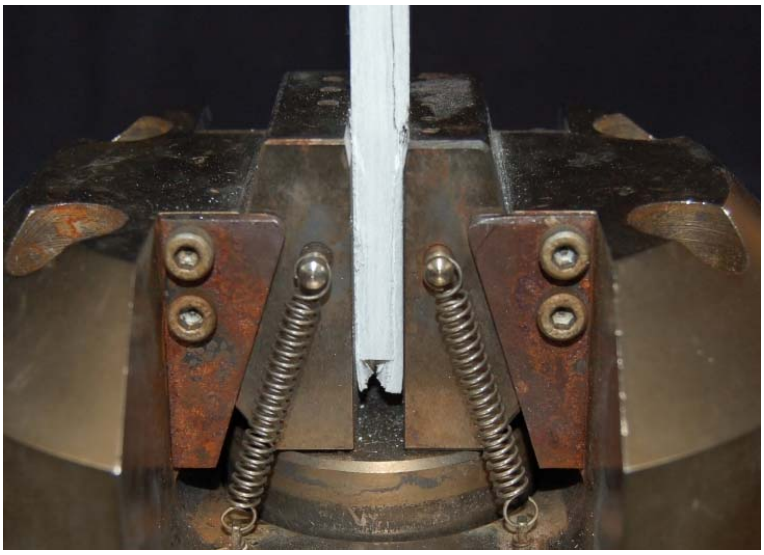

(b) T140-2

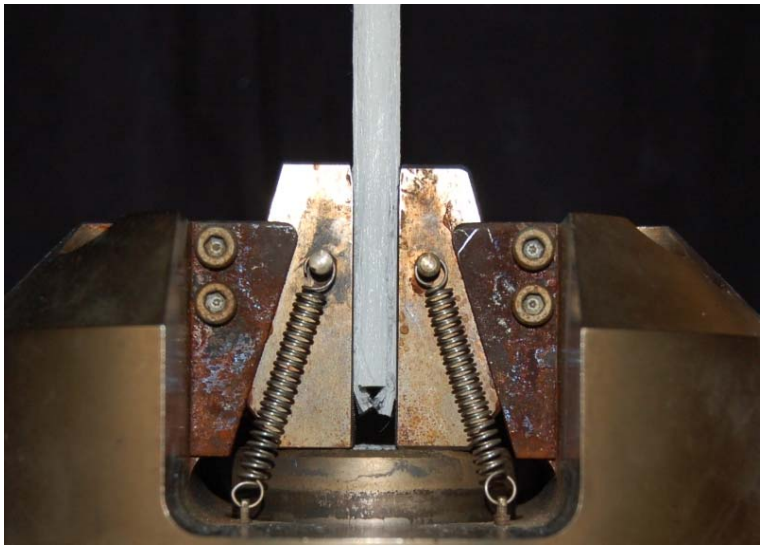

(c) T180-1

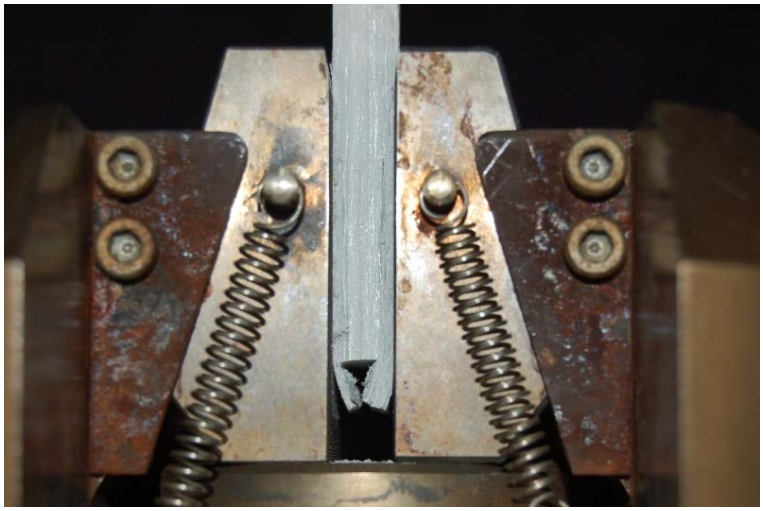

(d) T180-2

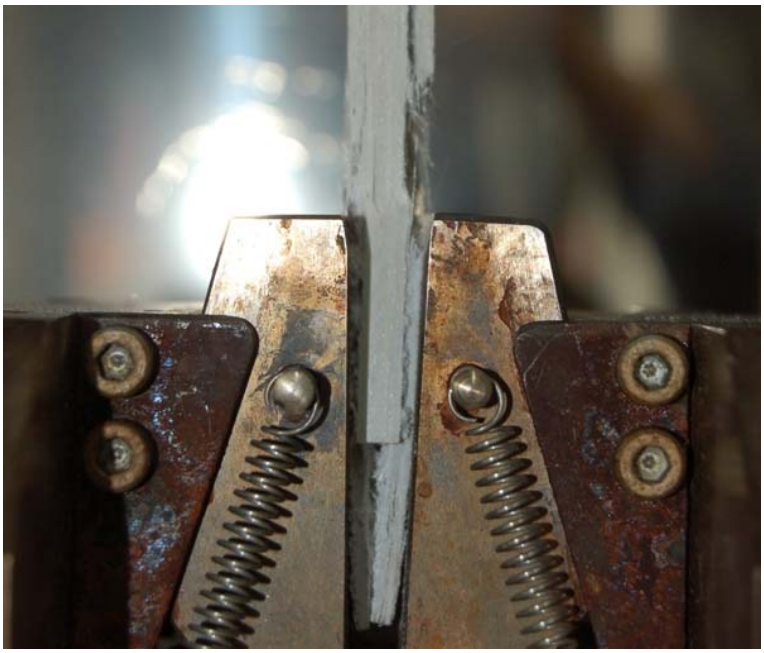

(e) T220-1

(f) T220-2

Fig. 11. Detail for scenarios T140, T180, and T220

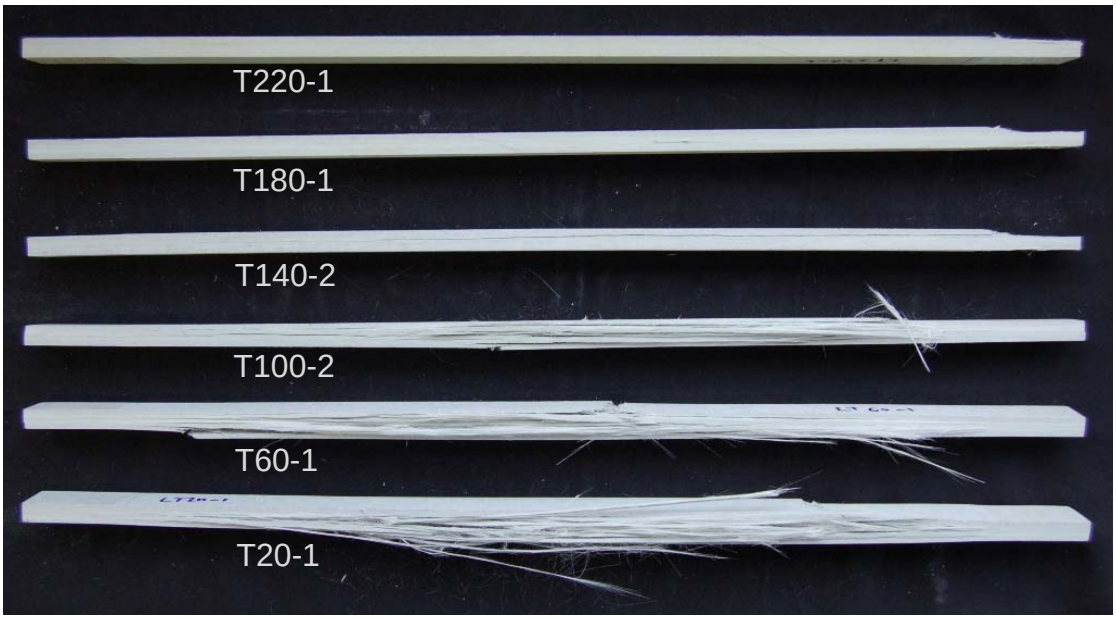

(a) Lateral view

(b) Frontal view

Fig. 12. Failure modes of typical specimens

Because of the change in failure modes, only the temperature-dependent ultimate tensile loads are summarized in Fig. 13.

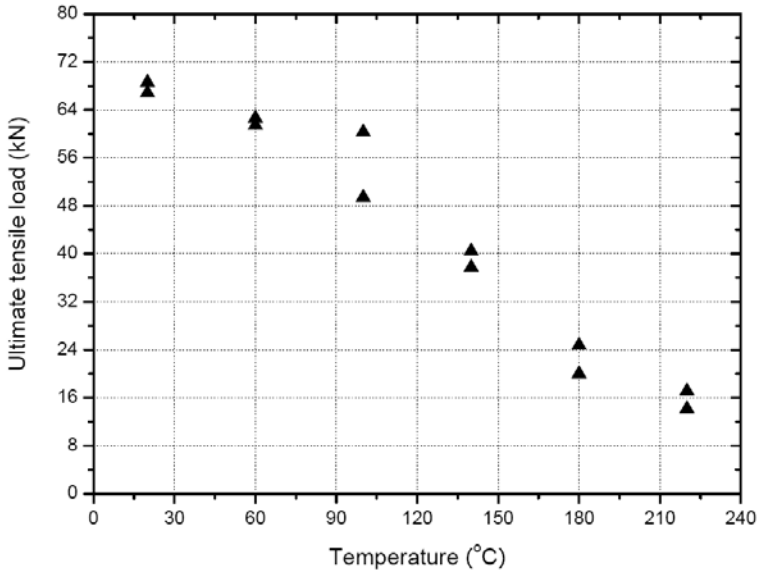

Fig. 13. Temperature-dependent ultimate tensile loads for all specimens in tensile experiments

A.3 Compressive strength

A.3.1 Experiments

Compressive experiments were conducted on pultruded GFRP tubes of 40/34-mm outer/inner diameters, 3-mm thickness and 300-mm free length (Fiberline Composites, Denmark). The tubes were tested under concentric compressive loading in a fixed-end setup, as shown in Figs. 14 and 15.

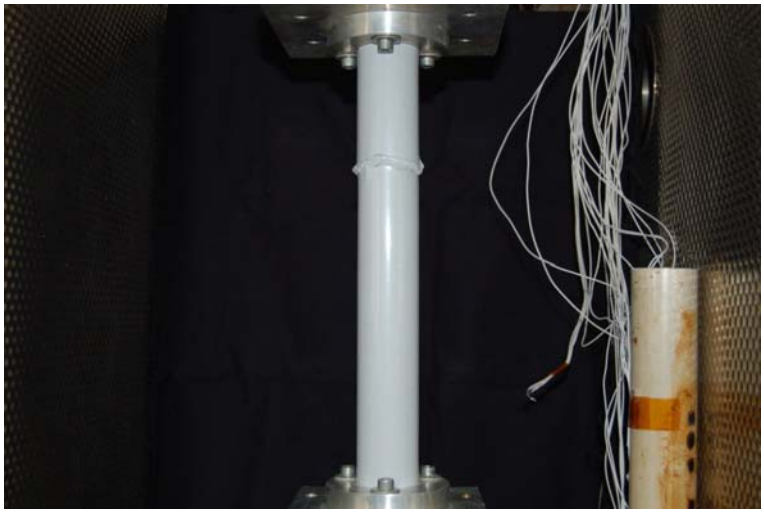

Fig. 14. Compressive experiment setup for nominal compressive strength

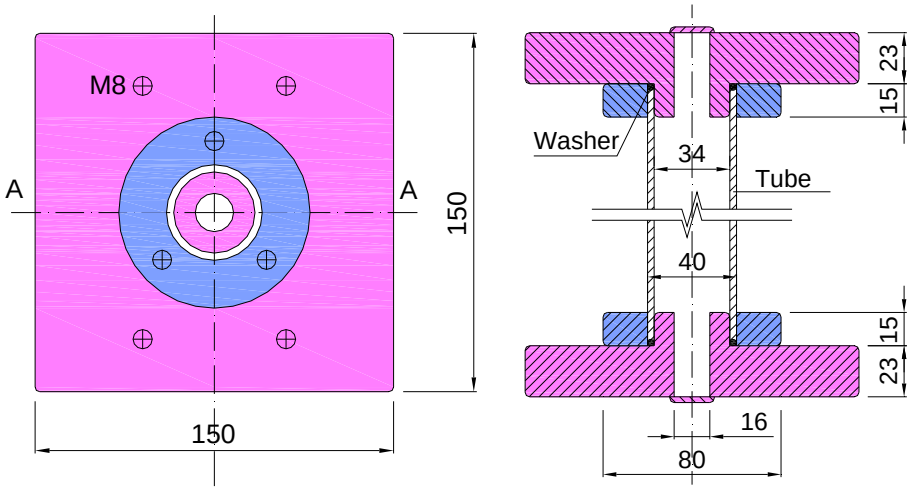

(a) Frontal view (b) A-A cross section

Fig. 15. Fixation system

Owing to the irregular tube thickness (due to a manufacturing inaccuracy), a specially designed fixation system was used. This consisted of two parts (indicated by two different colors) as shown in Fig. 15. In order to achieve a uniformly distributed compressive loading, a rubber washer (with a temperature resistance of up to 200°C, Maagtechnic, Switzerland) was placed between the fixation system and the end of the specimen prior to testing.

The target temperatures were the same as those in the shear and tensile experiments. Two specimens were tested at each temperature (designated C*xx*, with *xx* being the temperature). After the target temperature was reached, the axial compressive force was applied at a displacement rate of 1 mm/min up to specimen failure. Since the highest recommended temperature for use of the washer was lower than that considered in scenario C220, the washers were replaced after each test in this scenario.

As the failure load in scenario T20 exceeded the maximum load of the Instron machine (100 kN), specimens were tested using a Schenck machine (max. 1000 kN) without an environmental chamber, and no temperature reference specimen was used for this scenario.

A.3.2 Instrumentation

Since only the maximum load is of interest in this study, no strain gages were used for the mechanically tested specimens. The through-thickness temperature progressions were measured by three temperature sensors (PT100, Distrelec) embedded in the reference specimen (see Fig. 16).

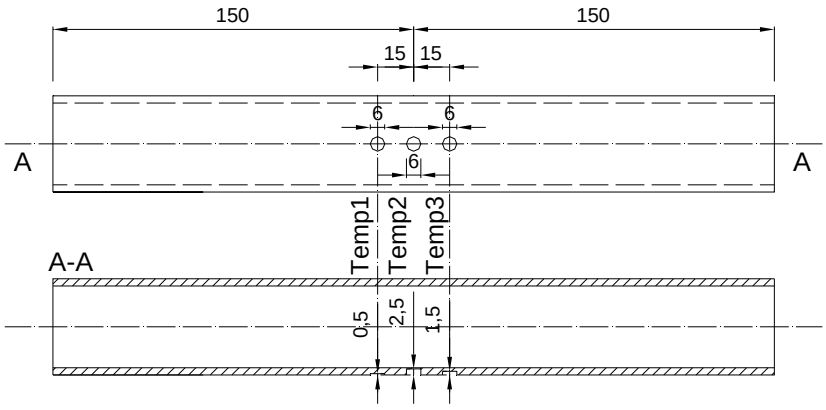

Fig. 16. Disposition of temperature sensors in reference specimen

A.3.3 Results

The load-axial displacement curves for all the scenarios are summarized in Fig. 17.

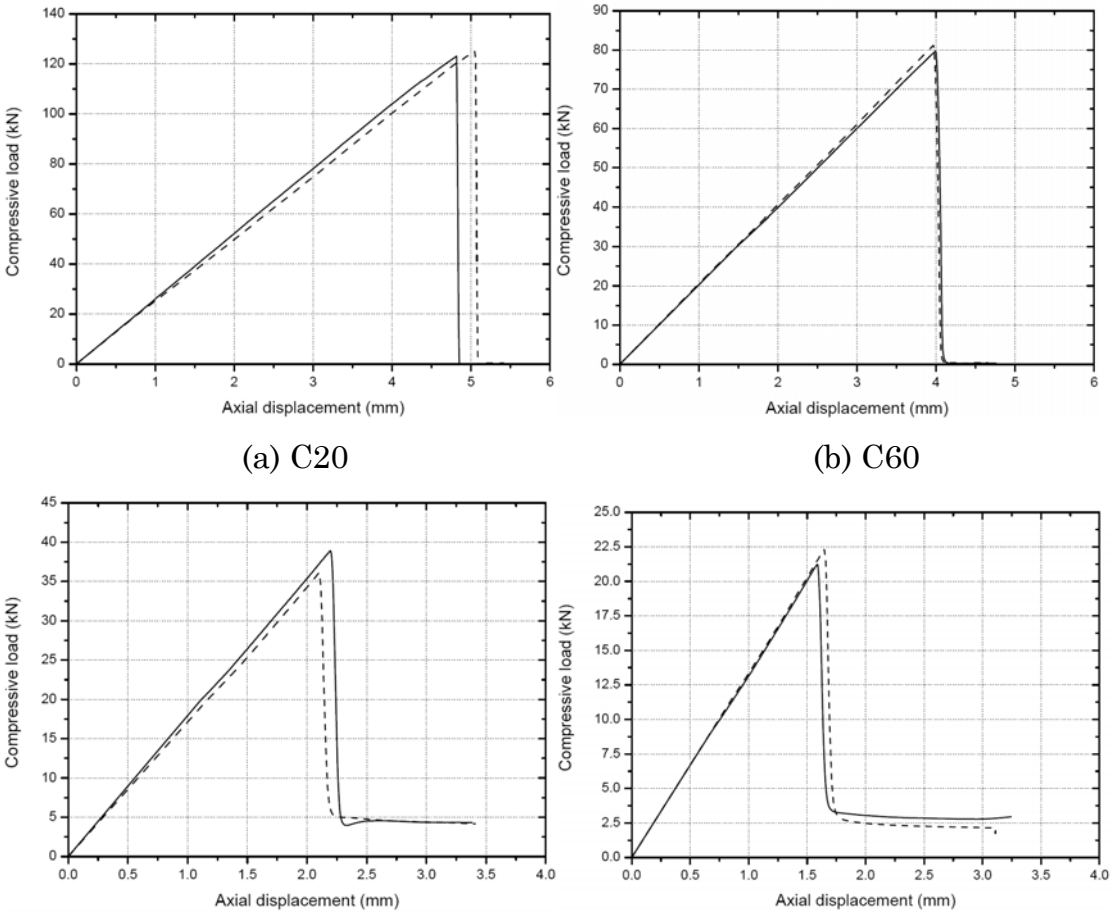

(a) C20 (b) C60

(c) C100 (d) C140

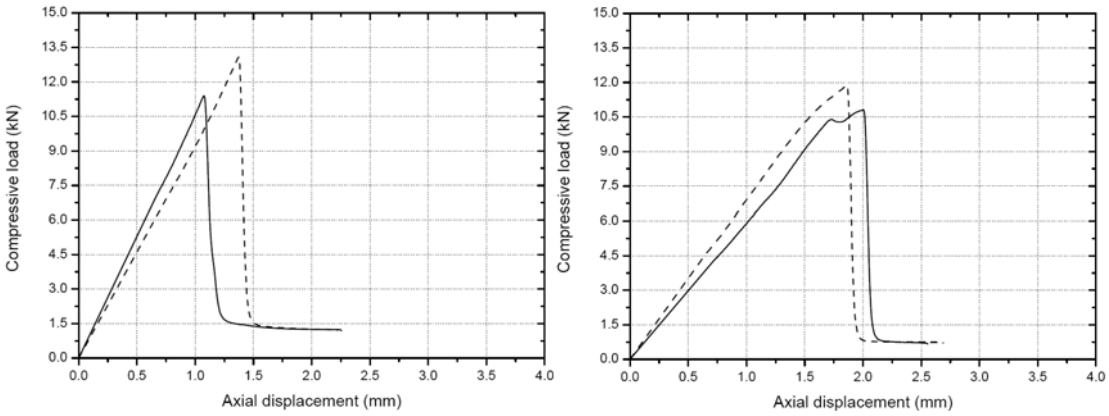

(e) C180 (f) C220

Fig. 17. Load-axial displacement curves for all scenarios in compressive experiments (C*xx*-1: solid line; C*xx*-2: dashed line)

The ultimate load and corresponding displacement were identified from Fig. 17 for each specimen, as summarized in Table 3.

Specimen	Ultimate load [kN]	Displacement [mm]	Compressive strength [MPa]
C20-1	123.1	4.8	358.6
C20-2	125.0	5.0	353.1
C60-1	79.3	4.0	228.6
C60-2	81.2	3.9	232.9
C100-1	39.0	2.2	111.8
C100-2	36.1	2.1	103.5
C140-1	21.2	1.6	60.9
C140-2	22.3	1.7	64.0
C180-1	11.4	1.1	32.8
C180-2	13.1	1.4	37.5
C220-1	10.8	2.0	31.0
C220-2	11.9	1.9	34.1

Table 3. Ultimate load, displacement and compressive strength for different scenarios from compressive experiments

The temperatures measured from the reference specimen in each scenario are summarized in Fig. 18.

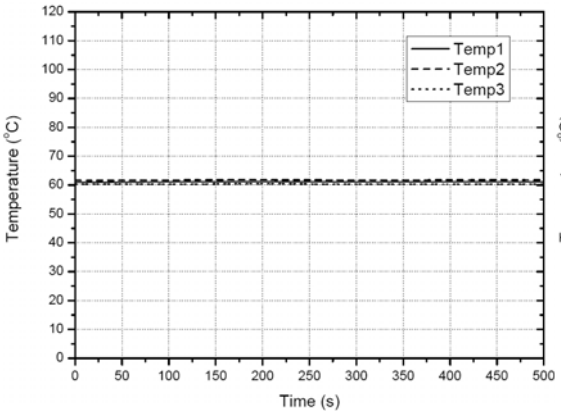

(a) C60-1

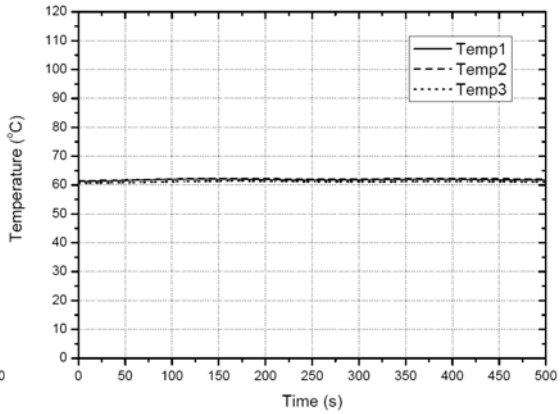

(b) C60-2

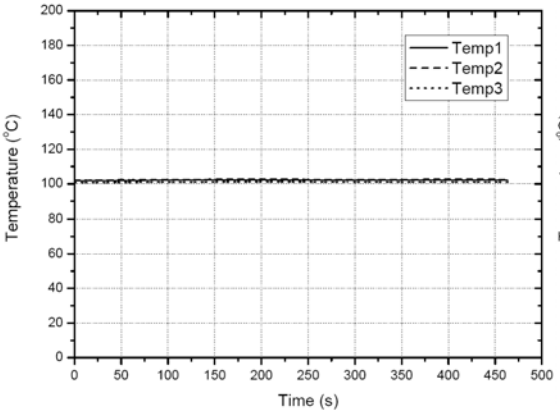

(c) C100-1

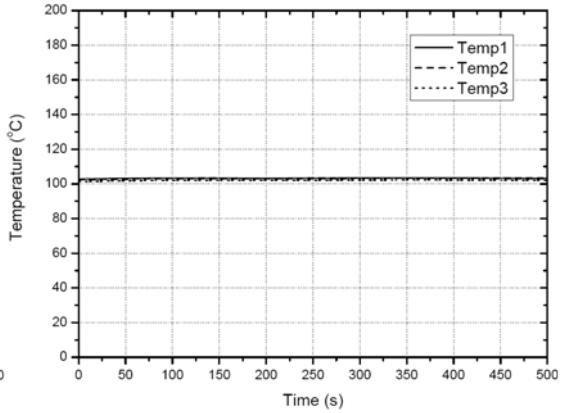

(d) C100-2

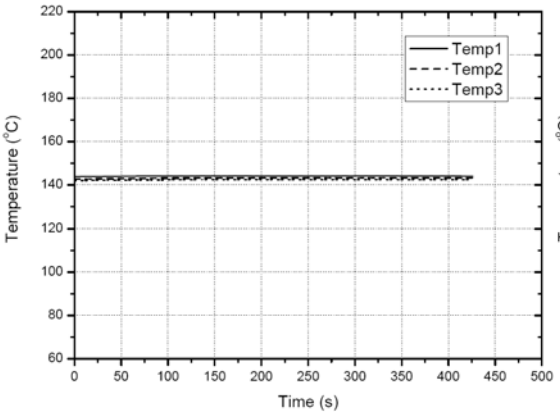

(e) C140-1

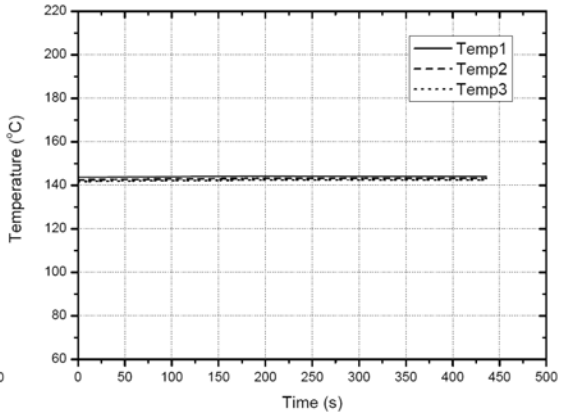

(f) C140-2

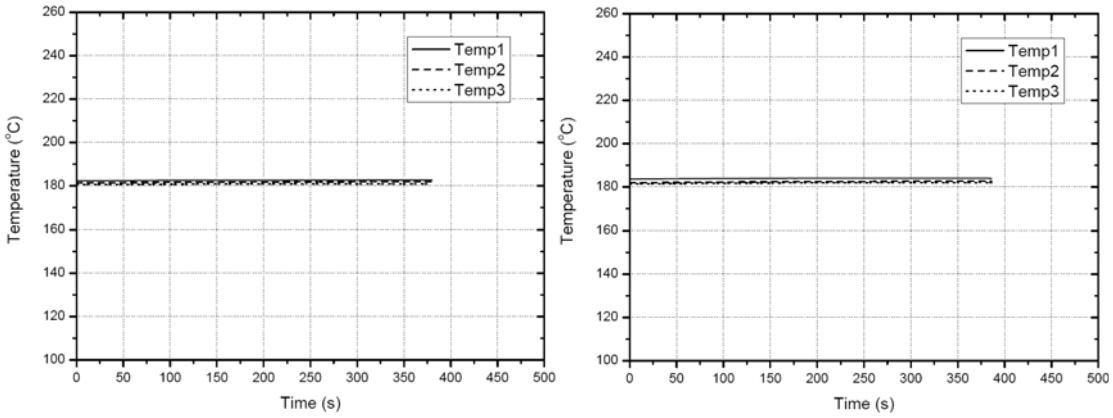

(g) C180-1 (h) C180-2

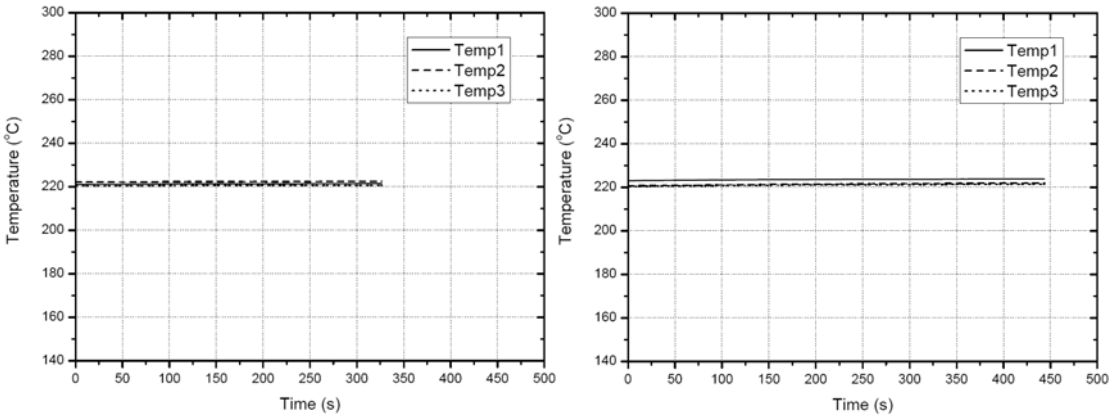

(i) C220-1 (j) C220-2

Fig. 18. Temperature measurements from reference specimen for each specimen in compressive experiments

The typical failure mode is shown in Fig. 19 for all the scenarios.

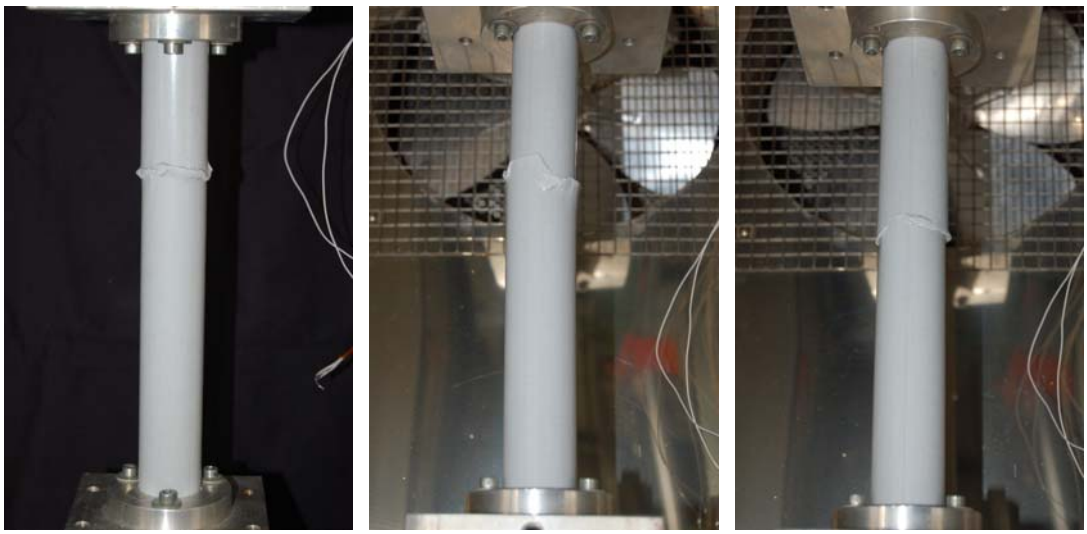

(a) C100-1 (b) C100-2 (c) C140-1

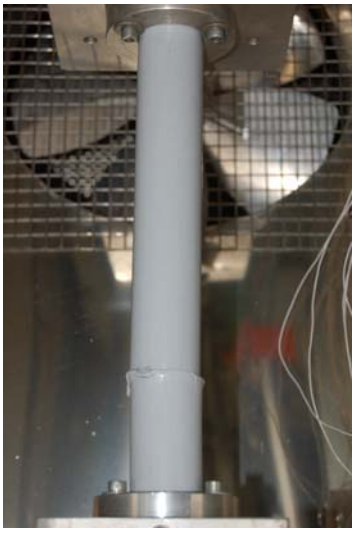

(d) C140-2

(e) C180-1

(f) C180-2

(g) C220-1

(h) C220-2

(i) Typical damaged specimens

Fig. 19. Failure modes of typical specimens

The nominal compressive strength, f_c, can be estimated as follows:

$$f_c(T) = \frac{P_U(T)}{A} \tag{2}$$

where $P_U\ (T)$ is the ultimate load at different temperatures. Thus the measured temperature-dependent nominal compressive strength was obtained, as shown in Fig. 20.

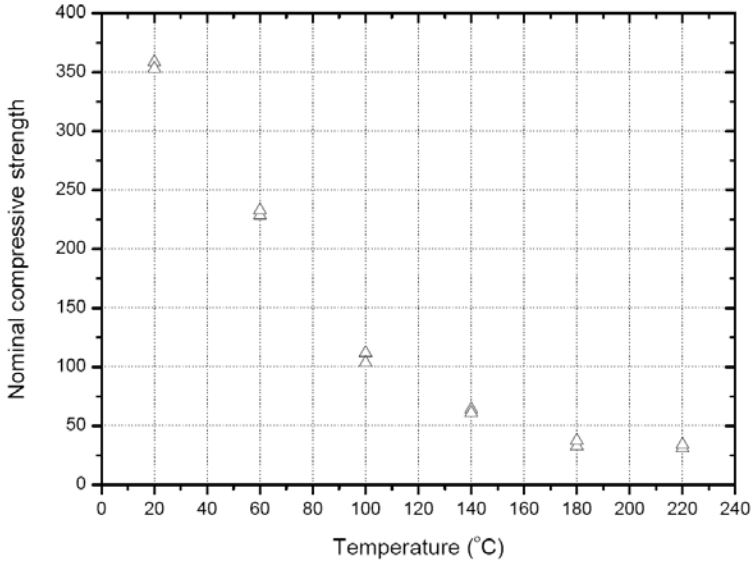

Fig. 20. Temperature-dependent nominal compressive strength for all specimens in compressive experiments

Appendix B

Experimental investigations concerning pultruded GFRP tubes with liquid-cooling system under combined temperature and compressive loading

B.1 Description of specimens

B.1.1 Materials and basic elements

The pultruded GFRP tubes were the same as those used for the compressive experiments in Appendix A.3, with the same fixed-end setup configuration as shown in Fig. 1(a). This fixation setup incorporated a water circulation system, indicated in green in Fig. 1(b).

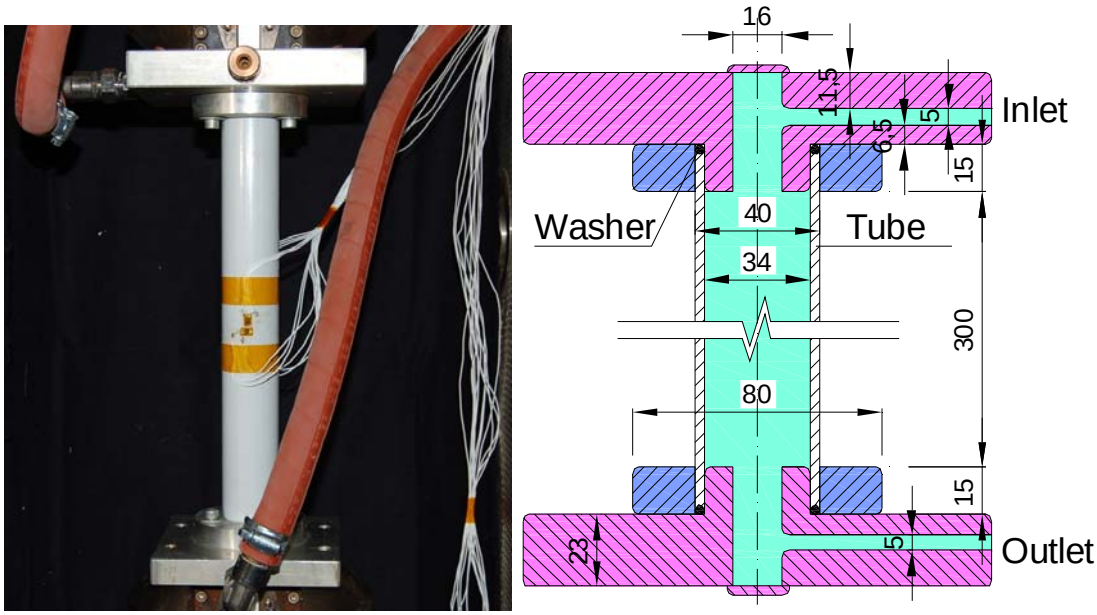

(a) Fixed-end setup (b) Water circulation system

Fig. 1. Fixed-end setup and water circulation system for GFRP tubes

B.1.2 Experimental scenarios

The experimental program comprised two parts: thermal response experiments and mechanical response experiments, with and without the water-cooling system for each part as summarized in Table 1.

	TN	TC1	TC2	MN1-1/2	MN2-1/2	MC1-1/2	MC2-1/2	MC3-1	MC4-1
Load level (kN/% of SLS load)	0/0	0/0	0/0	68/100	34/50	68/100	68/100	51/75	34/50
Fire protection	no	yes	yes	no	no	yes	yes	yes	yes
Flow rate (cm/s)	-	8	20	-	-	8	20	20	20
Increase in water temperature (°C)	-	-	-	-	-	5.6	2.1	-	-
Failure time for specimens 1/2 (min)	-	-	-	6.8/ 7.4	13.6/ 12.4	72.1/ 71.8	157.3/ 170.0	> 525	> 250

Table 1. Specimens and parameters for thermal response and structural endurance experiments (TN: thermal response scenario without water cooling; TC: thermal response scenarios with water cooling; MN: mechanical response scenarios without water cooling; MC: thermal response scenarios with water cooling. SLS load: load in serviceability limit state.)

As seen in Table 1, different load levels were considered in the mechanical response experiments. The SLS load, P_{SLS}, was determined by Eq. (1):

$$P_{SLS} = \frac{f_c \cdot A}{\gamma_M \cdot \gamma_F} = 68\text{kN} \quad (1)$$

where γ_M is the resistance factor,

$$\gamma_M = \gamma_{M,1} \cdot \gamma_{M,2} \cdot \gamma_{M,3} = 1.15\times1.1\times1.0=1.26 \quad (2)$$

$\gamma_{M,1}$=1.15 (properties derived from tests), $\gamma_{M,2}$=1.1 (pultruded material), and $\gamma_{M,3}$=1.0 (short-term loading). The load factor was assumed as being γ_F=1.4.

Two different flow rates were considered in the water-cooling scenarios: 8cm/s and 20cm/s, which were controlled by the water volume passing within a specified time unit.

Only one tube specimen was investigated for scenarios TN, TC1, TC2, MC3 and MC4, while two specimens were investigated for MN1, MN2, MC1 and MC2.

B.1.3 Instrumentation

In the thermal response experiments (TN, TC1 and TC2), the through-thickness temperature progressions were measured by six temperature sensors (PT100, Distrelec) in two groups (designated T1-1/2, T2-1/2 and T3-1/2) embedded in the reference specimen as shown in Fig. 2 (a). One temperature sensor was used to measure temperature progression in the environmental chamber, and one for the temperature progression of the water coming through the outlet (if any).

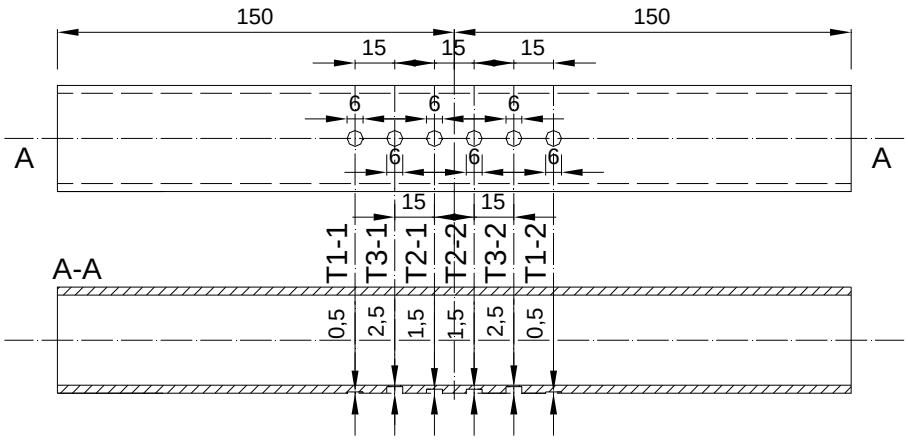

(a) Temperature sensors for thermal response experiments

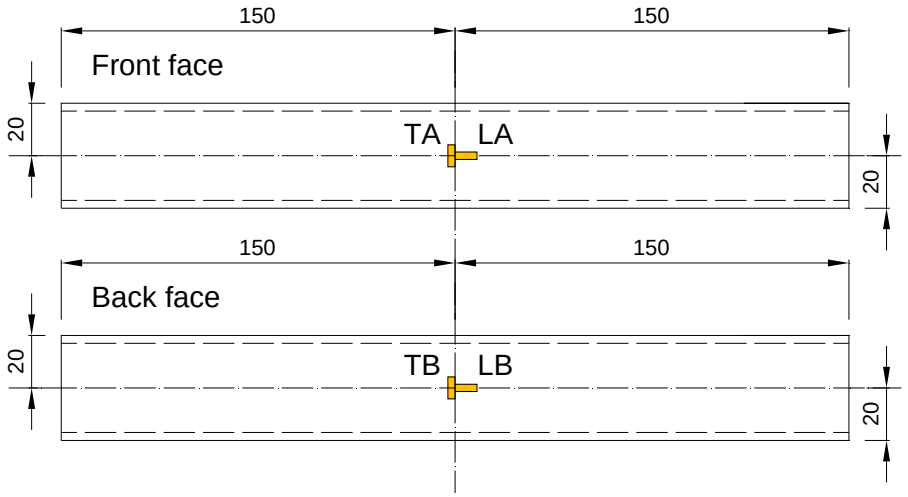

(b) Strain gages for mechanical response experiments

Fig. 2. Instrumentation for thermal response and mechanical response experiments

In the mechanical response experiments (MN1, MN2, MC1 to MC4), the tubes were not equipped with temperature sensors, only the chamber and water temperatures (if any) were recorded and it was assumed that through-thickness temperature progression was similar to that in the thermal response experiments. Four strain gages (LC11-3/120, HBM) were used for each mechanically tested specimen (except MC1-1): two in the longitudinal (pultrusion) direction (designated LA and LB), and two in the transverse direction (designated TA and TB) as shown in Fig. 2 (b). Another four strain gages (of the same type) were placed on another GFRP tube surface composed of the same materials, serving as compensating gages. The laminate was placed in the same chamber and subjected to the same

thermal loading. The prescribed value of the thermal expansion coefficient for the strain gages was 12.6×10^{-6}/°C for data acquisition in CatMan®, and the k-factor was taken from the strain gage data sheet. It should be noted that the measured strains may not reliably represent the mechanical strains due to the difference between the temperature progressions at the strain gage locations and those at the compensating gage locations, this effect being especially apparent in the case of the water-cooled specimens. However, since the ultimate load and time-to-failure were the most significant considerations in this investigation, no further attention was paid to strain measurements. The load-displacement curves were recorded for each specimen.

B.2 Experimental program

B.2.1 Temperature response experiments (TN, TC1 and TC2)

In these scenarios, the specimens were placed in free mode in the environmental chamber of a 100-kN Instron universal 8800 hydraulic machine (temperature range and accuracy of the chamber: -40°C to 250°C, ±2°C). Water was supplied by the fire plumbing of the test laboratory, and the flow rates were controlled by the water volume passing within a specified time unit. As shown in Fig. 2, the water passed through the inlet, flowed through the specimen, and then through the outlet. The thermal loading was applied when the outlet water temperature reached a constant value (i.e. when thermal equilibrium was achieved between the water temperature at the inlet (10°C) and the ambient temperature of the specimen). A heating rate of approximately 5°C/min was applied until the target temperature of 220°C was attained (selected as being between glass transition and decomposition temperatures), and the through-thickness temperatures of the specimens were stabilized. The temperature progressions of the chamber and water coming through the outlet were recorded.

B.2.2 Mechanical response experiments (MN1, MN2 and MC1 to MC4)

The tubes were fully fixed as shown in Fig. 1. In each scenario, the specimen was first loaded in a load-control mode to a prescribed level: 100%, 75%, and 50% of the SLS (serviceability limit state, see Table 1) load as shown in Fig. 2. The load was then kept constant during the subsequent thermal loading process. When the load level was reached, water was circulated at the same flow rates as those used in the thermal response experiments, see Table 1. Thermal loading was then applied (set as time t=0) according to the predefined temperature-time curve (the same as that defined in the thermal response experiments) until ultimate failure occurred or the prescribed time duration was reached.

B.3 Experimental results

B.3.1 TN, TC1 and TC2

The time-dependent temperature progressions measured by the temperature sensors are summarized in Figs. 3 to 5 for specimens TN, TC1 and TC2 respectively.

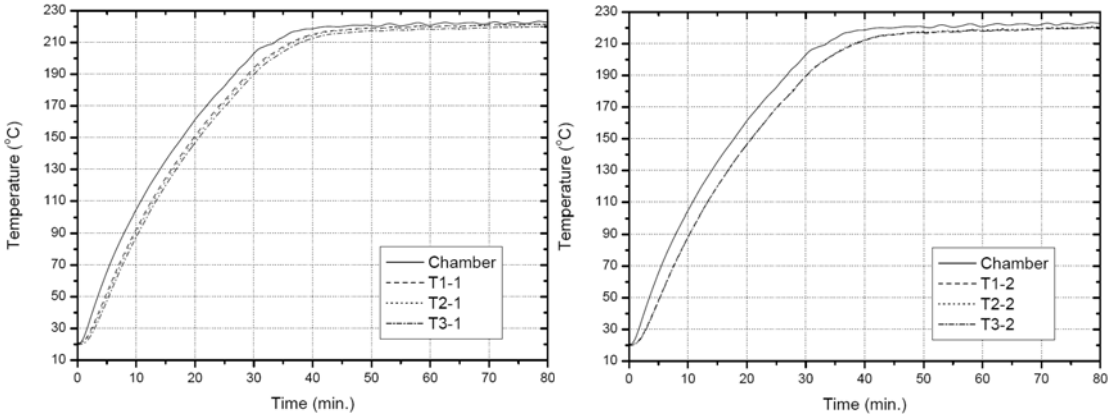

(a) Group1 (b) Group2

Fig. 3. Time-dependent chamber temperature and through-thickness temperature progression for non-cooled specimen TN

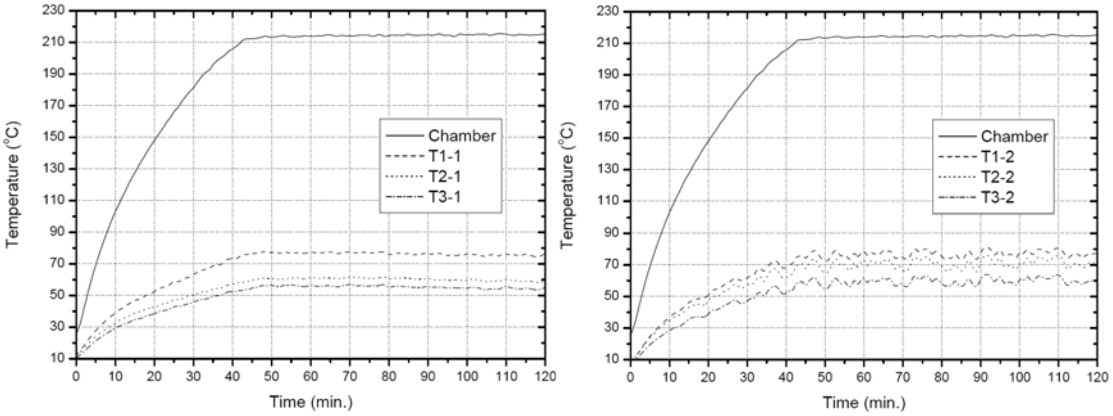

(a) Group1 (b) Group2

Fig. 4. Time-dependent chamber temperature and through-thickness temperature progression for water-cooled specimen TC1

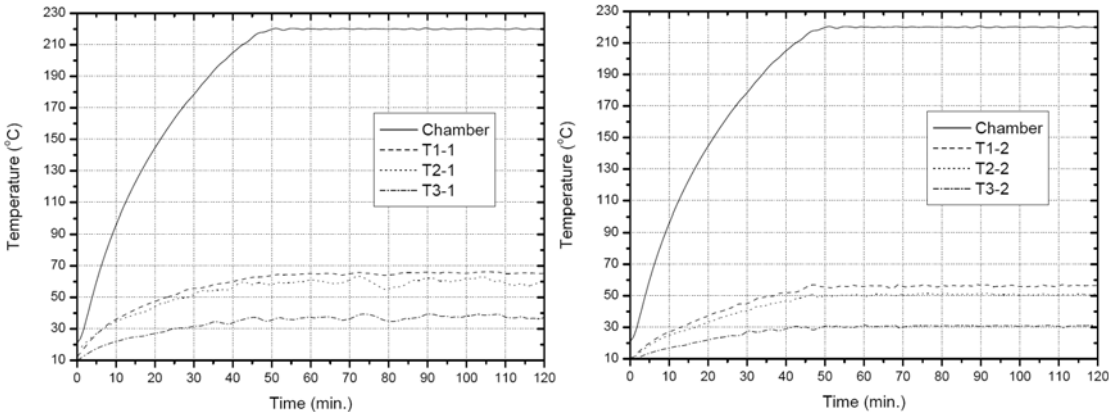

(a) Group1 (b) Group2

Fig. 5. Time-dependent chamber temperature and through-thickness temperature progression for water-cooled specimen TC2

B.3.2 MN1

The load-displacement curves for MN1-1 and 2 before thermal loading (i.e. before time t=0) are shown in Fig. 6; the load-strain curves before thermal loading are shown in Fig. 7; the time-dependent chamber temperature curves are shown in Fig. 8; the time-dependent load curves during thermal loading are shown in Fig. 9; the time-dependent axial displacement curves are shown in Fig. 10 and the time-dependent strain curves are shown in Fig. 11. Fig. 12 shows the failure modes.

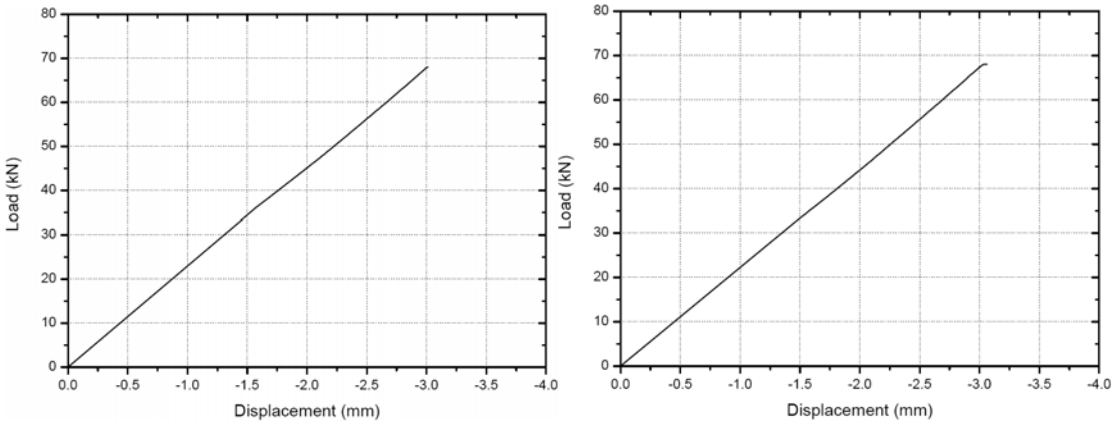

(a) MN1-1 (b) MN1-2

Fig. 6. Load-displacement curves for scenario MN1 before thermal loading (i.e. before time t=0; negative values indicate shortening)

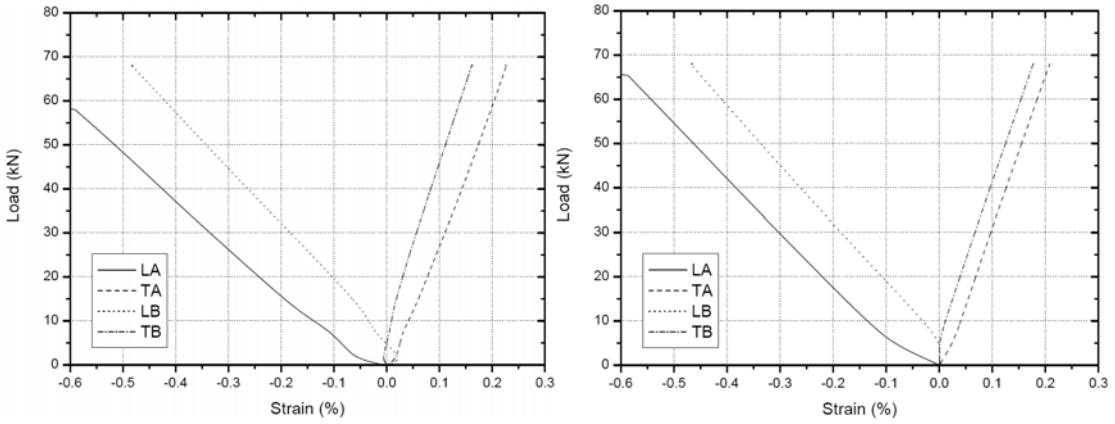

(a) MN1-1 (b) MN1-2

Fig. 7. Load-strain curves for scenario MN1 before thermal loading (i.e. before time t=0)

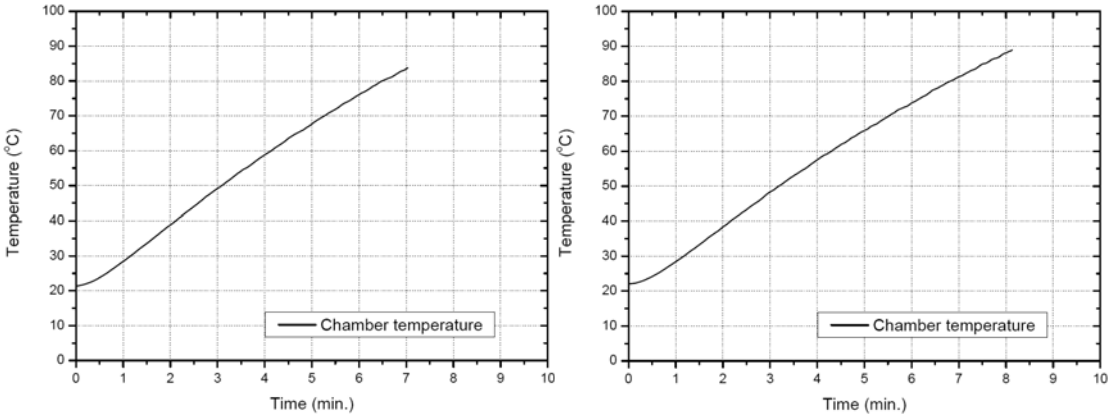

(a) MN1-1 (b) MN1-2

Fig. 8. Time-dependent chamber temperature progression for scenario MN1

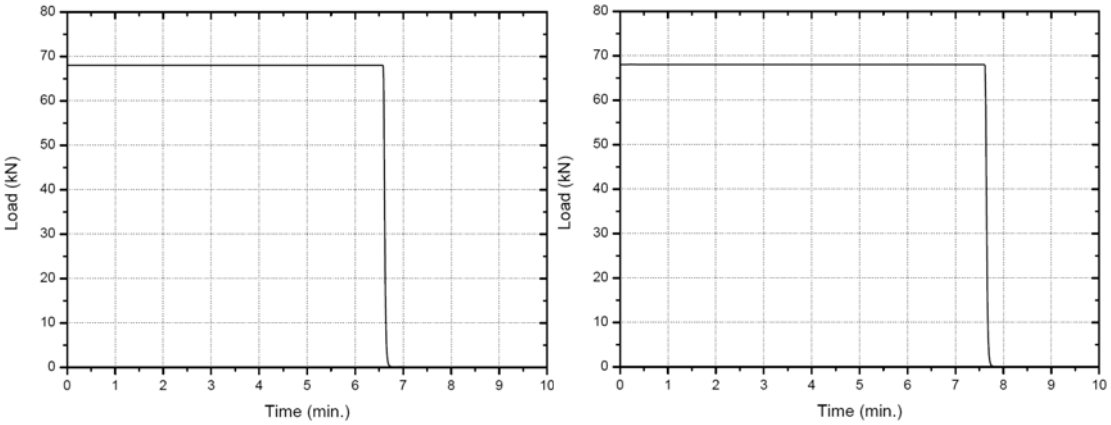

(a) MN1-1 (b) MN1-2

Fig. 9. Time-dependent load curves for scenario MN1 (failure times were identified in Table 1)

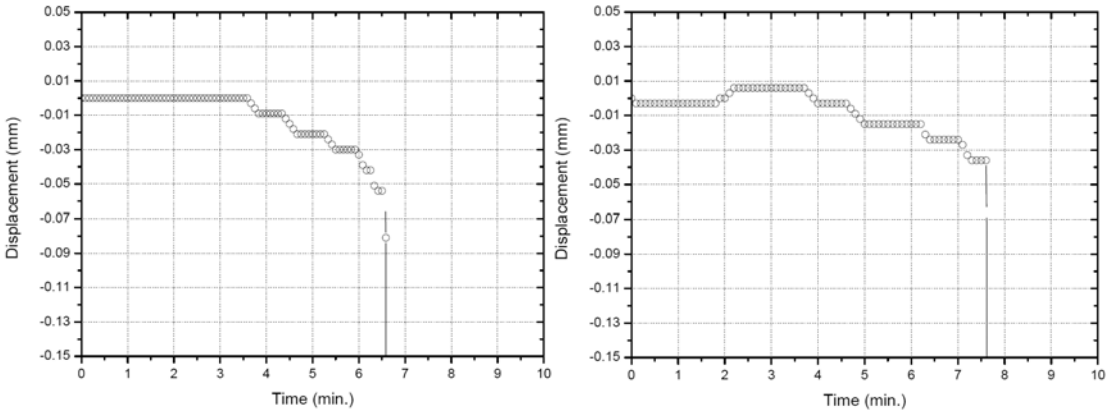

(a) MN1-1 (b) MN1-2

Fig. 10. Time-dependent displacement curves for scenario MN1 (negative values indicate shortening)

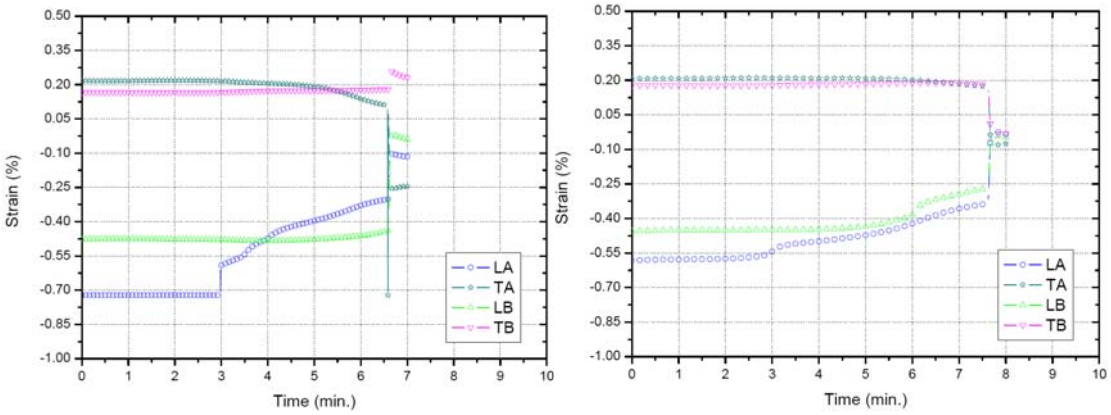

(a) MN1-1 (b) MN1-2

Fig. 11. Time-dependent strain curves for scenario MN1

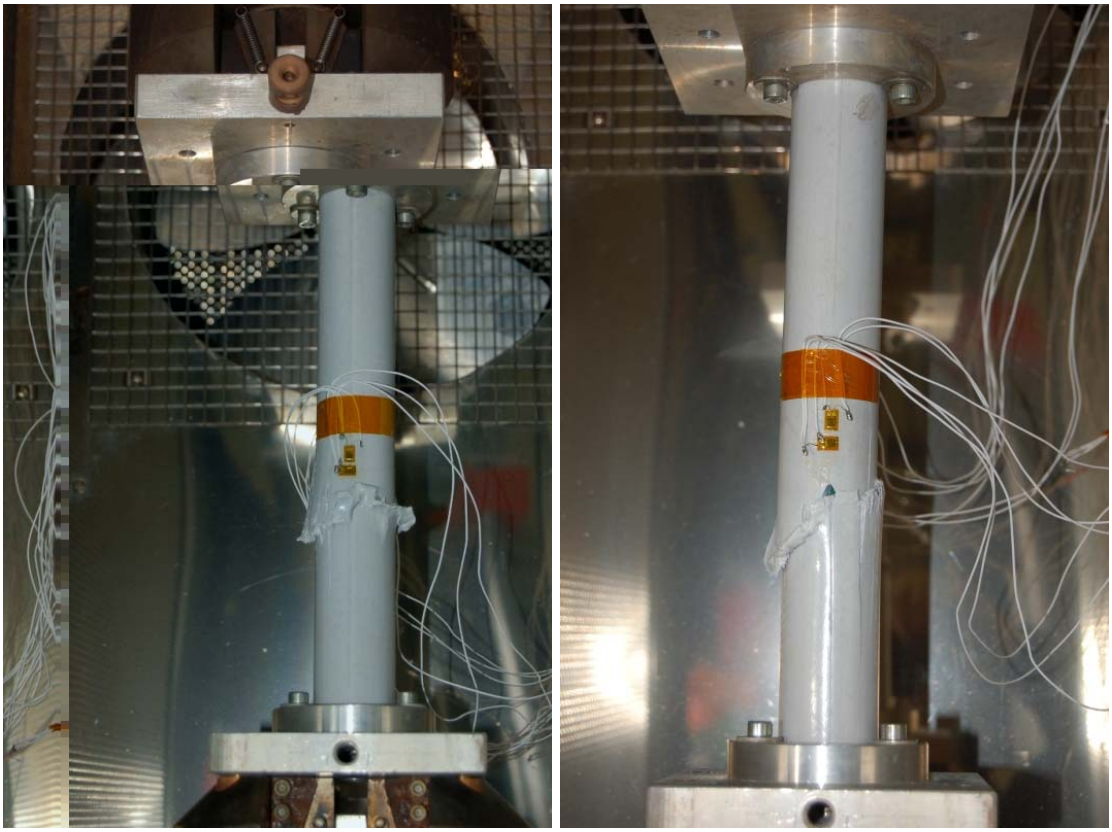

(a) MN1-1 (b) MN1-2

Fig. 12. Failure modes for scenario MN1

B.3.3 MN2

The load-displacement curves for MN2-1 and 2 before thermal loading (i.e. before time t=0) are shown in Fig. 13 and the load-strain curves before thermal loading are shown in Fig. 14. The time-dependent chamber temperature curves are shown in Fig. 15, with the temperature progression showing a sudden decrease during the testing of MN2-2 because the chamber window was opened once at around 60°C. The time-dependent load curves during thermal loading are shown in Fig. 16; the time-dependent axial displacement curves are shown in Fig. 17 and the time-dependent strain curves are shown in Fig. 18. The failure modes are summarized in Fig. 19.

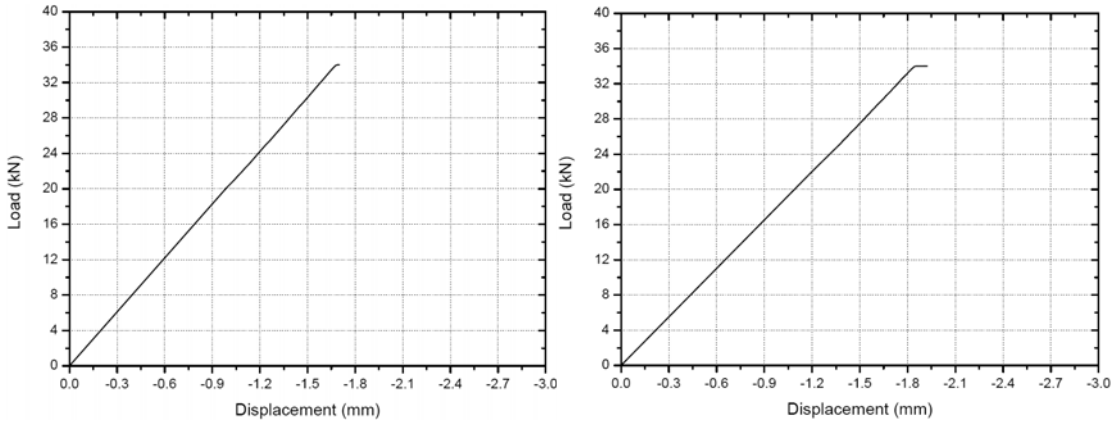

(a) MN2-1 (b) MN2-2

Fig. 13. Load-displacement curves for scenario MN2 before thermal loading (i.e. before time t=0; negative values indicate shortening)

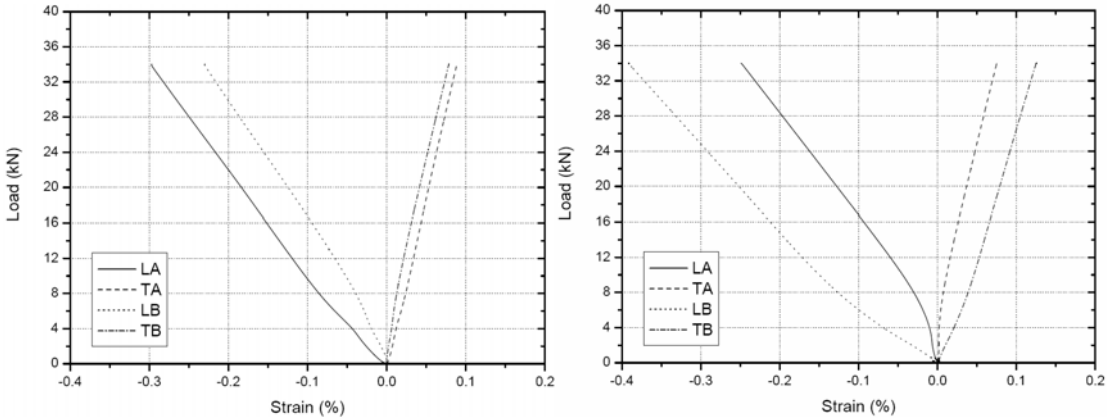

(a) MN2-1 (b) MN2-2

Fig. 14. Load-strain curves for scenario MN2 before thermal loading (i.e. before time t=0)

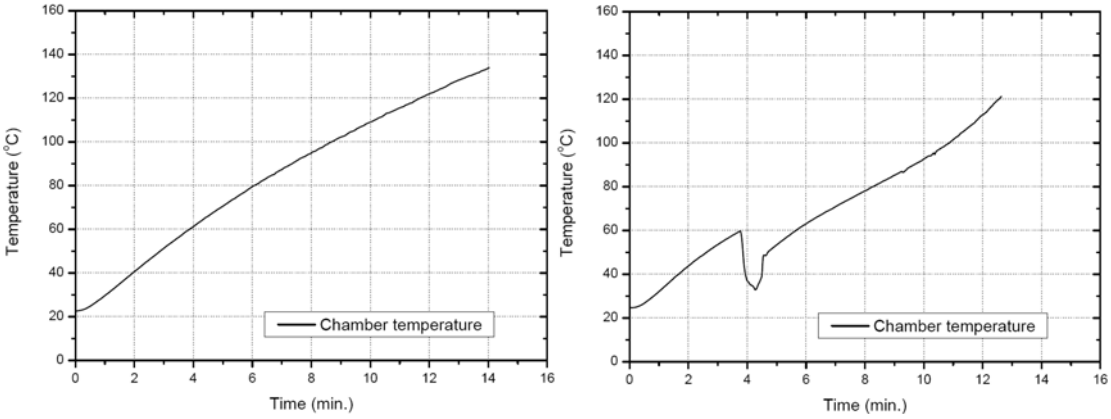

(a) MN2-1 (b) MN2-2

Fig. 15. Time-dependent chamber temperature progression for scenario MN2

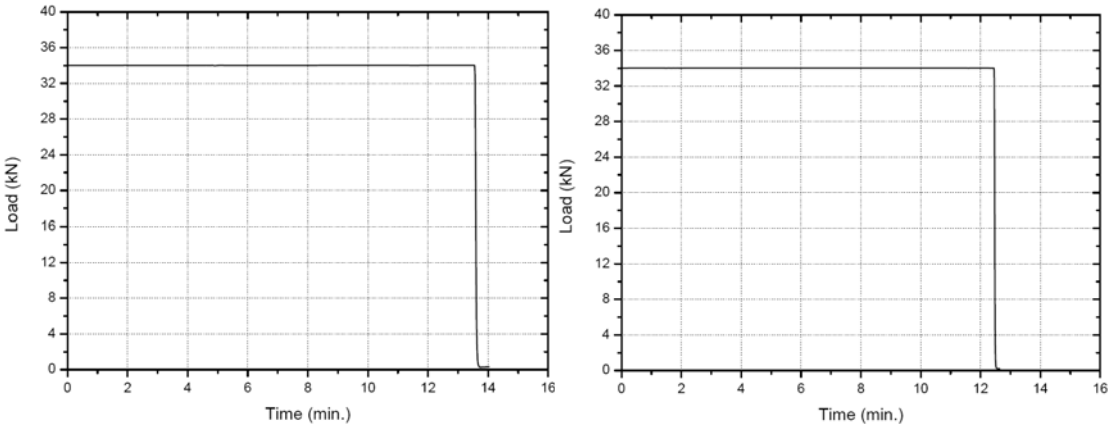

(a) MN2-1 (b) MN2-2

Fig. 16. Time-dependent load curves for scenario MN2 (failure times were identified in Table 1)

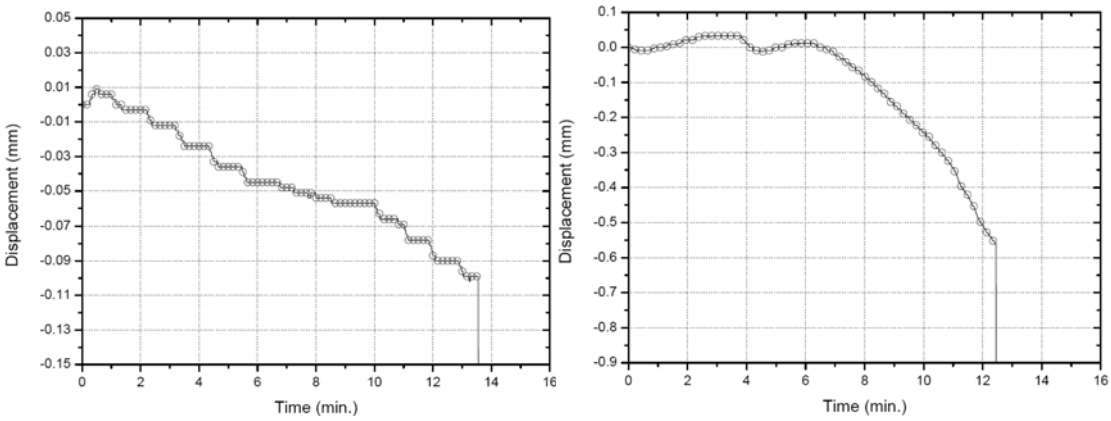

(a) MN2-1 (b) MN2-2

Fig. 17. Time-dependent displacement curves for scenario MN2 (negative values indicate shortening)

Compared with those of MN1-1/2 and MN2-1, the magnitude of the time-dependent displacement curve of MN2-2 seems too great, probably because the rubber washer was damaged (softened) due to thermal loading. New washers were used for the following tests.

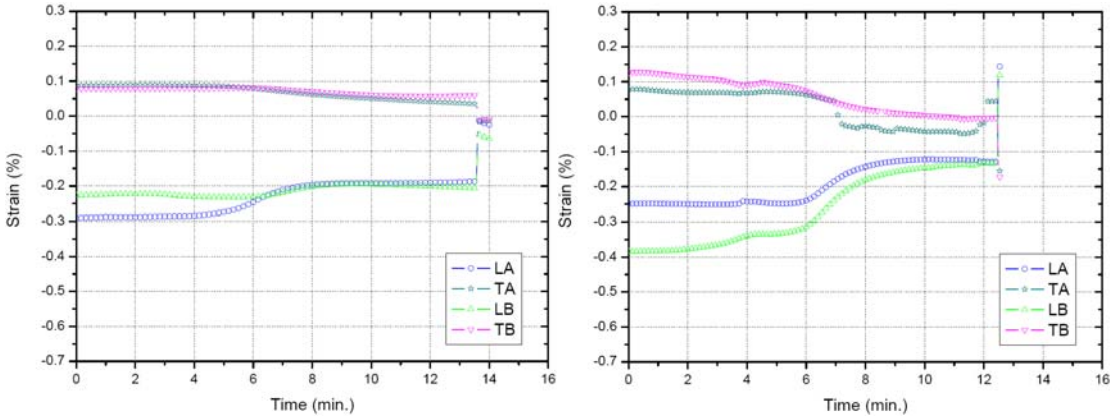

(a) MN2-1 (b) MN2-2

Fig. 18. Time-dependent strain curves for scenario MN2

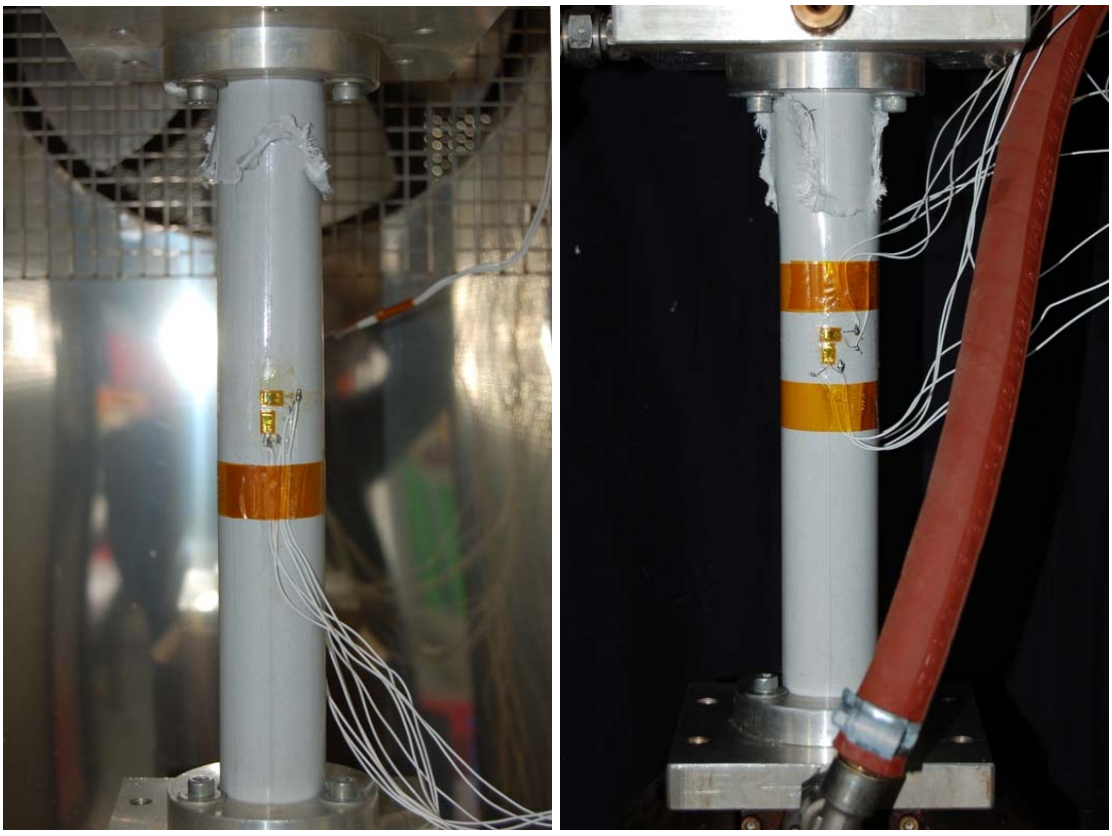

(a) MN2-1 (b) MN2-2

Fig. 19. Failure modes for scenario MN2

B.3.4 MC1

The load-displacement curves for MC1-1 and 2 before thermal loading (i.e. before time t=0) are shown in Fig. 20; the load-strain curves before thermal loading are shown in Fig. 21; the time-dependent chamber tempera-

ture curves are shown in Fig. 22; the time-dependent water temperature curves are shown in Fig. 23; the time-dependent load curves during thermal loading are shown in Fig. 24; the time-dependent axial displacement curves are shown in Fig. 25 and the time-dependent strain curves are shown in Fig. 26. The failure mode is shown in Fig. 27.

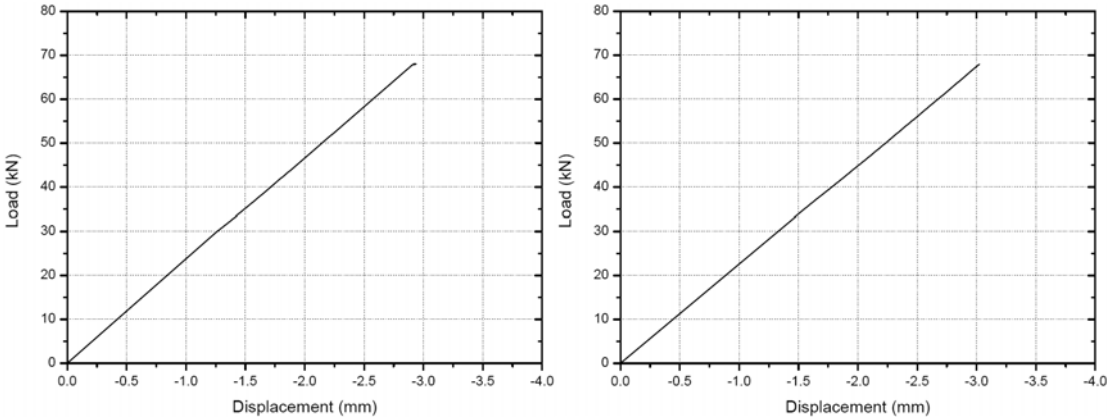

(a) MC1-1 (b) MC1-2

Fig. 20. Load-displacement curves for scenario MC1 before thermal loading (i.e. before time t=0; negative values indicate shortening)

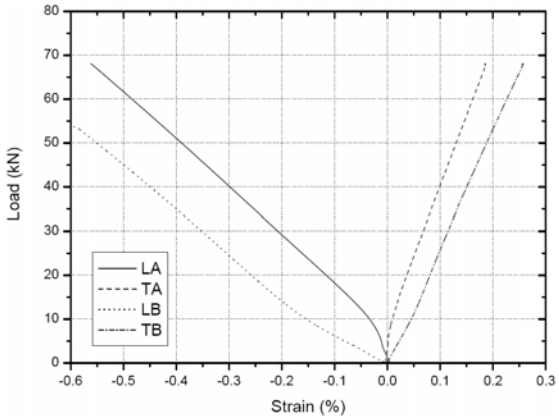

Fig. 21. Load-strain curves for specimen MC1-2 before thermal loading (i.e. before time t=0)

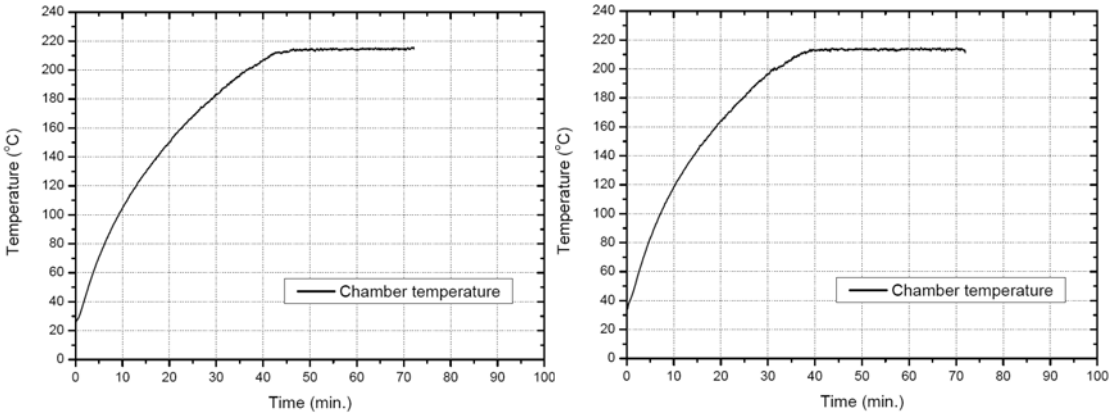

(a) MC1-1 (b) MC1-2

Fig. 22. Time-dependent chamber temperature progression for scenario MC1

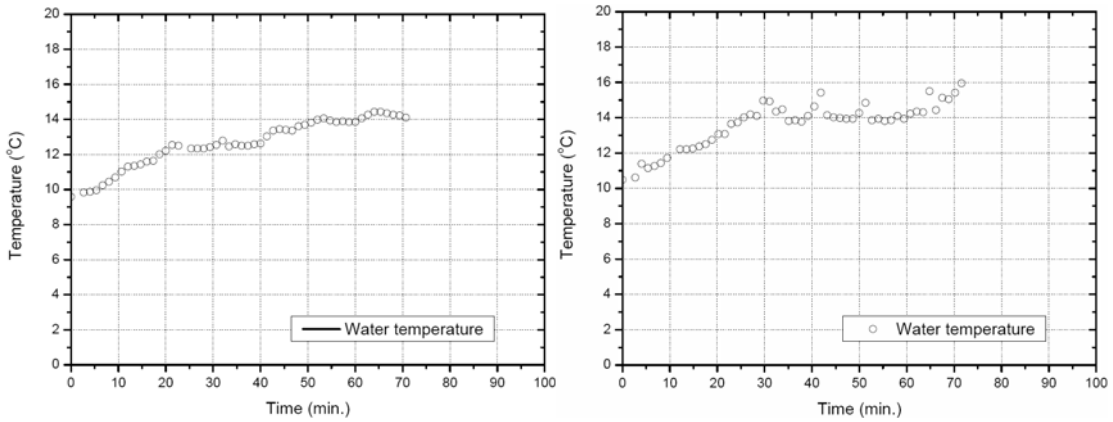

(a) MC1-1 (b) MC1-2

Fig. 23. Time-dependent water temperature progression for scenario MC1

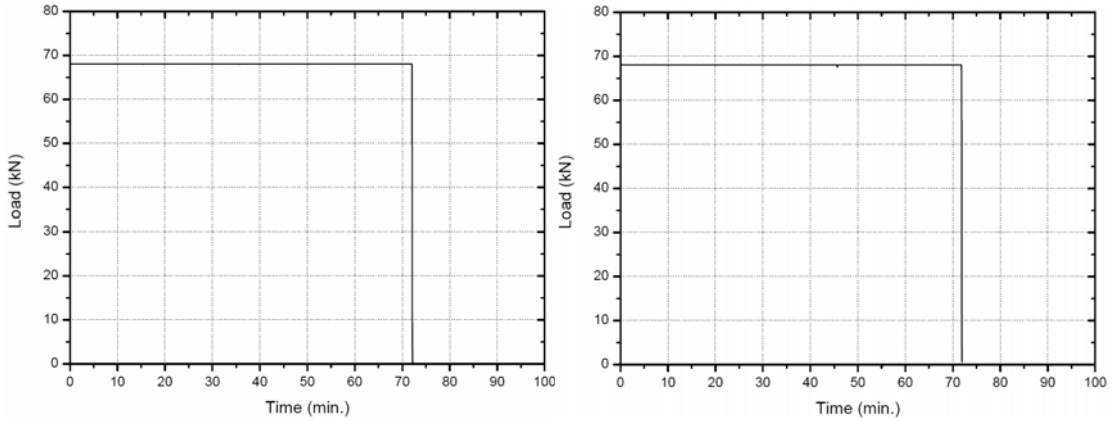

(a) MC1-1 (b) MC1-2

Fig. 24. Time-dependent load curves for scenario MC1 (failure times were identified in Table 1)

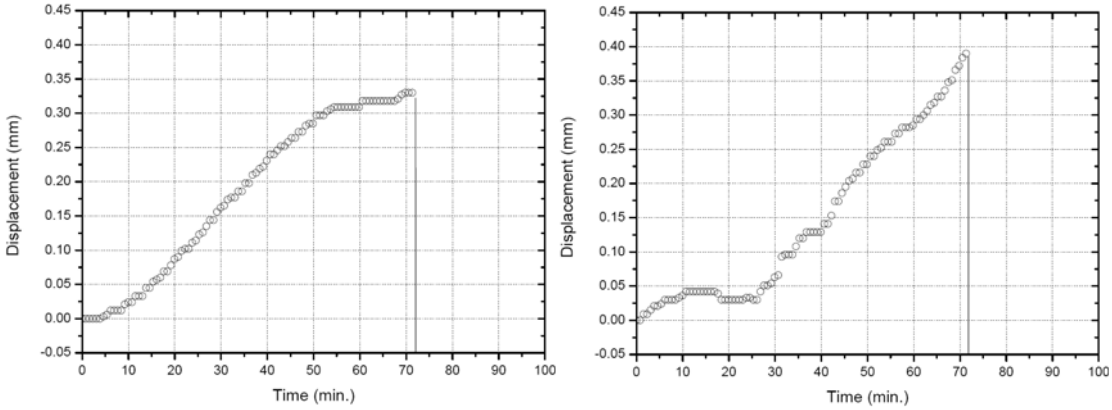

(a) MC1-1 (b) MC1-2

Fig. 25. Time-dependent displacement curves for scenario MC1 (positive values indicate elongation)

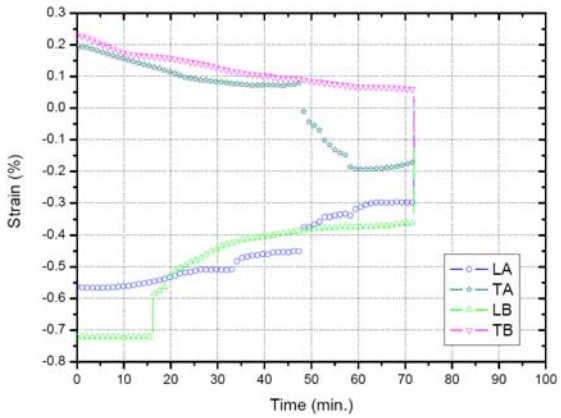

Fig. 26. Time-dependent strain curves for scenario MC1-2

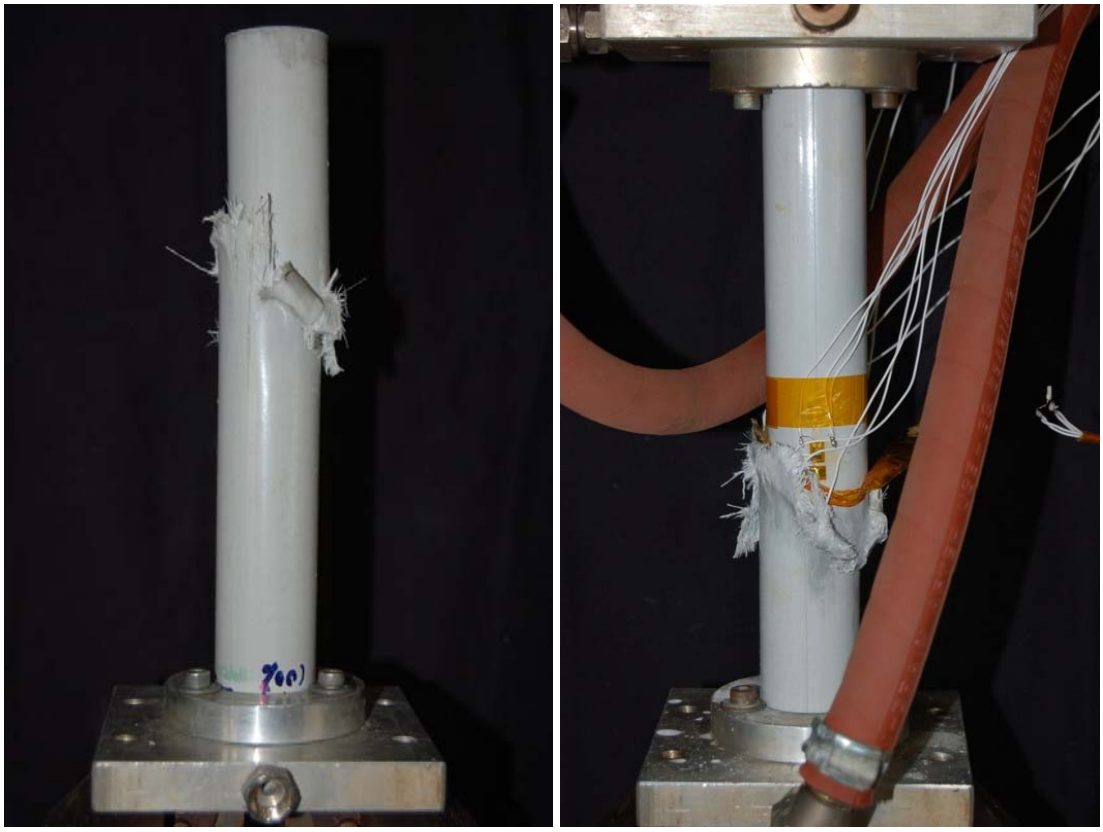

(a) MC1-1 (b) MC1-2

Fig. 27. Failure mode for scenario MC1

B.3.5 MC2

The load-displacement curves for MC2-1 and 2 before thermal loading (i.e. before time t=0) are shown in Fig. 28; the load-strain curves before thermal loading are shown in Fig. 29; the time-dependent chamber temperature curves are shown in Fig. 30; the time-dependent water temperature curves are shown in Fig. 31; the time-dependent load curves during thermal loading are shown in Fig. 32; the time-dependent axial displacement curves are shown in Fig. 33 and the time-dependent strain curves are shown in Fig. 34. The failure mode is summarized in Fig. 35.

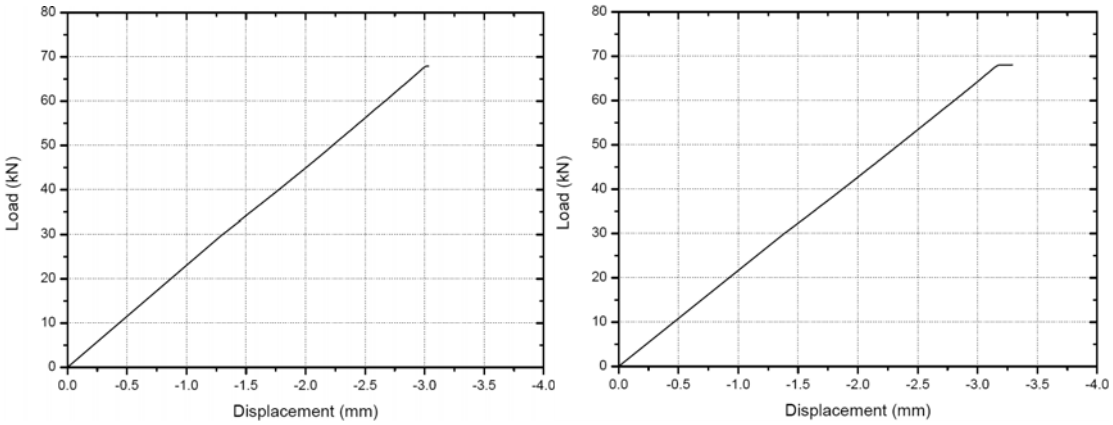

(a) MC2-1 (b) MC2-2

Fig. 28. Load-displacement curves for scenario MC2 before thermal loading (i.e. before time t=0; negative values indicate shortening)

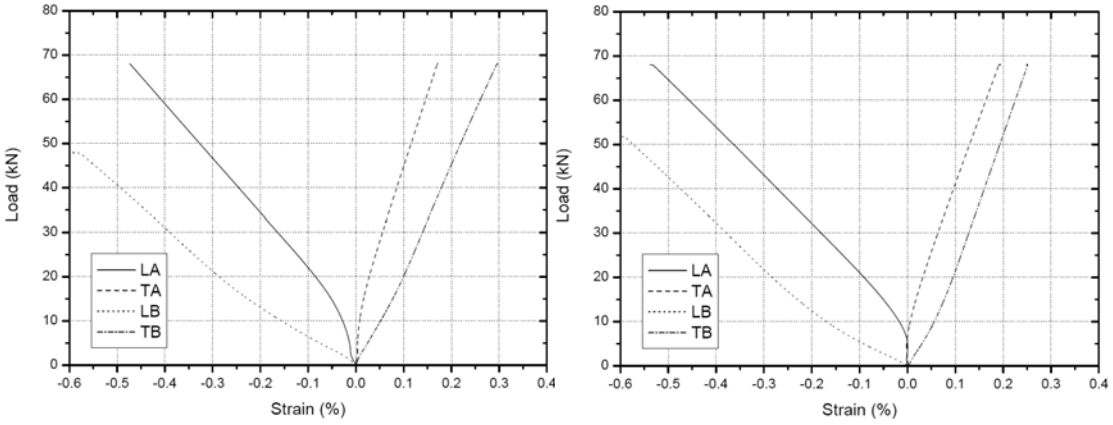

(a) MC2-1 (b) MC2-2

Fig. 29. Load-displacement curves for scenario MC2 before thermal loading (i.e. before time t=0)

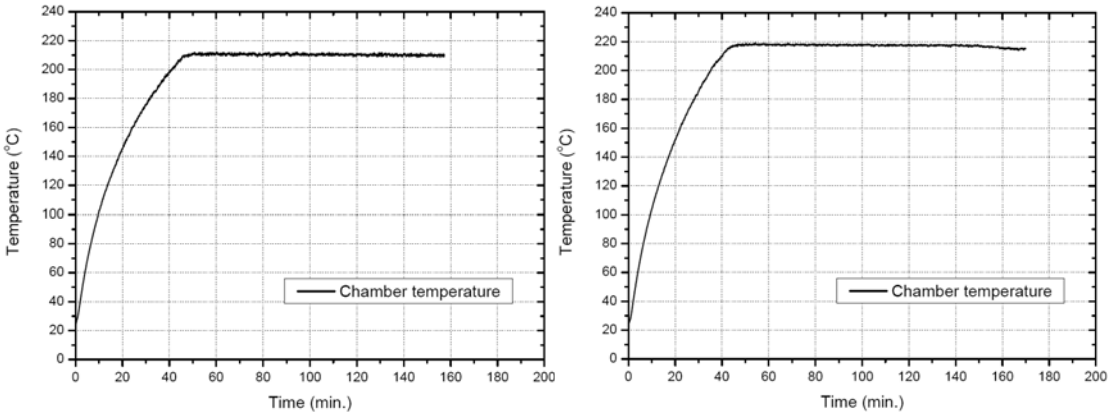

(a) MC2-1 (b) MC2-2

Fig. 30. Time-dependent chamber temperature progression for scenario MC2

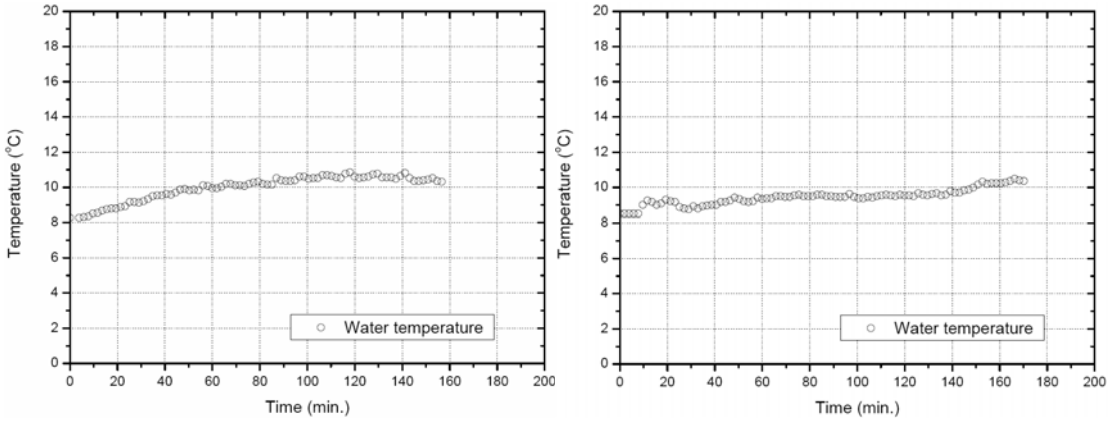

(a) MC2-1 (b) MC2-2

Fig. 31. Time-dependent water temperature progression for scenario MC2

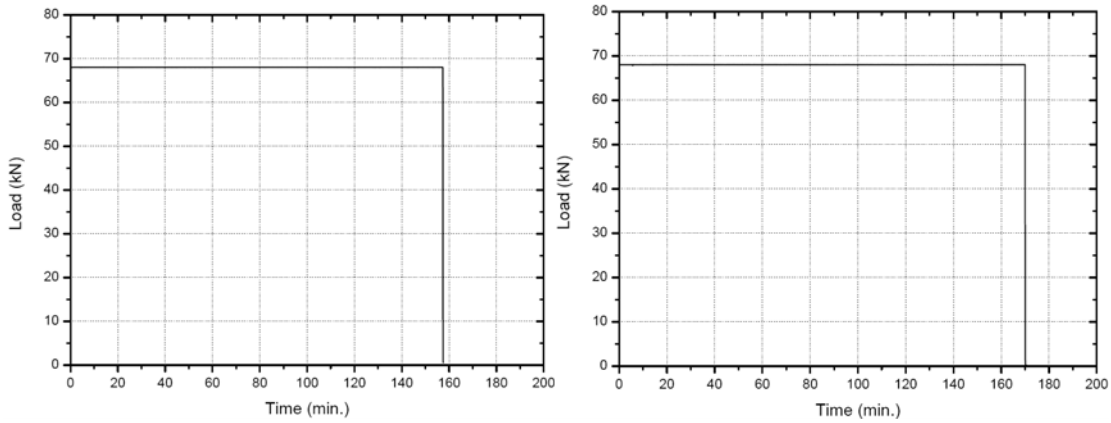

(a) MC2-1 (b) MC2-2

Fig. 32. Time-dependent load curves for scenario MC2 (failure times were identified in Table 1)

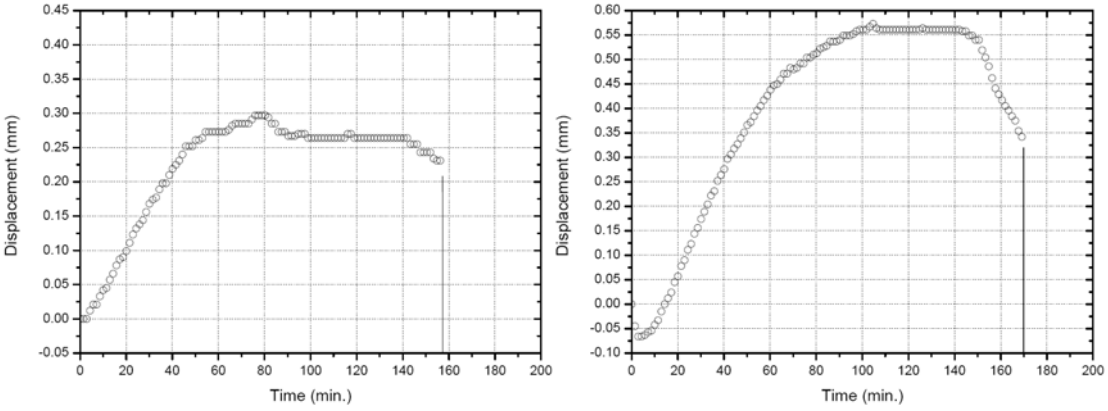

(a) MC2-1 (b) MC2-2

Fig. 33. Time-dependent displacement curves for scenario MC2 (positive values indicate elongation)

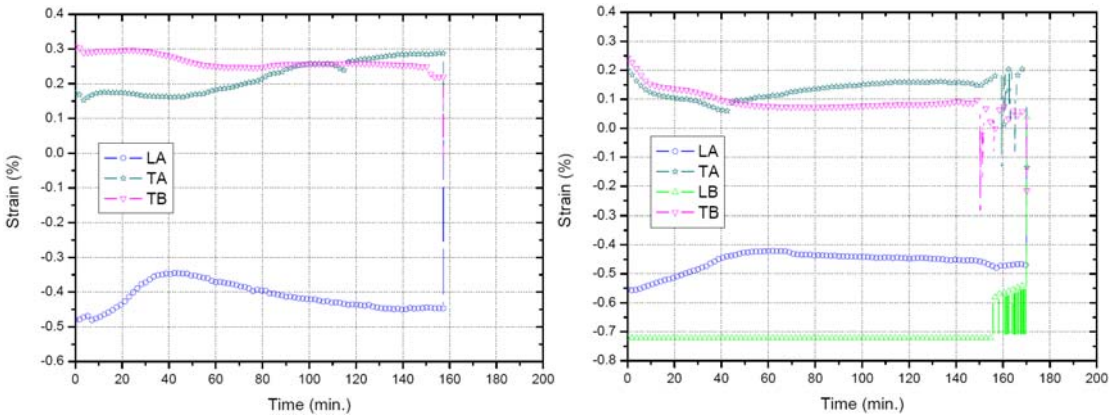

(a) MC2-1 (b) MC2-2

Fig. 34. Time-dependent strain curves for scenario MC2 (LB for MC2-1 was damaged after mechanical loading)

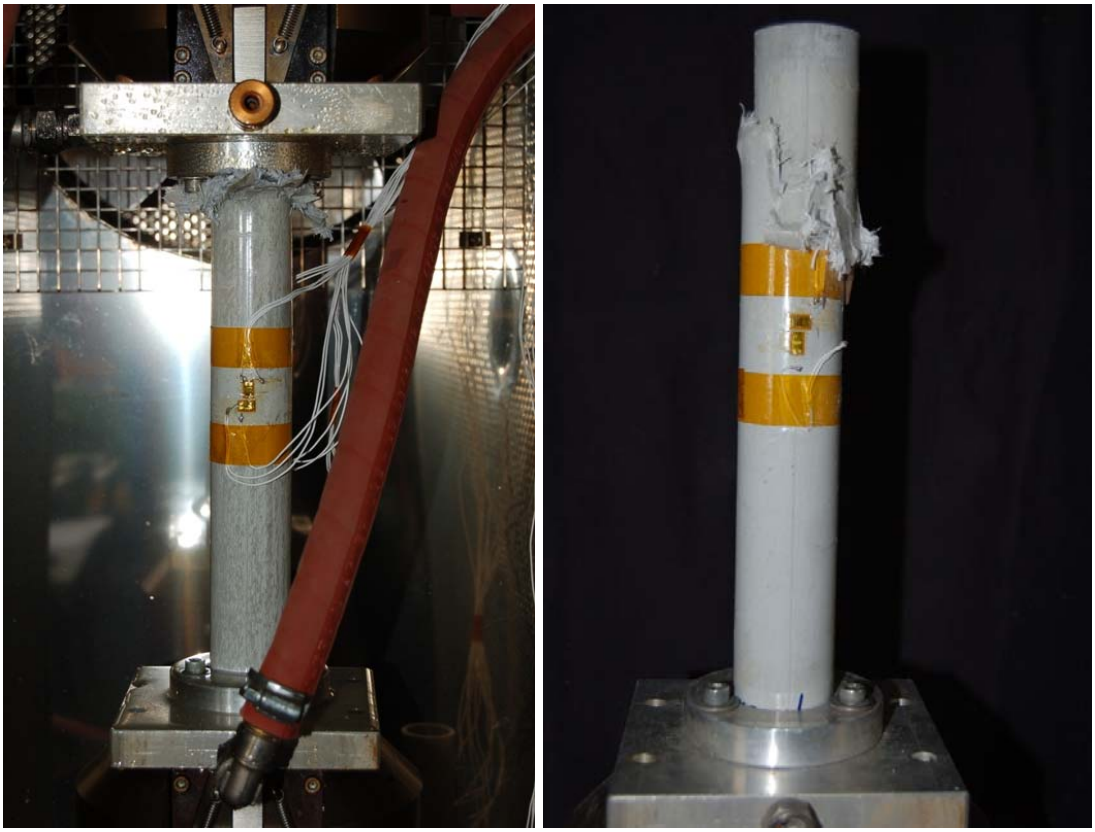

(a) MC2-1 (b) MC2-2

Fig. 35. Failure mode for scenario MC2

B.3.6 MC3 and MC4

The load-displacement curves for MC3-1 and MC4-1 before thermal loading (i.e. before time t=0) are shown in Fig. 36; the load-strain curves before

thermal loading are shown in Fig. 37; the time-dependent chamber temperature curves are shown in Fig. 38; the time-dependent water temperature curves are shown in Fig. 39; the time-dependent load curves during thermal loading are shown in Fig. 40; the time-dependent axial displacement curves are shown in Fig. 41 and the time-dependent strain curves are shown in Fig. 42.

Since failure did not occur during thermal exposure for MC3-1 and MC4-1, these two specimens were carefully removed from the chamber, and their post-fire status was visually inspected as shown in Fig. 43. The same fixation system was used on the Schenck machine (max. 1000 kN) for these two specimens as for the specimens in the compressive experiments in Appendix A.3. The axial compressive force was applied at a displacement rate of 1 mm/min up to specimen failure, and only the load-displacement curves were recorded and shown in Fig. 44 for MC3-1 and MC4-1 respectively. Fig. 45 shows the failure modes in the mechanical tests after thermal exposure for scenarios MC3 and MC4.

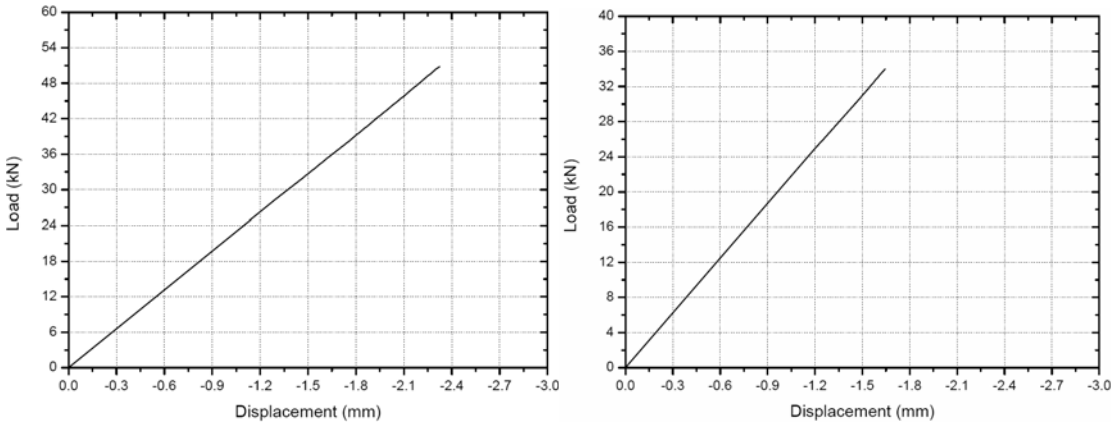

(a) MC3-1 (b) MC4-1

Fig. 36. Load-displacement curves for scenarios MC3 and MC4 before thermal loading (i.e. before time t=0; positive values indicate shortening)

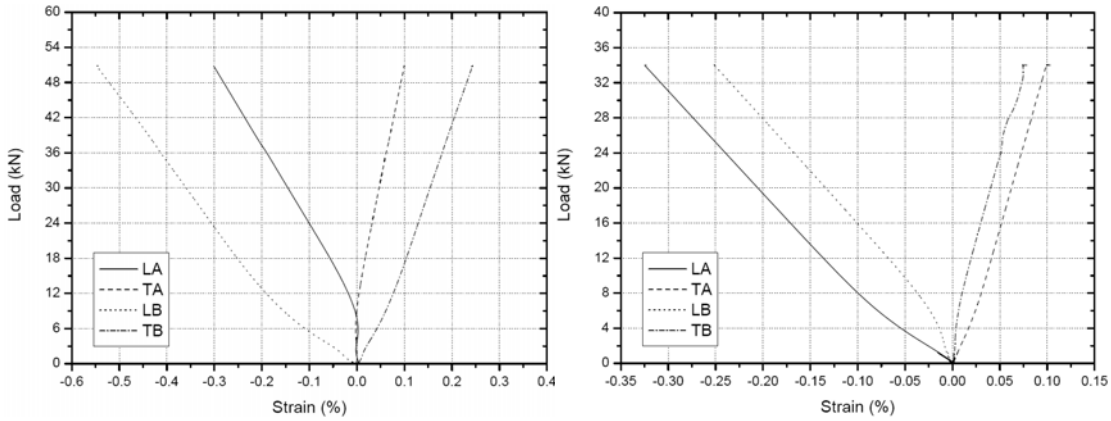

(a) MC3-1 (b) MC4-1

Fig. 37. Load-displacement curves for scenarios MC3 and MC4 before thermal loading (i.e. before time t=0)

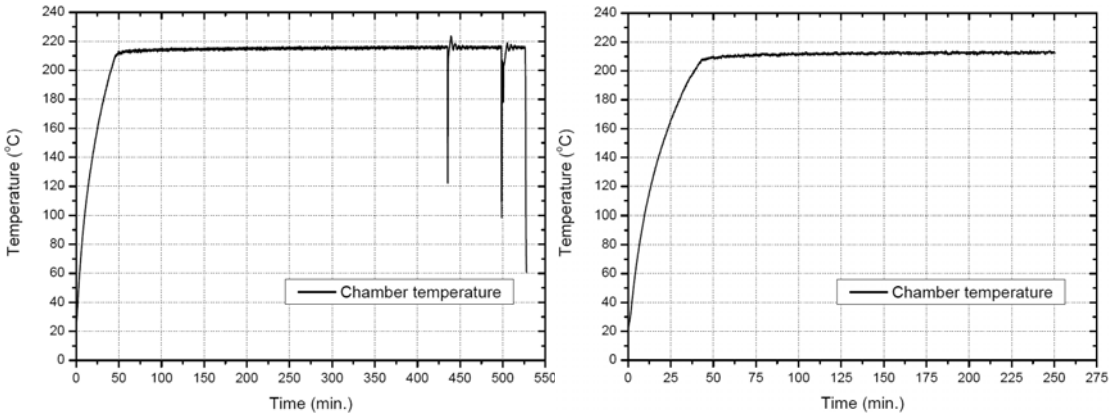

(a) MC3-1 (b) MC4-1

Fig. 38. Time-dependent chamber temperature progression for scenarios MC3 and 4

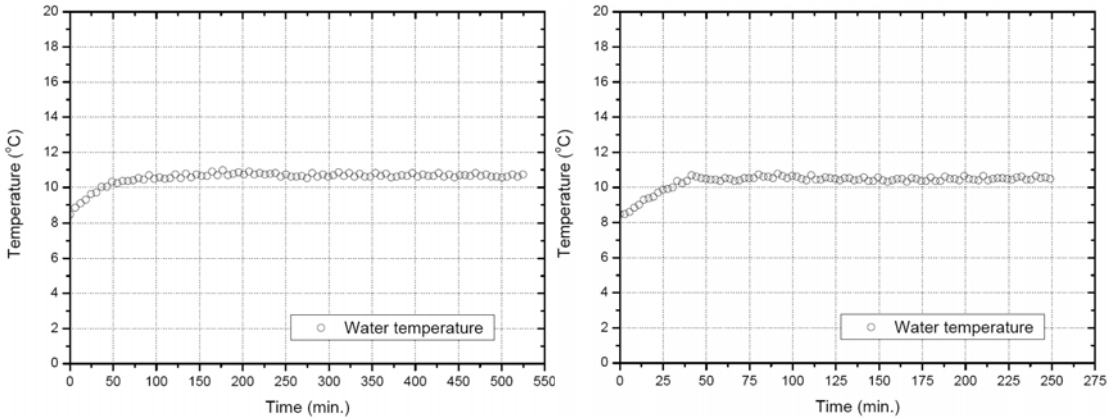

(a) MC3-1 (b) MC4-1

Fig. 39. Time-dependent water temperature progression for scenarios MC3 and MC4

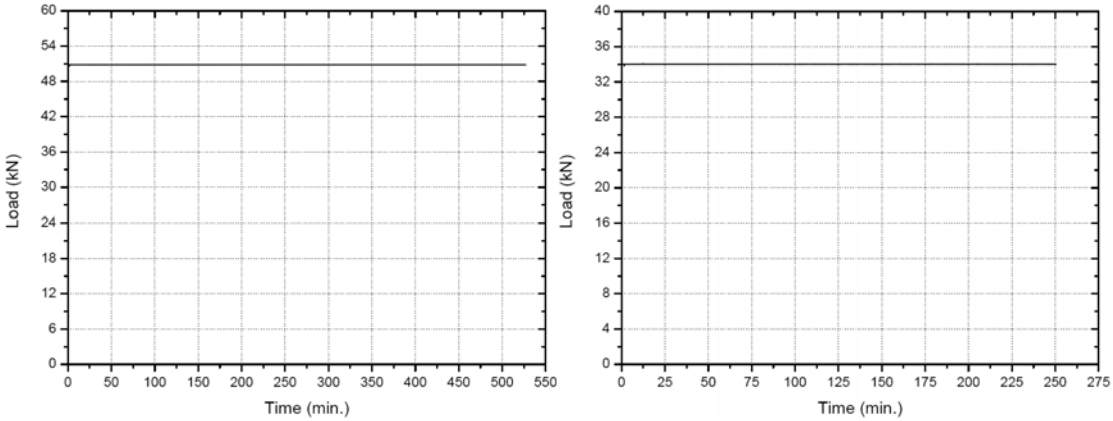

(a) MC3-1 (b) MC4-1

Fig. 40. Time-dependent load curves for scenarios MC3 and MC4 (failure did not occur during thermal exposure)

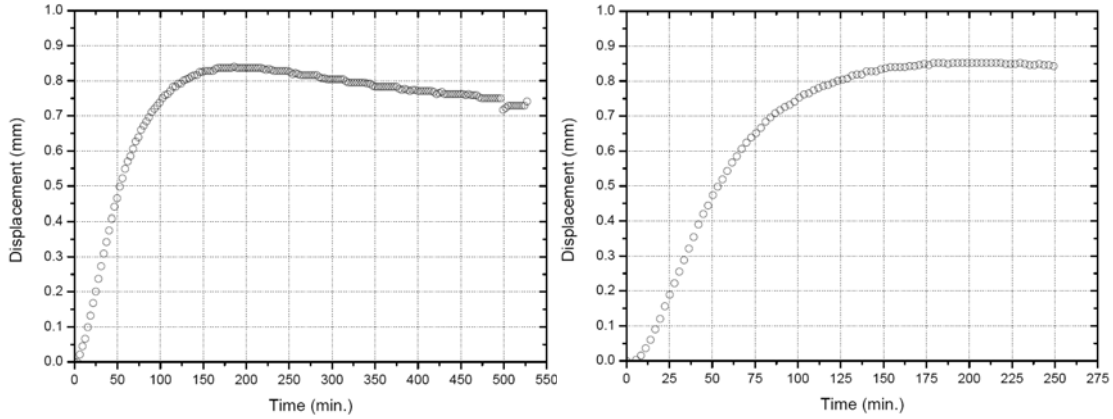

(a) MC3-1 (b) MC4-1

Fig. 41. Time-dependent displacement curves for scenarios MC3 and MC4 (positive values indicate elongation)

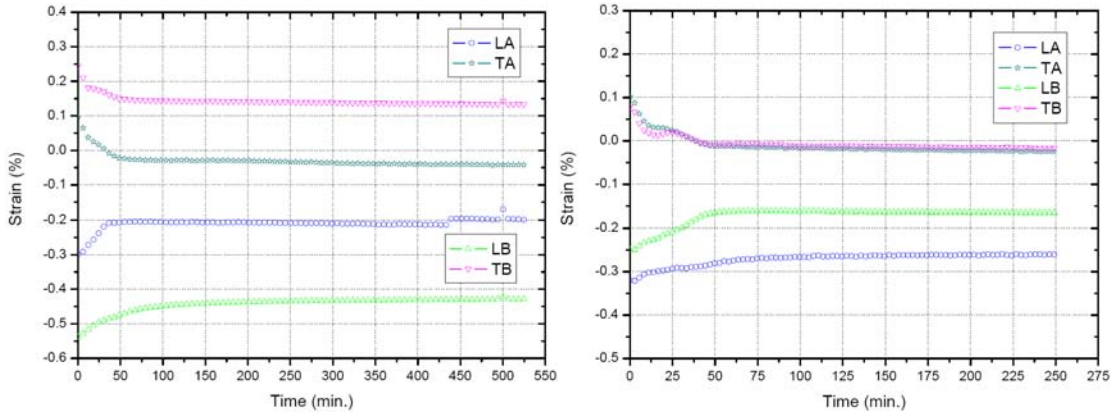

(a) MC3-1 (b) MC4-1

Fig. 42. Time-dependent strain curves for scenarios MC3 and MC4

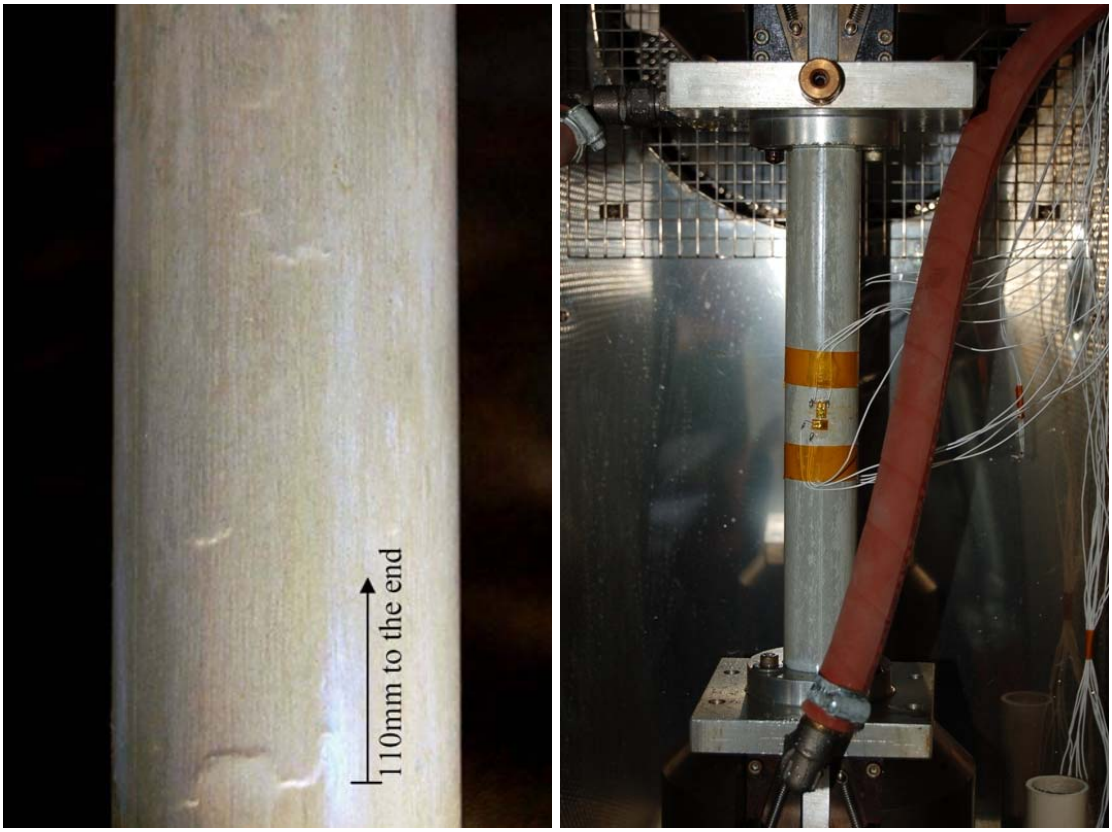

(a) MC3-1 (b) MC4-1

Fig. 43. Status after thermal exposure for scenarios MC3 and MC4 (failure did not occur during thermal exposure)

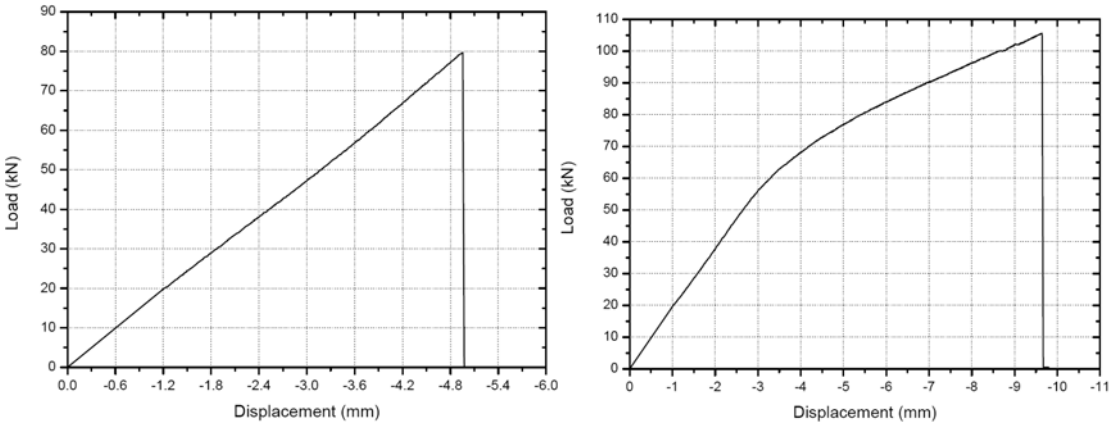

(a) MC3-1 (b) MC4-1

Fig. 44. Load-displacement curves for scenarios MC3 and MC4 after thermal loading (negative values indicate shortening)

(a) MC3-1 (b) MC4-1

Fig. 45. Failure modes in mechanical tests after thermal exposure for scenarios MC3 and MC4